Optimal synergy of multi-source data and hydraulic-hydrological models for the cartographic modeling of complex hydrosystems

Léo Pujol

To cite this version:

Léo Pujol. Optimal synergy of multi-source data and hydraulic-hydrological models for the cartographic modeling of complex hydrosystems. Environmental Engineering. Université de Strasbourg, 2022. English. NNT : . tel-03760662v1

HAL Id: tel-03760662
https://hal.science/tel-03760662v1

Submitted on 25 Aug 2022 (v1), last revised 9 Dec 2022 (v2)

UNIVERSITÉ DE STRASBOURG

ÉCOLE DOCTORALE: **MSII - Mathématiques, Sciences de l'Information et de l'Ingénieur**
Laboratoire ICube

THÈSE présentée par :
Léo Pujol
soutenue le 2 mai 2022

pour obtenir le grade de : **Docteur de l'université de Strasbourg**
Spécialité : **Hydrologie et hydraulique numérique**

OPTIMAL SYNERGY OF MULTI-SOURCE DATA AND HYDRAULIC-HYDROLOGICAL MODELS FOR THE CARTOGRAPHIC MODELING OF COMPLEX HYDROSYSTEMS

THÈSE dirigée par:	
M. GARAMBOIS Pierre-André	CR INRAE, Recover, AMU
M. MONNIER Jérôme	PR IMT, INSA Toulouse
M. MOSÉ Robert	PR, IUT Robert Schumann

RAPPORTEURES:	
Mme. DELENNE Carole	MCF UM, INRIA LEMON
Mme. SOARES-FRAZÃO Sandra	PR UCL, IMMC

AUTRES MEMBRES DU JURY:	
M. FLIPO Nicolas	DR UPSL, Mines ParisTech
Mme. LE BER Florence	DR ENGEES, ICUBE
Mme. ROUX Hélène	PR INPT, IMFT
M. WEILL Sylvain	MCF ENGEES, LHYGES

Contents

Résumé

Ces travaux de thèse s'intéressent à la modélisation hydrologique-hydraulique des réseaux hydrographiques et à l'intégration optimale de données multi-sources. La richesse informative croissante des jeux de données apportés par l'hydrométéorologie et la télédétection à haute résolution en complément des mesures in situ, est encore insuffisamment exploitée pour contraindre des modélisations hydrodynamiques fines à l'échelle des bassins. De telles représentations numériques sont pourtant cruciales pour l'estimation spatio-temporelle précise des états-flux, en vue de répondre à des enjeux socio-économiques majeurs comme la prévision des crues en contexte de changement climatique. Les quantités physiques d'intérêt vont des hydrogrammes de débit amonts et échanges latéraux jusqu'à leur traduction en hauteurs d'eau, vitesses et temps de submersion sur les plaines d'inondation en aval. De telles informations sont difficilement accessibles, en particulier pour les crues sur de larges territoires où de nombreux cours d'eau sont potentiellement non jaugés. Plusieurs problématiques sont reliées à la modélisation numérique hydrologique-hydraulique de bassin et à sa mise en cohérence avec des données multi-sources hétérogènes en espace, en temps et en nature.

Ce manuscrit présente des approches de modélisation des réseaux hydrographiques, basées sur des modèles hydrauliques-hydrologiques couplés et exploitant des méthodes d'assimilation variationnelle de données multi-sources. Ces approches sont basées sur la synergie entre, d'une part des modèles numériques complexes qui représentent des quantités physiques et, d'autre part, l'observabilité hétérogène de signatures hydrodynamiques à l'échelle des réseaux hydrographiques. Les développements des outils numériques sont effectués au sein de la plateforme d'assimilation variationnelle et de modélisation hydrodynamique DassFlow.

La première partie de ce travail porte sur l'estimation variationnelle de paramètres inconnus ou incertains (couple friction-bathymétrie, hydrogrammes latéraux) d'un modèle hydraulique 1D appliqué à large échelle spatiale, à partir d'observations altimétriques et optiques de déformations de la surface libre des rivières. La difficulté de cette estimation vient de l'effet corrélé des paramètres sur les signatures hydrauliques, de leur observabilité hétérogène et éparse en comparaison des échelles physiques des propagations et longueurs de contrôles hydrauliques. Les problèmes inverses considérés sont généralement mal posés et des méthodes de régularisation sont utilisées dans la méthode d'assimilation. Ce travail repose sur l'ajout de termes sources pour la prise en compte d'apports latéraux dans un modèle Saint-Venant 1D et sur l'analyse des signatures hydrauliques associées. Ces signatures apportent une information importante sur l'identifiabilité des paramètres qui les provoquent, en contexte d'observabilité éparse de la surface libre. Dans cette partie, des inférences très précises sont obtenues quand la quantité d'information contenue dans les observables et les informations a priori sont suffisantes au regard de la nature, de la quantité et du type des inconnues. Un modèle grande échelle d'un cours d'eau Amazonien anastomosé et alimenté par de nombreux affluents est construit à partir de données satellitaires optiques et altimétriques et est alimenté par des débits simulés avec le modèle hydrologique grande échelle MGB. Le modèle effectif calé sur des chroniques altimétriques historiques permet une représentation réaliste des signatures de crues. Leurs caractéristiques fréquentielles et leur visibilité par altimétrie large fauchée SWOT sont analysées à l'aide de cartographies d'identifiabilité. Des inférences simultanées de bathymétrie, friction et hydrogrammes latéraux spatialement distribués sont effectués sur ce modèle, à l'aide d'observations altimétriques large fauchée synthétiques. Ces dernières correspondent à celles qu'apportera la future mission SWOT, qui fournira une couverture spatiale sans précédent des rivières à l'échelle du globe. Cette mission aura une période de revisite suffisamment courte pour observer la propagation d'ondes de crue sur de grands bassins. Cette étude ouvre la voie vers l'utilisation d'observations SWOT pour l'estimation régionale de flux.

La deuxième partie de ce travail présente une nouvelle méthode pour la modélisation et l'assimilation hydraulique-hydrologique multi-échelle de réseaux hydrographiques, implémentée dans l'environnement de calcul parallèle et d'optimisation variationnelle de DassFlow. Un modèle hydraulique multi-dimensionnel est proposé, sur la base des équations de Saint-Venant 2D complètes résolues par un solveur volumes finis appliqué à des maillages 1Dlike-2D de réseaux hydrographiques complets. Il permet de répondre au besoin de modélisation 2D précise dans les zones d'intérêt, comme les plaines d'inondation et les confluences, à travers l'utilisation de maillages 2D localisés. Une stratégie de maillage "1Dlike" des cours principaux des rivières, pouvant utiliser des bases de données de masques d'eau issus d'images haute résolution, permet la modélisation hydrodynamique de ces tronçons à l'échelle du réseau tout en gardant un coût de calcul relativement bas. Le solveur hydraulique 2D est adapté pour gérer les interfaces entre les maillages 1Dlike et 2D. Le modèle hydrologique parcimonieux GR4H, dans sa version "espace-temps" qui est différentiable, est couplé au modèle hydraulique multidimensionnel et inclus à la chaîne d'assimilation DassFlow. La chaîne intégrée ainsi obtenue est validée sur des cas académiques et réels. L'inférence de champs de friction et bathymétries effectives permet de représenter fidèlement des lignes d'eau et la propagation de crues avec un modèle 1Dlike d'un bief de la Garonne. Des inférences de forçages hydrauliques temporels sont effectuées sur un modèle 1Dlike du réseau hydrographique de l'Adour, à partir d'observations in situ et permettent l'estimation de flux incertains. Un modèle 1Dlike-2D de l'Adour permet la modélisation haute résolution d'écoulements dans un grand réseau hydrographique et ses plaines d'inondation pour un coût de calcul relativement faible. Des inférences de paramètres hydrologiques sont effectuées sur un cas test synthétique, à partir d'observables hydrauliques en aval. Ces résultats démontrent la possibilité de remontée d'information dans la chaîne de modélisation sur un réseau hydrographique.

Mots-clés: Assimilation variationnelle, Modèles hydrauliques-hydrologiques, Équations de Saint-Venant, Altimétrie satellite, Observations multi-sourcées, Modèle Multi-dimensionnel

Abstract

This work studies the large scale hydraulic-hydrological modeling of hydrographic networks and the optimal integration of their multi-source observability. The growing wealth of information in data sets brought by hydrometeorology and high resolution remote-sensing, in complement to in situ measurements, is still insufficiently exploited to constrain fine, basin scale hydrodynamic models. Yet, such numerical representations are crucial for the accurate estimation of fluxes and states in hydrographic networks in order to answer major socio-economic issues, like flood prediction, especially in the context of climate change. The physical quantities of interest include inflow hydrographs, water depths, flow velocities and flood extents and durations. Information on such quantities is difficult to obtain, especially for floods over large areas, where multiple rivers are potentially ungauged. Several issues are related to the integration of multi-source data, heterogeneous in space, time and nature, into basin-scale hydraulic-hydrological models.

This manuscript presents modeling approaches based on hydraulic-hydrological models and using variational data assimilation methods with multi-source data. These approaches aim at the synergy of, on one hand, complex numerical models that represent physical quantities and, on the other hand, the heterogeneous observability of hydrodynamic signatures over a hydrographic network. Numerical implementation are carried out in the variational data assimilation and hydrodynamic modeling platform DassFlow.

The first part of this work deals with the variational estimation of uncertain or unknown model parameters (bathymetry-friction couple and lateral inflows), in a 1D hydraulic model at a large spatial scale, from altimetric and optic satellite observations of water surface deformations of river surfaces. The difficulty of the estimation lies in the correlated effect of parameters on hydraulic signatures and on their heterogeneous and sparse observability when compared to the physical scale of propagations and to the length of hydraulic controls. The considered inverse problems are ill-posed and regularization methods are used within the assimilation process. This work introduces source terms for the modeling of lateral inflows in a 1D Saint-Venant model and relies on the analysis of the associated hydraulic signatures. These signatures provide important information for parameter identifiability in the context of the sparse observability of the free surface. It is demonstrated that accurate inferences can be obtained when information provided by observables and a priori estimates are sufficient with regard to the nature, quantity and type of the sought parameters. A large scale model of an anastomosed Amazonian river inflowed by numerous tributaries is built from altimetric and optical satellite data and inflowed with the large scale hydrological model MGB. This effective model, calibrated using historic altimetric data, allows a fair modeling of flood signatures. Their characteristics and the visibility given by wide swath altimetry are analyzed with the help of identifiability maps. Simultaneous inferences of distributed bathymetry, friction and lateral inflow hydrographs are carried out on this model, using noisy wide-swath satellite altimetry. This synthetic observability is that of the upcoming SWOT mission, which features unprecedented spatial coverage of global rivers and sufficient revisit time to observe flood wave propagation. Inferences lead to accurate parameter estimations and this study paves the way towards uses of SWOT observations for the regional estimation of fluxes.

The second part of this work presents a new method for the multi-scale hydraulic-hydrological modeling of river networks implemented in the parallel computation and variational assimilation DassFlow framework. A multi-dimensional model is proposed using the full 2D shallow water equations, solved by a single finite volume solver applied to a 1Dlike-2D mesh of a complete hydrographic network. It answers the need for accurate 2D modeling in areas of interests such as floodplains and confluences through 2D meshes. A so-called "1Dlike" meshing strategy is applied to 1D reaches - it can make use of water masks database extracted from high resolution images - and allows hydrodynamic representation of these reaches at the network scale while keeping computational cost relatively low. The 2D hydraulic solver is adapted to handle interfaces between 1Dlike and 2D meshes. The parsimonious hydrological model GR4H, in its differentiable state-space version, is coupled to the multi-dimensional hydraulic model and integrated into the DassFlow assimilation tool chain. The obtained integrated chain is validated on synthetic and real cases. Effective bathymetry and friction allow fitting fine water surface elevations and signal propagation on a large scale 1Dlike model of a reach the Garonne river. Inferences of hydraulic temporal forcings are carried out on a 1Dlike model of the Adour network from in situ observability and lead to estimation of uncertain inflows. A 1Dlike-2D version of the Adour model allows the modeling of high resolution flow in a large network for a low computational cost. Inferences of hydrological parameters are carried out on a synthetic case using downstream hydraulic observable. These results demonstrate the possibility of informational feedback over a hydrographic network in the assimilation tool chain.

Keywords: Variational Data assimilation, Hydraulic-hydrological models, Shallow Water equations, Satellite altimetry, Multi-source observations, Multi-dimensional model

Introduction

In surface hydrology, the accurate estimation of fluxes is a key scientific problem, linked to important socio-economic issues, like flood and drought prediction. Indeed, river discharge is defined as an essential physical variable by the World Meteorological (see Global Climate Observing System Organization, 2011]). Climate change and the potential intensification of the hydrological cycle it implies make this goal even more crucial. To address it, fine, accurate, dynamic and spatially distributed modeling of basin-scale river network states and fluxes are needed. The physical quantities to represent include discharge and water levels, inundation extents and submersion times. Information on these states and fluxes is difficult to obtain at appropriate spatial and temporal scales, especially along large, potentially ungauged, river networks. However, the growth in size and quality of multi-source datasets given by high resolution hydrometeorology and satellite and airborne sensors provides an opportunity that is as of yet underexploited. In complement to in situ observations, this data can be integrated into hydraulic-hydrological models to improve flux prediction capabilities.

This PhD thesis studies the hydraulic-hydrological modeling of hydrographic networks and the optimal integration of multi-source observations. This integration consists in the coherent combination of, on one hand, complex numerical flow models and, on the other hand, observations of hydrodynamic signatures in river networks, heterogeneous in nature and in spatio-temporal patterns. In this work, hydraulic models solving the full Shallow Water equations, either 1D or 2D, are used in a variational data assimilation framework. Several issues are related to the hydrological-hydraulic modeling of river networks and to the fusion of heterogeneous multi-source observations.

One issue is the relatively sparse observability of the water surface compared to the hydraulic signatures at play. On one hand, in situ data is limited to static stations, that provide data that is dense in time but relatively sparse in space with regards to the scales of signatures related to hydraulic controls (bathymetry-friction and lateral exchanges), and costly data acquisition campaigns, that provide rich but localized information. On the other hand, current satellite observations provide global data, but their revisit time are still relatively large with regards to signal propagation times.

In view to enrich observability and to make the most of available data, satellite and in situ data can be combined, which leads to a second issue: their heterogeneity. That is an heterogeneity of spatial and temporal patterns and frequencies, of sensor/product accuracy and an heterogeneity in the type of observed quantities. Satellite radar altimetry provides water surface elevation over relatively large global rivers (over 50 to 100 m wide), while satellite optical sensors may provide river widths and flood extents. Spaceborne radars (Shuttle Radar Topography Mission, SRTM) enabled building a global Digital Elevation Model, while airborne LiDAR (Laser Imaging Detection and Ranging) can provide bathymetry over a region of interest, like a floodplain, with higher accuracy and resolution. In situ flow sensors can provide water depth and local discharge estimation, while fixed or airborne optical sensors, i.e. cameras, may provide 2D surface velocity fields.

Airborne measurement of river channels bathymetry remains difficult except for shallow and clear waters via penetrating LiDAR. Therefore most parameters required to model worldwide rivers networks remain poorly observed or not observed at all. Thus, the third issue is the inference of uncertain or unknown river flow model parameters. These include channel parameters, such as bathymetry and friction, distributed inflows but also hydrological parameters for integrated models. Given hydrodynamic flow models and partial flow observability, one faces difficult ill-posed inverse problems and the introduction of a priori knowledge and regularization strategies is necessary.

Another important issue lies in the difficulty to estimate distributed hydrological inflows over a river network. This pertains to the problem of spatially distributed hydrological model calibration and regionalization, that is prediction of discharge at ungauged locations. Considering sparse observability of hydraulic signatures, is it possible to infer semi-distributed hydrological parameters in a hydrological-hydraulic model using a VDA method? In other words, which information feedback is possible from the river network to upstream hydrological components ?

The above issues are studied is this PhD. All numerical developments are implemented in the hydrodynamic modeling and assimilation platform DassFlow.

In Chapter 1, hydraulic and hydrological modeling is presented in the scope of basin-scale hydrographic network observability. In Chapter 2, the identifiabilty of model parameters and temporal forcings is studied on synthetic and real-like 1D models using satellite altimetry. In Chapter 3, a new method for the multi-scale modeling of complex river network with data assimilation is developed. This work is concluded in Chapter 4, which contains work perspectives and the general conclusion.

Chapter 1

River networks modeling and remote sensing

Contents

This chapter presents the general context and scientific issues studied in this work, as well as the models and tools exploited or expanded upon. Recall that this thesis aims at the improvement of model-data synergy in river network hydraulic-hydrological models through the use of multi-source observations and data assimilation methods. Section 1 presents basin-scale hydraulic and hydrological phenomenons in the scope of their heterogeneous observations through diverse sensing methods. Section 2 presents the mathematical hydraulic models and resolution methods used in the following chapters of this work, along with a summary of state-of-the-art computational hydraulic models. Section 3 introduces hydrological modeling and contains a detailed presentation of two hydrological models used in the following chapters. Considering multi-source river flow observations and hydraulic-hydrological models, the inverse problems of interest are formulated in Section 4 and the variational data assimilation method used in the following chapters is presented.

1.1 Fluvial hydraulics and hydrological variabilities

Water circulation on Earth, in the so-called "great water cycle", represents a dynamic equilibrium. Surface hydrology aims at studying the spatio-temporal variability of continental freshwater storage and fluxes (see e.g. Chow [1964]; Dingman [2009]). In this section, large scale hydrological processes are recalled before focusing on river network flows in a multi-source observability context (in situ, spaceborne and airborne sensors).

1.1.1 Catchment hydrology

Given a river cross-section (XS), one can define a topographical catchment as the upstream geographical area, delineated by its water divide line ("ligne de partage des eaux" in French, see Musy and Higy [2004]). The amount of freshwater within a catchment is largely driven by climate variability, through effective precipitation that feeds the compartments of hydrosystems (i.e. rivers, lakes, biosphere, aquifers and unsaturated soils (Milly [1994], Fig. 1.1).

Freshwater residence times can vary from hours, to days, to thousands years depending on the hydrological compartment (De Marsily [2012]). Average residence time is estimated to be in the tens of days for river networks, of a few years in wetlands and upper soil layers, of decades in lakes and of thousands of years for aquifers and glaciers (Anctil [2005]).

Hydrological responses, in terms of water storage and fluxes, result from the complex combination of meteorological signals with catchment properties, involving soil-biosphere-atmosphere couplings, at play in the so-called continental water cycle (see e.g. Oki et al. [1999]). The heterogeneous physical properties, organization and connectivity of hydrological compartments modulate the distribution and dynamics of water flow (see e.g. Flipo et al. [2014]; Schuite et al. [2019]).

Complex non-linear and coupled physical processes are at play in the soil-vegetation zone and in the unsaturated superficial soil layers. They determine the partition of water between vertical and lateral flow components such as infiltration, surface and sub-surface runoff and percolation to bedrock/aquifers.

Name	**Average yearly precipitation** (cm)	**Localization**
Equatorial humid	200	Inland and coasts (e.g. Amazon basin)
Subtropical humid	100-150	Inland and coasts (e.g. Yangtze river basin, eastern Mississipi basin)
Subtropical dry	25	Inland and coasts (e.g. Sahara region)
Intertropical coastal	150	Coasts (e.g. eastern central America)
Temperate continental	10-50	Inland (e.g. American great plains)
Temperate oceanic	100	Inland and coasts (e.g. western Europe, 80-200 cm/year in metropolitan France)
Polar and arctic	30	North of 60^{th} parallel (e.g. northern Canada)

Table 1.1: Worldwide pluviometric regimes (adapted from Fabre [1990])

Solid and liquid precipitation accounts for most of the water inputs in a catchment (orders of magnitudes of yearly precipitation given by climate types in Table 1.1). A significant part of this precipitation is evaporated from the soil, from open water surfaces or through plant transpiration. The remaining water integrates the surface and sub-surface storage and flows.

Soil, a porous medium, has a limited local infiltration capacity. Part of the infiltrated water remains in the upper soil layers, while another part is percolated deeper, in the aquifer, through the action of gravity. When the local infiltration capacity limit is reached, excess water participates in surface runoff (Anctil [2005]).

Surface runoff descends towards the lowest point of a catchment, forming naturally linked drainage channels (called hydrographic network). Before reaching the oceans, except in the case of endorheic basins such as the Okavango basin in sub-equatorial Africa, freshwater passes through hydrographic networks.

Sub-surface water may interact with the hydrographic network through lateral flows (e.g. Schuite et al. [2019] and references therein) and water exchanges can occur between distinct topographical catchments because of groundwater or human-induced fluxes (e.g. Mul et al. [2007]).

Exchanges between surface, sub-surface and groundwater compartments can be vertical or lateral, depending on compartment levels: during low-flow periods, exchanges are directed towards the river network (a low frequency signal) while in high-flow periods, surface hydrological processes transmit a high frequency flood signal (Flipo et al. [2012]). The propagation of upstream hydrological signals within a river network is studied in fluvial hydraulics.

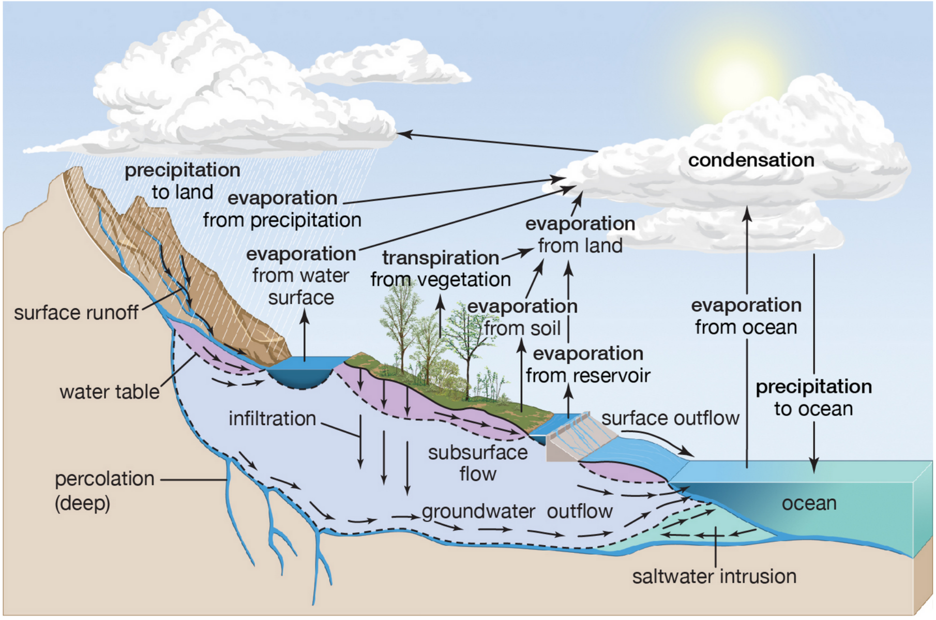

(a) Qualitative representation from Britannica [Accessed 28 October 2021]. Athmospheric, surface and sub-surface exchanges are included.

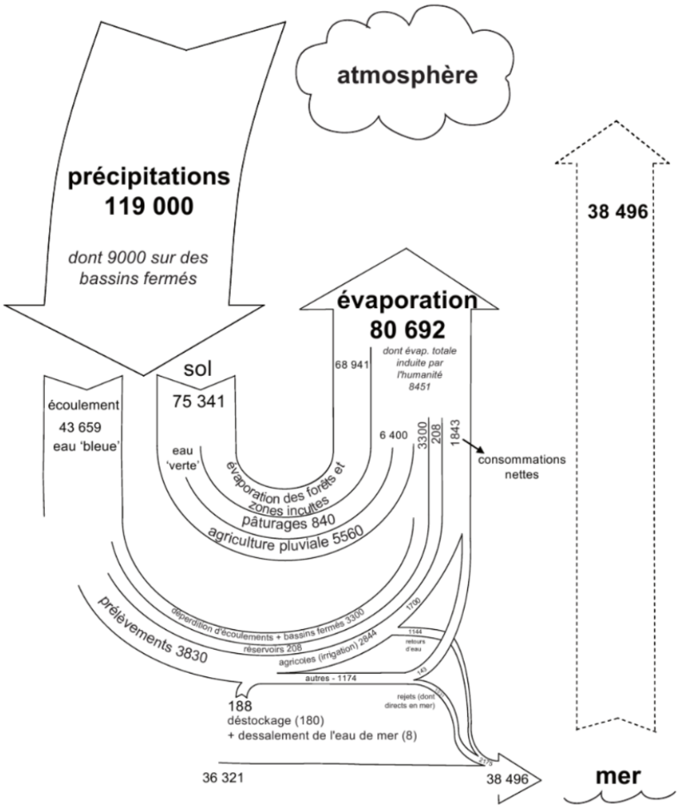

(b) Quantitative representation from Margat and Andréassian [2008]. Exchanges between the main hydrological compartments are represented. Green water is water evaporated from or transpired by plants (from forests, uncultivated fields). Blue water is water involved in surface (roughly 15%) and sub-surface (roughly 85%) flows.

Figure 1.1: Complete continental water cycle.

1.1.2 River discharge

River discharge, resulting from the aggregation of upstream and past hydrological processes, is a crucial physical quantity for hydraulic studies and for the characterization of hydrological phenomenons. It has been defined as an essential climate variable by the World Meteorological Organization (WMO) in the Global Climate Observation System (GCOS, see int [2016]). Worldwide rivers discharges span a significant range of scales, as can be seen for the sample rivers presented in Table 1.2.

The largest river discharge module - or average inter-annual flow - on Earth is that of the Amazon River, about 209 000 m^3/s near its estuary, and its two major upstream tributaries, the Solimoẽs and Negro rivers have a respective module of 103 000 m^3/s and 28 400 m^3/s and drainage areas of 2 147 700 km^2 and 279 900 km^2 (see Table 1.2, see also Ouillon [1993]; Filizola [2003] for solid discharges). Such large and hard-to-access basins are difficult to instrument and remote sensing provides an unprecedented observability of large rivers, as discussed later in Section 1.1.4.

Smaller rivers are also observable, such as the Garonne river (France) around Toulouse (see Biancamaria et al. [2017]) which represents the lower limit of observability of current altimetric satellites. Its module at the Gironde estuary is 1000 m^3/s for a drainage area of 56 000 km^2.

Let us define river discharge from a fluid kinematics approach, that is a mathematical description of a flow field without accounting for the forces and conditions that create it. Under the usual hypothesis of fluid continuum and considering fluid particles in a Cartesian coordinate system (see e.g. Chassaing [1997]), the instantaneous volumic discharge through a section A and at a given time is defined as the integration of the flow velocity through this section as:

$$Q = \int_A \vec{u} . \vec{n} \, \mathrm{d}A \tag{1.1}$$

with $\vec{u} = \left(u_x, u_y, u_z\right)^T$ $[\mathrm{m/s}]$ the local velocity vector of the flow and $\vec{n}$ the outer normal vector to the flow section A $\left[\mathrm{m}^2\right]$ and with Q $\left[\mathrm{m}^3/\mathrm{s}\right]$ the volumic discharge. River flows are predominantly free surface flows, which means that the surface of the fluid, i.e. its interface with the atmosphere, is not subject to shear stress. In fluvial hydraulics studies, a XS orthogonal to the main flow vein is commonly chosen. A realistic velocity profile for a free surface channel flow is shown in figure 1.2.

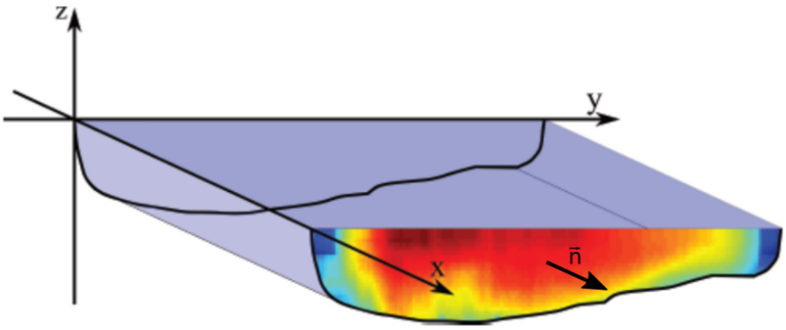

Figure 1.2: Cross-sectional variability of flow velocity, as given by Acoustic Doppler Current Profiler (ADCP) measurements (from Negrel [2011]).

River	Basin surface (km^2)	Discharge module (m^3/s)
Amazon [4]	7 050 000 (at estuary)	209 000
Negro	279 900 [83](at Serrinha station)	28 400 [4] (14% of the Amazon module)
Solimoẽs	2 147 700 [83] (at Manacapuru station)	103 000 [4](49% of the Amazon module)
Niger	2 117 700 [266] (at estuary)	5 589 [3] (at Lokoja, historical extremes are 27 600 m^3/s and 500 m^3/s)
Garonne [240]	56 000 (at estuary)	1 000
Rhine [56]	185 000	2 200 (with average high and low flows around 6 000 m^3/s and 1 000 m^3/s)
Moselle [56]	27 100 (at Cochem station)	288 (with average high and low flows of 3 740 m^3/s and 9.7 m^3/s)

Table 1.2: Sample of world rivers observable by satellite altimetry, orders of magnitude of their discharges and drainage basin areas

1.1.3 Fluvial hydraulics

Fluvial hydraulics, also called open channel flows in civil engineering, governs the motion of water in river networks and is an essential discipline to the study of hydrology (Dingman [2009]). Indeed, river networks are generally composed of river channels and floodplains and convey the water fluxes that stem from hydrological processes occurring within a catchment. Fluvial hydraulics is an applicative sub-discipline of fluid dynamics (hydrodynamics or aerodynamics) that studies the motion of fluids (liquids or gas). Fluid dynamics offer a systematic structure based on empirical and semi-empirical laws derived from flow measurements (see e.g. Chassaing [1997]; Ancey [2018]). Its foundational axioms, based on classical mechanics, are conservation laws such as conservation of mass and linear momentum considered in the following (see Section 1.2).

In river flows, diverse physical processes are at play at multiple scales, from very localized structures in boundary layers (e.g. Nikora et al. [2013]) to larger scale wave propagations (e.g.

Dingman [2009]; Thual [2010]). The two main forces at play in open channel flows are gravitational and shear forces. Gravitational force, that is a body force acting on each fluid particle, is responsible for motion, whereas a shear force opposed to motion arises from frictional resistance of the solid boundary with viscous and turbulent effects (Kline et al. [1967]). Another surface force at play is the pressure force. The variabilities of free surface flows arise from the mass balance and forces balance that are reflected in free surface deformations and can be predicted by hydraulic theory (see e.g. Thual [2010]; Ancey [2018]; Dingman [2009]). The complexity of flows within a river reach can vary depending on lateral exchanges, channel shape and sinuosity, slopes, banks and bottom rugosity, the presence of vegetation, of confluences or diffluences, or of inline (bridges, weirs, logjams) or lateral man-made structures (lateral weirs, dykes), see Graf and Altinakar [2000]. The observation of river flows variabilities is of great importance for physics and engineering applications and is discussed hereafter.

1.1.4 River networks monitoring

Human societies developed in close relation with water because of irrigation and transportation needs, drinking water supply. Therefore, the observation of river flows has early become a subject of interest. Let us mention historical observations of river flows such as for the Nile River in ancient Egypt (from Arab records starting in the 7^{th} century, see Toussoun and international de géographie [11: 1925: Le Caire]) or more recent observations of the Rhône River, with records dating up to the 16^{th} century (see Pichard [1995]). These historical measurements, typically of flood peak heights at local sites of importance, have evolved into distributed sensor networks. In the last decades, satellite observations have offered the opportunity to complement these in situ observations. Even more recently, airborne sensors, carried by planes and drones, have further contributed to increase the observability of river networks.

Nowadays, the monitoring of river networks involves a variety of sensors, aimed at observing rivers flows variabilities. In the following, we differentiate between local measurements, that include permanent stations and local remote-sensing, and global satellite observations.

1.1.4.1 Local measurements

In situ measurements can be divided into: i) permanent local stations gathering temporally dense data (see e.g. Musy and Higy [2004] for measurement tools and techniques) and ii) impermanent data acquisition campaigns that focus on areas-of-interests over a shorter time period (see e.g. Hauet et al. [2014]; Altenau et al. [2017] and details below).

Local stations provide either water depth measurements (e.g. through limnimetric physical scales or limnigraphic automated sensors, see Fig. 1.4b(a)) or discharge estimation (e.g. through stage-discharges relations, called rating curves (RC), or direct measurement, see Fig. 1.4b(b)), over large time scales and at relatively low time steps. Permanent stations are distributed heterogeneously around the surface of the Earth. In France, a network of limnimetric and current meters (the French Banque HYDRO[1], Fig. 1.3, left)regroups 3200 current stations for 670 000 km^2 of drained area (or 210 km^2 per station on average). This network finds use in hydraulic and hydrological studies but also in real-time flood warning systems such as in the French vigilance

---

[1] http://hydro.eaufrance.fr

system for floods, Vigicrue[2], and for flash floods, Vigicrue Flash[3]. Other regions are less densely gauged, like the Amazon basin (Fig. 1.3, right), with a few hundreds of stations for 7×10^6 km^2 of drained area). Overall, permanent station number is in decline worldwide with some regional disparities (see Fekete and Vorosmarty [2002]).

Impermanent observation means include: at-a-section measurements, e.g. through simple helix-based current meters or more advanced Acoustic Doppler Current Profilers (ADCP, see Fig. 1.6) that provide depth and width dependent water velocity measurements (see Fig. 1.5(a)), and longitudinal measurements, e.g. through on-board GPS altimeters that can provide spatially dense WS elevation and WS slope data across a river reach or river network (see Fig. 1.5(b)).

New remote-sensing methods are also deployed at the local scale. Airborne sensors, carried by plane (e.g. Altenau et al. [2017]) and, more recently, by drones (e.g. Tauro et al. [2016]; Strelnikova et al. [2020]), bring lower cost and more flexibility to data acquisition. Recent progress in measurement techniques, such as penetrating blue LiDAR operated from low altitude overflight (e.g. Lee and Wang [2018]; Hopkinson [2007]), provide high resolution and accurate bathymetry of floodplains and relatively shallow main channels. Furthermore, remote non-intrusive optical sensors (i.e. cameras), either fixed in place or mobile, can provide bi-dimensional fields of surface velocities extracted by Large Scale Particle Image Velocimetry (LSPIV) methods, see Le Coz et al. [2010]. For example, Dramais et al. [2011] presents channel discharge estimations using static cameras.

Local measurements represent a large part of the available observability of rivers. Local in situ bathymetric surveys are crucially needed in river engineering and modeling, for most river channels and especially at deeper locations. In situ stage and flow measurements generally provide temporally dense observation of the water depth variations. In turn, both permanent and impermanent local data sources are necessary to constrain at a station stage-discharge laws (e.g. in Getirana et al. [2010]; Malou et al. [2021] and references therein) or more complex hydraulic models (e.g. in Papanicolaou et al. [2011]; Pujol et al. [2020] and references therein).

---

[2] https://www.vigicrues.gouv.fr/
[3] https://apic-vigicruesflash.fr

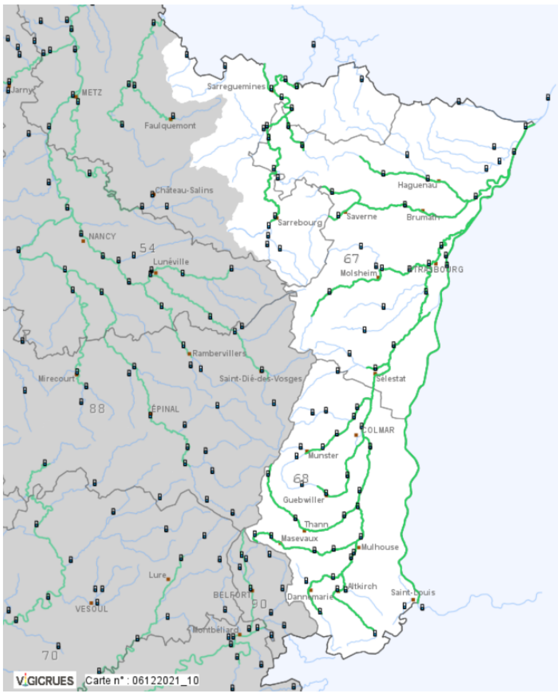

(a) Map of river network and Banque HYDRO stations of the Rhin-Sarre territory. 84 gauging stations for an area (in white) of around $1.1 \times 10^4\,\mathrm{km}^2$ (or $1310\,\mathrm{km}^2$ per station on average).

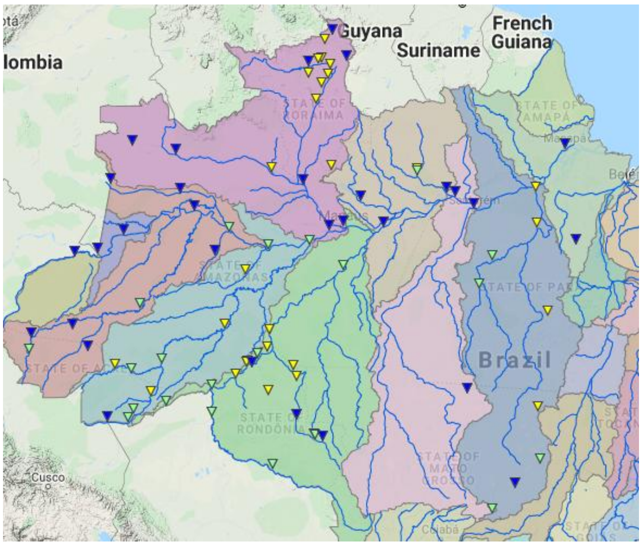

(b) Water level gauging stations given by the ANA, CotaOnline, RHN and GDH databases (available from http://www.snirh.gov.br). 82 active stations cover a drainage area around $7 \times 10^6\,\mathrm{km}^2$ (or $85\,000\,\mathrm{km}^2$ per station on average). Note that only 58% of this area is in Brazil, further upstream observability may be derived from other gauging networks, notably in Peru, Bolivia, Colombia and Venezuela.

Figure 1.3: Metropolitan France and Amazon in situ observation station networks.

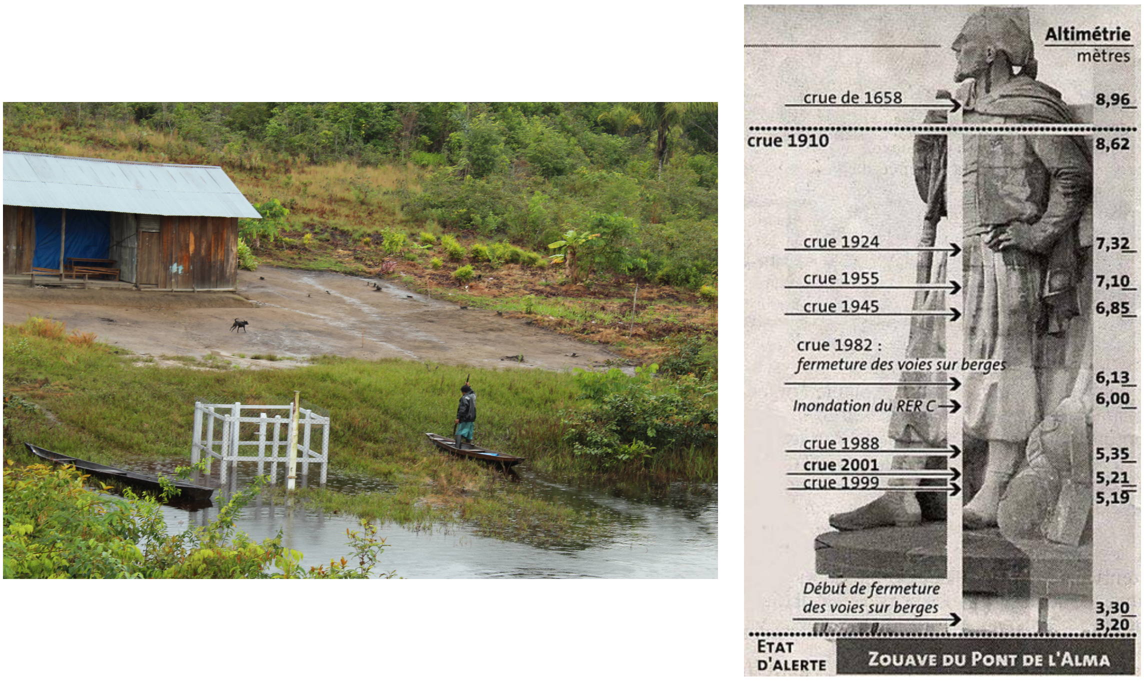

(a) Left: A limnimetric scale on the Negro river, far upstream from Manaus, near Taracua (photograph by author, 2018). Measurements are written down by a local resident at a sub-daily time step. Right: Historic floods of the Seine visualized on the Alma bridge zouave.

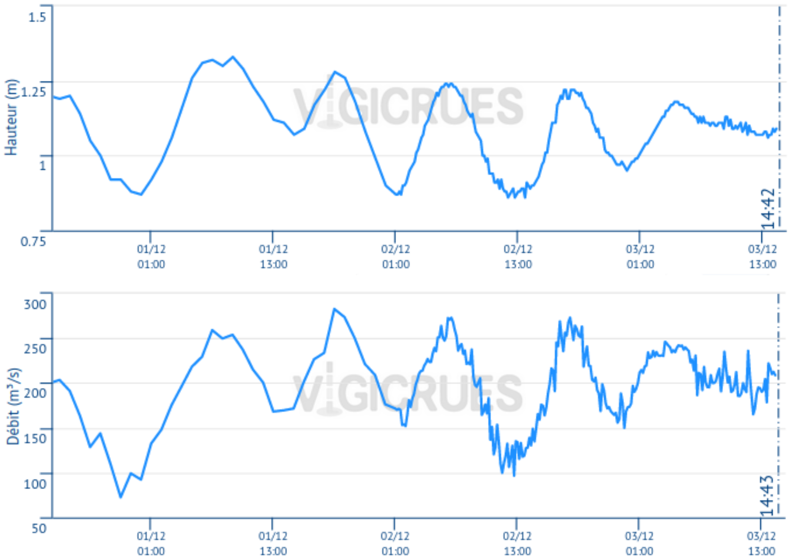

(b) Measured water depth and discharge at the Austerlitz ultrasonic flow measurement station, near the Alma bridge. Data accessed at 14:42 on December 3rd at https://www.vigicrues.gouv.fr. The Vigicrue flood risk information service provides real-time unexpertized data freely over the last 30 days and expertized data over the station life-time.

Figure 1.4: In situ observation station measurements

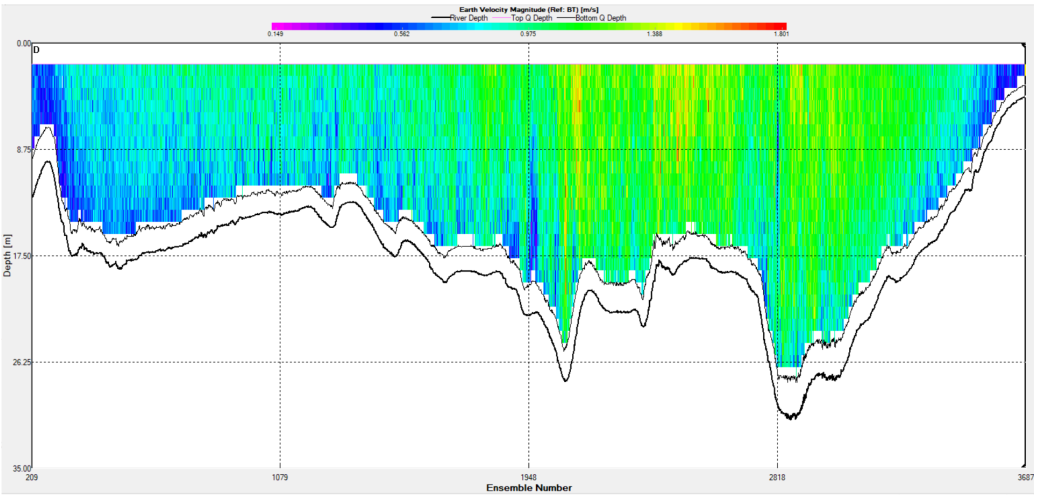

(a) ADCP measurements results on the Solimoẽs river near Manacapuru (see sensor setup in Fig. 1.6). The color heatmap is a cross-sectional flow velocity field. The boat took 28 minutes to cross the 2950 m of river width. Estimated total flow is around 50 900 m^3/s (for a river module of 103 000 m^3/s, see Table 1.2).

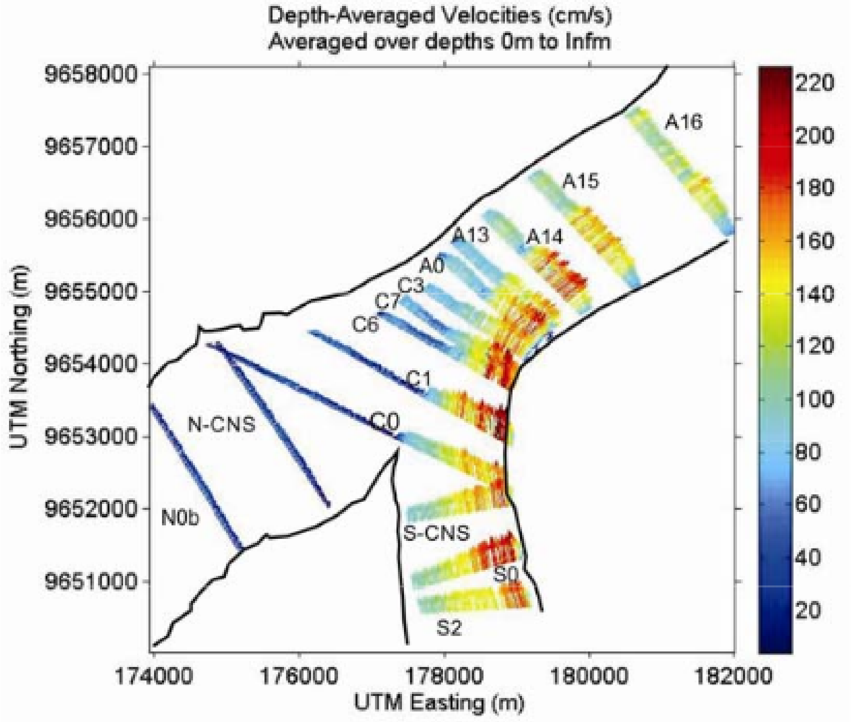

(b) Top-down representation of an ADCP campaign results. Depth-averaged velocities of ADCP transects at the confluence of Negro and Solimões Rivers (Trevethan et al. [2016]).

Figure 1.5: Impermanent data acquisition mission results (1)

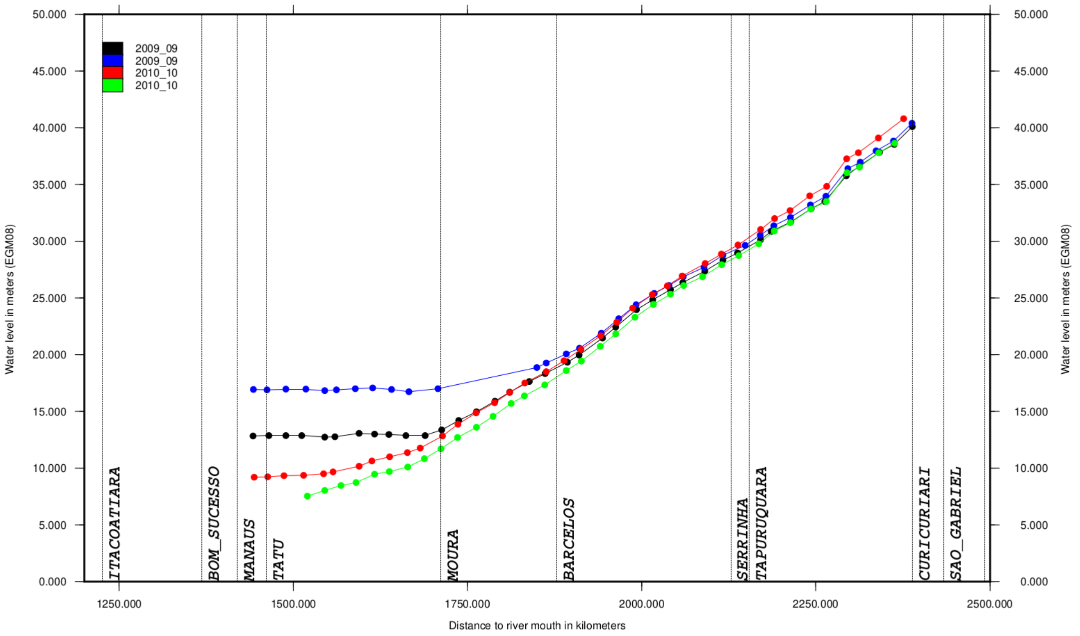

(c) GPS altimetry measurements of the Negro river WS elevation upstream from its confluence with the Solimoẽs river, using boat-carried onboard GPS altimeter. This data is used to build a large scale 1D model in Chapter 2. Data comes from 4 different descents of the river in 2009 and 2010, during low flow season, and is aggregated over 25 km steps (courtesy of D. Moreira and the Companhia de Pesquisas de Recursos Minerais (CPRM)). Note that raw data is much denser, with an average step of around 2 km. The average measured slope is 3×10^{-5} m/m, with much lower slopes in the downstream part.

Figure 1.5: Impermanent data acquisition mission results (2)

Figure 1.6: ADCP sensors mounted on a small boat (photograph by author, 2018). The top part of the metal bar is fitted with a GPS to track the boat position during a transect.

1.1.4.2 Satellite observations

Global observation of the oceans dates back to the mapping of oceans for sailing purposes, through not only coast but also wind and current maps. In 1957, the first satellite launch opened up a new way to observe the Earth, first through orbiting Laser and Doppler sensors for geodesic measurements[4]. In 1978, the first satellite mission aimed at ocean surface observation, notably using nadir altimetry, is launched. Since then, increased efforts to observe the Earth with space-borne sensors have been made, bringing unprecedented datasets on ocean, atmosphere and continental surfaces.

Recent satellite missions provide an increasing amount of observations related to the global hydrological cycle and basin properties: precipitation, surface soil moisture, surface temperatures, ice sheet surfaces, large scale water storage, oceanic and continental water surfaces elevation and extent, topography and soil occupation (see summary of satellite missions in Table 1.3, see also freely available Sentinel mission imagery in Fig. 1.8). The satellite-based remote sensing of hydraulic and hydrological signatures (see Subsection 1.1.1) can provide a global complement to in situ hydrometric networks (review in Balsamo et al. [2018]), which are declining in some regions worldwide (see Fekete and Vorosmarty [2002] and references therein). Notably, higher vertical accuracy of altimetric data has enabled a larger observability of the hydrological cycle (e.g. altimetry on rivers down to 50 m in width expected with the forthcoming SWOT mission, see Pavelsky et al. [2014]). Furthermore, advances in high-performance computing have enabled representation of the Earth at unprecedentedly fine scales and exploitation of this new wealth-of-information. For example, in Mizielinski et al. [2014], high resolutions satellite data have been used to build a finer global climate model ($25 \times 25\,\mathrm{km}^2$ tiles, 85 vertical levels, worldwide) run on supercomputers.

In the present work, we focus on radar altimetry as a rich source of information on catchment scale hydrodynamic responses (see relevant satellite missions in Table 1.4, see sample nadir and large swath observability in Fig. 1.7). Initially, satellite altimetry over continental surfaces enabled measurements over ice sheets (Ridley and Partington [1988]; Remy et al. [1989]) and large inland water surfaces such as over the the Amazon river (Koblinsky et al. [1993]). Koblinsky et al. [1993] suggests that an observational Root Mean Square Error (RMSE) of 10 cm would allow the monitoring of large river water levels, although measurements at the time (from the Geosat mission) reached only 50 cm in RMSE and had insufficient spatio-temporal coverage. Since then, decades of nadir altimetry (see Frappart et al. [2006]; Birkett [1998]; Da Silva et al. [2012]; Calmant et al. [2008, 2016]) and imagery (e.g. Allen and Pavelsky [2018]) of inland waters have been exploited and detection capabilities have been improved: observable river widths were around 1 km in Birkett [1998] (TOPEX/POSEIDON mission) and are currently around 100 to 50 m (Cryosat, Jason, Sentinel and SWOT missions, see Table 1.4). This enables global observation of many worldwide rivers.

Notably, the upcoming Surface Water and Ocean Topography (SWOT, see Rodríguez [2012]; Fu et al. [2012]) mission (to be launched 2022) will use a new wide-swath altimeter (see Table 1.4 for resolution). This would offer extensive global observations with a relatively dense spatio-temporal sampling and decimetric vertical accuracy (discussed below, see also Rodríguez et al. [2018, 2020]). Pavelsky et al. [2014] estimates that observing 50 m wide rivers would allow dis-

---

[4] https://www.aviso.altimetry.fr/en/techniques/altimetry/history.html

charge estimation on more than 60% of catchments with an area of 10 000 km^2 and above. In the case of the Amazon basin SWOT observations enables to depict hydrological processes such as regional rainfall-evapotranspiration patterns, inter-basin fluxes or floodplain storage (see review in Fassoni-Andrade et al. [2021]).

Thus, multi-satellite observations contain important information on WS deformation observations, from a combination of diverse spatio-temporal patterns and resolutions. An aggregated multi-satellite product, especially including the most recent and upcoming missions, would provide extensive observations of global hydrodynamic signatures to be analyzed, learned and assimilated into fine river network models. Spatially distributed observations of river surfaces deformations can provide interesting information on local geometric-friction parameters (see Hostache et al. [2010]; Brisset et al. [2018]; Garambois et al. [2020] and references therein), while temporally dense observations may carry information on the local hydrodynamic response of the global hydrographic network (see Brisset et al. [2018] and references therein). The latter scientific issue is studied in Chapter 2.

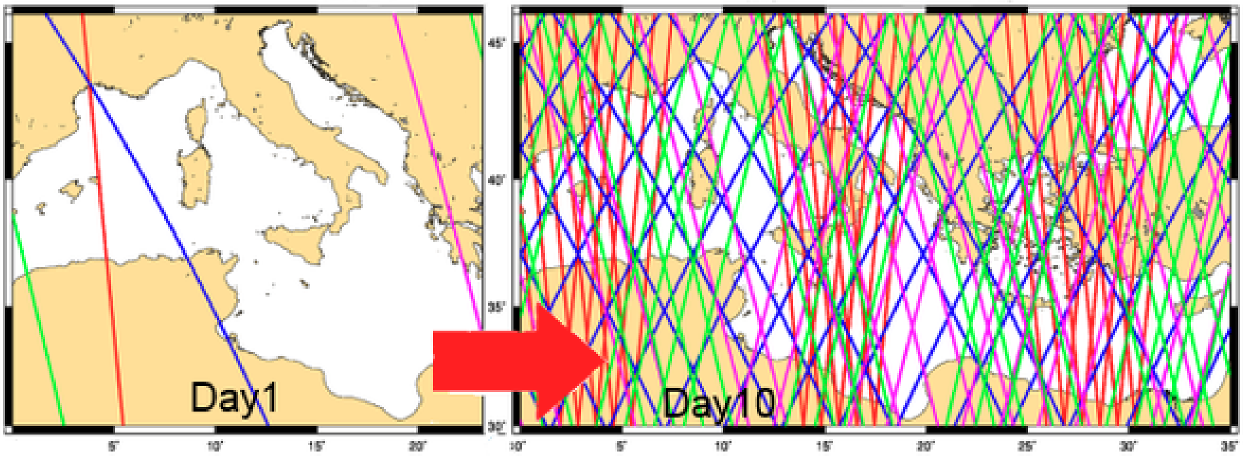

(a) Ground tracks of multiple altimetric missions over the Mediterranean sea (from AVISO). In blue: Jason-2, in green: Saral, in red: CryoSat, in pink: HY-2A.

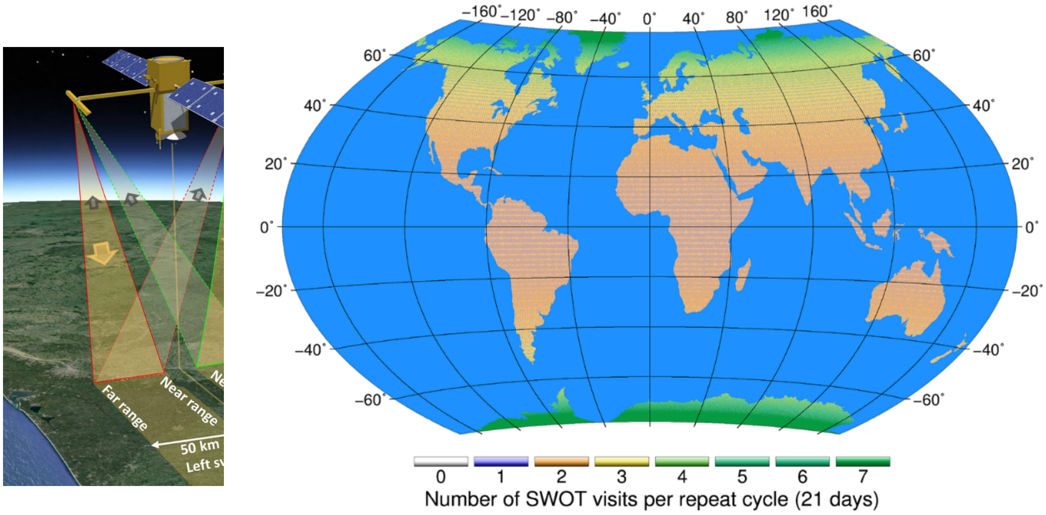

(b) Schematic representation of SWOT wide-swath altimetry coverage and global map of SWOT revisit numbers during its 21 days cycle (from Biancamaria et al. [2016]).

Figure 1.7: Satellite observability of the Earth from altimetric sensors.

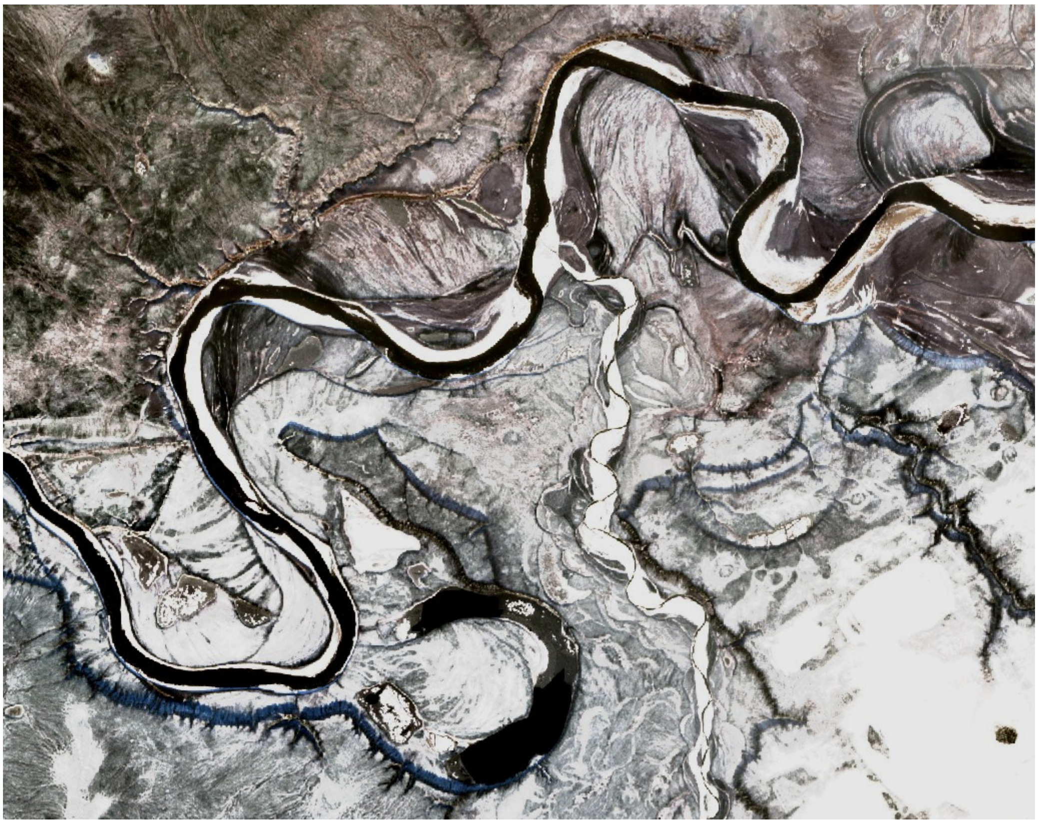

(a) The Yukon river at Old Crow Flats. A single channel meandering river in an arctic region. Around 500 m in width at this point.

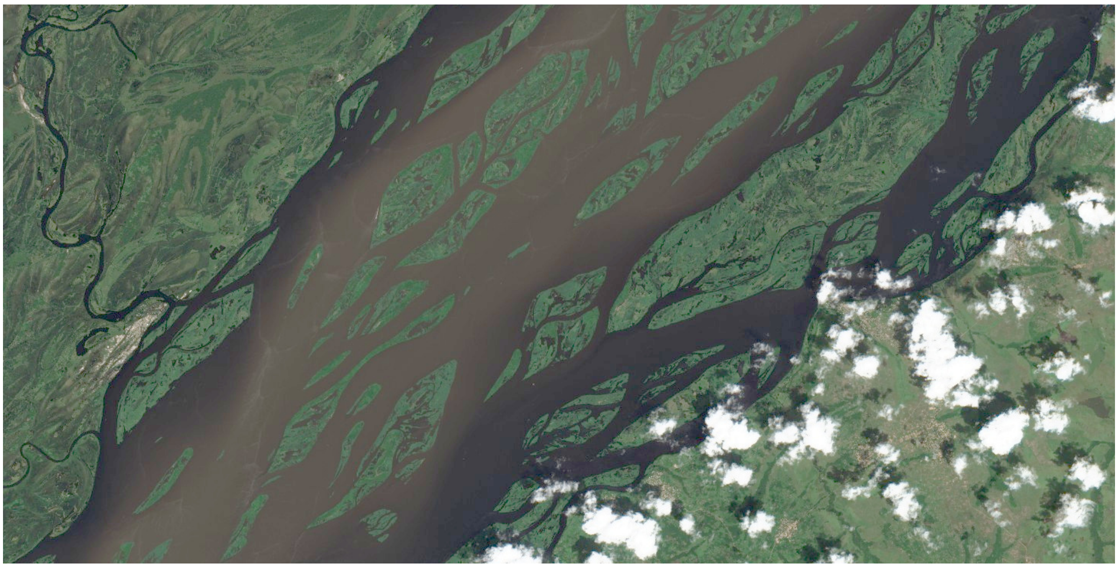

(b) The Congo River around 300 km upstream from Kinshasa. A heavily anastomosed river in a tropical region. Around 10 km in total width at this point.

Figure 1.8: Sentinel mission imagery, featuring contrasted lateral river variabilities (accessed through https://apps.sentinel-hub.com/sentinel-playground).

Observed variable	Mission	Instruments	Spatial resolution	Revisit period
Precipitation	Constellation GPM & geostationary satellites	Optical sensors, microwave radiometers, radar	10 to 100 km	1 h to 1 d
Water and snow surface	Aqua et Terra, Landsat-7/8, PROBA-V, Sentinel-2 and 3, SPOT-6/7, Suomi NPP and NOAA-20	Shortwave optical sensors	$\sim$ 1 to 500 m	1 d to $\sim$ 15 d
	GCOM-W1, SMOS	C and L-band microwave radiometers	25 km	$\sim$ 1 d
	TerraSAR-X, Tandem-X, Radarsat-2, Sentinel-1	C and X-band radars	$\sim$ 1 to 40 m	A few days
Water surface altimetry	CryoSat-2, HY-2A, Jason-2, Jason-3, SARAL, Sentinel-3/6, Sentinel-3 NG, SMASH	Nadir radar altimeters	$>$ 50 m	10 d to $>$ 1 y , 1 d
	SWOT	Large swath radar altimeters	Rivers width $> 100 - 50$ m, 60 km swaths, large areas $> 250x250\,\mathrm{m}^2$	1 to 4 revisits per 21 d
	ICESat-2	LiDAR	Local (single point)	91 d
Sedimentary load, alluvial wetlands	Aqua et Terra, Suomi NPP and NOAA-20, Sentinel-2 and 3	Shortwave optical sensors	$\sim$ 10 m to 1 km	1 d to $\sim$ 15 d
	SMOS	L-band microwave radiometer	$\sim$ 40 km	$\sim$ 1 d
Evapotranspiration	Aqua et Terra, ECOSTRESS, Landsat-7/8, Pléiades, Sentinel-2, VENUS, TRISHNA, LSTM	Infrared and shortwave optical sensors	$\sim$ 1 to $500m$	1 d to $\sim$ 15 d
	SMOS, SMAP	L-band microwave radiometer	$\sim$ 40 km	$\sim$ 1 d
Soil humidity	Aqua, GCOM-W1, MetOp, ENVISAT, SMOS, SMAP, SMOS-Next	C and L-band microwave radiometer, B-band altimeters	40 to 50 km	$\sim$ 1 d
	Constellation GNSS, CYGNSS	Bistatic L-band radars	A few km	1 to 2 weeks
Glacier mass (excl. polar caps)	Pléiades, SPOT-6/7, Terra, CO3D	Stereoscopic optical shortwave sensors	$\sim$ 1 to 500 m	1 d to $\sim$ 15 d
Global water mass balance	GRACE, GRACE-FO, Marvel	Satellite to satellite distance	$\sim$ 300 km	1 month

Table 1.3: Main satellite missions used in hydrology (adapted from Observatoire Midi-Pyrénées (OMP)).

1.1.4.3 Signal scales and measurement error

We define hydraulic signatures as information on hydrological cycle components carried by water surface deformations. From a hydraulic modeling perspective, model state variables carry the hydraulic signature of model parameters and temporal forcings (see Section 1.4). To inform on hydraulic signatures, observations of water surface deformations must have sufficient i) accuracy and ii) spatial and temporal sampling, with regards to the phenomenons at play.

In terms of accuracy, satellite altimetry remains less accurate than most in situ measurements. For spaceborne sensor products, vertical altimetric uncertainties range in the tens of centimeters. The SWOT mission will provide data over its 3 years planned mission lifetime, over a 120 km large swaths, and its requirements are a 10 to 25 cm vertical accuracy and down to 1.7 cm/km slope accuracy (Rodríguez [2012]). To achieve this accuracy, wide swath data will be treated and averaged over large surfaces, i.e. accuracy may be lower or observations may be less dense in smaller river. For in situ station measurements of water depth, uncertainties tend to be under 10 cm, although in situ network quality may vary globally. Lang et al. [2006] estimates that piezoresistive (resp. bubble-based) sensors, used in the French observation network, have an accuracy of 0.1 % (resp. 0.3 %) of their total range, which translates to less than decimetric accuracy. In situ sensors tend to be sensitive to sediment load and water and air temperature, whereas radar sensors are insensitive to temperature.

In terms of hydraulic signature temporal scales, Allen et al. [2018] estimates that the global median flood wave propagation time across a network is around 6 days, with a majority of networks having wave propagation time of less than a day. Allen et al. [2018] uses simple geomorphological considerations and approximates the flood wave to a kinematic wave. Temporally dense data from in situ stations would provide good local observability of such signatures. Missions with relatively low revisit time, like SWOT (1 to 4 pass every 21 days "repeat" cycle depending on latitude, see also Fig. 1.9), would provide data relevant to the scale of river discharge variations. For example, regional flood wave propagations, that can take place over the course of a week or more over large basins, would be observable.

Then arises the question of the spatial dimension of the observed signatures. Several spatial scales can be considered in the study of fluvial hydraulics, from the very local to the regional scale:

- Near the flow boundary layer, the localized impact of basal friction (from banks, bottom friction) or drag effects on obstacles, can be seen in the water surface. Satellite observations generally do not yield meaningful information on these phenomenons. These localized phenomenons are studied in laboratory-scale experiment (e.g. Nikora et al. [2004]).

- At the local scale, the longitudinal scale of phenomenons is lower than their lateral scale. Phenomenons include local backwater effects, small singularities of section or slope and change of flow regimes. High resolution satellite sensors and some impermanent measurements, e.g. using LSPIV and ADCP, may provide observability at this scale.

- At the reach scale, the longitudinal scale of phenomenons is higher or equal to their lateral scale. For this scale, we define fluvial hydraulic controls (HC) as characterized by a maximal deviation of the water depth from the normal depth following Montazem et al.

[2019]. They can be exerted by control sections (e.g. reduced width, in-line structure, confluence) over up to hundreds of kilometers upstream (see Allen and Pavelsky [2015, 2018]). Multi-satellite altimetry offers coverage at this scale and, depending on station density, permanent in situ networks may too.

- At the network scale, hydrological and hydrogeological phenomenons impact water surface deformations.

The observability of hydrodynamic signatures given by current available sensors networks, that is in situ stations and campaigns and satellite sensors, is extensive, yet heterogeneous. The combination of observations from satellite and local measurements, each providing specific and crucial information at the basin scale, should be strived for with the goal to enable the estimation of hydraulic parameters and hydrological fluxes. This thesis work aims at proposing methods to achieve this synergetic combination.

Mission	**Start**	**End**	**Cycle period (days)**
Seasat	1978	1978	17
Geosat	1986	1989	17
ERS-1 (5 missions)	1991 to 1995	1992 to 1996	3 to 168
Topex/Poseidon	1992	2005	10
ERS-2	1995	2003	35
Jason-1 and 2	2001 and 2008	2014 and 2019	10
Envisat	2002 and 2010	2010 and 2012	35 and 27
CryoSat-2	2010	-	91
SARAL	2013	-	35
Jason-3	2016	-	10
Sentinel-3A and 3B	2016 and 2018	-	27
GRACE	2002 and 2018	2017 and -	4
SWOT	2022/2023	-	21 (1 to 4 obs per cycle)

Table 1.4: Main satellite missions providing altimetric observations of inland water surfaces. Note that the number of passes per cycle period varies based on latitude and satellite trajectory.

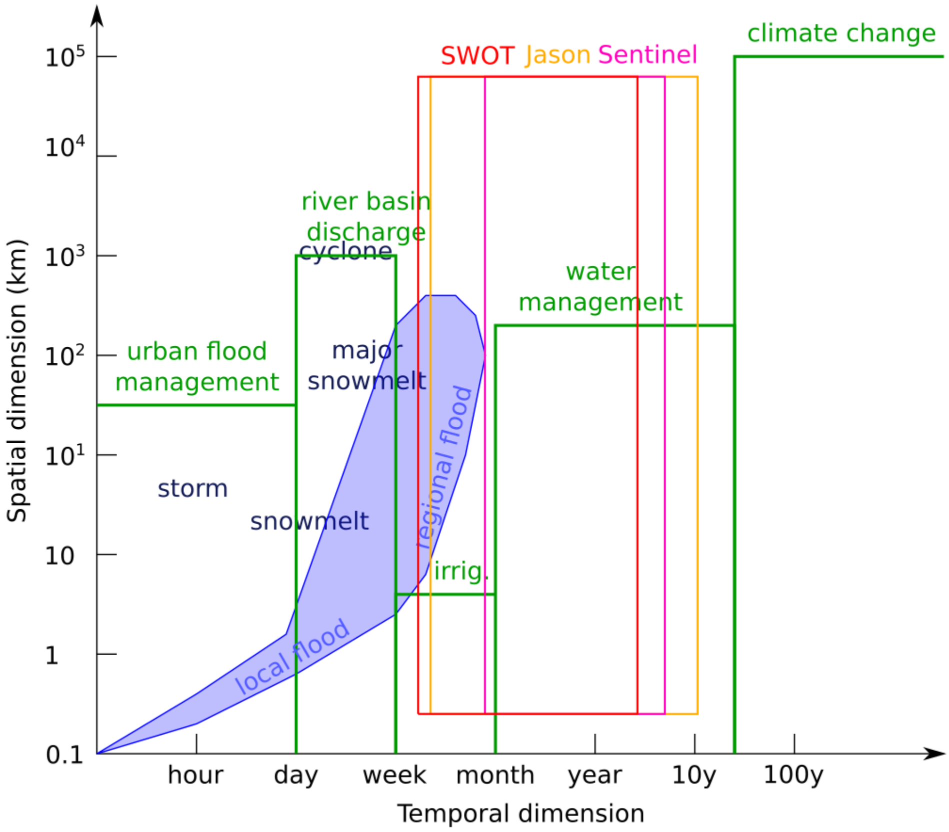

Figure 1.9: Spatio-temporal scale and satellite observability of hydrological cycle components (see Tavakolifar et al. [2017], adapted from Uhlemann [2013]; Hirschboeck [1988]). In green, spatio-temporal domain of hydrological phenomenons. In blue, river network and floodplain domain of variability. In red, orange and purple, observation windows of the upcoming SWOT wide-swath altimetry mission and of the Jason and Sentinel-3 nadir altimetry missions.

1.2 Hydraulic models

In this work, we use hydraulic models as a mean to represent flow states in river networks. They are a simplified representation of real flow physics and consist in partial differential equations describing the motion of water in a free surface flow. More precisely, shallow water equations (SWE) are considered. The 2D SWE equations (Eq. 1.6, presented below) are obtained by vertical integration of the 3D Navier-Stokes equations which are based on the principles of mass and momentum conservation applied to a volume of fluid (see e.g. Thual [2010]). The 1D SWE equations (Eq. 1.2, presented below) are obtained from integration of the 3D Navier-Stokes equations over a flow section. Both versions are widely used in fluvial hydraulics; their demonstration from the Navier-Stokes equations is presented in Appendix A. Classical hypotheses for establishing those flow models are (see e.g. Chow [1959]; Carlier [1982]; Guinot [2010]; Ancey [2018]):

- The fluid is of constant volumic mass ρ, which implies it is incompressible and that no sediment transport is considered.

- The flow is gradually varied, which implies that the flow surface is close to a plane and varies slowly in space, and that there is no sharp change in the flow section. Thus, flow lines are parallel to each other and close to parallel to the river bottom, and vertical velocities are negligible. This is also called the long wave assumption, as it means that with regards to the water depth, signal wavelength is high (Boussinesq [1871]).
- The bottom slope (and thus the water surface slope) is low, such that the water depth can be measured as perpendicular to the river bottom.

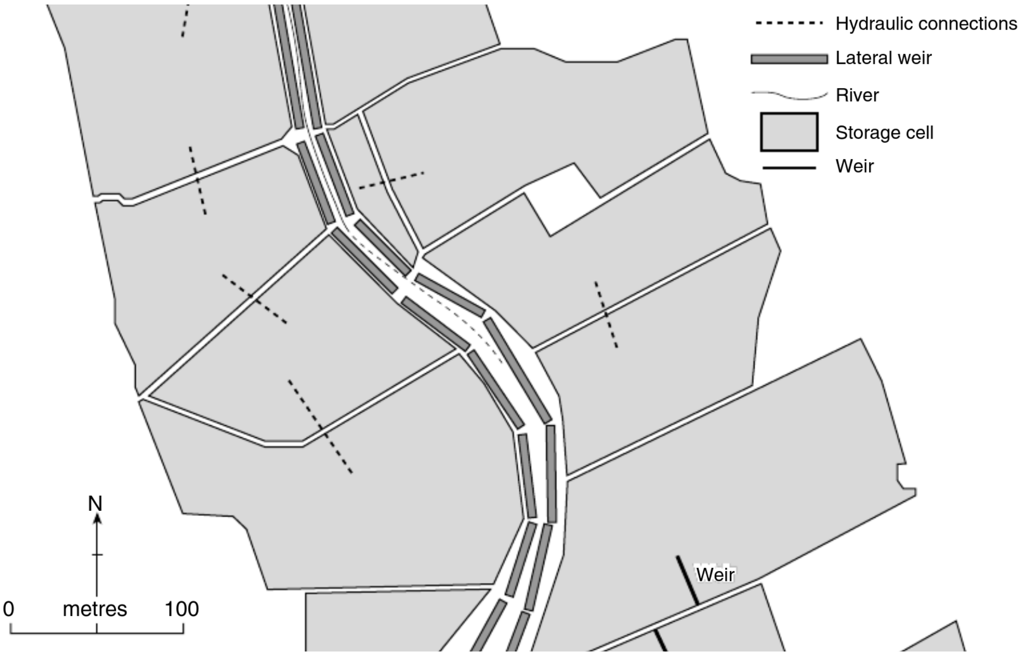

Figure 1.10: Proposed modeling method for flood modeling using a 1D model (from Tayefi et al. [2007]). A 1D river channel (modeled with HEC-RAS) is laterally coupled to a series of interconnected storage cells through weir laws. Storage cells are linked between themselves through transfer laws as well. The article compares a computationally costly 2D approach to adapted, less computationally costly 1D methods for flood modeling.

Furthermore, since the Navier-Stokes equations are obtained far-from-everything, i.e. outside of the influence of liquid domain borders and without interaction between fluid layers, it does not account for shear stress and turbulence (Dingman [2009]). Thus, to account for this important phenomenon in fluvial hydraulics applications, a frictional source term is added and classically given by the empirical Manning-Strickler formulation established for uniform flows (or other similar variants of the original analytical Darcy-Weisbach formula). As an empirical relation, the friction source term accounts for all sources of momentum loss that are not specifically modeled (e.g. through an additional drag force term). Therefore, friction coefficient values may differ between SW models.

Hydraulic models are physically-based, deterministic and spatially distributed. The resolution of a hydrodynamic model requires data to describe river geometry and friction, but also to set boundary conditions for upstream, lateral and downstream flow conditions. The amount of data required depends on the modeling goals and the underlying hypotheses. Examples of applications taken from current bibliography include flood modeling with a 1D hydraulic model and connected lateral storage cells (Tayefi et al. [2007], Fig. 1.10) or with a 2D model (Mulatu et al. [2021], Fig. 1.11(a)) and 2D modeling of within-banks flows with adaptative mesh for morphodynamic models (Langendoen et al. [2016], Fig. 1.11(b)).

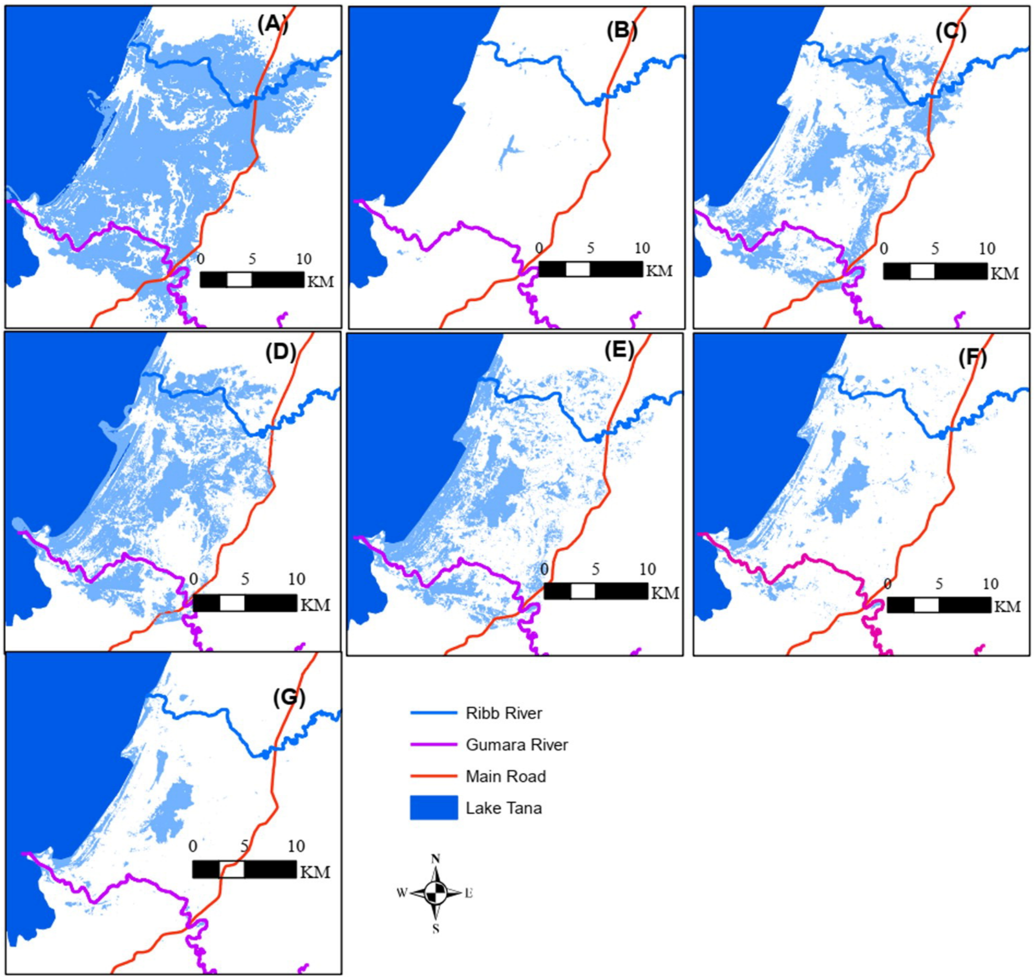

(a) Simulated flooding extents for different events using a 2D model with a Cartesian grid (from Mulatu et al. [2021]). This recent applied engineering article investigates the impact of a dam project on flooding events using a weak coupling of the hydrological model HEC-HMS and the 2D solver of the hydraulic model HEC-RAS.

Figure 1.11: Hydraulic models: 2D hydraulic models used for river reach and floodplain modeling (1)

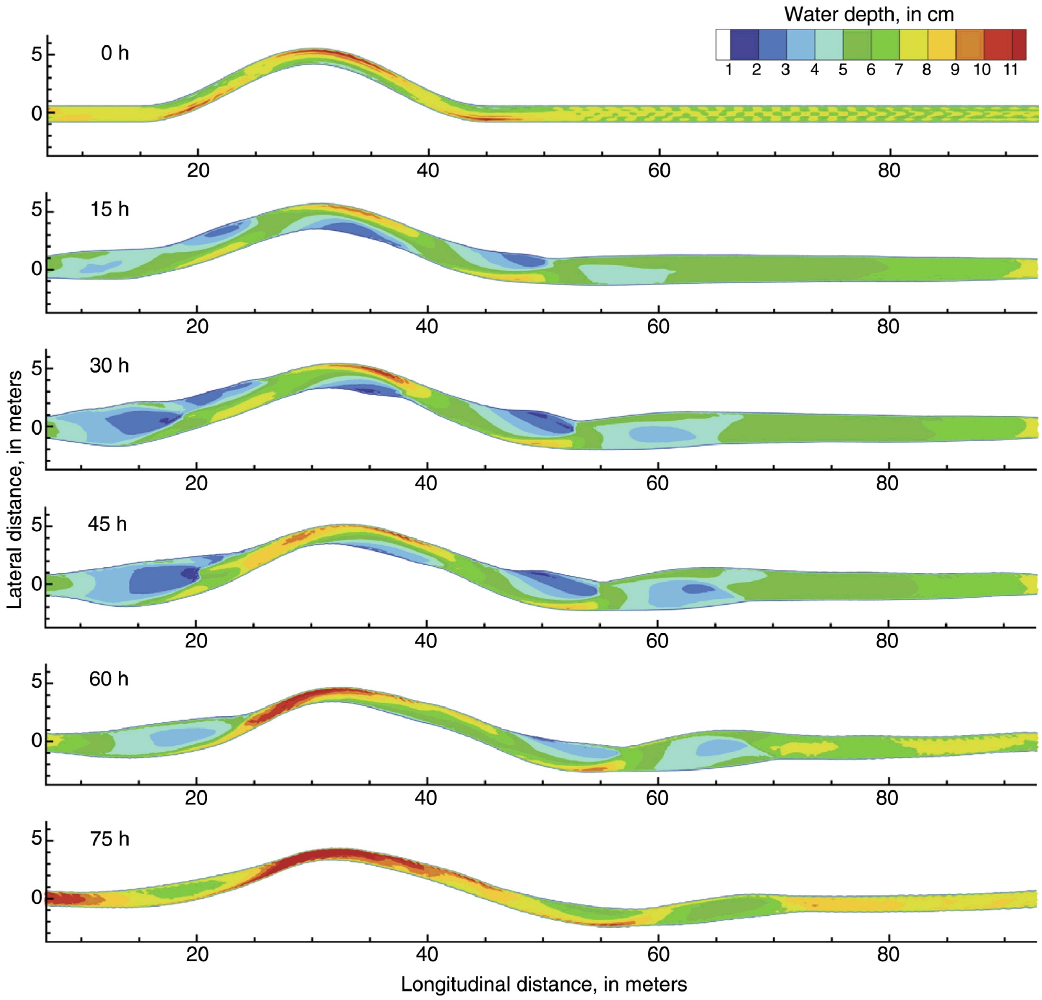

(b) Simulated water depth at successive snapshots over a non-Cartesian grid for within-banks flow (from Langendoen et al. [2016]). The article presents numerical methods for adaptative mesh in morphodynamic models using Telemac-Mascaret.

Figure 1.11: Hydraulic models: 2D hydraulic models used for river reach and floodplain modeling (2)

This section presents the 1D and 2D SWE (see demonstration in Appendix A), as well as an overview of numerical schemes used to solve these equations in the current work. The section also presents some widely used hydraulic models and discusses their design, intended uses and the integration of data assimilation methods.

1.2.1 Mathematical flow models

Mathematical flow models describe movement in a continuous medium. In this work, the medium is an incompressible Newtonian fluid modeled from an Eulerian perspective. The fundamental equations are the 3D Navier-Stokes equations that stem from applying conservation laws of mass and linear momentum to an infinitesimally small fluid volume (Chassaing [1997]; Thual [2010]; Dingman [2009], see Fig. A.1 in Appendix A). In fluvial hydraulics, these equations integrated over water depth to lead to a 2D formulation (Eq. 1.6), and to the 1D formulation (Eq. 1.2) when integrated over a XS. Both integrated forms are known as Shallow Water equations. Adhémar Barré de Saint-Venant, a French physicist and mathematician, was the first to mathematically describe quasi-monodimensional flows in 1871 (Barré de Saint-Venant [1871]), from a heuristic perspective. Hence 1D SW equations are also called Saint-Venant equations.

This section presents the classically used 1D and 2D SW equations, models and the resolution methods performed in the DassFlow computational platform that is used in this work.

1.2.1.1 Rivers shape and notations

Let us define model parameters and state variables in 1D and 2D frameworks. Let t denote the time and x the spatial location.

In 1D models, $x \in \mathbb{R}$ denotes a curvilinear abscissa on a filar network representation. River reaches are represented as a series of XS (defined over separate y axes, see Fig. 1.12(b)), where XS profiles $\tilde{b}\left(x,y\right)$ and friction parameters are defined. The water depth $h\left(x,t\right)$ is given by $Z\left(x,t\right) - b\left(x\right)$, where $b\left(x\right) = min_y\left(\tilde{b}\left(x,y\right)\right)$. The top width $w\left(x,t\right)$ is given by the position of the banks and the water depth at t. The state variables are $A\left(x,t\right) = \int_{y_G(x,t)}^{y_D(x,t)} \int_{\tilde{b}(x,y)}^{Z(x,y,t)} dzdy$ $\left[\mathrm{m}^2\right]$, the flow section, and $Q\left(x,t\right) = \int_{y_G(x,t)}^{y_D(x,t)} \int_{\tilde{b}(x,y)}^{Z(x,y,t)} u_x dzdy$ $\left[\mathrm{m}^3/\mathrm{s}\right]$, the flow crossing A (see Fig. 1.12(a)). Note that $Q/A = U$, where U is the section-averaged flow velocity.

In 2D models, $x \in \mathbb{R}^2$ denotes the spatial coordinates. The state variables are the water depth $h\left(x,y,t\right)$ $\left[\mathrm{m}\right]$ and the depth-averaged velocity $\boldsymbol{u} = \left(u,v\right)^T$ $\left[\mathrm{m}/\mathrm{s}\right]$. They are evaluated at each model cell, see Fig. 1.12(b)).

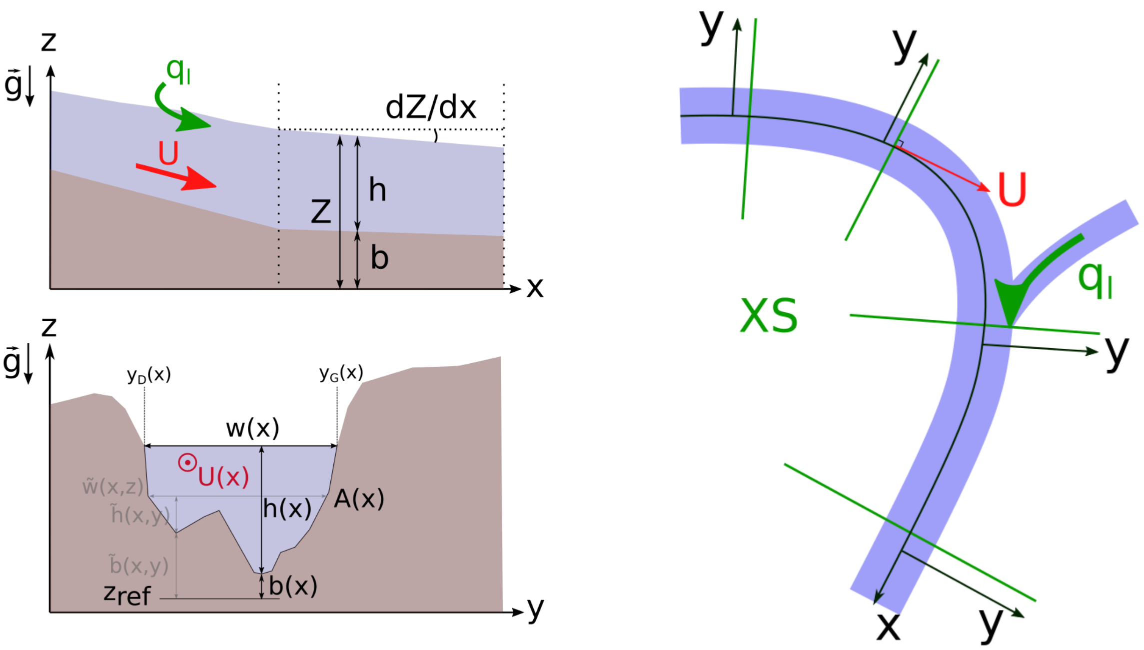

(c) Left: Longitudinal and cross-sectional view. q_l is a lateral inflow, see e.g. Eq. (1.2). y_G and y_D denote the position in a XS of the left and right banks respectively. z_{ref} is the reference altitude. Right: Top-down view. In 1D models, the curvature is neglected, hence $Q\,(u_x)$.

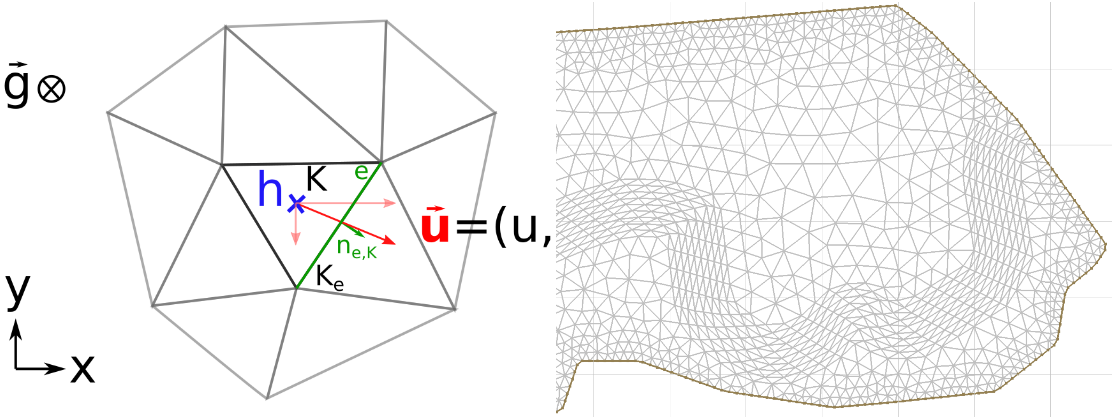

(d) Left: 2D notations. Right: Example mesh intended for overbank flow modeling, with gradually varied edge lengths/cell sizes between river bed and floodplain.

Figure 1.12: Notations in 1D (A, Q) and 2D (h, u, v) models. (a) Longitudinal and cross-sectional notations of parameters and variables used in Eq. (1.2). (b) Notations of cell variables used in Eq. (1.6) and sample mesh of river bed and the surrounding floodplain (from Christopher and Arturo [2013]).

1.2.1.2 1D Saint-Venant equations

We consider a 1D river domain $\Omega^{1D} \subset \mathbb{R}$ and denote by $t \in]0, T]$ the physical time. Let $A\,(x,t)$ $[\mathrm{m}^2]$ be the flow cross sectional area and $Q\,(x,t)$ $[\mathrm{m}^3/\mathrm{s}]$ the discharge such that $Q = UA$ with

$U(x,t)$ defined as the longitudinal XS averaged velocity $[\mathrm{m/s}]$ (see Fig. 1.12(a)). The 1D SWE or Saint-Venant equations in (A,Q) variables with lateral flows writes as follows (see also Appendix A):

$$\begin{cases} \dfrac{\partial A}{\partial t} + \dfrac{\partial Q}{\partial x} & = q_l \\ \frac{\partial Q}{\partial t} + \frac{\partial}{\partial x}\left(\frac{Q^2}{A}\right) + gA\frac{\partial Z}{\partial x} & = -gAS_f + Uq_l \end{cases} \tag{1.2}$$

$$(1) \qquad (2) \qquad (3) \qquad\qquad (4) \qquad (5)$$

where $Z(x,t)$ is the WS elevation $[\mathrm{m}]$ and $Z = (b+h)$ with $b(x)$ the river bed level $[\mathrm{m}]$ and $h(x,t)$ $[\mathrm{m}]$ the water depth, g $\left[\mathrm{m/s^2}\right]$ is the gravity magnitude and $q_l(x,t)$ is the lineic lateral discharge $\left[\mathrm{m^2/s}\right]$. A description of the five momentum equation terms is made at the end of this subsection.

The non-linear friction term S_f is classically parameterized with the empirical Manning-Strickler law established for uniform flows:

$$S_f = \frac{|Q|\,Q}{K^2 A^2 R_h^{4/3}} \tag{1.3}$$

with K the Strickler friction coefficient in $\left[\mathrm{m^{1/3}/s}\right]$, $R_h(x,t) = A/P_h$ $[\mathrm{m}]$ the hydraulic radius and $P_h(x,t)$ $[\mathrm{m}]$ the wetted perimeter, .

In order to deal with the non conservative term $gA\frac{\partial b}{\partial x}$, as proposed in Vila [1986b], one can introduce a "relative pressure term" P such that:

$$P\left(x,\tilde{S},t\right) = g\int_0^{h(x,t)} \left(h-\tilde{h}\right)\tilde{w}\,d\tilde{h} \tag{1.4}$$

with $\tilde{S}$ and $\tilde{w}$ respectively corresponding to the flow area and width at depth $\tilde{h} \in [0,h]$. As done e.g. in Brisset et al. [2018], without lateral flows, the 1D SWE in (A,Q) variables can be written as:

$$\begin{gathered} \frac{\partial}{\partial t}\mathbf{U} + \frac{\partial}{\partial x}\mathbf{F}(\mathbf{U}) = \mathbf{S}(\mathbf{U}) \\ \mathbf{U} = \begin{bmatrix} A \\ Q \end{bmatrix}, \; \mathbf{F}(\mathbf{U}) = \begin{bmatrix} Q \\ \dfrac{Q^2}{A} + P \end{bmatrix}, \\ \mathbf{S}(\mathbf{U}) = \begin{bmatrix} 0 \\ g\displaystyle\int_0^h \left(h-\tilde{h}\right)\frac{\partial \tilde{w}}{\partial x}\,d\tilde{h} - gA\frac{\partial b}{\partial x} - gAS_f \end{bmatrix} \end{gathered} \tag{1.5}$$

As shown in Couderc et al. [2013], the jacobian matrix of $\mathbf{F}(\mathbf{U})$ has two eigenvalues $U + c$ and $U - c$, with $U = Q/S$ and $c = \sqrt{\dfrac{\partial P}{\partial S}}$. Given that A is also strictly positive, the system Eq. (1.5) is strictly hyperbolic.

In order to obtain a well-posed problem, it is necessary to add initial and boundary conditions. Upstream, lateral and downstream boundary conditions are imposed on flow state variables depending on flow regimes and detailed in the following case studies. For the fluvial flows of interest, inflow hydrographs $Q_{in}\left(t\right)$ and $q_{l,d}\left(t\right)$ at $d \in [1..N_d]$ are classically imposed respectively upstream of the river domain and at known injection cells along the river domain using the main channel flow speed. Let us define the Froude number $\mathrm{F}r = U/c = Q^2 w/\sqrt{gA^3}$ comparing the average flow velocity U to wave celerity c. The initial conditions are set as the steady state backwater curve profile $Z_0\left(x\right) = Z\left(Q_{in}\left(t_0\right), q_{l,1..N_d}\left(t_0\right)\right)$

Signification of the momentum conservation equation terms (see e.g. Ancey [2018]):

(1) Local acceleration term: describes velocity change over time.

(2) Convective acceleration term: describes velocity change over space and accounts for heterogeneous velocity speeds. It allows to model progressive hydrograph skewness as the flood wave is propagated in the network and hysteresis behavior in h-Q relations. Nullifying this term transforms the SWE into the diffusive wave equations.

Terms (1) and (2) constitute the "inertial" term and are omitted in some simplified hydraulic models.

(3) Pressure gradient term: accounts for heterogeneous water depths and allows to model wave attenuation as the flood wave is propagated in the network. Nullifying this term transforms the SWE into a kinematic wave equation.

(4) Friction source term: accounts for momentum loss due to all sources of momentum dissipation (bank and bottom friction, eddies, obstacles, ...). It can be complemented by additional terms (e.g. a drag force source term).

(5) Injected flow momentum term: this additional term accounts for the momentum added by the injection of a lateral flow.

1.2.1.3 2D Shallow Water equations

We consider a 2D river domain $\Omega^{2D} \subset \mathbb{R}^2$ and denote by $t \in]0, T]$ the physical time. The 2D SWE including the Manning-Strickler friction term in their conservative form write as follows (see e.g. Guinot [2010]; Ancey [2018] and Appendix A):

$$\begin{gathered}
\tfrac{\partial}{\partial t}\mathbf{U} + \tfrac{\partial}{\partial x}\mathbf{F}(\mathbf{U}) + \tfrac{\partial}{\partial y}\mathbf{G}(\mathbf{U}) = \mathbf{S}_g(\mathbf{U}) + \mathbf{S}_f(\mathbf{U}) \\
\mathbf{U} = \begin{bmatrix} h \\ hu \\ hv \end{bmatrix}, \mathbf{F}(\mathbf{U}) = \begin{bmatrix} hu \\ hu^2 + \dfrac{gh^2}{2} \\ huv \end{bmatrix}, \mathbf{G}(\mathbf{U}) = \begin{bmatrix} hv \\ huv \\ hv^2 + \dfrac{gh^2}{2} \end{bmatrix}, \\
\mathbf{S}_g(\mathbf{U}) = \begin{bmatrix} 0 \\ -gh\nabla b \end{bmatrix}, \mathbf{S}_f(\mathbf{U}) = \begin{bmatrix} 0 \\ -g\dfrac{n^2 \|\mathbf{u}\|}{h^{1/3}}\mathbf{u} \end{bmatrix}
\end{gathered} \tag{1.6}$$

with h the water depth [m] and $\mathbf{u} = (u, v)^T$ the depth-averaged velocity [m/s] being the flow state variables (see Fig. 1.12(b)). The flow model parameters are g $\left[\mathrm{m/s^2}\right]$, the gravity magnitude, b [m], the bed elevation, and n $\left[\mathrm{s/m^{1/3}}\right]$, the Manning-Strickler friction coefficient. $\mathbf{F}(\mathbf{U})$ is the flux of the variable $\mathbf{U}$, $\mathbf{S}_g(\mathbf{U})$ is the gravitational source term, $\mathbf{S}_f(\mathbf{U})$ is the mass and friction source term.

1.2.2 Resolution methods

1.2.2.1 1D SW model resolution with DassFlow1D

As a matter of facts, the analytical resolution of the set of non linear partial differential equation (PDE) Eq. (1.2) or Eq. (1.5) with initial and boundary conditions is not possible. The approximation of solutions is classically performed using a numerical resolution method based on spatio-temporal discretization of the river and temporal domain. Classical initial and boundary conditions adapted to real cases are considered in numerical resolution methods in DassFlow platform (see Monnier et al. [2016]; Couderc et al. [2013]). In this work, the numerical resolution of the 1D SW equations (Eq. 1.2) is performed with a classical semi-implicit finite difference scheme (a Preissmann scheme, see e.g. Cunge et al. [1980]). The 1D SW equations (Eq. 1.5) are solved with an explicit finite volume scheme (a HLL scheme, for Harten-Lax-van Leer, see Harten et al. [1983]; Toro [2009]). Solvers are used on a regular grid of spacing Δx and with a time step Δt, either fixed or adaptative. Both are implemented into the computational software DassFlow (Couderc et al. [2013]; Larnier et al. [2021]). Source terms corresponding to lateral flows have been implemented in the present work in DassFlow1D, for HLL and Preissmann schemes. The detailed Preissmann scheme discretization of 1D SW model with lateral flows, is given in Appendix B. The addition of a lateral inflow source term is not documented here.

1.2.2.2 2D SW model resolution with DassFlow2D

In DassFlow2D (see Couderc et al. [2016]), finite volume Godunov-type schemes (Godunov and Bohachevsky [1959]) with well-balancing properties are used to solve the SWE. A classical first order Euler explicit time-stepping and an Implicit-Explicit (IMEX) Runge-Kutta time-stepping scheme with global second order accuracy are used with a HLLC Riemann solver. The solver is an improvement over the HLL scheme from Harten et al. [1983] using a three-wave model for flux calculation, see Toro [2009]. The second order scheme is notably accurate and robust in wet/dry front propagation scenarios (see Couderc et al. [2016] for more details).

Remark that given a discretization of the computational domain $\Omega^{2D} \subset \mathbb{R}^2$, finite difference schemes solve for variables at a spatial point, while finite volume schemes solve for averaged variables over a cell. Explicit schemes depend on variables at the previous time-step, whereas implicit schemes depend on current and previous time-steps.

Over a given cell K of area m_K, consider the piece-wise constant approximation $\mathbf{U}_K = \frac{1}{m_K} \int_K \mathbf{U} dK$. Recall that the finite volume approach applied to the homogeneous part of the hyperbolic system of equations 1.6 - that is without the source terms $\mathbf{S}_g$ and $\mathbf{S}_f$ - writes as follows:

$$\mathbf{U}_K^{n+1} = \mathbf{U}_K^n - \frac{\Delta t^n}{m_K} \sum_{e \in \partial K} m_e \mathbf{F}_e \left(\mathbf{U}_{K,i}^n, \mathbf{U}_{K_e}^n, \mathbf{n}_{e_i,K} \right) \tag{1.7}$$

where $\mathbf{U}_K^n$ and $\mathbf{U}_K^{n+1}$ are the piece-wise constant approximations of $\mathbf{U}$ at time t^n and t^{n+1} (with $t^{n+1} = t^n + \Delta t^n$), $\mathbf{F}_e$ stands for Riemann fluxes through each edge e of the border ∂K of the cell K, with each adjacent cell K_e. The length of edge e is m_e and $\mathbf{n}_{e,K}$ is the unit normal to e oriented from K to K_e.

Source term treatment During a computational time step, the full conservative SW equations are solved first, independently from non-conservative source terms in $\mathbf{S} = \mathbf{S}_g + \mathbf{S}_f$. Then, source terms are handled by a two-step splitting algorithm. This can be written as:

$$\begin{cases} \bar{\mathbf{U}}_i^{n+1} & = \mathbf{U}_i^n - \Delta t^n \dfrac{\mathbf{F}_{i+1/2}^n - \mathbf{F}_{i-1/2}^n}{\Delta x_i} \\ \mathbf{U}_i^{n+1} & = \bar{\mathbf{U}}_i^{n+1} + \Delta t^n \mathbf{S}_f \left(\bar{\mathbf{U}}_i^{n+1} \right) \end{cases} \tag{1.8}$$

with $\bar{\mathbf{U}}_i^{n+1}$ an intermediate value of the computed variables and Δt the computational time step. This time-splitting method is implemented in first and second order schemes in DassFlow2D (see Couderc et al. [2016]). Details on the 2D solver and on friction source term implicitation are provided in Subsection 3.A.

1.2.3 Computational hydraulic models

Computational hydraulic models are common tools, that include numerical methods required to solve the flow models detailed in Subsection 1.2.1. The following paragraphs presents some widely-used hydraulic models, distinguished between 1D and 2D approaches, numerical schemes and resolution methods, solved hydraulic equations and applied data assimilation methods.

1D numerical hydraulic models are widely used in river engineering applications but also in water level forecasting since they require relatively few data and are not computationally costly. 2D models generally require more information, like fine 2D bathymetry, and their computational cost is higher. They are used for local and detailed hydraulic studies where estimating dynamics 2D flow patterns is part of the modeling goals, e.g. dynamic flood mapping in urban areas.

Simplified 2D hydraulic models, that are less computationally costly but also have more limited applicability, are also used for larger scale applications such as regional flood modeling. Some existing 1D and 2D hydraulic models are presented in Table 3.1 along with a description of their main features in terms of model, numerical scheme, and in some cases optimization and assimilation methods. Multi-physics features such as sediment transport and erosion-deposition in river channels (e.g. Langendoen et al. [2016]; Gibson et al. [2015]) are out of scope here.

1D hydraulic models enable to simulate meaningful spatio-temporal variabilities of flow sections/lines and discharge, from the reach scale to the river network scale, see e.g. Vozinaki et al. [2017] with HEC-RAS, Barthélémy et al. [2018] with Mascaret or Pujol et al. [2020]; Malou and Monnier [2021] with DassFlow1D. Moreover, effective parameterizations enable to account for the effect of various hydraulic structures (such as frontal or lateral weirs, culverts, ...) or for lateral exchanges of mass with floodplains via "casiers" (see Brunner [1995] and references therein) or even mass and momentum exchange with effective floodplain flows (e.g. ISM model, Proust et al. [2009] and references therein, see also Bousmar and Zech [1999]). Among reference 1D models, one can cite the widely used HEC-RAS (Brunner [1995]) or Mike11 (Havnø et al. [1995]) models. Note that the unsteady solver of HEC-RAS uses a locally inertial simplification (LPI, see Fread et al. [1996]) and a Preissmann numerical scheme (see Cunge et al. [1980] and references therein). A full 1D hydraulic model is solved in MAGE (Preissmann scheme, Guertault et al. [2016]), Mascaret (HLL scheme, see Goutal and Maurel [2002]) and DassFlow1D (Preissmann and HLL schemes, see Brisset et al. [2018]). Note that in DassFlow1D, an accurate finite volume scheme is implemented using a "pressure term" pre-balancing in the continuous model (Eq. 1.5) as proposed by Vila [1986b], next used by Goutal and Maurel [2002].

Full 2D SW numerical models enable to simulate high resolution dynamic flooding of floodplains (e.g. Finaud-Guyot [2009]; Galland et al. [1991] and references therein), including complex urban flooding (SW2D, see Guinot et al. [2017]; Steinstraesser et al. [2021]), but also recently at the scale of a river network of a medium sized catchment of 808 km^2 in Nguyen et al. [2016]. In Fleischmann et al. [2020] with the MGB model or in Grimaldi et al. [2018]; Uhe et al. [2020] with LISFLOOD-FP, raster based inundation modeling over very large domains is performed with a simple 2D storage cell inundation model obtained from 1D inertial model (Bates et al. [2010] following Hunter et al. [2008], recently adapted to unstructured meshes in Sridharan et al. [2021]). In Hocini et al. [2020], an original 2D hydraulic modeling approach proposed by Davy et al. [2017] and based on "precipiton" is used to compute steady inundation maps of various return periods at high resolution (5 m) for river networks and floodplains at catchment scale (several thousands of square kilometers, up to 5050 km^2). In Nguyen et al. [2016], a full unsteady 2D hydraulic model (BreZo, Begnudelli and Sanders [2006]) is applied at relatively high resolution (10 or 30 m) in the river network and floodplains on a 808 km^2 catchment. One can also cite the interesting macroscopic approaches inspired by flows in porous media (see Guinot et al. [2017] and references therein), with a reduced computational cost compared to high resolution full 2D models, though it is still faced with the issue of sub-grid parameters estimation to approximate flows physics (either fine 2D or real flows).

In order to combine local accuracy and computational efficiency, a combination of full 1D and 2D hydraulic models is appropriate for simulating a basin-scale network in a way that is both practical and adequately accurate. Methods for coupling models of different dimensions have been developed (Miglio et al. [2005a,b]; Amara et al. [2004]), classically using domain decomposition (Gervasio et al. [2001]), or more recently using 2D 'zooms' overlapping with the 1D domain, in a variational data assimilation framework (Gejadze and Monnier [2007]; Marin and Monnier [2009]). An iterative coupling strategy is applied in Barthélémy et al. [2018] between a 1D operational model and a 2D operational model with a sequential assimilation technique for water level forecasting.

Reaching high resolution accuracy and computational hydraulics efficiency for large scale applications remains a difficult challenge given multi-scale hydrodynamics and multiple uncertainty sources. The accuracy of high resolution computations may still be affected by complex dynamics with wet-dry front propagations, uncertain quantities at open boundaries (upstream inflows but also lateral ones, downstream controls and backwater effects), multi-scale and uncertain topography-structures and flow model parameters (e.g. friction effects), internal in/outflows in urban areas, and large computational domains (e.g. Monnier et al. [2016]).

In the river hydraulics community, the most employed data assimilation methods are based on sequential algorithms, using Kalman filters and variants. Let us cite for example Roux and Dartus [2005, 2006] who estimate flood hydrographs in the 1D Saint-Venant model from dense water surface width measurements; the bathymetry and friction are given. Variational data assimilation algorithms based on the adjoint method have been proposed for 2D hydraulic modeling (Monnier et al. [2016] and references therein) or 1D hydraulic modeling (Brisset et al. [2018]; Larnier et al. [2021]) and implemented in the DassFlow platform. Using VDA, one can infer boundary conditions like upstream hydrographs, as in Honnorat et al.; Hostache et al. [2010] in 2D or as in Garambois et al. [2020]; Larnier et al. [2021] in 1D, and distributed bathymetry-friction parameters, from multi-source data. VDA is particularly adapted to address high dimensional inverse problems with non-linear dynamic hydraulic models. In the hydraulic community, the calibration of model friction, usually set as spatially uniform by lack of constraining data, is often performed manually or with simple optimization methods. Note that Monte Carlo simulations have been applied with full 2D hydraulic models in Aronica et al. [2012] for flood hazard evaluation or in Chen et al. [2018] for computing Sobol sensitivity indices of a 2D SW model (Telemac2D) applied for flood modeling over urban street networks, but remain computationally expensive.

The DassFlow[5] computational platform is used in this work. This platform allows for the resolution of 1D and 2D full shallow water equations with finite difference schemes and well balanced finite volume schemes respectively (more details in Subsection 1.2.2), as well as the use of variational data assimilation using adjoint code obtained via automatic differentiation (Tapenade tool, Hascoet and Pascual [2013]). To our knowledge, DassFlow is the first numerical tool proposing large scale multi-D river network modeling with VDA capabilities.

---

[5] http://www.math.univ-toulouse.fr/DassFlow/

Platform	Model	Mathematical model	Max order	Coupling 1D-2D SWE	Parallel computation	DA	Sources available
HEC-RAS [40]	1D-2D	(A, Q) and (h, u, v), both locally non-inertial SWE	1	Internal (2 solvers)	No	-	No
BreZo [232]	2D	(h, u, v), porosity	2	No	Yes	-	No
FullSWOF [71]	1D and 2D	(h, u, v) for both, full SWE	1	No	Yes	-	Yes
SW2D-LEMON [242; 121]	2D	(h, u, v), porosity	1	No	No	-	Yes
Floodos [68]	2D	(h, u, v), non-inertial SWE	1	No	No	-	Yes
b-flood [144]	2D	(h, u, v), full SWE	1	No	Yes	-	Yes
Telemac-Mascaret [96; 111]	1D and 2D	(A, Q) and (h, u, v), full SWE	1	External (2 solvers)	Yes	EnKF	Yes
LISFLOOD-FP [23]	1D-2Dlike	(A, Q) non-inertial SWE	1	No	Yes	EnKF	Yes
DassFlow2D [179]	2D-1Dlike	(h, u, v), full SWE	2	Internal (same solver)	Yes	Var	Yes
DassFlow1D [38]	1D	(A, Q), full SWE	1	-	No	Var	Yes

Table 1.5: Some established freeware hydraulic models. The equations resolved are either formulated in (A, Q) (flow section $[\mathrm{m}^2]$ and at-a-section discharge $[\mathrm{m}^3/s]$) or in (h, u, v) (water depth $[\mathrm{m}]$ and 2D depth-integrated flow velocities $[\mathrm{m}/s]$). "Max order" refers to the maximum demonstrated scheme order.

1.3 Hydrological models

As discussed in Subsection 1.1.4, the measurement of hydraulic variables at the catchment scale is difficult and data are generally lacking, especially for larger domains. To estimate inflows to be injected into basin-scale river network hydraulic models, hydrological models can be used and coupled to them. Hydrological models used in this work were "weakly" coupled, i.e. the hydrological model generates inputs for the hydraulic model without being influenced by its parameters or states.

Hydrological models aim to predict how atmospheric forcings translate into catchment response, i.e. stream flow at the model outlet (Beven [2000]), especially for forecasting of extremes (floods and droughts). They generally take into account meteorological inputs in the form of rain, snow, evaporation and transpiration, as well as some catchment characteristics appropriate to the modeling approach. Modeling scales can range from upstream catchments (e.g. Roux et al. [2011]; Perrin et al. [2007]) to large basins (Collischonn et al. [2007]; Paiva et al. [2013a]).

1.3.1 Modeling approaches

As a matter of facts, hydrological processes are difficult to observe and contrarily to hydraulics, "first principle" hydrological laws do not exist. Therefore, approaches with a certain degree of empirism have been proposed in the literature to represent catchment scale hydrological processes. So-called downward approaches consider the inputs and outputs first in model design, while upward approaches start from physically-based relationships.

- Empirical relations can be established from time series of catchments inputs and outflows, e.g. through frequency analysis (Xu et al. [2017]). Pure data driven models have recently been proposed using deep learning techniques such as "long short term memory" (LSTM) neural networks (see Kratzert et al. [2019], study of hydrological regimes in France in Hashemi et al. [2021]). Although these models can be accurate, they work as a "black box" and carry no information on the physical catchment itself. Moreover, their extrapolation capability is still limited outside of the learning set but their "interpolation power", especially for tough problems as regionalization (prediction at ungauged locations) is interesting as shown in Kratzert et al. [2019]; Hashemi et al. [2021].

- Conceptual models separate identified hydrological processes into a series of conceptual relations. Bucket-type models divide catchment processes into water stores linked by drainage laws such as in GR4 model (Perrin et al. [2003]; Mathevet [2005]). The latter consists in a parsimonious and robust model structure, lumped in space, established on large catchment sets to model their outlet discharges. The conceptual basis of those models makes internal state variables and parameters difficult to relate to real catchment states (such as soil moisture) and physiographic characteristics.

- Physical models include physically-based relations for hydrological fluxes (e.g. the Green-Ampt infiltration model (Green and Ampt [1911])) and for flow calculation (e.g. the kinematic wave approximation of SWE in Singh [1997]). Parameters of those models can be inferred from physiographic data but one is generally faced with scale issues, overparameterization and data requirements.

Another distinction can be made between spatially lumped or distributed approaches. The former handle in-catchment variabilities through sub-catchment discretization and modeling, for example using lumped models linked by transfer laws. The latter spatially discretize in-catchment parameters and variables. For example, a version of the GR hydrological model (Santos et al. [2018]) is adapted in a semi-distributed version called GRSD, to account for the effect of rainfall spatial variability Lobligeois [2014], recently adapted to account for rainfall intensity in Peredo et al. [2022].

Recall that modeling is generally a trade-off between modeling goal(s), data availability and model complexity as discussed for hydrological models in Grayson and Blöschl [2001] (see Fig. 1.13).

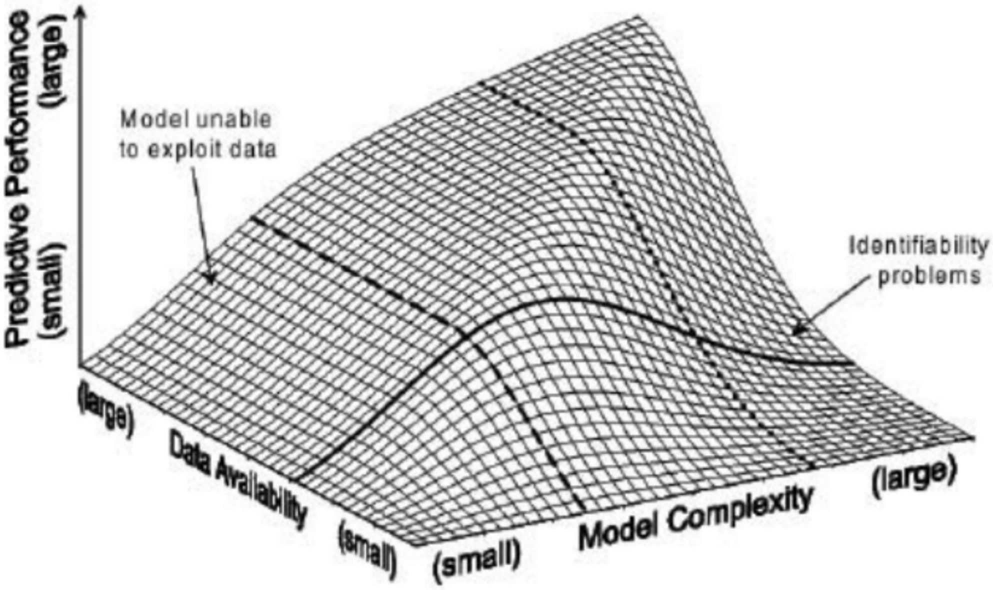

Figure 1.13: Conceptual trade-off between goals, data availability and model complexity in hydrological models (from Grayson and Blöschl [2001]).

Given a 2D-spatial domain $\Omega_{rr} \subset \mathbb{R}^2$ (a basin/catchment/watershed), a hydrological model can be viewed as a dynamic operator $\mathcal{M}_{rr}$ relating state variables $h_{rr}(x,t)$, $\forall x \in \Omega_{rr}$ (e.g. internal water storage and fluxes) with several observable input fields $\boldsymbol{I}(x,t)$ (precipitation, evaporation, ...), observable outputs $Y_{rr}(x,t)$ (e.g. discharge) and "unobservable" parameters $\theta_{rr}(x)$. Note that the number of unobservable parameters and states coupled to their correlated influence on observable signals renders the inverse problem for hydrological model ill-posed (see Subsection 1.4.1). This means its solution is non-unique since several parameter-and-states set can lead the same observable signal (so called equifinality problem Bertalanffy et al. [1968]; Beven [2006]). The calibration of hydrological models is complex and often involves feeding a priori information to the calibration method such as, for example, proximity constraints in a calibration algorithm applied to the GRSD hydrological model on a river network De Lavenne et al. [2019]).

In this work, hydraulic models are coupled to spatially distributed conceptual hydrological models in the context of river network modeling and parameter inference from multi-source data. First, the large scale MGB model (Collischonn et al. [2007]; Pontes et al. [2017]) is used for inflowing a large scale 1D hydraulic modeling. Next, the coupling of the GR4H model (Perrin et al. [2007]), used in a semi-distributed setup, to a 2D hydraulic model is investigated. More precisely, in view to investigate inverse problems with a hydraulic-hydrological assimilation chain, the source code of GR4H, in its state-space version (Santos et al. [2018]), is included in the DassFlow2D source code and differentiated to obtain its adjoint. The GR4H and MGB models used in this work are detailed after.

1.3.2 MGB: a large scale hydrological model

MGB is a large scale semi-distributed rainfall-runoff model designed to simulate discharge in large river basins (Collischonn et al. [2007]; Pontes et al. [2017]) schematized in Fig. 1.14. The model discretizes basins into "unit catchments", themselves divided into hydrological response units (HRUs). It takes into account precipitations, interception, evapotranspiration and infiltration in order to model surface, sub-surface and groundwater flows, and finally inflows to the river network.

The hydrological module applied to each unit catchments consists in a soil reservoir where the partition between surface runoff and infiltration is described with a variable contributing area (VIC) model (concept from Liang et al. [1994]; Zhao et al. [1980]; Todini [1996]; Ludwig and Bremicker). Evaporation from soil and vegetation is described with a Penmann-Monteith model (e.g. Wigmosta et al. [1994]). Subsurface flow is taken from the soil reservoir and described with a function similar to the Brooks and Corey non-saturated hydraulic conductivity equation (Rawls et al. [1992]). A linear relation is used to model percolation from the soil reservoir to the groundwater reservoir. The three lateral fluxes, arising above or from soil reservoir for each HRU of a unit basin, are simply collected and delayed with one linear reservoir for each. The river flow routing scheme, a Muskingum Cunge based method (see Paiva et al. [2013b] and references therein), is expected to represent wave delay and attenuation along the network, but not backwater controls or loss of mass and momentum in the main channel due to floodplain exchanges.

MGB exists in 1D and 2D versions that are compared in Fleischmann et al. [2020]. In the 1D version (Collischonn et al. [2007]), large numbers of hydrological catchments are linked by a routing model based on the inertial flood wave routing method (solving simplified SWEs). In the hydraulic part of the model, these catchments are considered as storage units. The routing equations are simplified and aimed at modeling stream flow at a large scale. They allow taking advantage of altimetric WS observations (e.g. through sequential DA methods in Paiva et al. [2013c]). In the 2D version, the basin is discretized into a regular Cartesian grid in which simplified SW equations (locally inertial diffusive formulation) are solved. Floodplain flows are computed between each orthogonal neighbor based on the LISFLOOF-FP sub-grid model (Neal et al. [2012]), while channel flows may be further informed by sub-grid DEM and computed between cells connected by identified channels (Fleischmann et al. [2020]).

In this work, MGB was used in weak coupling to DassFlow1D to compute spatially distributed hydrological inflows into the river network. This assumption is based on the good performance at flow gauge of the spatially distributed and regionalized MGB model (Pontes et al. [2017]).

1.3.3 GR4H: a bucket-type rainfall-runoff model

The GR4H model (Mathevet [2005]) is a lumped continuous model that runs at the hourly time step. It is based on the GR4J model formulation of Perrin et al. [2003] and uses a robust and parsimonious production function proposed in (Michel [1989]). This model is widely used and has been compared to other hydrological models (see e.g. Tian et al. [2013]; Nepal et al. [2017]). It is used in this work because it is a well established, parsimonious and robust model, based on Ordinary Differential Equations (ODEs, state-space version only (Santos et al. [2018])) hence differentiable. This property is interesting in the present work as it is a necessary condition to

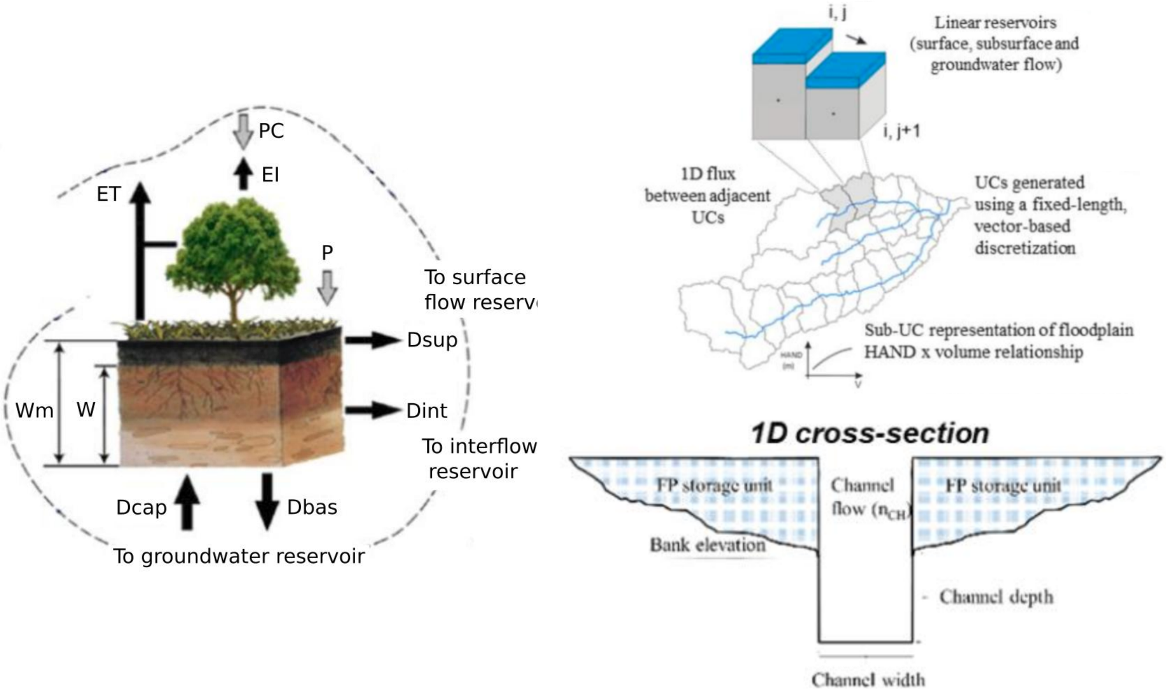

Figure 1.14: MGB model reservoirs and propagation modeling (adapted from Fleischmann et al. [2020]; Collischonn et al. [2007]). Three linear reservoirs (for surface flow $Dsup$, subsurface flow $Dint$ and groundwater reservoir $Dbas$) link the temporal forcings (over-canopy precipitation PC, evapotranspiration from the soil reservoir ET and from the canopy and vegetation interception reservoir EI) to flow in a simplified channel representation (routing model). W and Wm are respectively the current and maximum soil water storage.

generate an adjoint code for variational data assimilation (see Section 1.4).

Several GR models exist, featuring varying amounts of parameters, stores and time steps (see Perrin et al. [2007]). The "state-space" version of the GR4H model (see Fig. 1.15) is described by the following set of ordinary differential equations:

$$\begin{pmatrix} \dot{S} \\ \dot{S}_{h,1} \\ \dot{S}_{h,2} \\ \vdots \\ \dot{S}_{h,nres} \\ \dot{R} \end{pmatrix} = \begin{pmatrix} P_s - E_s - Perc \\ P_r - Q_{Sh,1} \\ Q_{Sh,1} - Q_{Sh,2} \\ \vdots \\ Q_{Sh,nres-1} - Q_{uh} \\ Q_9 - Q_r + F \end{pmatrix} \tag{1.9}$$

It consists in a production store S, a routing store R and a series of 11 Nash cascade stores $S_{h,i}$, $\forall i \in [1..11]$, that replace a unit hydrograph function from the classical GR4H version. The precipitation input P_n is divided between the production store S and the upper Nash cascade store $S_{h,1}$. The production store R loses water to an evapotranspiration relation and is linked to the upper Nash cascade store $S_{h,1}$ by a discharge law ($Perc$). The reservoirs of the Nash cascade are identical and linked in a chain by discharge relations ($Q_{Sh,i}$, $\forall i \in [1..10]$). The last cascade reservoir outlet $S_{h,11}$ is linked to the routing store R and the model output through a 9-1 tenth repartition. The routing store S and direct routing branch can both exchange water through flux F which represents an exchange for example with aquifers.

The internal model variables are the 13 store levels. Four parameters ((x_1, x_2, x_3, x_4), see Subsections 3.3.3 and 3.C), rule the draining of the production store, of the routing store, of the 11 identical cascading stores and the non-conservative exchange law. They are given per catchment, i.e. spatially distributed. Initial store states are given using a 1 year warm-up period. A series of parameters used in flux calculations are fixed (values and fluxes are given in Subsection 3.C). A R-based global optimization method for the classical GR4 formulation can be found here[6] and was used for background value estimation in this work.

In this work, the state-space" version of GR4H was integrated to the DassFlow2D assimilation tool-chain. The weakly-coupled hydrological module was used to model semi-distributed catchments linked to a 2D full SWE hydraulic model. Calibration of hydrological parameters using WS elevation and discharge observations were carried out using the gradient-based descent algorithm from the DassFlow framework to reach a local optimum.

1.4 Inverse problems and data assimilation

Given the rising availability, accuracy and resolution of river network monitoring products, the development of hydraulic-hydrological models should strive to account for their exploitation. The synergy between models and data can be achieved through data assimilation methods that enable to solve inverse problems, i.e. methods that use observations of reality to correct model states and parameters so that they better fit that reality. This section first introduces inverse problems in hydraulic models, the solving of which is a step toward synergy between hydraulic models (presented in Section 1.2) and river network observability (presented in Subsection 1.1.4). Then, data assimilation methods are described. They are linked to a unifying Bayesian approach, given Gaussian priors and linear models. Finally, the iterative variational data assimilation algorithm used in the following chapters is described summarily (more details can be found in the following chapters).

1.4.1 Direct and inverse problems

1.4.1.1 Definitions

Determining the cause of a phenomenon occurring in a physical system through its observation is a key question in various scientific domains. Solving a direct problem means using a cause to determine an effect, while solving an inverse problem means observing the effect to determine its cause (see Tarantola [2005] for theory of inverse problems).

Modeling a physical system generally consists in determining state variables that verify a physical model given parameters and boundary conditions. In the context of hydrodynamic modeling, the cause is a set of unknown/estimated parameters in the form of spatial fields and temporal forcings and the effect is composed of heterogeneous water surface observables. This problem and model are naturally the direct problem, as the hydraulic models describing the

---

[6] https://webgr.inrae.fr/logiciels/airgr/

variability of flow mass and momentum in terms of state variables (A, Q) in 1D (Eq. 1.2) or (h, u, v) in 2D (Eq. 1.6). Nevertheless, in practice, boundary conditions, initial conditions and parameters can be uncertain or unknown, because of imperfect modeling and observability of the physical system of interest (see river network observability in Section 1.1.4). For example, for river models, bathymetry-friction or lateral exchanges of mass and momentum in SW models (see Section 1.2) can be poorly-known, which can lead to insufficient accuracy on the simulated state variables. The inverse problem consists in finding unknown or uncertain model parameters that enable to fit observations of physical system response (e.g. Tarantola [2005]). Consequently, the observed quantities have to be calculable from model variables.

One of the main difficulties encountered in inverse problems resolution is ill-posedness. As defined by the mathematician J. S. Hadamard, a mathematical modeling problem of a physical phenomenon is a well-posed problem if the solution exists, is unique and depends continuously on model boundary and initial conditions, and parameters.

1.4.1.2 Inverse problems

This work aims to infer uncertain or unknown parameters of hydraulic and hydrological models using multi-source river flow observations provided by various in situ or satellite measurements. In particular, this work focuses on the optimization of control vectors of coupled hydraulic-hydrological models. The considered datasets are heterogeneous in nature with observations among WS deformations (WS elevation, width, slope), flow velocity (at the free surface or not), flow depth or discharge estimates. The unknown or uncertain parameters of the direct hydraulic models (Eq. 1.2 or Eq. 1.6) weakly coupled to a hydrological model (Eq. 1.9) are among bathymetry, friction and lateral exchanges, including inflows from hydrological models. The unknown or uncertain parameters of the conceptual hydrological model (Eq. 1.9) considered in this work are among reservoir and sub-catchment exchange parameters. An underlying hypothesis of hydrological parameter inference in this work is that the conceptual representation of hydrological catchment introduced in GR4 (i.e. reservoir number and connections) is pertinent for the considered catchments and thus these parameters are not inferred. The correction of model forcings and reservoir states also represent interesting problems.

In hydraulic models, the inference of at least two type of unknowns among river bathymetry-friction-inflow discharge from WS signature observations is an ill-posed problem (see Garambois and Monnier [2015]; Larnier et al. [2021]). Indeed, these flow controls have a correlated influence on water surface deformations. For example, as remarked in Garambois and Monnier [2015], an infinity of bathymetry-friction couples can lead to the same local WS elevation.

A supplementary difficulty arises from the spatio-temporal heterogeneity of data and the relatively sparse sampling they provide of the physical processes of interest. For example, inferrable flood frequency patterns, using sparse altimetric sampling of a relatively short river reach by a single satellite (SWOT like data), are studied at the river reach scale in Brisset et al. [2018]. Regarding the spatialization of controls, a higher spatial density of controls than of observation leads to under-determined inverse problems, as discussed for bathymetry and friction inference of 1D hydraulic models from satellite data in Garambois and Monnier [2015]; Garambois et al. [2020]; Larnier et al. [2021]. See also bathymetry inferences in Lai and Monnier [2009] or friction inferences on a 2D hydraulic model from in situ and Synthetic Aperture Radar (SAR) data in Hostache et al. [2010]. Those studies suggest the combination of sparse satellite data with a priori physical knowledge and in situ data to better constrain the inferences.

Given the increasing amount of multi-source observations of river surface deformations, in combination with ancillary data and physical knowledge, arises the question of information feedback in integrated hydraulic-hydrological models, from local observation scale to upstream hydrological modules. Can we "do backward hydrology" (Kirchner [2006])? With which type and spatio-temporal density of model controls and data? More precisely, the inverse calibration problem of a distributed hydrological model, from multi-source observations in the river network, will be studied in this work.

Adapting the complexity of direct models and inverse methods, to both modeling goals, features and available observations, is necessary in view to progress in the integration of multi-source information and is studied in this PhD.

1.4.2 Data assimilation

Data assimilation is a mathematical discipline that aims to optimally combine a model with observations of a physical system in order to exploit the physical informative content of data (see e.g. Bouttier and Courtier [2002]; Carrassi et al. [2018]; Monnier [2021]). It has been used for decades in meteorology or oceanography (see e.g. Ghil and Malanotte-Rizzoli [1991]) or more recently in hydrology (see e.g. Park and Xu [2013]; Seo et al. [2009]).

The prediction of a flow model is generally fitted to observations by adjusting a parameter. In meteorology, this sought parameter is usually the initial condition of numerical models, which represents an important challenge for weather forecasting given the chaotic nature and relatively short relaxation scales of atmospheric flows (Carrassi et al. [2022]). In this work, the parameter, called control, and denoted c, is composed of boundary conditions and flow models parameters (see e.g. Larnier et al. [2021] and references therein). Such composite controls, composed of different types of unknowns, lead to multivariate data assimilation problems. Moreover, the controls of non-linear hydrodynamic models considered in this work are distributed in space and time and are of a relatively high dimension.

Schematically, data assimilation has been developing around two families of methods: the variational approach that stems from the optimal control theory (see e.g. the work of J. L. Lions on the optimal control of PDE) and the statistical estimation with sequential methods. In sequential methods, model states are corrected recursively at discrete observation times, only using previous system state and observations (Carrassi et al. [2018]). Sequential methods notably include Kalman filters (Swerling [1959]; Kalman [1960]) and smoothers (Carrassi et al. [2018]). In the former, model states are corrected at observation times only. In the latter, model states are constrained/smoothed at unobserved times. In variational methods, all observations are accounted for simultaneously and guide the model trajectory. The Bayesian framework offers a unifying framework for the two approaches.

In this work, the variational approach is used. It is an adapted approach to deal with non-linear dynamic models and with heterogeneous observations in space and time, but also to deal with multivariate data assimilation problems and large control vectors. It is an efficient approach that is well suited to solve the inverse problems of interest (defined above in Section 1.4.1), as experienced for hydraulic inferences in satellite observability context (e.g. Brisset et al. [2018];

Larnier et al. [2021]) or for spatially distributed hydrological calibration problem (Castaings et al. [2009]; Jay-Allemand et al. [2020]). Moreover, note that global optimization algorithms are not adapted for the present inverse problems and local descent algorithms will be used in the variational approach.

1.4.2.1 Problem statement

The mathematical framework used in data assimilation is briefly recalled here (see DA course, e.g. Carrassi et al. [2018]; Bouttier and Courtier [2002]; Monnier [2021]; Asch et al. [2016]). Let $\mathcal{U}$ be the space of the input variables (controls) of flow models (Eq. 1.2) or (1.6) or (1.6 weakly coupled to 1.9). Considering $c \in \mathcal{U}$, a finite dimension real-valued control vector, Let c^b denote the background control vector, called "prior" in statistics, and c^a the analysis that is expected to best approximate, in a sense to be defined, the true control value c^t. Note that because of uncertainties on the components of c, the prior is the best available guess and writes:

$$c^b = c + \epsilon^b \tag{1.10}$$

Let us assume that model state variables are observed in a set $Y = H(c) \in \mathcal{Y}$ with $\mathcal{Y}$ the observation space and $H : \mathcal{X} \mapsto \mathcal{Y}$ the observation operator from state space $\mathcal{X}$ to observation space $\mathcal{Y}$. The actual observation is $Y^o = Y + \epsilon^o$ with ϵ^o the observation uncertainty arising for example from measurement noise.

In the Bayesian framework, the posterior probability density of c conditioned on observations Y^o can be written with the Bayes formula:

$$p\left(c|Y^o\right) = \frac{p\left(Y^o|c\right)p\left(c\right)}{p\left(Y^o\right)} \tag{1.11}$$

Searching for the mode of the posterior density $p\left(c|Y^o\right)$, that is maximizing $p\left(c|Y^o\right)$, is the essence of data assimilation (see Gejadze and Malaterre [2017]). Assuming Gaussian prior and observations uncertainties, that is $\epsilon^o \sim N\left(0, O\right)$ and $\epsilon^b \sim N\left(0, B\right)$ with B and O respectively the background and observation covariances, maximizing $p\left(c|Y^o\right)$ is equivalent to minimizing the cost function:

$$j\left(c\right) = \frac{1}{2}\left\|O^{-1}\left(H\left(c\right) - Y^o\right)\right\|^2 + \frac{1}{2}\left\|B^{-1}\left(Y - Y^b\right)\right\|^2 \tag{1.12}$$

This is a classical definition of the cost function $j\left(c\right) = j_{obs} + j_{reg}$. The first term j_{obs} is the observation term measuring the misfit between model prediction and observations. The second term is a Tikhonov regularization term (Tikhonov and Arsenine [1977]; Kaltenbacher et al. [2008]). The latter helps to add a priori constraint on the sought solution and "convexifying" the original ill-posed problem with observation term only. As matter of fact, background covariance is generally not known.

1.4.2.2 The optimization algorithm

The variational data assimilation problem consists in the following optimization problem (Bouttier and Courtier [2002]; Larnier et al. [2021]; Monnier et al. [2016], see 1.16):

$$c^a = \operatorname{argmin} j\left(c\right) \tag{1.13}$$

The first order optimality condition of this optimization problem reads: $\nabla j\left(c\right)=0$. The optimization problem (Eq. 1.13) is numerically solved with a Quasi-Newton descent algorithm: here the classical L-BFGS algorithm or its bounded version L-BFGS-B (see Zhu et al. [1997]). The iterative process requires, at each iteration, the gradient of the cost function with regards to control vector components.

The gradient of the cost function is computed with the adjoint state method enabling to consider large control vectors (see e.g. Larnier et al. [2021]; Oubanas et al. [2018a]; Brisset et al. [2018]). The adjoint code is obtained by applying the automatic differentiation tool Tapenade to the forward numerical codes: DassFlow1D (Larnier et al. [2021]; Brisset et al. [2018]) or DassFlow2D (Monnier et al. [2016]) in the following. The automatic differentiation tool Tapenade (Hascoet and Pascual [2013]), based on the derivation rule of composite functions, provides the tangent and adjoint codes of a forward code. Given a function $F: X \in \mathbb{R}^n \mapsto Y \in \mathbb{R}^n$ evaluated over $[0, T]$ in the form of a computer program P, Tapenade provides an adjoint code P' by computing the analytical derivative of each elementary mathematical operation of P. This adjoint code evaluates $\bar{X}=\bar{Y}\times F'\left(X\right)$ over $[T, 0]$ (Hascoet and Pascual [2013]). Detailed know-hows and historical references can be found for example in courses (Carrassi et al. [2018]; Bouttier and Courtier [2002]; Monnier [2021]).

Trajectory change during the iterative process can be represented within the parameter space, that is a N-dimension space (with N the number of components of the control c) within which the misfit to observations (or cost) is evaluated. In the present VDA method, a single local minimum is sought, using a gradient-based descent algorithm, background parameters and initial conditions.

Mono-objective DA refers to approaches that use a single kind of observable in their cost function (e.g. WS elevation), while multi-criteria cost functions and multi-objective methods use multiple (e.g. WS elevation and at-a-section discharge). See Efstratiadis and Koutsoyiannis [2010] for a review of multi-objective problems in hydrology. Mono-variate DA refers to methods inferring a single parameter type (potentially discretized in space and time), while multi-variate methods aim to simultaneously infer composite control vectors (e.g. the upstream inflow and bathymetry-friction couple in Garambois et al. [2020]).

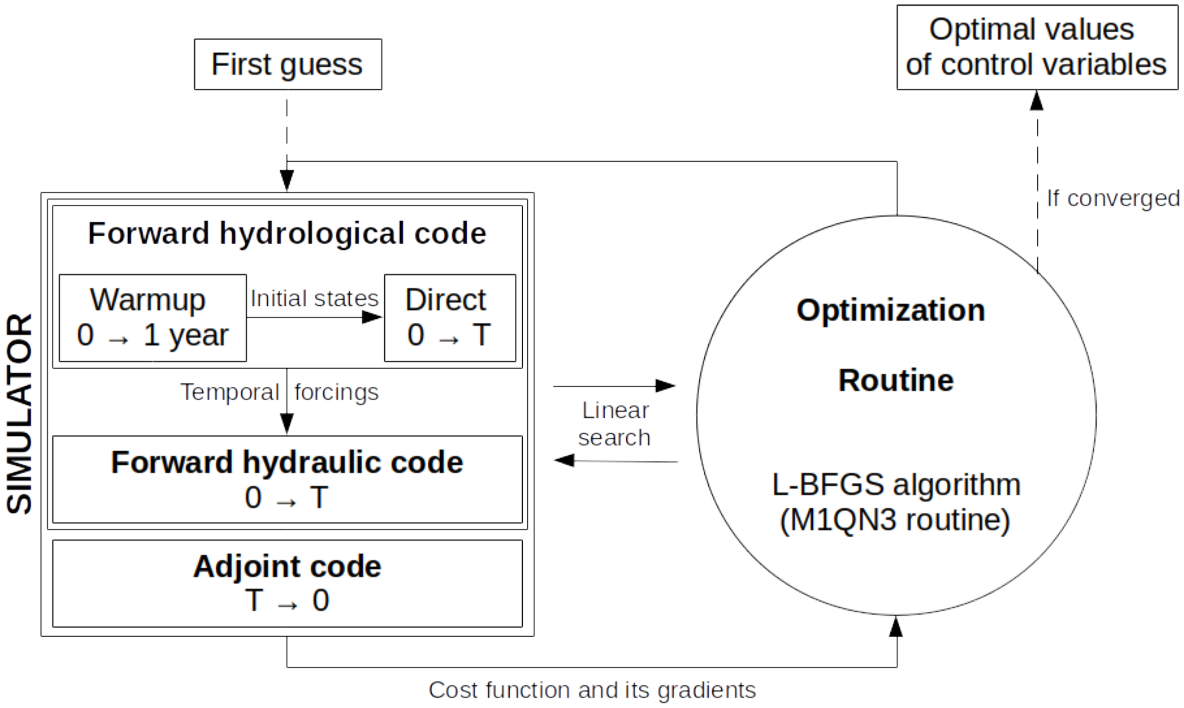

Figure 1.16: Complete VDA hydraulic-hydrological tool-chain

1.5 Python Wrapping of DassFlow

Python has become the most used computer language in 2021, overtaking C and Java, according to the Tiobe index[7]. Python packages and libraries are freely available and cover uses such as data representation, scientific computing, global optimization, statistical analysis, Geographic Information System (GIS) tools and Machine Learning (ML) libraries. Python is easy to use and is an interpreted language that does not need to be compiled. The DassFlow computational platform is written in Fortran, a low-level compiled language. Fortran is capable of efficient matrix computations and high performance computing, but does not have access to numerous libraries like those for Python and is, in general, less practical to use.

The “wrapping” of a code consists in creating an interface between two programming languages. Python has emerged as a key language to interface older codes to, thanks to its ease of use and numerous libraries and toolboxes. The Python wrapping of DassFlow consists of the interfacing of its Fortran efficient computational core to Python. This allows preserving the core code and handling the pre- and post-processing, as well as some of the other less computationally costly parts of the code.

The wrapping of the DassFlow Fortran code (see Huynh [2020]; Ma [2021]) has seen the interfacing of most variables and parameters structures, the launch of both direct and inverse models through a Python script, and the adding of a Python-based minimizer instead of the previous Fortran one. Note that the gradient calculation is a computationally costly step, while the minimization of the cost function, given the gradient, is not.

---

[7] https://www.tiobe.com/tiobe-index/

The wrapping tool is f90wrap, a Python-Fortran interface generator developed by James Kermode Kermode [2020] and that builds on the f2py Python package. The code is open-source and available at https://github.com/jameskermode/f90wrap. The tool generates modules (.mod files) and .py and .f90 interfacing files. These files are then used to generate a importable Python module with f2py. It allows to read and write chosen Fortran variables and routines from .py files. Multi-thread parallel computation is handled as well. More details on the wrapping methodology and development process are available in Huynh [2020]; Ma [2021], technical details can be found in Monnier et al. [2022].

1.6 Context summary and thesis objectives

Strong societal issues drive the need for the cartographic representation of hydrological cycle phenomenons. The corresponding scientific challenges are the improvement of state and fluxes representation in hydrographic network models and the synergy of these models with new data sources and data types. Depending on modeling objectives (e.g. river discharge, water depth or flood extent) and data availability, multiple model scales with different degrees of complexity have been developed. 1D approaches are generally used to model near mono-dimensional hydraulic phenomenons at local, regional and global scales. 2D models are used to model bi-dimensional phenomenons at local scale but, due to their higher computational cost, are generally used with simplified hydraulic equations and rough spatial resolution at regional or global scales. However, the use of full SW models and adapted numerical schemes is needed for accurate modeling of wet/dry front propagation at the local scale. Over a river network, both 1D and 2D approaches can have their advantages. Coupled 1D-2D modeling approaches theoretically allow to use the best of both approaches (e.g. by limiting costly 2D computation to pertinent regions), but add a layer of difficulty regarding their coupling/interfacing. Hydraulic network models are generally inflowed by hydrological models to feature complete basin-scale state-fluxes numerical representations. At such scale the accurate estimation of both hydraulic and hydrological parameters remains an important difficulty.

Observations of hydrological phenomenons are given by a growing array of sensors, with increasing accuracy and spatial and temporal resolution. This leads to an increasing number of multi-scale, multi-sourced heterogeneous data products that contain an often under-exploited wealth of information, especially for ungauged river network portions. Single data products are usually integrated in models through data assimilation methods, classically with sequential DA methods. Variational methods are less common, especially because of the difficulties related to the obtention of an adjoint model. Yet, they are very pertinent for the inference of large multi-variate control vectors of hydrodynamic models. Inferences, in SW models, of channel parameters (the bathymetry-friction couple), initial and boundary conditions and temporal forcings (inflows) using multi-sourced altimetric measurements of the WS and other flow measurements have been carried out in recent works using data assimilation methods. The resolution of these ill-posed problems is a current scientific issue in hydraulic modeling at the reach and catchment scale. In hydraulic-hydrological models, the inference of hydrological parameters and states from upstream feedback of hydraulic signatures is also a current scientific issue. Given the growing observation data resolutions and the consequent potential to infer spatially dense parameters, this work uses variational data assimilation in the context of remotely-sensed and multi-sourced observations. It builds on a powerful VDA framework from the DassFlow platform and investigates complex inverse problems with hydrodynamic models from multi-source flow observations.

This work focuses on the following scientific problems: i) the effective representation of river networks through multi-D basin-scale hydraulic-hydrological models, ii) the integration of multi-source multi-scale heterogeneous observations in such models, iii) from this data, the inference of spatio-temporally distributed river channel parameters and inflows through a variational data assimilation method and iv) the upstream informational feedback of river network observations to integrated hydrological models. To answer these questions, the variational data assimilation platform DassFlow was expanded upon, notably by implementing spatio-temporally distributed temporal forcings and integrating a conceptual hydrological model to the variational tool-chain. A new method for 1D-2D modeling of catchment scale river networks was developed using a single finite volume solver. Numerous inferences of large composite control vectors using multi-sourced heterogeneous data were carried out on 1D and 1D-2D models coupled with hydrology with the VDA method.

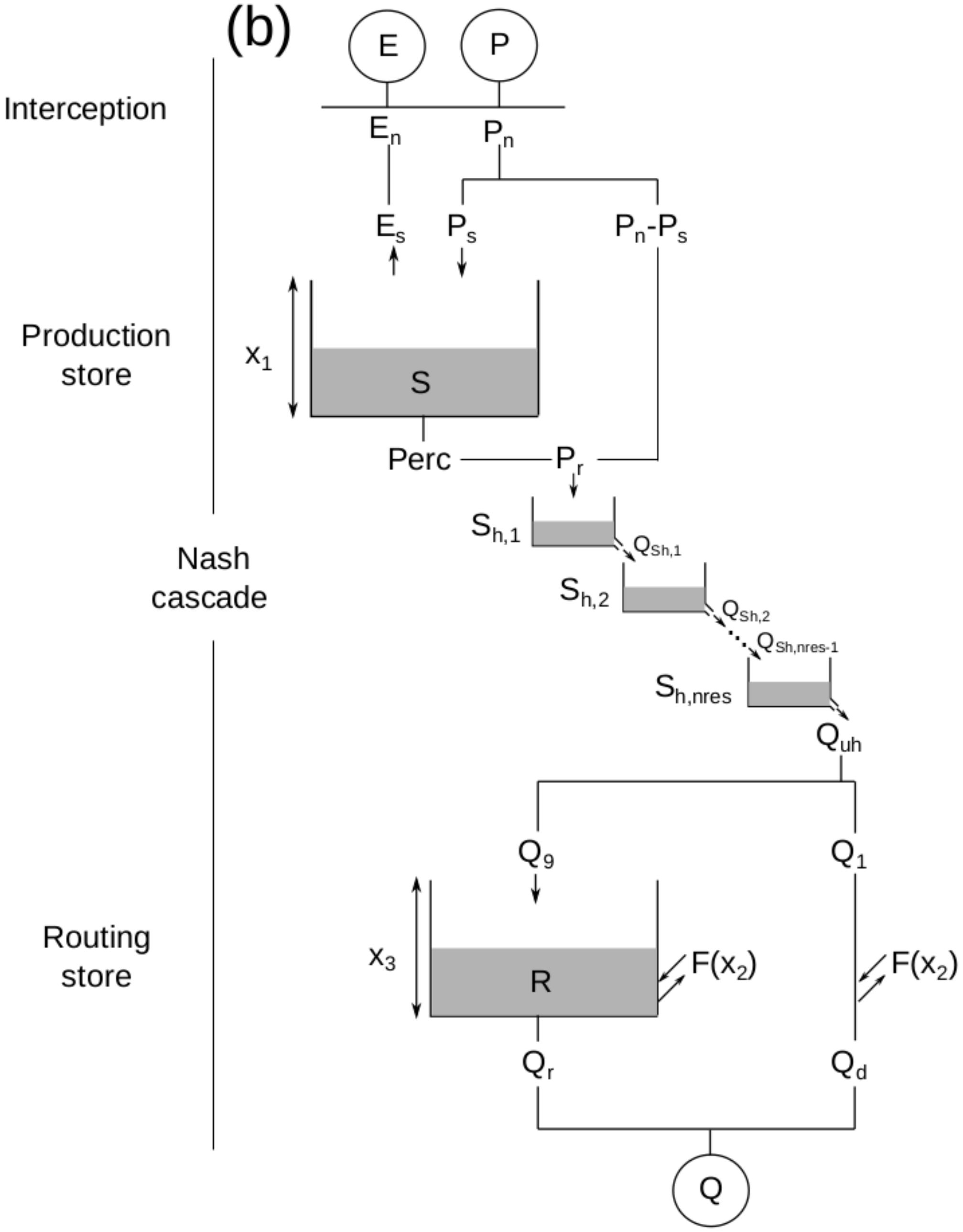

Figure 1.15: GR4 state-space conceptual model (Santos et al. [2018])

Chapter 2

Large scale 1D network hydraulic-hydrological modeling

Contents

This chapter is based on Pujol et al. [2020]. The article's content is featured with minor layout and notation adjustments.

2.1 Extended abstract

With the upcoming SWOT satellite mission, which should provide spatially dense river surface elevation, width and slope observations globally, comes the opportunity to assimilate such data into hydrodynamic models, from the reach scale to the hydrographic network scale. Based on the HiVDI (Hierarchical Variational Discharge Inversion) modeling strategy (from Larnier et al. [2021]), this study tackles the forward and inverse (see runs in Subsection 1.4.1) modeling capabilities of distributed channel parameters and multiple inflows from multi-satellite observations of river surface. The considered model solves the full 1D (A, Q) SW equations with a lateral inflow source term (see Subsection 1.2.1). The lateral inflow source term was implemented in the DassFlow platform in a Preissmann scheme (see Appendix B) and a HLL scheme, for direct and inverse modeling.

It is shown on synthetic cases that the estimation of both lateral inflows $q_l(x,t)$ and the bathymetry-friction couple $(b(x), K(x))$ is achievable with a minimum spatial observability between inflows as long as their hydraulic signature is sampled. Next, a real case is studied: 871 km of the Negro river (Amazon basin) including complex multichannel reaches, 21 tributaries and backwater controls from major confluences. An effective modeling approach is proposed using (i) WS elevations from Envisat data and dense in situ GPS flow lines (Moreira [2016]), (ii) average river top widths from optical imagery (Pekel et al. [2016]), (iii) upstream and lateral flows from the MGB large-scale hydrological model (Paiva et al. [2013a]). The calibrated effective hydraulic model closely fits satellite altimetry observations and presents real like spatial variabilities; flood wave propagation and water surface observation frequential features are analyzed with identifiability maps following Brisset et al. [2018] (see Fig.2.1). Synthetic SWOT observations are generated from the simulated flow lines and allow to infer model parameters (436 effective bathymetry points, 17 friction patches and 22 upstream and lateral hydrographs) given hydraulically coherent prior parameter values. The unprecedented spatial coverage provided by the SWOT wide-swath altimeter enables to infer relatively densely discretized parameters at a cartographic scale. Inferences of channel parameters carried out on this fine hydraulic model applied at a large scale give satisfying results using noisy SWOT-like data at reach scale (see Fig.2.2). Inferences of spatially distributed temporal parameters (lateral inflows) give satisfying results as well, with even relatively small scale hydrograph variations being inferred accurately on this long reach. This study brings insights in: (i) the hydraulic visibility of multiple inflows hydrographs signature at large scale with SWOT; (ii) the simultaneous identifiability of spatially distributed channel parameters and inflows by assimilation of satellite altimetry data; (iii) the need for prior information; (iv) the need to further tailor and scale network hydrodynamic models and assimilation methods to improve the fusion of multi-source information and potential information feedback to hydrological modules in integrated chains.

Section 2.3 presents the modeling approach with the 1D Saint-Venant flow model and the inverse computational method. Section 2.4 investigates the capabilities of the inverse method for identifying spatially distributed inflows with and without unknown channel parameters given observation patterns of WS signatures including overlapping backwater effects. Section 2.5 presents the effective modeling approach from multi-satellite data applied to 871 km of the Negro river (Amazon basin) and the analysis of flow propagation features against SWOT observability. Section 2.6 proposes inference tests for spatially distributed inflows with and without unknown parameters on the Negro case in the presence of strong backwater effects. The original article conclusion is featured in Section 2.7.

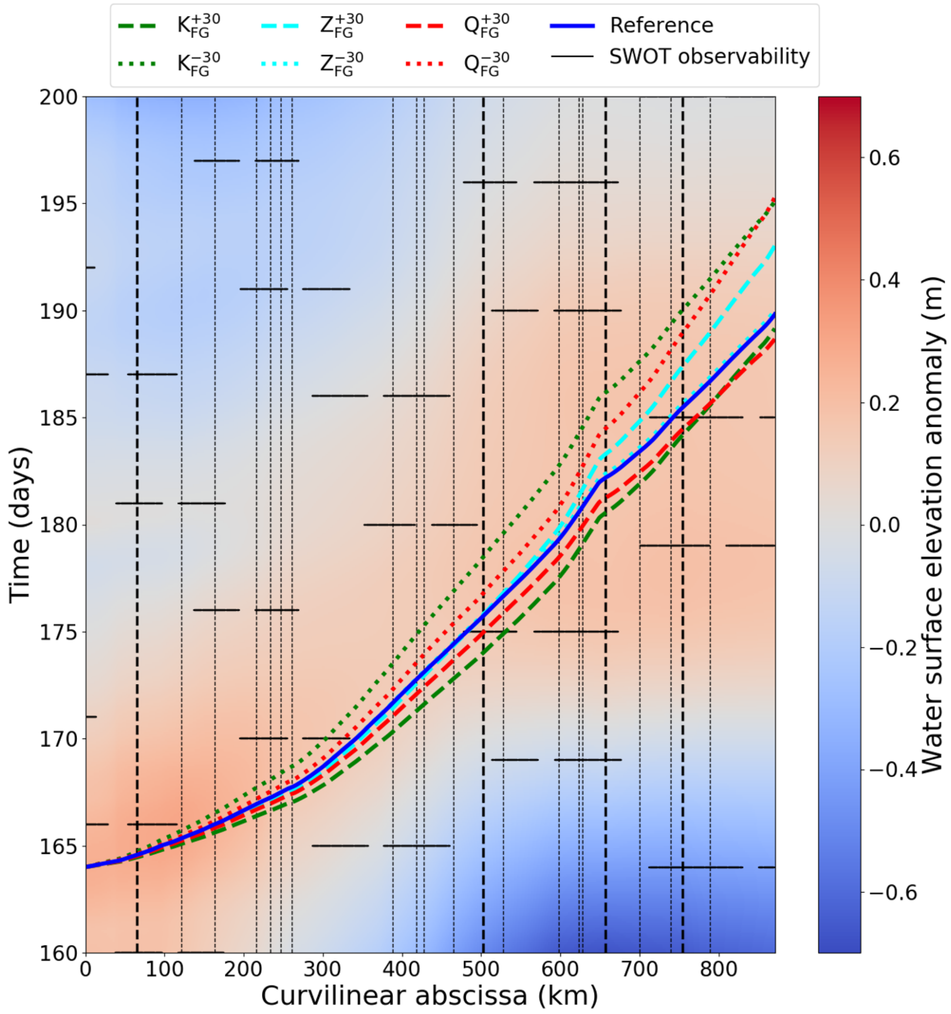

Figure 2.1: Identifiability map of a flood wave on a 871 km reach of the Negro river in a large scale 1D model.

The red-blue heatmap gives the WS elevation anomaly with regards to the average local WS elevation $Z_{ano}(x,t) = Z(x,t) - \overline{Z(x)}$, where $\overline{Z(x)}$ is the average local WS elevation over the seasonal flood peak (may-june).

The blue line represents the travel of an intumescence traveling through the reach at the modeled kinematic speed ($5/3u$) and starting at the upstream BC at the time of the flood peak at this point, in a base model calibrated with satellite altimetry. Dotted colored lines show the sensitivity of this travel time estimation to model parameters and forcings: variations of $+30\%$ and -30% from the base model are represented for the Manning friction parameter K (in green), the bathymetry b (in cyan) and all model inflows (in red).

The vertical bars indicated lateral inflows $q_l(x,t)$ for a total of 21 lateral mass and momentum contributions (bold lines are denote the major tributaries). Horizontal bars represent observability given by the SWOT large swath altimeter.

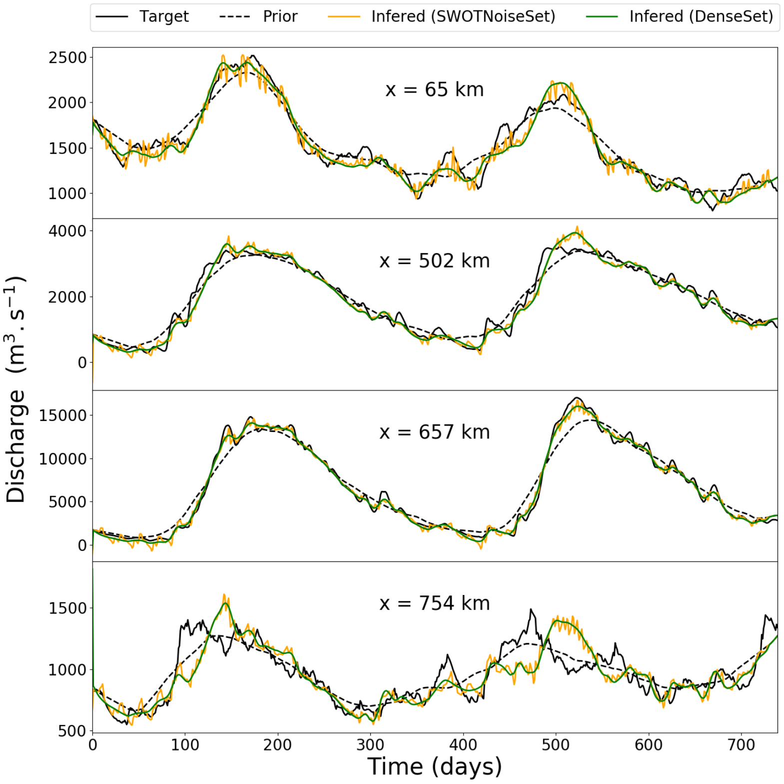

(a)

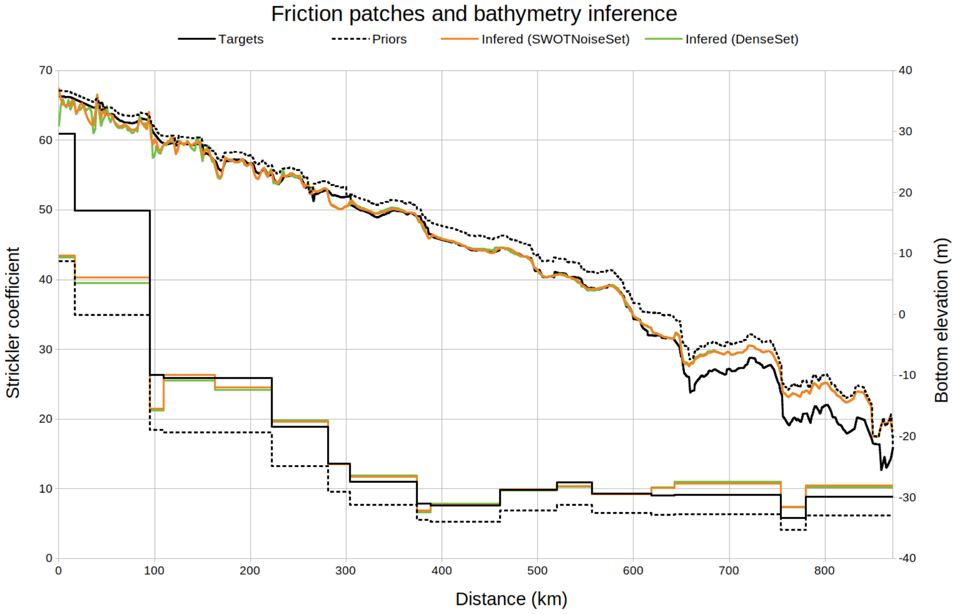

(b)

Figure 2.2: Simultaneous inferences of lateral inflows $q_l(x,t)$, bathymetry $b(x)$ and friction patches $K(x)$ in a twin experiment setup on the Negro river 1D model. The control vector is composed of bathymetry points, friction patches and select lateral inflow hydrographs and writes $c_{ext} = (Q_{l,1}(t), Q_{l,2}(t), Q_{l,3}(t), Q_{l,4}(t), b(x), K(x))$. Considered observations are noisy SWOT observations from the SWOT simulator (inferences in orange) and spatially and temporally dense observations (inferences in green).

2.2 Introduction

Hydrographic networks represent major flow paths for freshwater in the water cycle and an interface with the space of human societies. It is of prior importance in a context of climate change to improve the knowledge and representation of continental water fluxes, including river discharge, defined as an essential physical variable (see Global Climate Observing System Organization, 2011]). However, modeling flows structure in the different compartments of a catchment remains a hard task (see Schuite et al. [2019] and references therein) especially at poorly gauged locations. In complement of in situ sensors networks, which are declining in several regions (e.g. Fekete and Vorosmarty [2002]), new generations of earth observation satellites and sensors provide increasingly accurate and dense measurements of water surface variabilities.

The Surface Water and Ocean Topography (SWOT) satellite, to be launched in 2021, will bring observations of water surface (WS) with an unprecedented spatio-temporal coverage Alsdorf et al. [2007]; Durand et al. [2010]; Rodríguez [2012]; Biancamaria et al. [2016]; Rodríguez et al. [2018]. This will yield greater hydraulic visibility (see definition in Garambois et al. [2017]; Montazem et al. [2019]; Rodríguez et al. [2020]) of hydrological responses through WS signatures from the local scale to the hydrographic network scale, hence an opportunity to better characterize hydrological fluxes and potentially constrain local to integrated hydrodynamic models and inverse problems. However, estimating river discharge Q from "geometric" observables of flow surface (elevation Z, width W and slope S) remains a difficult inverse problem particularly in case of poor knowledge on river bathymetry and friction (see Garambois and Monnier [2015]; Larnier et al. [2021] and references therein).

Hydraulic inverse problems with various model complexities, data-unknowns types and amounts are investigated by recent studies in a satellite data context (see Biancamaria et al. [2016] for a review). A few studies started to test the benefit of assimilating (synthetic) SWOT WS observations with sequential methods in simplified hydraulic models, for estimating inflow discharge assuming known river friction and bathymetry Andreadis et al.; BIA [2011] or inferring bathymetry assuming known friction Durand et al. [2008]; Yoon et al. [2012]. Next, methods based on low-complexity models have been proposed for estimating river discharge from WS observables in case of unknown bathymetry b and friction K, based on the low Froude model Durand et al. [2014]; Garambois and Monnier [2015], hydraulic geometries Gleason and Smith [2014] or empirical algebraic flow models Bjerklie et al. [2018]. The inter-comparison of low complexity methods in Durand et al. [2016] highlights the difficulty of estimating the so-called unknown triplet (Q, K, b) from WS observables as well as the importance of good prior guesses on the sought parameters.

The combined use of dynamic flow models of river systems and optimization methods enables to solve hydraulic inverse problems, as shown for upstream flood hydrograph(s) estimation by Roux and Dartus [2006] from WS width time series and a 1D Saint-Venant model or by Honnorat et al.; Hostache et al. [2010]; Lai and Monnier [2009] using variational assimilation of flow depth time series in a 2D shallow-water model. The variational data assimilation (VDA) approach (see e.g. Cacuci et al. [2013] and references therein) is suitable to address the present hydraulic inverse problem from WS observations (see Gejadze and Malaterre [2017]; Brisset et al. [2018]; Oubanas et al. [2018b]; Garambois et al. [2020]; Larnier et al. [2021] and references therein - single upstream hydrographs in all studies except multiple "step-wise" off-takes on synthetic and densely observed irrigation-like cases in Gejadze and Malaterre [2017]). It consists in fitting the modeled flow features to observations through the optimization of control parameters in a variational framework. To be solved efficiently, such an ill-posed inverse problem needs to be regularized: see Kaltenbacher et al. [2008] for the theory of regularization of such inverse problems and Gejadze and Malaterre [2017]; Larnier et al. [2021] for the present inverse flow problem.

Crucial aspects of this difficult inverse problem are (i) the spatio-temporal sparsity of altimetric observations regarding flow controls – as analyzed in Brisset et al. [2018] for inferrable hydrographs frequencies with the introduction of the *identifiability maps* and in Garambois et al. [2020] for inferrable channel parameters patterns; (ii) the sensitivity of the triplet inference to good prior guesses on the sought parameters as highlighted in a SWOT context by Garambois and Monnier [2015]; Yoon et al. [2016]; Tuozzolo et al. [2019]; Garambois et al. [2020]; Larnier et al. [2021]. The latest is highlighted by recent discharge estimates (in a triplet setup) from synthetic SWOT data on the Pô, Garonne and Sacramento Rivers in Larnier et al. [2021] (see also Oubanas et al. [2018a]), from AirSWOT airborne measurements on the Willamette River in Tuozzolo et al. [2019] or from Envisat altimetric data on an anabranching portion of the Xingu River Garambois et al. [2020]. Using a biased prior hydrograph results in a biased estimate of inflow hydrograph despite a correct temporal variability at observation times - see Larnier et al. [2021] for detailed analysis. A hierarchical modeling strategy HiVDI (Hierarchical Variational Discharge Inversion) is proposed in Larnier et al. [2021] including low complexity flow relations (Low Froude and locally steady-state) for providing robust prior guesses to the VDA process by taking advantage of databases or regional hydrological models.

Most studies mentioned above tackle the estimation of a single upstream inflow discharge hydrograph from WS observations on relatively short river reaches regarding the spatio-temporal sparsity of (satellite) observations sampling and without complex flow zones - confluences, multichannel portions (except Garambois et al. [2020]), floodplains. Moreover, few recent studies address the effective modeling of (ungauged) river channels using multi-satellite data Garambois et al. [2017]; Schneider et al. [2017]; Garambois et al. [2020]; O'Loughlin et al. [2019].

The present study investigates the challenging inference of multiple inflows and channel parameters patterns from hydraulic signatures in a SWOT context. Particular attention is paid to the difficult inference of HC with correlated effects on WS signatures including overlapping backwater effects. Moreover, we present an effective hydraulic modeling approach based on multi-satellite observations of WS and accounting for hydrological model inputs. It is applied to a long river reach including confluences with tributaries and strong backwater effects in the Amazon basin. The computational inverse method, based on the full 1D Saint-Venant equations, is that presented in Brisset et al. [2018]; Larnier et al. [2021] with a spatially distributed friction power law in water depth and a simple piece-wise linear channel bathymetry Garambois et al. [2020]. It is adapted here to account for lateral inflows/off-takes and is weakly coupled to the large scale MGB hydrological model Collischonn et al. [2007]; Pontes et al. [2017]; Paiva et al. [2013a]. Numerical investigations of the resulting WS signatures and identifiability tests are presented along with sensitivity analysis to the parameters of both the (forward) hydraulic model and the inverse method. The challenging inference of multiple inflows and channel parameters patterns is investigated with various observations densities including the assimilation of synthetic SWOT ones.

2.3 Modeling Approach

2.3.1 The flow model

The Saint-Venant equations (Barré de Saint-Venant [1871]) consist in the unidirectional form of the shallow water equations and are commonly used to describe open channel flows (see e.g. Chow [1964]; Ancey [2018]; Guinot [2010] for detailed assumptions including the long wave one). In what follows, x denotes the curvilinear abscissa from upstream to downstream along a reach of length $\mathcal{L}$ (usual simplifying hypothesis are used) and $t \in [0, T]$ denotes the time. In this representation, let $A(x,t)$ $\left[\mathrm{m}^2\right]$ be the flow cross-sectional area and $Q(x,t)$ $\left[\mathrm{m}^3.\mathrm{s}^{-1}\right]$ the discharge such that $U = Q/A$ $\left[\mathrm{m.s}^{-1}\right]$ represents the longitudinal XS-averaged velocity . The Saint-Venant equations in (A, Q) variables at a flow XS read as follows:

$$\begin{cases} \frac{\partial A}{\partial t} + \frac{\partial Q}{\partial x} & = k_l q_l \\ \frac{\partial Q}{\partial t} + \frac{\partial}{\partial x}\left(\frac{Q^2}{A}\right) + gA\,\frac{\partial Z}{\partial x} & = -gAS_f + k_l U q_l \end{cases} \tag{2.1}$$

where $Z(x,t)$ $[\mathrm{m}]$ is the WS elevation and $Z = (b+h)$ $[\mathrm{m}]$ with $b(x)$ $[\mathrm{m}]$ the river bed level and $h(x,t)$ $[\mathrm{m}]$ the water depth, $R_h(x,t) = {}^{A}/_{P_h}$ $[\mathrm{m}]$ the hydraulic radius , $P_h(x,t)$ $[\mathrm{m}]$ the wetted perimeter, g is the gravity magnitude $\left[\mathrm{m.s}^{-2}\right]$, $q_l(x,t)$ is the lineic lateral discharge $\left[\mathrm{m}^2.\mathrm{s}^{-1}\right]$, and k_l is a lateral discharge coefficient chosen equal to one here since we consider inflows only. In DassFlow, the friction term S_f is classically parameterized with the empirical Manning-Strickler law established for uniform flows:

$$S_f = \frac{|Q|Q}{K^2 S^2 R_h^{4/3}} \tag{2.2}$$

The Strickler friction coefficient K $\left[\mathrm{m}^{1/3}.\mathrm{s}^{-1}\right]$ is defined as a power law in h:

$$K(x, h(x,t)) = \alpha(x)\ h(x,t)^{\beta(x)} \tag{2.3}$$

where α and β are spatially distributed parameters. This spatially distributed friction law enables a variation of friction effects in function of the flow state (see effective modeling of multichannel flows in Garambois et al. [2020]).

Inflow hydrographs $Q_{in}(t)$ and $q_{l,d}(t)$ at $d \in [1..D]$ are classically imposed respectively upstream of the river domain and at known injection cells, that is in-between two computational XSs along the river channel. Let us recall the Froude number definition $\mathrm{Fr} = {}^{U}/_{c}$ comparing the average flow velocity U to pressure wave celerity $c = \sqrt{gA/W}$ where W is the flow top width $[m]$. Considering subcritical flows ($\mathrm{Fr} < 1$) in a satellite observability context (see Garambois and Monnier [2015]), a boundary condition is imposed at the downstream end of the model using the Manning-Strickler equation depending on the unknowns $(A, Q, K)_{out}$. The initial condition is set as the steady state backwater curve profile $Z_0(x) = Z\left(Q_{in}(t_0), q_{l,1..D}(t_0)\right)$ for hot-start. This 1D Saint-Venant model (Eq. (2.1)) is discretized using the classical implicit Preissmann scheme (see e.g. Cunge et al. [1980]) on a regular grid of spacing Δx using a double sweep method enabling to deal with flow regimes changes, Δt is precised in numerical cases. This is implemented into the computational software DassFlow Couderc et al. [2013].

2.3.2 The computational inverse method

The paper studies the estimation of spatially and temporally distributed flow controls from WS observables using the inverse method presented in Larnier et al. [2021] (see also Brisset et al. [2018]) with an augmented composite control vector c; the method is detailed in 2.A. The principle of the inverse method is to estimate (discrete) flow controls by minimizing the discrepancy between observed and simulated flow lines, Z_{obs} and $Z\left(c\right)$ respectively, the latter depending on the unknown parameters vector c through the hydrodynamic model (Eq. (2.1)). This discrepancy is classically evaluated with the observation cost function term $j_{obs}(c) = \frac{1}{2}\left\|(Z\left(c\right) - Z_{obs})\right\|_{O}^{2}$ computed on the observation spatial and temporal grids, see details in 2.A.

The control vector c contains temporally and spatially distributed unknown "input parameters" of the 1D Saint-Venant model: a friction law (Garambois et al. [2020]) and lateral inflows, unlike in Larnier et al. [2021], where there is a spatially uniform friction law $K\left(h\right)$ without lateral flows. It reads:

$$c = \left(Q_{in}^{0}, ..., Q_{in}^{P}\,;\, Q_{l,1}^{0}, ..., Q_{l,1}^{P}, Q_{l,2}^{0}, ..., Q_{l,D}^{P}\,;\, b_1, ..., b_I\,;\, \alpha_1, ..., \alpha_N\,;\, \beta_1, ..., \beta_N\right)^{T} \tag{2.4}$$

where Q_{in}^{p} is the upstream discharge (the superscript $p \in [1..P]$ denotes the observation time), $Q_{l,d}^{p}$ is the lateral discharges injected in the inflow cell $d \in [1..D]$ (note that $Q_{l,d} = q_{l,d}\Delta x$), b_i the river bed elevation ($i \in [1..I]$ denotes the computational XS index in space) and, for each patch $n \in [1..N]$ with $N \leq I$, the spatially distributed parameters α_n and β_n of the friction law (Eq. (2.3)) depending on the flow depth.

The inversion consists in solving the following minimization problem: $c^{*} = \text{argmin}_{c}\ \text{j}(c)$ starting from the so-called prior c_{prior} in the parameter space. This minimization problem is solved using a first order gradient-based algorithm, more precisely the classical L-BFGS quasi-Newton algorithm (see 2.A). Note that the sought parameters have a correlated influence on the modeled flow lines, therefore leading to an ill-posed inverse problem. In order to be solved efficiently, the optimization problem is "regularized" as detailed in 2.A. The main steps of the method are illustrated in Fig. 2.3.

2.4 Inference capabilities from WS signatures: synthetic test cases

In order to calibrate the parameters of a hydraulic model (Eq. (2.1)) from WS observables, one has to identify and understand the influence of these parameters on the observable(s): in our case the WS profile. Fluvial flows are studied here in the context of satellite altimetry (see Garambois and Monnier [2015]). Following Montazem et al. [2017], the influence of the parameters on the modeled flow lines is referred to as their "hydraulic signature" (HC) and a reach is defined in-between two fluvial HCs. Fluvial HCs can be defined in steady state (see Montazem et al. [2017]) as *"local maximal deviations of the flow depth from the normal* depth h_n (equilibrium), *imposing the upstream variation of the water depth profile* $h\left(x\right)$ *over the so-called control length* Samuels [1989]". They can stem from a change in either the hydraulic resistance, XS shape, bottom slope or total flow variation through lateral exchanges.

This section studies the influence of inflows on hydraulic signatures, the capabilities of the

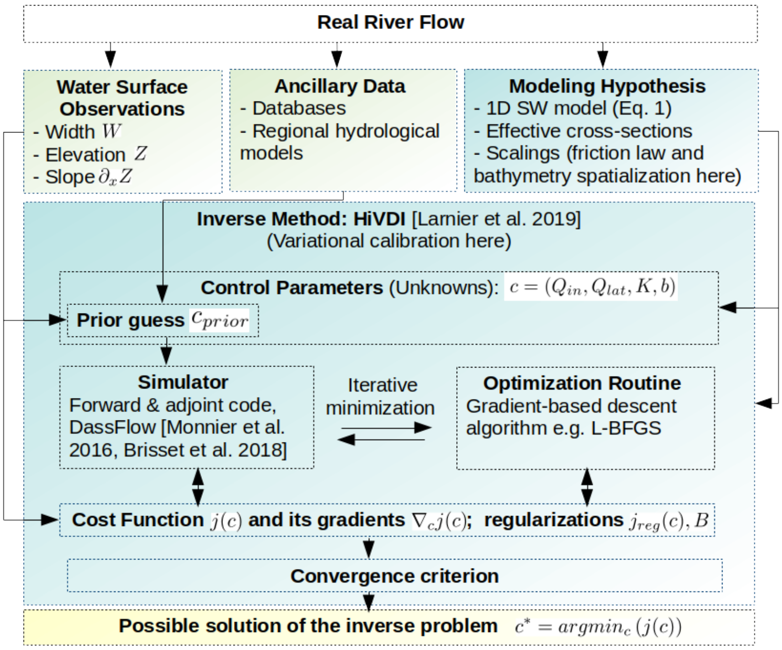

Figure 2.3: Flowchart of the method using the HiVDI inverse method Larnier et al. [2021] for variational calibration, adapted from Monnier et al. [2016]; Garambois et al. [2020]; Monnier [2021].

inverse method described above to infer multiple inflows and channel parameters (either spatially constant or not), with a focus on the influence of the spatial observability of those hydraulic signatures.

2.4.1 Test case design

Three test cases configurations representing typical hydraulic-observations setup of increasing complexities involving lateral inflows are presented (see Fig. 2.4). Cases $Ch1$ and $Ch2$ are designed to study the effect on the inference of the overlapping signatures triggered by the propagations of, respectively, one or two lateral hydrographs, concomitantly with the one of the upstream inflow hydrograph. Case $Ch3$ is a complexification of $Ch2$ through the introduction of a non-flat bottom and a variable friction pattern $K = \alpha(x)$ as needed in a real river case in the next sections ($\beta = 0$ in Eq. ((2.3)) - see investigations on spatialized friction laws with multi-scale bathymetry controls in Garambois et al. [2020]).

For all three channels the boundary conditions (fluvial) consist in: (i) a normal depth (equilibrium) imposed downstream and (ii) sinusoidal hydrographs (see Tab. 2.1) imposed upstream and at lateral injection cells. The simulation time step is set to $\Delta t = 20\,\mathrm{s}$ for all cases. They are set up as twin experiments, where a forward run of the flow model (Eq. (2.1)) is used to generate perfect WS elevation observations which are then used to infer an unknown parameter vector c (Eq. (2.4)) with the inverse method described in section 2.3.2 and 2.A. The inferences are started from erroneous prior guesses $c^{(0)}$ that verify Manning-Strickler law for hydraulic consis-

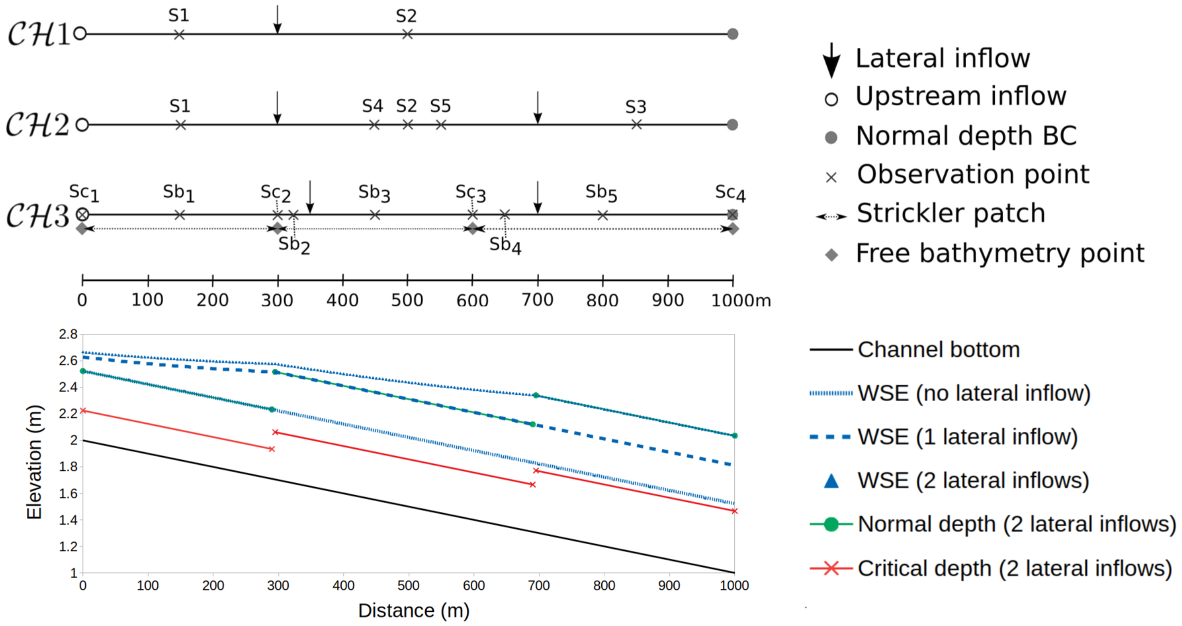

Figure 2.4: Spatial hydraulic signature of lateral inflows on an academic test case.
Top: Academic test cases configurations. Rectangular channels of length $\mathcal{L} = 1000\,\text{m}$ and constant XS width $W = 300\,\text{m}$, constant bottom slope of $10^{-3}\,\text{m/m}$ for $\mathcal{C}h1, 2$ and varying between 10^{-4} and $10^{-2}\,\text{m/m}$ for $\mathcal{C}h3$ - the bottom $b(x)$ is defined by linear interpolation between the 4 bathymetry points (diamonds, $b = \{2, 1.88, 1.28, 1.12\}$ m) - and friction defined by constant values on 3 patches ($\alpha = \{30, 12.5, 30\}\ \text{m}^{1/3}/\text{s}$). Upstream inflow at $x = 0$; for $\mathcal{C}h1, 2, 3$ respectively lateral injections at abscissae (in m): $x = 300$, $x = \{300, 700\}$, $x = \{350, 700\}$, and observations at $\{x_{S1}, ..., x_{S5}\} = \{150, 500, 850, 450, 550\}$, $\{x_{Sb1}, ..., x_{Sb5}\} = \{150, 325, 450, 600, 800\}$, $\{x_{Sc1}, ..., x_{Sc4}\} = \{0, 300, 600, 1000\}$.
Bottom: Sample waterlines with visible upstream and downstream controls and signatures. For the sake of clarity here, upstream and injected flow are set at $100\,\text{m}^3/\text{s}$ ($\text{Fr} \sim 0.12 - 0.3$). Using the identifiability index $I_{ident} = T_{wave}/\Delta t_{obs}$ introduced in Brisset et al. [2018] with $T_{wave} = \mathcal{L}/c_k$ and the kinematic wave velocity for a rectangular channel $c_k = 5/3U$ ($c_k = 1.16\,\text{m/s}$ considering average speed $U = 0.69\,\text{m/s}$) and a high observation frequency ($\Delta t_{obs} = 20\,\text{s}$), gives a high identifiability index $I_{ident} = 43$ for the present flow observation configuration.

Case	Q_{in}			$Q_{l,1}$			$Q_{l,2}$			Froude range
	Q_0	a_Q	T	Q_0	a_Q	T	Q_0	a_Q	T	
$\mathcal{C}h1$	100	0	6300	100	20	6300	-			0.13-0.29
$\mathcal{C}h2a$	100	20	6300	100	20	6300	100	20	6300	0.12-0.3
$\mathcal{C}h2b$				400	80	6300				0.05-0.55
$\mathcal{C}h2c$				100	20	630				0.1-0.33
$\mathcal{C}h2d$				100	20	6300				0.12-0.3
$\mathcal{C}h3$				100	20	6300				0.09-0.53

Table 2.1: Parameter values for sinusoidal hydrographs $Q\left(x,t\right) = Q_0\left(x\right) + a_Q\left(x\right)\sin\left(\frac{2\pi}{T}t\right)$ used in synthetic channels and resulting modeled Froude ranges. Flows in m^3/s, time T in $[s]$.

tency, that is unbiased priors (see investigations in Garambois et al. [2020]; Larnier et al. [2021]); hydrograph priors are constant values equal to the average value of the target hydrographs.

Increasingly challenging inverse problems are considered, with increasing number of unknowns sought simultaneously and various observations densities. Cases $\mathcal{C}h1$ and $\mathcal{C}h2$ are used to infer temporal parameters only, given a channel of constant slope and friction. Case $\mathcal{C}h3$ is the most challenging case with all inflows and non constant channel parameters sought simultaneously.

2.4.2 Informative content of hydraulic signatures: inflow inferences

The fluvial signature from a single lateral inflow is divided in two parts (see $\mathcal{C}h1$ on Fig. 2.4, bottom): (i) in the reach downstream of the injection point, the cumulative flow ($Q = Q_{in} + Q_{lat,1}$) is uniform with a water depth corresponding to the normal depth imposed downstream, (ii) in the reach upstream of the injection point an M1 backwater curve profile (see Chow [1959], Montazem [2018]; Montazem et al. [2017] in the present “altimetry context”) is obtained given the upstream flow Q_{in} and the water depth imposed downstream of this reach as the normal depth corresponding to the cumulative flow. In the case of two distinct lateral injections ($\mathcal{C}h2$), WS signatures overlap in the most upstream reach because of the stronger backwater effect created by two downstream inflows, which represent a more challenging inference problem.

Inference trials in case $\mathcal{C}h1$ with control vector $c_1 = \left(Q^0_{l,1}, ..., Q^P_{l,1}\right)^T$, assuming a known constant $Q_{in}\left(x=0,t\right)$, show that a single observation point in space with a dense sampling in time, placed either upstream ($S1$, in Fig. 2.4, top) or downstream ($S2$) from the lateral inflow, is sufficient to infer one lateral inflow hydrograph perfectly - noiseless twin experiments - (not presented). Indeed, the hydraulic signature of a lateral inflow is visible and fully informative either upstream from it because of its downstream control on the upstream flow line or downstream from it, in the signature of the cumulative flow. This means that as long the river is well temporally-observed regarding its response time (see Brisset et al. [2018] without lateral inflows) and that the temporal variations of the observed system stem from a single control, only one spatial point is needed to infer this parameter.

In the case of two distinct lateral injections ($\mathcal{C}h2$), WS signatures overlap in the most upstream reach because of the stronger backwater effect created downstream by the two inflows, which represents a more challenging inference problem considering the unknown control vector $c_2 = \left(Q_{in}^0, ..., Q_{in}^P; Q_{l,1}^0, ..., Q_{l,1}^P, Q_{l,2}^0, ..., Q_{l,2}^P\right)^T$. Several variants of $\mathcal{C}h2$ are considered to study the possible misattribution of flow controls (locations, amplitudes and frequencies) in case of identical inflow hydrographs ($\mathcal{C}h2a$), the backwater influence of inflow hydrographs on Q_{in} downstream signature observed at $S1$ given 4 times larger inflow amplitude ($\mathcal{C}h2b$) or 10 times higher frequency ($\mathcal{C}h2c$), different observations samplings "mixed" inflows signatures (see Fig. 2.4 and Tab. 2.1).

2.4.2.1 Inference of multiple inflows

For all cases, using perfect and dense observations in space (1 every 10 m) and also in time leads to quasi perfect inferences. The influence of a sparser sampling and of the observability patterns of overlapping WS signatures on the identifiability of multiple inflows with the present inverse method is studied here - without a priori weighting of the parameters in the inverse method, that is equal and unadjusted $\sigma_\square$ values (see 2.A). The inferred hydrographs are summed up in Fig. 2.5. Scores are given in Tab. 2.2, including cost function values and iterations number at convergence.

Variant *Ch2a* Given only one observation station by reach ($S1$, $S2$, $S3$) very satisfying inferences of the 3 inflows are obtained(Fig. 2.5, red line). Hence sufficient information is provided by those three stations observing distinct signatures in each reach from upstream to downstream: ($S1$) propagation of the inflow $Q_{in}(x = 0, t)$ in presence of the overlapping backwater effects due to $Q_{l,1}\,(x = 300, t)$ and $Q_{l,2}\,(x = 700, t)$; ($S2$) propagation of $Q_{in}\,(x = 0, t) + Q_{l,1}\,(x = 300, t)$ in presence of the overlapping backwater effect due to $Q_{l,2}\,(x = 700, t)$; ($S3$) the propagation of the total discharge without downstream control.

Variant *Ch2b* Assimilation is more difficult than in $\mathcal{C}h2a$ but inferred hydrographs (Fig. 2.5, red line) are still accurate (Tab. 2.2). This testifies to the ability to discriminate multiple sources of various amplitudes given observations of hydraulic signatures at higher frequency and at pertinent locations ($S1$, $S2$ and $S3$).

Interestingly, this case highlights the expected misattribution behavior between inflow sources as shown by an intermediate iteration (Fig. 2.5, orange line) and remaining to a lesser extent at convergence (red line): Q_{in} and $Q_{l,1}$ are respectively over- and underestimated). This may be due to the relatively higher contribution of Q_{in} to the observed signature (it impacts WS elevation at $S1$, $S2$ and $S3$) and consequently its contribution in the cost function (observation part).

Note that the final overestimation of Q_{in} in $\mathcal{C}h2b$ is slightly greater than in $\mathcal{C}h2a$. This is likely due to greater WS elevation variation at $S1$ caused by backwater from $Q_{l,1}$, which is first attributed to Q_{in} since it has more impact on the cost function. Remember that, with perfect observations of WS signatures, at the end of the optimization process, nearly perfect hydrographs are inferred. However, the small flow misattributions during this optimization shows the difficulty of inferring multiple controls using an observation located in a strong backwater signal.

Variant *Ch2c* Perfect inferences are obtained. An intermediate iteration (Fig. 2.5, orange line) shows that the expected misattribution of frequencies for all 3 inflows is present, though it disappears at convergence (Fig. 2.5, red line). This testifies to the ability to discriminate multiple sources of various frequencies given observations of hydraulic signatures at higher frequency and at pertinent locations ($S1$, $S2$ and $S3$).

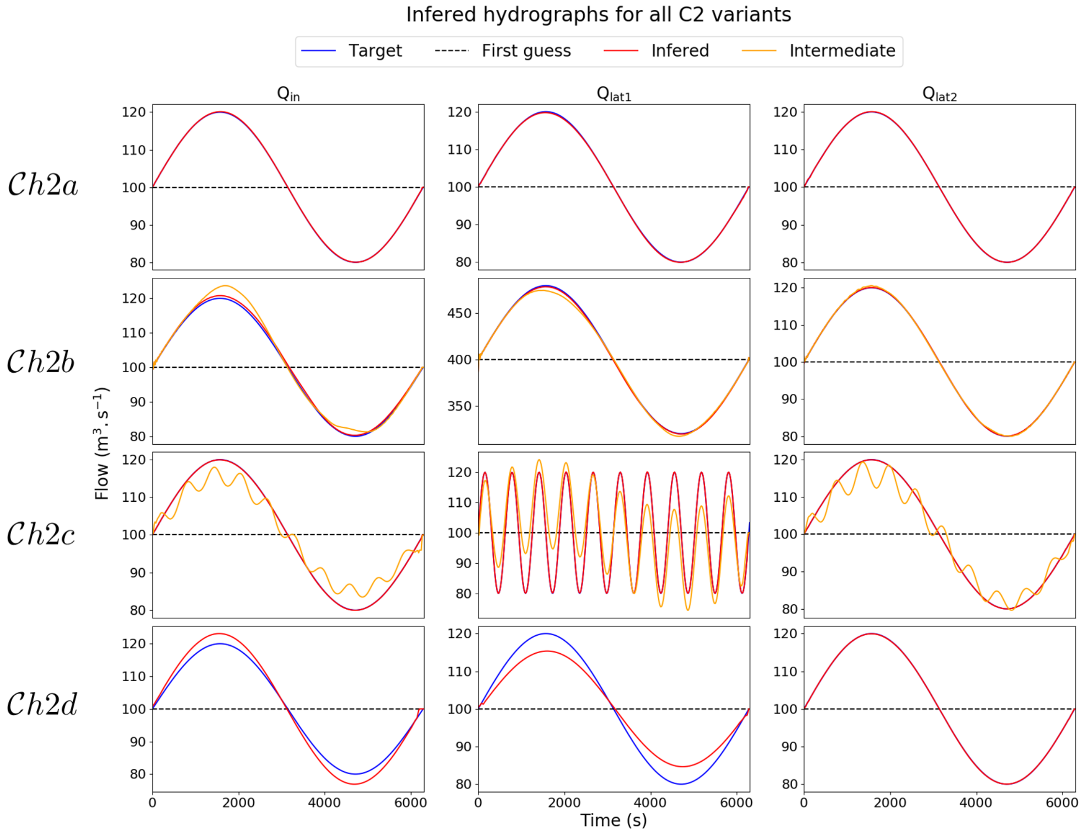

Figure 2.5: Inflows inferences from WS observations for all *Ch*2 variants. Intermediate iteration in the assimilation process are represented for *Ch*2*b* and *Ch*2*c* ; they are hand-picked to illustrate "intermediate" behaviors before convergence ("inferred").

Variant *Ch*2*d* Convergence is achieved but the flow upstream of *S*4 is misattributed between Q_{in} and $Q_{l,1}$. Signatures of Q_{in} and $Q_{l,1}$ are only observed mixed, downstream of $Q_{l,1}$ (at *S*4 and *S*5) and downstream from both $Q_{l,1}$ and $Q_{l,2}$ (at *S*3). Given that all stations are located in the downstream influence of both inflows, the distribution of flow between them makes little difference on the observed WS dynamics. This confirms the need to have at least one observation station between each sought inflow in order to be able to "separate" them.

2.4.2.2 Synthesis

These first tests showed that for inferring multiple inflows, i.e. spatially distributed temporal controls, a minimal spatial observability of their WS signature is required with one observation point between each inflow here. In case of observation stations affected by backwater influence, the potential difficulty of separating multiple inflows from their "mixed signature" is highlighted; using a higher spatial density of (simultaneous) observations leads to improved inferences in the present configuration. Moreover, using observations with high temporal density (with regards to the response time in the considered river system) and low spatial density,

Case	Q_{in}		$Q_{l,1}$		$Q_{l,2}$		Cost	N_{ite}
	RMSE	rRMSE ($\times 10^{-6}$)	RMSE	rRMSE ($\times 10^{-6}$)	RMSE	rRMSE ($\times 10^{-6}$)		
$Ch2a$	0.08	2.5	0.15	4.7	0.05	1.6	8.0×10^{-6}	54
$Ch2b$	0.72	22.9	1.34	10.6	0.08	2.7	9.4×10^{-6}	261
$Ch2c$	0.06	1.9	0.27	8.7	0.04	1.3	7.7×10^{-6}	78
$Ch2d$	2.21	70.0	3.31	105.0	0.03	0.9	7.9×10^{-6}	24

Table 2.2: Inferred parameters misfits to the truth for $Ch2$ variants. The RMSE $\left[\mathrm{m}^3/\mathrm{s}\right]$ and rRMSE represent the misfit of the inferred parameters, while the cost function used in the assimilation process represents the misfit of variables.

$$RMSE = \sqrt{\frac{1}{n}\sum_{i=1}^{n}\left(Q^i_{target} - Q^i_{infered}\right)^2},\ rRMSE = RMSE/\sum_{i=1}^{n} Q^i_{target}$$

different frequencies can be correctly attributed to multiple inflows (as highlighted for a single upstream inflow in Brisset et al. [2018]). Furthermore, note that if a supercritical regime occurs in a reach between inflows, their hydraulic signatures are disconnected (not shown), effectively reducing the assimilation problem to that of case $Ch1$.

2.4.3 Multiple and composite controls inference

In this section multiple inflows are sought simultaneously with channel parameters on case $Ch3$. Three friction patches are consistently applied to sub-reaches in-between the 4 sought bathymetry points. The control vector is:

$$c_3 = \left(Q^0_{in}, ..., Q^P_{in}\,; Q^0_{l,1}, ..., Q^P_{l,1}, Q^0_{l,2}, ..., Q^P_{l,2}\,; b_1, b_2, b_2, b_4\,; \alpha_1, \alpha_2, \alpha_3\right)^T \tag{2.5}$$

. Searching both inflows and channel parameters creates a configuration (intently) prone to equifinality problems on the sought parameters having correlated influence in the water surface signal. Three observation configurations (see Fig. 2.4) are studied: one with a high station density ($Ch3a$: 100 stations, 1 every 10 m), another with fewer stations ($Ch3b$: 9 stations, Sb$_{1..5}$ and Sc$_{1..4}$) and a third one with even fewer stations ($Ch3c$: 4 stations, Sc$_{1..4}$). Priors for inflows are those defined for case $Ch2$ (subsection 2.4.2.1), priors for channel parameter are hydraulically consistent with flow priors and initial flow line. For this equifinality prone configuration, the $\sigma_{\square}$ values used in the inverse problem regularization, related to the sought parameters (see section 2.A) and denoted as weights, are given in Tab. 2.3.

Inference results are presented in Fig. 2.6. In red, the final estimate of c_3 for $Ch3a$ with the "default" weights set (see Tab. 2.3). In green, final inferences for variant-specific parameter weights adjusted through trial and error. In orange, intermediate inferences with the "default" set of parameter weights. Equal values of 1, corresponding to "no weighting", were also tested: they lead to inaccurate inferences (not shown) and thus the "default" weights producing more interpretable results are preferred. In further iterations, after the ones plotted in orange, behaviors similar to the $Ch3a$ “default” weights inferences (Fig. 2.6, in red) appear (not shown), i.e. a shift of inferred hydrographs and Strickler coefficients away from the target. Also note that the inferred flow oscillation in the first time step stems from the influence of the initialization scheme (see section 2.3.1) in the optimization on this quickly responding channel.

Variant $\mathcal{C}h3a$ Q_{in} is underestimated while the local friction is overestimated, denoting a local tendency to equifinality. This is linked to a strong backwater influence, created by both $Q_{l,1}$ and the increase in friction at $x = 300\,\text{m}$. This local inflow error leads to compensation in downstream hydrographs. By adjusting parameter weights through trial and error, accurate inferences are obtained (Fig. 2.6, in green). This means that dense observations of the WS elevation are not sufficient for inferring all flow controls contained in c_3 and that spatially distributed regularization parameters, acting as weights in the parameter search, are required.

Variant $\mathcal{C}h3b$ and $\mathcal{C}h3c$ With sparse observations, the “default” weight set leads to worse inferences. However, the existence of a set of adjusted weights that lead to good inferences (Fig. 2.6, in green) is enough to show that the minimum observation spatial density of 1 station between each inflow can be sufficient to infer the extended control vector c_3. Note that adjusted weight for $Ch3b$ and $Ch3c$ are different from adjusted weights for $Ch3a$ (see Tab. 2.3).

Using less observation points in space, the influence of spatial parameters decreases without loss of meaningful information and thus the relative influence of inflows increases. This simple test highlights the weighting influence of the $\sigma_{\square}$ parameters in the regularization method in the present flow configuration. The spatial distribution and density of WS observations along with the weights change the hydraulic representativity of spatially distributed parameters in the optimization process.

The main difficulty uncovered with these academic cases is the challenge presented by simultaneous inferences of multiple inflows and channel parameters from their potentially overlapping hydraulic signatures. However, in the case of unbiased prior parameters and dense WS observation patterns relatively to those of spatio-temporal controls, satisfying inferences are obtained with the present inverse method. A real and complex river case is considered hereafter.

Case		$\sigma_{Q_{in}}$ ($\mathrm{m^3 s^{-1}}$)	$\sigma_{Q_{l,1}}$ ($\mathrm{m^3 s^{-1}}$)	$\sigma_{Q_{l,2}}$ ($\mathrm{m^3 s^{-1}}$)	σ_α ($\mathrm{m^{1/3} s^{-1}}$)	σ_b (m)	Cost	N_{ite}
"Default"	$\mathcal{C}h3a$	50	50	50	600	2	0.54	180
	$\mathcal{C}h3b$						0.54	97
	$\mathcal{C}h3c$						0.63	54
"Adjusted"	$\mathcal{C}h3a$		30	30	400		0.23	156
	$\mathcal{C}h3b$	1	0.9	1.2	300		0.25	108
	$\mathcal{C}h3c$						0.26	100

Table 2.3: Parameter weight sets in $\mathcal{C}h3$ variants

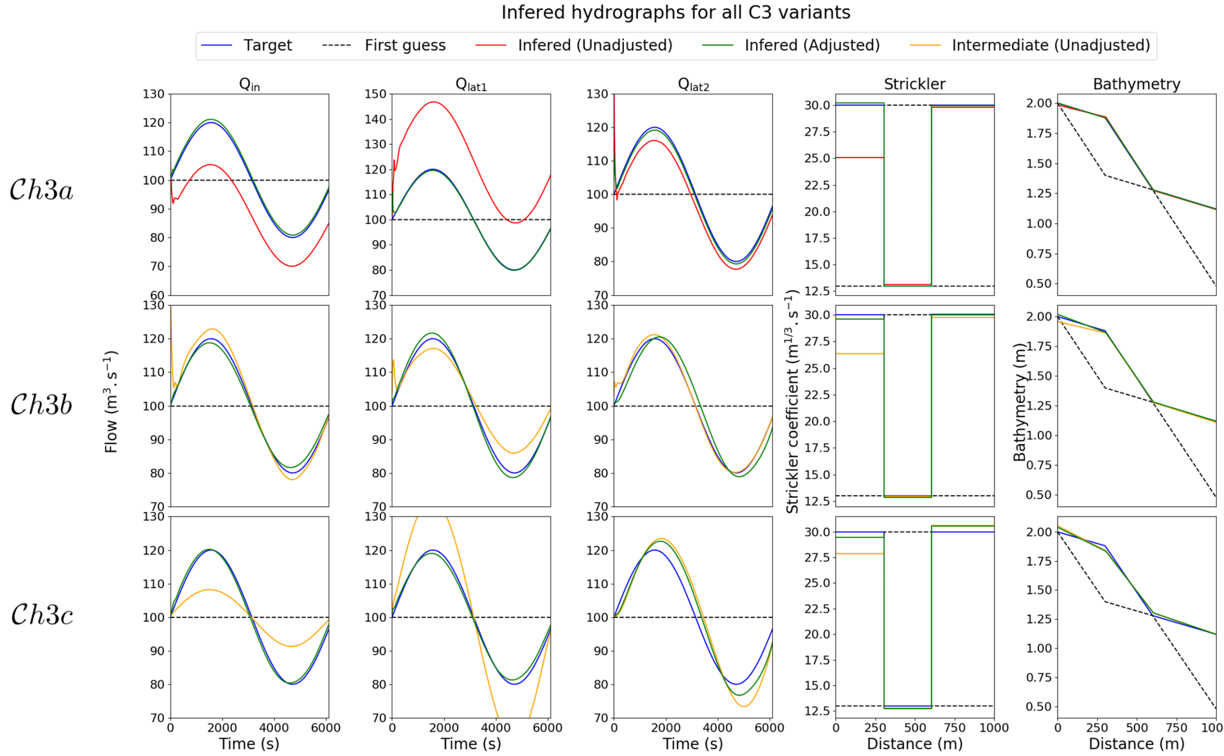

Figure 2.6: Inflow, bathymetry and friction patch inferences from WS observations for all $\mathcal{C}h3$ variants. In red, final inference with "default" parameter weights (see Tab. 2.3). In green, final inference with adjusted parameter weights. In orange, intermediate inferences with "default" parameter weights.

2.5 Effective hydraulic model of the Negro river

After addressing increasingly challenging hydraulic inverse problems on synthetic test cases in the previous section, a real complex river flow case is now considered. It consists in 871 km of the Negro river, including several confluences with tributaries and anabranching flow zones. The reach is located upstream of the Solimões-Negro confluence which is responsible for significant backwater effects (see e.g. Montazem et al. [2017]). This section presents the elaboration of effective flow models in view of performing forward and inverse flow modeling from WS observations of varying sparsity in the next section.

The modeling approach consists in (i) a 1D hydraulic model (full Saint-Venant equations, see subsection 2.3.1) (ii) based on effective XSs defined from multi-satellite and in situ data and (iii) weakly coupled to the large scale hydrological model MGB Collischonn et al. [2007]; Pontes et al. [2017]; Paiva et al. [2013a]. The idea is to build an effective river flow model both in coherence with the main hydrological signals (inflows) propagations along with observable flow surface signatures and HCs (see Montazem et al. [2017]). As shown in what follows, this 1D approach allows for a fair representation of flow propagation and longitudinal signatures, which are the core focus of this paper.

2.5.1 Study zone

The study domain corresponds to the main stream of the Negro river, a major “left-bank” Amazon tributary draining the north part of the basin, with an average discharge of 28 400 m^3/s Agência Nacional de Águas e Saneamento Básico (ANA). The reach covers the 871 km upstream of its confluence with the Solimões and presents singular channel morphologies such as multichannel flow zones mainly located in two large grabens (Latrubesse and Franzinelli [2005]). Part of the reach is strongly influenced by the control imposed by the Solimões river at its confluence (average discharge of 100 819 m^3/s according to ORE HYBAM gauge data Cochonneau et al. [2006], their confluence gives birth to the Amazon river). This HC is due to higher discharge and a consequently lower slope of the Negro river in its lower reach when compared to the Solimões river near to the confluence Filizola et al. [2009]; Callède et al. [2013]. The reach of interest has been crosscut by 18 Envisat ground tracks every 35 days from 2003 to 2010 (see Da Silva et al. [2012]), representing 68 to 79 measurements of WS elevations at each of the 18 Virtual Stations (VS). Note that the measurements are not simultaneous for each station.

2.5.2 Effective models construction

This section presents the elaboration of effective flow models from multi-satellite data. First, a $\mathcal{G}1$ “sparse” channel geometry is built from effective bottom elevations at Envisat VS resolution. Next, in view to test the additional constraints brought by spatially dense satellite data (synthetic SWOT), a more spatially detailed effective channel geometry $\mathcal{G}2$ is built using a high resolution water mask and an in situ flow line as explained below.

2.5.2.1 Effective geometry $\mathcal{G}1$ from altimetry and optical data

An effective 1D channel with effective rectangular XSs is set up from available multi-satellite data (altimetry, optical) and a large scale hydrological model following Garambois et al. [2017,

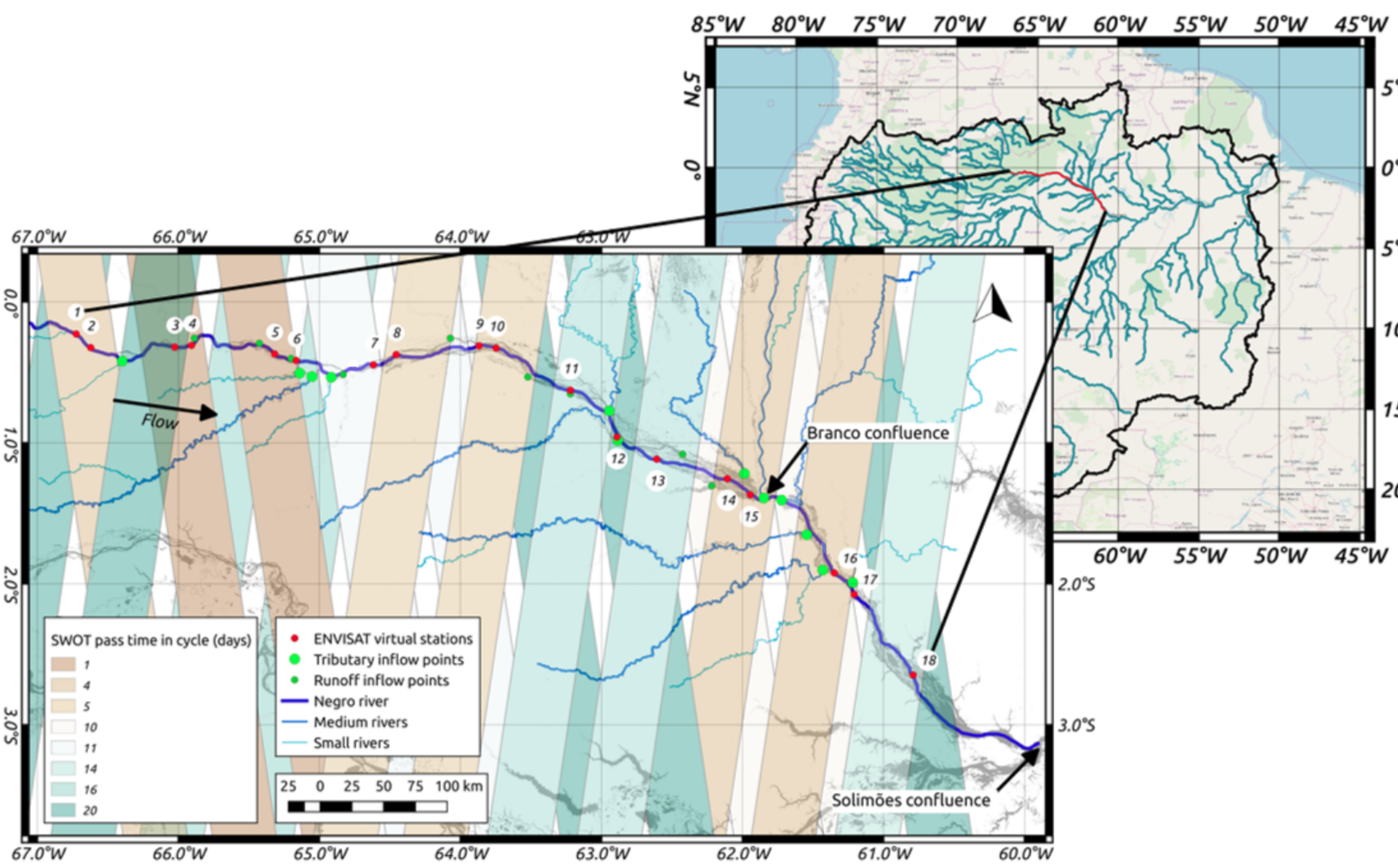

Figure 2.7: Study zone on the Negro river. Envisat Virtual Stations (red points) are numbered from 1 to 18 starting from upstream. The boundaries of the studied reach are defined by stations 1 and 18. The 21 tributaries (green points) are divided between actual rivers (light green) and inflow points from the hydrological model (dark green). SWOT swaths give an almost full spatial coverage of the reach. The average water extent map (from Pekel et al. [2016], in gray) was used to extract width values.

2020]. According to Latrubesse and Franzinelli [2005], high width to depth ratios make the rectangular channel a pertinent effective modeling approach of the true geometry, even in highly anastomosed reaches - where an error on the actual hydraulic perimeter P_h hence R_h (see Subsection 2.3.1) is expected. This is supported by a qualitative analysis of some additional ADCP measurements of river flow and cross-sectional bathymetry.

- The river centerline from Allen and Pavelsky [2015], formed by 30×30 m pixels, is used to calculate the river length and to project all spatial objects, such as VS, widths and inflow points, on a single one-dimensional reference.
- A longitudinal profile of cross-sectional WS width W is calculated from the average river extent map derived from 31 years (1984-2015) of optic Landsat imagery by Pekel et al. [2016]. A single width value per centerline point is extracted in order to build a 1D rectangular geometry. For multi-channel reaches, the effective width is the sum of the widths of all channels. This underestimates the actual hydraulic perimeter. Specific hand-filtering based on hydraulic expertise was necessary in some anabranching parts of the model where the water extent may include inactive flow zones not accounted for in the present 1D effective model. Note that Park and Latrubesse [2017] concurs to the necessity of reach-scale flow zone evaluation in the Amazon river catchment.
- An effective channel bottom elevation b_{env} is obtained at each VS (Fig. 2.8, in red) from altimetric rating curves (RC) from Paris et al. [2016]. Its slopes range from -7.1×10^{-5} to 2.0×10^{-4} m/m with an average of 7.0×10^{-5} m/m. RCs were obtained by adjusting the parameters (γ, δ) of a stage discharge relationship $Q = \gamma\left(Z_{sat} - b\right)^{\delta} S_{sat}^{0.5}$ using WS elevations Z_{sat} and slopes S_{sat} gained by satellite altimetry and discharge Q simulated with the large scale hydrological model MGB (Collischonn et al. [2007]; Pontes et al. [2017]; Paiva et al. [2013a]) on the temporal window of interest.

Effective rectangular XS geometries are defined at the $R = 18$ VS using the above defined effective bottom elevations $\{b_{env}\}_{r\in[1..R]}$ and river widths $\{W_1\}_{r\in[1..R]}$. The final model geometry ($\mathcal{G}1 = \{b_{env}, W_1\}_{r\in[1..R]}$) is obtained by linear interpolation between those 18 effective XSs on the model grid with $\Delta x = 200$ m.

2.5.2.2 Effective geometry $\mathcal{G}2$ at increased spatial resolution

Spatially dense WS elevation data is introduced in the form of an in situ GPS flow line with $G = 579$ spatial points. It was collected by survey ship along the whole studied reach over 7 days during the low-flow period in december 2010 (Moreira [2016]); it provides local WS elevations Z every 1.4 km on average and WS slopes S for every 25 km reach (ranging between 2.0×10^{-5} and 8.11×10^{-5} m/m, averaging at 3.4×10^{-5} m/m). Under the hypothesis of a wide rectangular XS and a steady uniform flow, the Manning equation writes:

$$Q = K\left(Wh\right)^{5/3}\left(W + 2h\right)^{-2/3}\sqrt{S} \tag{2.6}$$

The water depth writes $h = (Z - b)$ and the bottom elevation is sought using (i) the fixed WS width pattern W_2 from imagery, (ii) the WS elevation Z_{GPS} and slope S_{GPS} given by the GPS profile and (iii) the discharge Q from the hydrological model (see Subsection 2.5.1) on the river

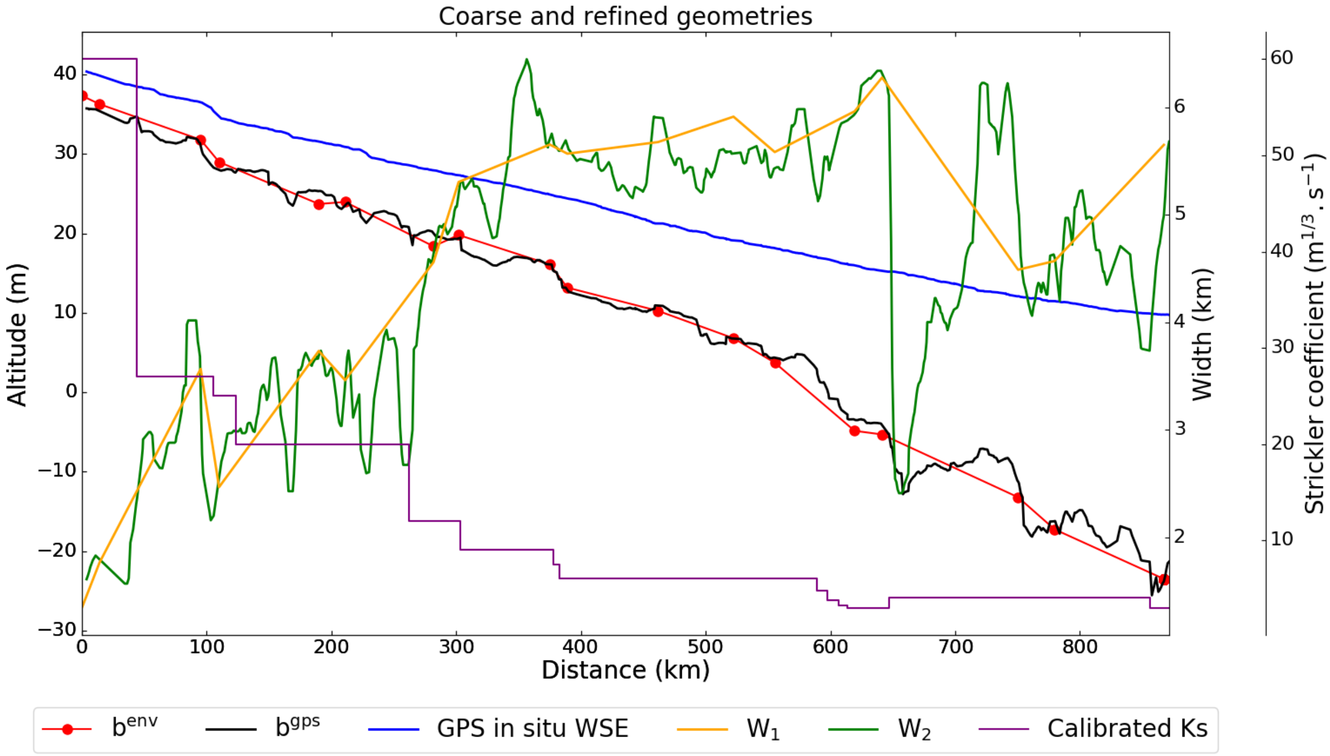

Figure 2.8: Effective river channel bottom and width for spatially sparse, $\mathcal{G}1 = \{b_{env}, W_1\}_{r\in[1..R]}$, and spatially dense, $\mathcal{G}2 = \{b_{GPS}, W_2\}_{G\in[1..G]}$, model geometries and a low-flow GPS waterline from Moreira [2016].

domain at the corresponding time t_*. We invert an effective bathymetry b_{GPS} using equation 2.6 by minimizing the square sum of misfits to b_{env} at Envisat stations through the modification of $M = 14$ friction values $((\alpha_m, \beta_m = 0)\,, m \in [1..M]$, friction law Eq. ((2.3))). They are simply spatialized into M "hydraulic" patches consistent with large scale morphological features classified as follows: single channels, multiple channels (from 2 to 3), lightly anastomosed and heavily anastomosed (Fig. 2.8, in purple). The friction coefficient values are coherent with the physical properties of the classified reaches.

The new bathymetry b_{GPS} is coherent with the best available reference data and its corresponding set of physically distributed Strickler patches. The final model geometry is $\mathcal{G}2 = \{b_{GPS}, W_2\}_{G\in[1..G]}$.

In the following, using either geometry $\mathcal{G}1$ or $\mathcal{G}2$, the hydraulic model is inflowed with time series at a daily time step upstream of the river domain and at 21 tributaries (both river tributaries and runoff inflows) corresponding to the 21 catchment cells feeding into the Negro river cells in the large scale hydrological model MGB (Pontes et al. [2017]; Collischonn et al. [2007]). The largest of these tributaries is the Branco river at 657 km.

2.5.3 Effective Models calibration against altimetry

The friction of the hydraulic model (Eq. (2.1)) is calibrated against altimetric WS elevation time series following Garambois et al. [2020], i.e. $\left\{Z_{s,p}^{obs}\right\}_{S=16,P\in[68..79]}^{env}$ at Envisat VS, the most downstream VS being used as BC (see Subsection 2.3.1). The friction law is distributed using $N=17$ "Envisat" patches with constant $(\alpha_n, \beta_n = 0)$, $n \in [1..N]$ values for each reach between two successive VS. This choice is made to avoid spatial "overparameterization" in the calibration process regarding the spatial sparsity of Envisat observations of WS signatures. The aim of parameter calibration is to obtain a "real-like" model as close as possible of the sparse observation set. Three models are considered, to assess the impact of the bathymetry refinement and of the downstream BC on the modeled hydraulic signatures and on inverse problems: a "sparse" model ($M1$) using channel geometry $\mathcal{G}1$ and the WS elevation time series from VS 18 as BC, a refined model ($M2a$) with channel geometry $\mathcal{G}2$ including all the spatial variability from multi-source data described above while keeping the same BC and a further changed refined model ($M2b$) where the BC is changed to an altimetric RC which is of interest for "operational-like" applications in other rivers and basins.

The inverse method presented in Larnier et al. [2021] and described in Subsection 2.3.2 and 2.A is used here, without regularization terms, for friction calibration. Effective Strickler patches, starting from priors corresponding to average values of the "hydraulic" patches used above (Fig. 2.8, in purple), are calibrated following Garambois et al. [2020] who use observations of the same nature. Friction patterns $c^*_{\mathcal{G}1}$, $c^*_{\mathcal{G}2a}$ and $c^*_{\mathcal{G}2b}$ found with the inverse method are shown in Fig. 2.9. Most differences in calibrated friction from $M1$ (Fig.2.9, in red) to $M2a$ (Fig. 2.9, in blue) correspond to their difference in bathymetry at the virtual station point (Fig.2.9, gray line), i.e. a lower slope in $M2a$ leads to a higher inferred Strickler parameter in order to match WS observations (e.g. in patch 2 and 6. Inferred parameters for $M2b$ roughly match those of $M2a$, with some discrepancies in patch 2, 15 and 17. Using a different BC influences WS sensitivity to parameters and the relative contribution to the cost function of local WS misfits, which explains differences in patch 15 and 17 ; the one in patch 2 stems for the high friction values, hence lower WS sensitivity as analyzed after.

2.5.3.1 Water levels analysis

The following presents a detailed analysis of the effective hydraulic model for configuration $M1$, along with an analysis of changes obtained for configurations $M2a$ and $M2b$.

The simulated WS elevation are compared to observed WS elevation at each Envisat virtual station in Fig. 2.10 - other time series are available in 2.B. For the 3 models calibrated above, the modeled WS are fairly close to observed WS given the limited modeling complexity and data uncertainties. More precisely, the fit to the altimetric WS elevation time series is fairly good, as shown for $M1$ in Fig. 2.10, and nearly unbiased as shown in Fig. 2.11(left). The WS elevation global RMSE is at 0.936 m for $M1$; similar results are found with $M2a$ (see Tab. 2.4). Errors are greater in low and high flows, with consistent underestimations of flow amplitude upstream (VS $1-4$) which turns into overestimation downstream (VS $9-13$), before disappearing closer to the BC (VS $14-18$). VS 5 to 8 are particularly accurate. Error metrics are coherent with those from current state of the art models using satellite data (see e.g. O'Loughlin et al. [2019] on the Congo river).

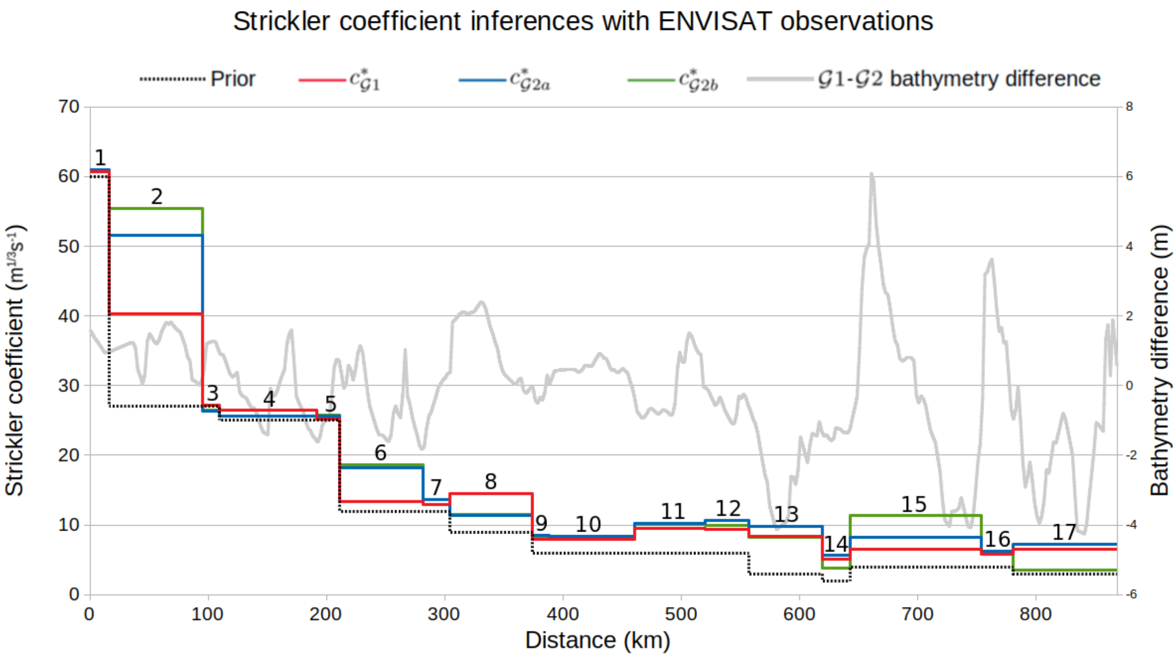

Figure 2.9: Friction patches after calibration against Envisat WS elevation observations. Inferred Strickler coefficient values are very close for all configurations for patches 1, 3 to 5 , 9 to 14 and 16. Patches 2, 6 and 15 are especially sensitive to model variations.

The analysis of the time series for $M1$ gives insight on the 1D model behavior regarding the real flow physics sampled with the sparse nadir altimetry data and dense in situ low flow line. Modeling errors can stem from either an (expected) improper representation of the channel and flow complexity or uncertain (ungauged) inflows and data.

Concerning the hydraulics, from downstream to upstream, relative errors are lower in anabranching reaches outside of the backwater influence starting at the Branco tributary ($x = 657$ km up to around $x = 350$ km) and in the backwater influence of the (known "perfect") downstream BC. Overall, relative errors are higher upstream, in single channeled, low water height reaches and in the Branco backwater influences. Note that 2D complex lateral flows in floodplains or retention behaviors from "igarape" rivers may happen in high flow periods (see Fleischmann et al. [2019]; Fassoni-Andrade et al. [2020]). These unaccounted phenomenons may decrease flood wave velocities and cause hydrograph skewness (Collischonn et al. [2017]; Alsdorf et al. [2007]; Fleischmann et al. [2016]).

The 1D modeling of water levels compared to altimetry observations (Fig. 2.10) can first be analyzed as follows:

- Stations 14 to 18 are located in reaches with different morphological properties. Stations 14 and 15 are located in a densely anastomosed reach upstream of the Branco river confluence, a major tributary. Stations 16 and 17 are in single channel reaches, upstream from the confluence with the Solimões river. Station 18 is in a densely anastomosed reach at the location of the BC forcing on WS elevation. Their low relative misfits do not testify to the absence of complex hydraulic behaviors in this area but rather to the dominating influence of the BC.

- Stations 5 to 13 are located in mostly homogeneous anastomosed reaches, with stations 5 to 8 in a less densely anastomosed region than stations 9 to 13. This spatial division corresponds to two trends in relative misfit, where lower misfit is seen in the less anastomosed reaches. This testifies to the difficulty of modeling potentially 2D hydrodynamics using 1D approach. Indeed, the more channels there are, the further away the simulated wetted perimeter is from the true wetted perimeter (and so the hydraulic radius). Note that parameterizing the Strickler coefficient as described in Eq. ((2.3)) and including $\beta(x)$ in the control vector during the calibration process, instead of the simpler $\beta(x) = 0$ used here, does not yield a better fit in this complex case modeled with a single rectangular channel.

- Stations 1 to 4 are located on single channel reaches. Although the area seems the most suitable to be modeled in 1D, it still has the highest relative misfit to Envisat observations. For stations 1 and 2, this is partly due to effective width estimation errors being more prevalent in the relatively narrow channel (around 2 km in width). Furthermore, note that effective channel bottom elevation for these stations are respectively 37.3 m and 36.3 m while the lowest Envisat WS elevation observation are respectively 36.6 m and 35.8 m. This corresponds to low-flow water heights of 0.7 m and 0.5 m which do not fit field measurements. Consequently, relatively high friction coefficients are inferred between station pairs 1-2 and 2-3 to fit low water depth. This misfit might be due to data error, including effective width errors for stations 3 and 4 located in areas of sharp width variations. Note that the higher the friction values, the less sensitivity of the modeled WS elevation, which explains the highest spread of Strickler coefficient ($K = 40$ to $55\,\mathrm{m}^{1/3}/\mathrm{s}$) in reach 2 found during calibration for the 3 models (Fig. 2.9).

The introduction of the refined geometry $\mathcal{G}2$ in $M2a$, recall for generating spatially distributed SWOT data and to perform inference tests hereafter, has low impact on WS elevation bias and errors at Envisat VS (see Fig. 2.11), with only stations 1, 2 and 3 showing significant change. Using a rating curve as downstream BC in $M2b$ mostly impacts the downstream part of the model where some misfit to altimetry data appears. Indeed, it is more difficult, using a simple power law depending on the local flow variables, to capture the influence of the confluence with the Solimões river - not modeled. The latest having strong discharge variations out of phase with the one of the Negro river itself (e.g. Montazem et al. [2019]).

	Global RMSE (m)	Global Average bias (m)	Upstream RMSE (m)	Upstream Average bias (m)
M1	0.94	−0.02	0.88	−0.08
M2a	0.94	−0.02	0.91	−0.01
M2b	1.72	0.23	0.90	−0.05

Table 2.4: RMSE and bias over 8 years for the $M1$, $M2a$ and $M2b$ models. Upstream metrics are calculated for stations 1 to 9 only, which are outside of the BC's backwater influence. The high global RMSE for $M2b$ comes from the known dephasing of the Solimões and Negro peak flow, which is not reproduced by the RC.

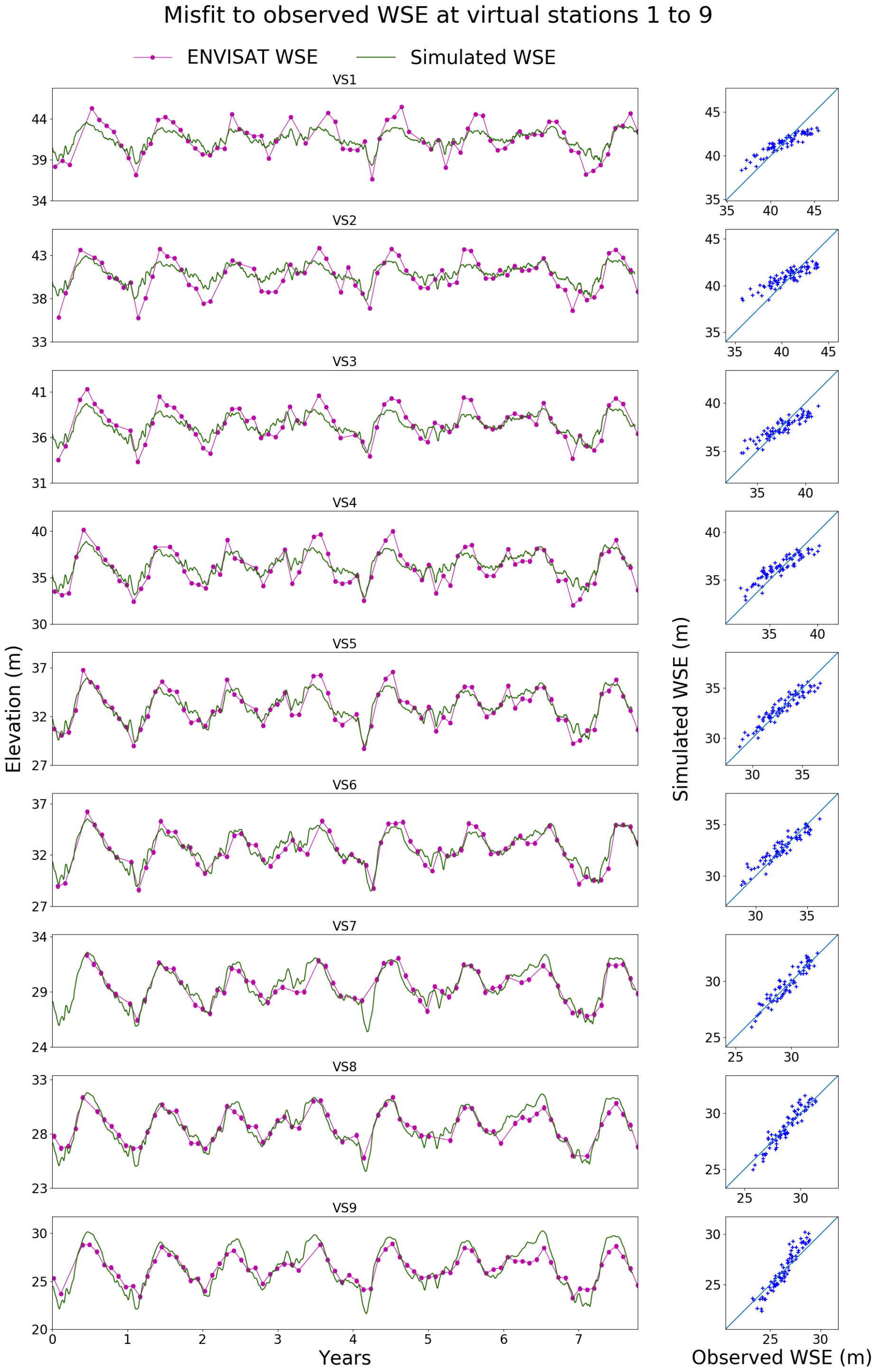

(a)

Figure 2.10: Modeled and observed WS elevation at Envisat VS after friction calibration at all stations for $M1$ (1)

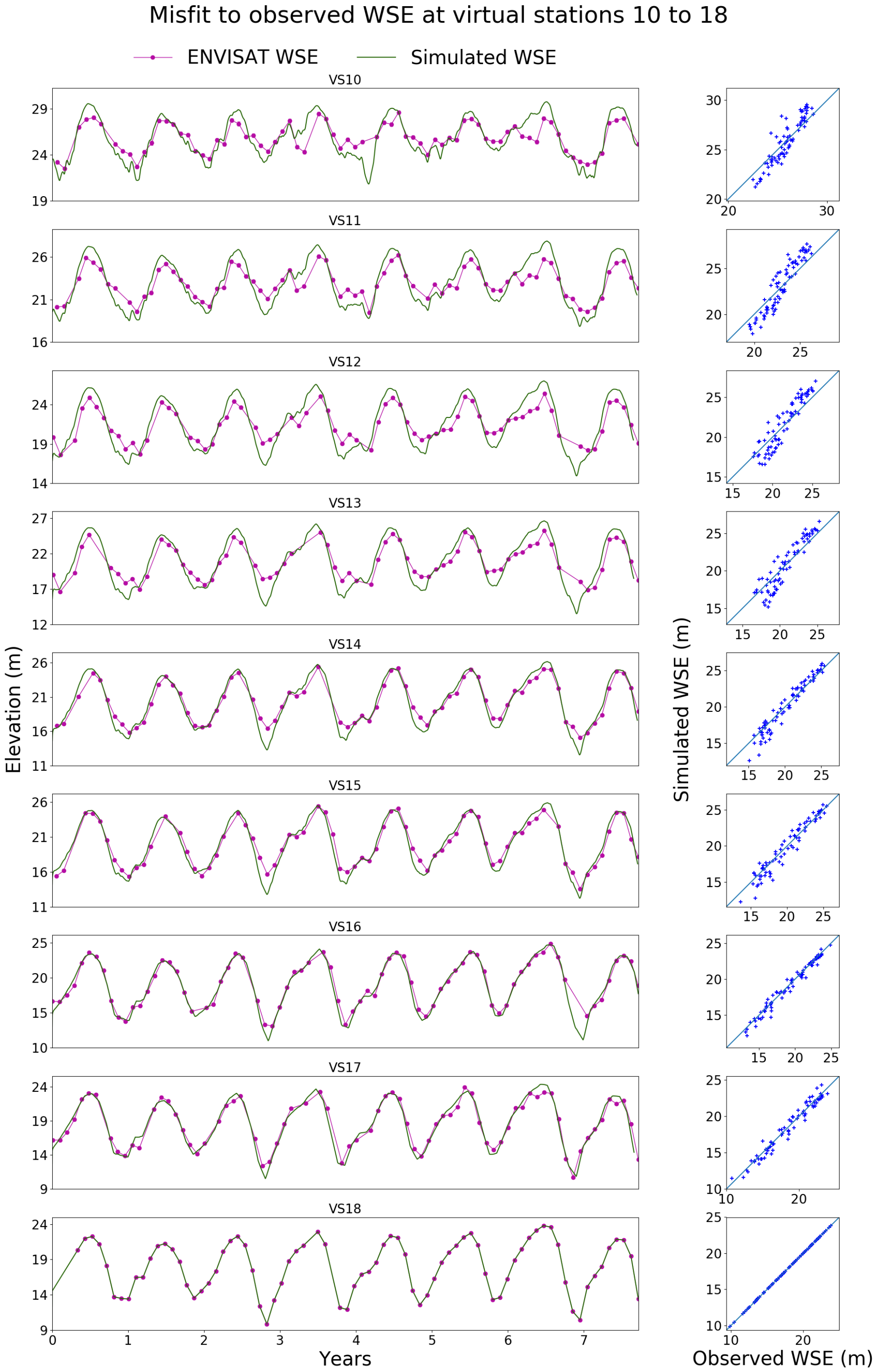

(b)

Figure 2.10: Modeled and observed WS elevation at Envisat VS after friction calibration at all stations for $M1$ (2)

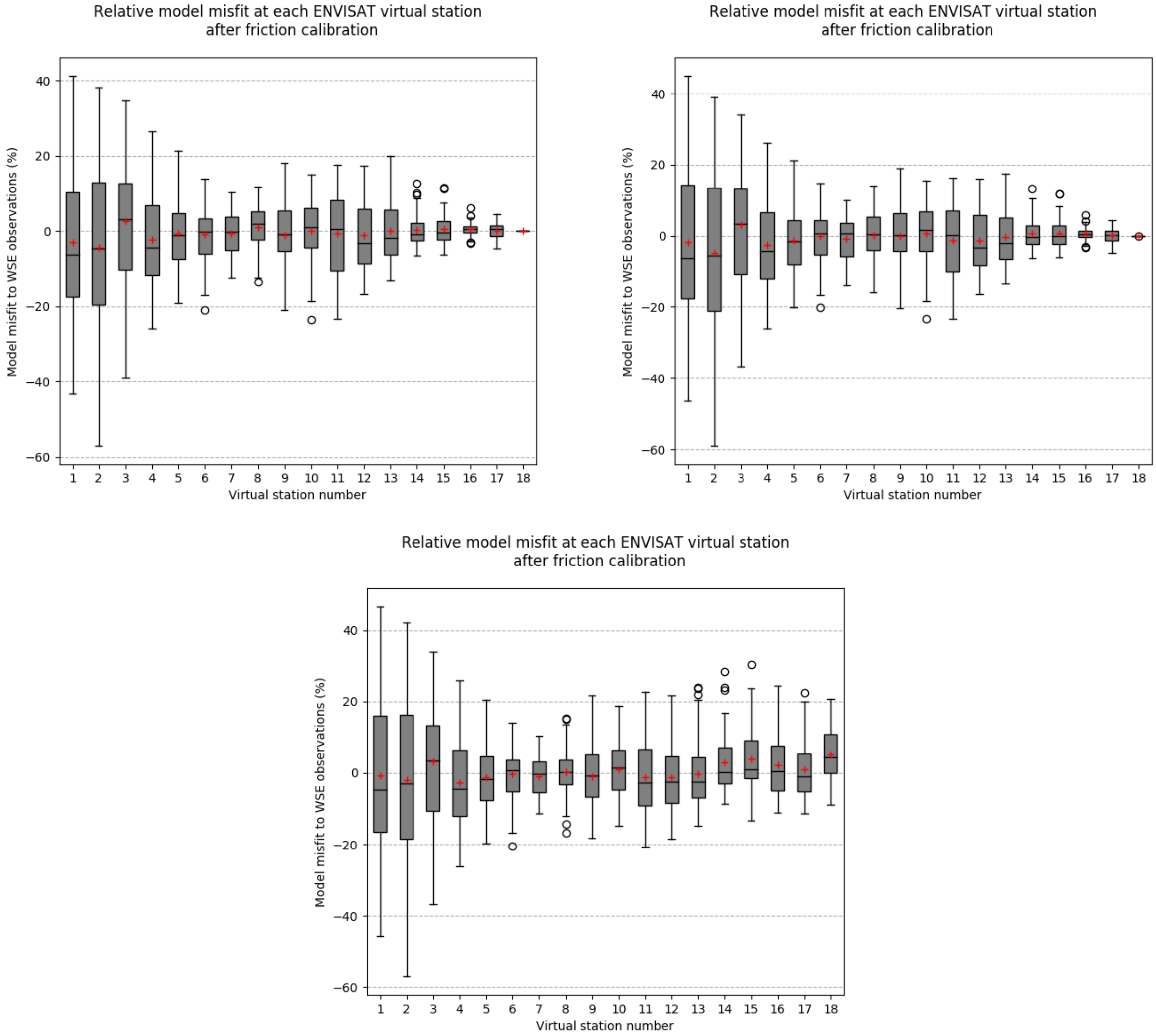

Figure 2.11: Relative misfit between modeled and observed WS elevation at Envisat for $M1$ (left, base model) $M2a$ (middle, WS elevation at downstream BC) and $M2b$ (right, rating curve at downstream BC). Crosses are average values, horizontal bars are median values.

2.5.3.2 Effective model analysis

As a preliminary to hydraulic parameters inference from WS observables, this subsection studies the spatio-temporal features of the simulated hydraulic signatures, their sensitivity to model parameters and their observability given a SWOT sampling. First, an analysis of a flood wave propagation, resulting from multiple inflows, and its hydraulic signature visibility is performed using identifiability maps following Brisset et al. [2018]. The latter consist in a space-time representation of the WS signal and flow propagation features against the observability pattern. These maps, inspired by the theory of characteristics (see Thual [2010]; Guinot [2010]), enable to read how the sought upstream discharge information is sampled in the downstream WS deformations and help to estimate inferrable hydrograph frequencies. Next, a numerical sensitivity evaluation of the flow model is carried out.

In the context of regional hydrological modeling including river networks representation, the sensitivity of the present flow model is studied by using erroneous inputs. These inputs are also used in Section 2.6 as erroneous priors for various assimilation setups.

- Inflow: two hydrograph sets (containing lateral inflows and the upstream BC inflow) corresponding respectively to 70% and 130% of the true hydrographs are used as erroneous values for sensitivity trials and are referred to as Q_{FG}^{-30} and Q_{FG}^{+30} respectively.
- Friction: two Strickler repartitions, with coefficient values worth respectively 70% and 130% of the truth are used as erroneous values for sensitivity and are referred to as K_{FG}^{-30} and K_{FG}^{+30} respectively.
- Bathymetry: the inflow sets Q_{FG}^{-30} and Q_{FG}^{+30} and the true Strickler values are used to dig two bathymetries as described in Section 2.5.3. The bathymetry derived from underestimated flows is referred to as b_{FG}^{-30} (it overestimates the true bathymetry), and the other is referred to as b_{FG}^{+30}.

Identifiability map SWOT will provide spatially distributed observations with interesting revisit frequencies at the scales of the current river domain and hydrological signal propagations. Fig. 2.12 shows the evolution of the simulated WS elevation anomaly during the yearly peak flow (red-blue heatmap) as well as its multiple SWOT observability (in black). Based on the modeled flow, accounting for several inflows, the propagation of an intumescence corresponding to the annual flood wave signature is represented along the river through the maximum WS elevation in time (following Montazem [2018]) (Fig. 2.12, top, blue points). This intumescence propagation is visible on the upstream 400 km of the river from day 164 to day 173. It is detected by a SWOT swath at $t = 166\,\mathrm{d}$ and another one at $t = 170\,\mathrm{d}$. It is more difficult to detect this signature in the downstream part of the river ($x > 400\,\mathrm{km}$) affected by the strong downstream control imposed by high water depths at the Negro-Solimões confluence; a downstream control due to the Branco tributary also overlaps from $x = 657\,\mathrm{km}$ to around $x = 400\,\mathrm{km}$. This control can be seen through the tracked WS elevation maximum (Fig. 2.12, top, in gray), where an early rise in WS elevation originates from $x = 657\,\mathrm{km}$, and through the extreme waterlines (Fig. 2.12, bottom, in blue), which highlights the change in length of this influence in low and high flows. As a consequence, WS observations on the downstream part may contain combined information due to the upstream hydrographs propagation but also to the expression of downstream controls.

The maximum WS elevation is tracked for simulations with erroneous parameters as defined above (Fig. 2.12, top, in red, green and cyan). They are not plotted where the flow displays "pool behavior" (gray points). They highlight the sensitivity of propagation to model parameters which is also an important point when they are varied during an optimization process as featured in Section 2.6. The propagation time from 0 to 400 km can be evaluated to around 10 days, and is estimated as follows for the rest of the river domain.

The conservative part of the Saint-Venant equations (i.e. without source terms) is hyperbolic: some quantities depending on the water depth and velocity (known as the Riemann invariants) are transported by waves at speeds different from the flow speed (see e.g. Thual [2010]; Guinot [2010]). The wave celerities are $U + c$ and $U - c$ with $c = \sqrt{gh}$ for rectangular XSs (see analysis of propagation features in Brisset et al. [2018]). For the fluvial regime of interest here ($\mathrm{Fr} = U/c < 1$), information propagates both downstream and upstream and the Riemann invariants are modified along the wave due to the source term effects. The wave celerities obtained on the Negro river model are given by reach in Table 2.5, relatively high wave speeds are obtained hence propagation of information both upstream and downstream, with spatio-temporal variability. The WS signature (and the discharge) thus reflects the nonlinear combination of information coming from both upstream (due to inflows variations) and downstream (due to local HCs or downstream BC - see the method of characteristic in Guinot [2010]). This highlights the difficulty of inferring multiple inflows from sparse observations of WS signature, especially given uncertain channel parameters and backwater effects.

Nevertheless interesting frequential information can be gained from the identifiability map as introduced in the case of a single inflow. Using the kinematic wave speed $\frac{5}{3}U$ (Fig. 2.12, top, dashed blue line) which compares fairly well to the intumescence speed on the upstream part of the reach (Fig. 2.12, top, $x < 400\,\text{km}$). This gives an approximate propagation time $T_{wave} = 26\,\text{d}$ on the whole domain, greater than the SWOT observation cycle period of 21 days. This brings the reach identifiability index to $I_{ident} = 1.23$ (defined as $I_{ident} = T_{wave}/\Delta t_{obs}$, i.e. the average number of time a wave is observed, see Brisset et al. [2018]). However, in the present case, the notion defined by Brisset et al. [2018] accounts for a single upstream inflow, not spatially distributed lateral inflows with potential upstream backwater controls. Actual identifiability indices for reaches in between each lateral inflow would be much lower (estimated identifiabilities in between each inflow pair are given in Tab. 2.5 considering a fictitious $\Delta t_{obs} = 1\,\text{d}$ full domain observability). Furthermore, SWOT swaths observations consist in WS snapshots on different parts of the river domain at given times, hence containing various and mixed signatures (in the sense introduced in Section 2.4) of both several inflows and channel parameters - the more downstream, the more aggregated is the inflow information. Inferences of multiple inflows and frequential analysis are presented in the next section given known or uncertain channel parameters, spatio-temporally dense or sparse (SWOT) observations.

2.6 Inferences from satellite observables

This section studies the challenging inference of ungauged channel parameters and multiple inflows on the Negro river case, which represents a real and complex large scale problem. Typical inverse problems in hydraulic-hydrological modeling are studied here considering SWOT WS observations. The inference of channel parameters or/and inflows in the 1D Saint-Venant model is addressed using the inverse method presented in Subsection 2.3.2 (see also Section 2.A). The downstream BC is set as a known altimetric rating curve. Three observation sets are generated: spatially and temporally dense ($\Delta t = 600\,\text{s}$) observations (DenseSet), SWOT observations from the hydraulic model outputs masked by SWOT swaths (SWOTSet) and noisy SWOT observations using the large scale simulator CNES to add realistic measurement noise (SWOTNoiseSet). We first present inferences of inflows only, then of channel parameters, and finally of all those spatio-temporal controls simultaneously.

2.6.1 Multiple hydrographs inferences

Depicting flow structure within a river network and a catchment is a key issue in hydrological modeling, especially in ungauged basins. Seeking to infer, from distributed WS observations,

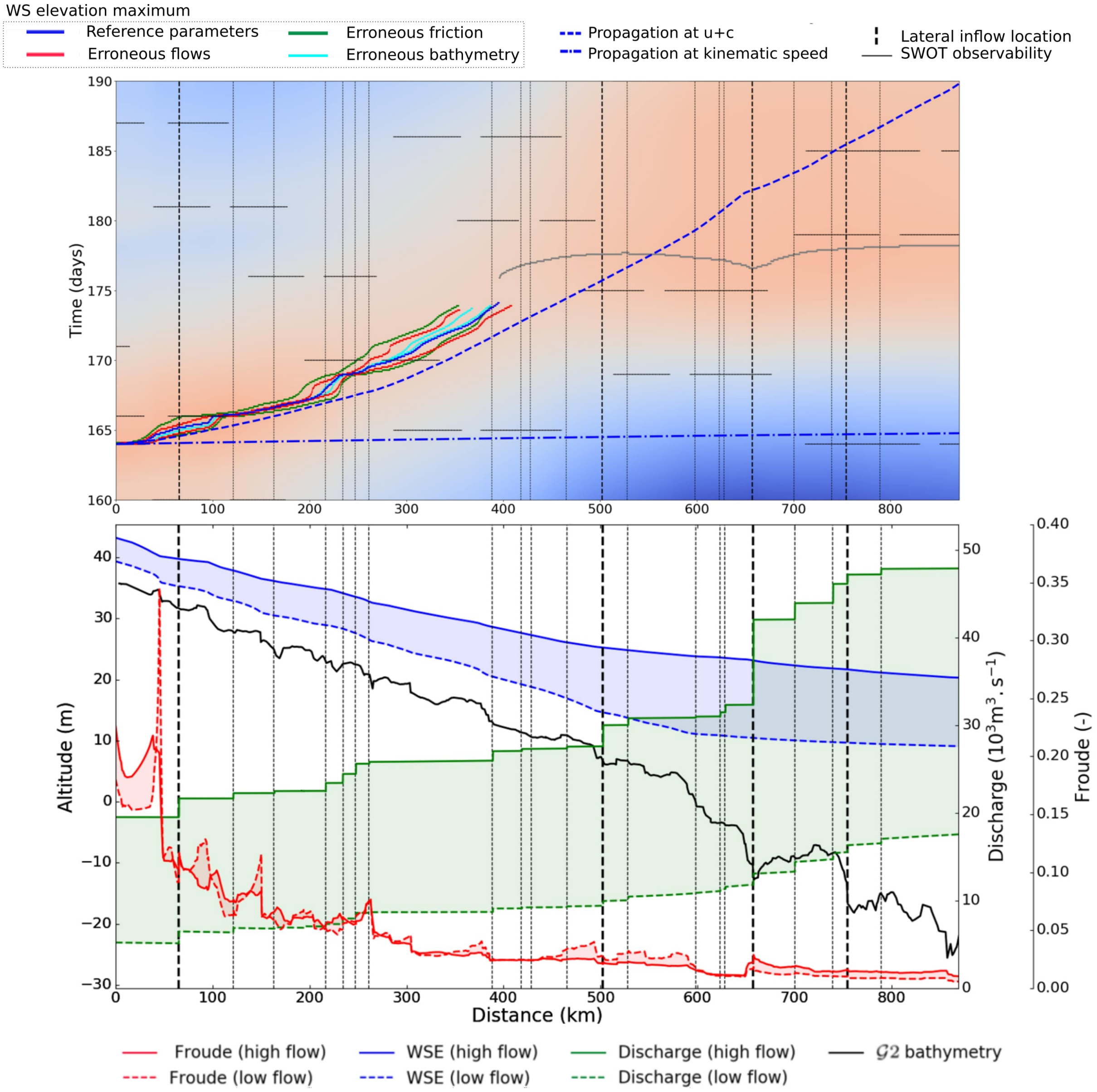

Figure 2.12: Identifiability map, flood wave propagation estimation and spatial variabilities of the large scale Negro river 1D model.
Top: Identifiability maps and flood wave propagation during the yearly peak flow (may-june) in the Negro river model. The WS anomaly (heatmap) is given by $Z_{ano}(x,t) = Z(x,t) - \overline{Z(x)}$, where $\overline{Z(x)}$ is the average local WS elevation from day 160 to 190. Blue dotted line: tracking of maximum WS elevation value $Z_m(x) = \max_{t \in [0,365]} Z(x,t), \forall x \in [0, L]$. Gray points: tracking of maximum WS elevation in the downstream pool. Dashed blue lines: fictitious trajectory at kinematic speed (sparse dashes) $c_k = 5/3U$ and at $U + c$ (dotted dashes), starting at $x = 0$, at the time of the local WS elevation peak. The speeds are calculated from the simulated flow speed U and water height h and updated every $\Delta x = 200\,\text{m}$, such as $t^{p+1} = t^p + \frac{\Delta x}{c_k^p}$.
Bottom: Extreme flow forcings and flow model variables over a 2 year period. Blue lines: Extreme simulated waterlines. Red lines: corresponding extreme Froude values. Green lines: corresponding cumulative injected flows.
Vertical black dashes are lateral inflow locations. Bold vertical dashes are inflows inferred in Subsection 2.6.3.

x (km)	0 65	121	163	193	216	388	418	465	502	528	598	623	628	657	700	739	754	789	1000
$\frac{5}{3}\bar{u}_{HF}$	2.35	1.42	1.22	1.07	1.02	0.75	0.50	0.52	0.53	0.50	0.48	0.35	0.32	0.41	0.61	0.47	0.44	0.47	0.44
c_{HF}	8.32	9.23	9.71	10.31	10.36	11.19	12.52	12.61	12.62	13.49	13.95	15.90	16.28	16.82	17.93	17.26	17.56	19.37	19.69
$u_{HF}+c_{HF}$	9.74	10.08	10.44	10.95	10.97	11.64	12.82	12.92	12.93	13.79	14.23	16.11	16.47	17.06	18.29	17.54	17.82	19.65	19.95
$u_{HF}-c_{HF}$	-6.92	-8.38	-8.98	-9.67	-9.75	-10.73	-12.22	-12.29	-12.30	-13.19	-13.66	-15.68	-16.09	-16.57	-17.56	-16.99	-17.29	-19.09	-19.42
$I_{ident,HF}$	0.32	0.46	0.40	0.33	0.26	2.64	0.69	1.04	0.81	0.60	1.69	0.82	0.18	0.82	0.81	0.97	0.39	0.86	2.14
$\frac{5}{3}\bar{u}_{LF}$	1.40	0.96	0.83	0.70	0.69	0.52	0.34	0.37	0.45	0.40	0.41	0.25	0.22	0.26	0.31	0.26	0.24	0.24	0.23
c_{LF}	5.54	6.16	6.54	7.13	7.05	7.72	8.70	8.59	7.87	8.71	8.81	11.30	11.83	12.54	14.11	13.37	13.78	16.09	16.59
$u_{LF}+c_{LF}$	6.38	6.74	7.04	7.54	7.47	8.03	8.91	8.81	8.14	8.94	9.06	11.45	11.96	12.70	14.30	13.52	13.93	16.24	16.72
$u_{LF}-c_{LF}$	-4.70	-5.58	-6.04	-6.71	-6.64	-7.40	-8.50	-8.37	-7.60	-8.47	-8.56	-11.15	-11.70	-12.39	-13.93	-13.22	-13.64	-15.95	-16.45
$I_{ident,LF}$	0.54	0.67	0.58	0.50	0.39	3.80	1.03	1.47	0.95	0.76	1.97	1.16	0.26	1.29	1.61	1.76	0.73	1.71	4.21

Table 2.5: Identifiability indexes between each pair of inflow at low and high flow (see Fig. 2.12, bottom). Speeds are given in m/s. I_{ident} is given for a reach of length L and an observation time step $\Delta t_{obs} = 1\,\mathrm{d}$ by $I_{ident} = \frac{L}{\frac{5}{3}\bar{u}\Delta t_{obs}}$.

flow controls that are both temporally and spatially distributed can represent a very challenging inverse problem, as previously highlighted on synthetic cases.

Inferences of $L = 21$ inflow hydrographs from 2 years of SWOT synthetic observations are studied here. The channel geometry, friction and BCs are assumed to be known, hence the control vector reduced to $c = \left(Q_{l,1}^{0}, ..., Q_{l,1}^{P}, Q_{l,2}^{0}, ..., Q_{l,D}^{P}\right)^{T}$. The inferences are started from a prior guess $c^{(0)}$ consisting in true hydrographs affected by uncertainties of ±30%, that is Q_{FG}^{+30} and Q_{FG}^{-30} as defined above. Note that the inference is started from a hydraulically consistent initial state using an unbiased prior in the first time steps (see investigations in Garambois et al. [2020]; Larnier et al. [2021]); the prior values of regularization parameters σ_{Q_l} correspond to inflows magnitudes.

The inferred hydrographs from inflow prior Q_{FG}^{-30} are presented in Fig. 2.13 for DenseSet (green lines) and SWOTNoiseSet observations (orange lines). Results from prior Q_{FG}^{+30} are available in 2.C. SWOTSet and SWOTNoiseSet give almost identical inferences, therefore only the SWOTNoiseSet inferences are presented. For under- and overestimated priors, the assimilation of dense and SWOT observations enables to infer the true hydrographs fairly well. RMSE ranges from 8.86 $\mathrm{m^3s^{-1}}$ at $x = 465$ km up to 578.31 $\mathrm{m^3s^{-1}}$ for the Branco tributary at $x = 657$ km. RMSE for all inferences presented in Fig. 2.13 can be found in Section 2.C. Some inferences show global under- or overestimations (e.g. $x = 216, 388, 789$ km). These biases are linked to the prior bias. Strong and numerous overlapping backwater signals may also influence flow misattribution, as discussed in the academic cases (Section 2.4) for a small scale model. As tested in numerical experiments (not shown), increasing a scalar value $\sigma_{Q_{l,d}}$ can give more effective weight to an hydrograph $Q_{l,d}$ in the inference and it can be found further away from its prior guess, which highlights the role of the covariance matrix used for regularization.

Note that temporal oscillations appear on the inferred hydrographs when using SWOTNoiseSet which is "temporally sparse" observation patterns compared to flow propagation, which is not the case of DenseSet. These oscillations are especially present in downstream inflows, which may link them to particular hydraulic responses in the BC influence zone, although they can be seen in upstream inflows as well. They tend to be prevalent in declining limbs of hydrographs (e.g. in Fig. 2.13, at 789 km, from day 120 to 300).

Note that, regardless of oscillations, inferences tend to be further from the truth in decreasing hydrographs. These oscillations are not the effect of signal misattribution, as they are present with any number of inferred hydrographs (not shown), nor are they caused by the prior's shape, as filtered priors also lead to oscillations (not shown). Instead, the oscillations seems to stem from the combination of the low observation frequency compared to the spatially distributed inflow hydrographs and the nonlinear hydraulic response. Keep in mind that we track flow information through WS elevation deformations caused by the nonlinear propagation of parameter signatures (see Subsection 2.5.3.2).

A sample illustration of those oscillations on the simulated WS elevation is presented in Fig. 2.14, at 870 km, downstream for three oscillating inferred hydrographs (at $x = 738, 754$ and 789 km). The inferred waterline from SWOTNoiseSet is compared to the truth at all simulated times and at SWOT pass times only. The misfit is logically lowest at SWOT pass times (goal of the optimization), while unobserved periods exhibit a slightly oscillating (unconstrained) misfit. Higher frequency observations, such as DenseSet, prevent this behaviors through a more complete spatio-temporal observability of the WS signatures, hence constrain the spatio-temporal parameters inference further. Some model configurations where temporal parameters are discretized at a greater time step than observation one do no exhibit such behaviors (e.g. results with DenseSet, Garambois et al. [2020]). As already shown in Brisset et al. [2018] for the identification of a single hydrograph, the identification is possible only in time windows representing the wave propagation time $T_{wave} \sim 26\,\text{days}$ in the present case, yet with multiple inflows and observation sample (see Subsection 2.5.3.2). As a consequence, outside the "identifiable time windows", the inferred values are not necessarily representing reality (see related WS misfit in Fig. 2.14). They are the optimal solution corresponding to the considered priors of the optimization problem. In practice, this means that introducing an additional regularization term j_{reg}, like $\int_0^t \frac{\partial^2 h}{\partial t^2} dt$ at observation points, would smooth (as following a spline curve) between the identifiable windows instead of the obtained oscillations. This smooth discharge curve would not be more physical than the present oscillations and we made the choice to not hide this well understood phenomena. It is a logical consequence of the disparity between the samplings of observations and parameters and does not impede interpretations of hydraulic signatures and identifiability.

Seeking to infer a control that is both temporally and spatially distributed represents a challenging assimilation problem. In the present case: (i) the observation frequency now plays a role in identifying the hydraulic signature, on top of its spatial density and resulting flow propagation: (ii) varying nonlinear flow propagation, and so WS signatures, can result in different inferences depending whether they are performed from observations of rising/declining hydrographs propagations (local $Q(Z)$ hysteresis) and (iii) indirect contributions to parameter weight in the inverse method appear, as successive hydrographs influence the whole downstream water line (established in Subsection 2.4.2), which gives greater "effective weight" to upstream hydrographs as the cause of the misfit is observed in more stations and thus accounted for multiple times in the cost function. The inferred flow variations may be compensating for errors made at upstream stations with different SWOT pass times, impacting their WS elevation either through backwater control or through the modification of the BC and its own backwater effect.

2.6.2 Spatial parameters inference

The inference of effective channel parameters is studied here considering a control vector composed of all friction coefficient values and bathymetry points. The bathymetry is composed of $I = 436$ free points (1 every 2000 m) between each of which it is obtained by linear interpolation. SWOTSet is used, with a spatial observations sampling (1 point every 200 m), i.e. 10 times greater than the sought bathymetry for observed reaches. Two inferences from hydraulically consistent priors are presented, one with the refined bathymetry b_{FG}^{-30} introduced in Subsection 2.5.3.2 (Fig. 2.15, in green) and another one with $b_{env}^{+2.6m}$, a shifted bathymetry from the $M1$ model in Subsection 2.5.2.1, in red. The 2.6 m correspond to the spatially averaged shift of b_{FG}^{-30} compared to b_{env}. $b_{env}^{+2.6m}$ does not contain a priori information on target bathymetry shape - such as a coarse DEM prior. The friction prior is K_{FG}^{-30} for both inferences.

Using b_{FG}^{-30} and $b_{env}^{+2.6m}$ as priors, the inference of channel parameters (friction and bathymetry) respectively reach a RMSE of $\left(4.362\,\text{m}^{1/3}\text{s}^{-1}, 1.231\,\text{m}\right)$ and $\left(4.762\,\text{m}^{1/3}\text{s}^{-1}, 1.913\,\text{m}\right)$. Upstream ($x = 0 - 110\,\text{km}$), irregularities appear in both inferred bathymetries and correspond to un-

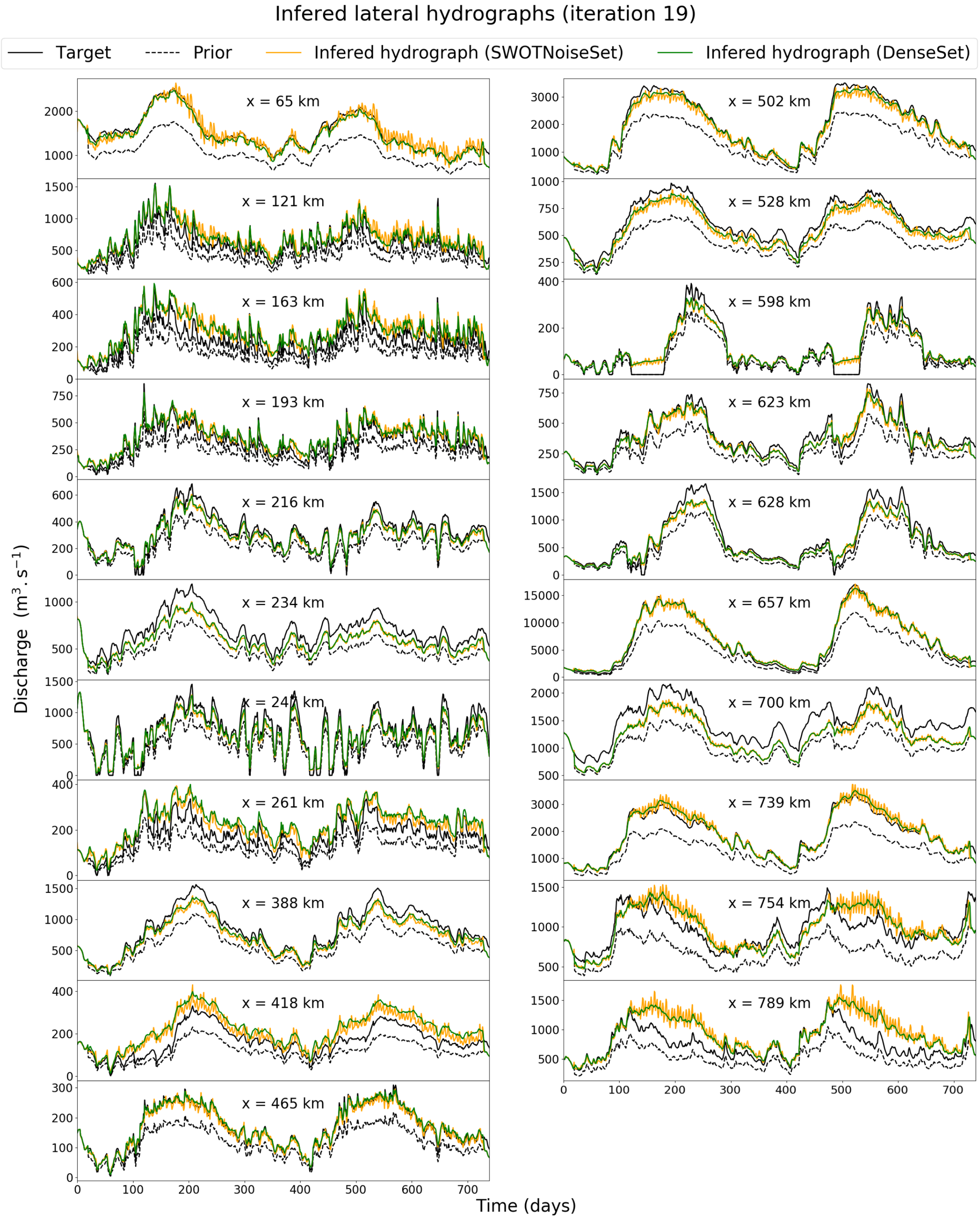

Figure 2.13: Lateral hydrographs inferences from SWOTNoiseSet and DenseSet, using the Q_{FG}^{-30} inflow prior

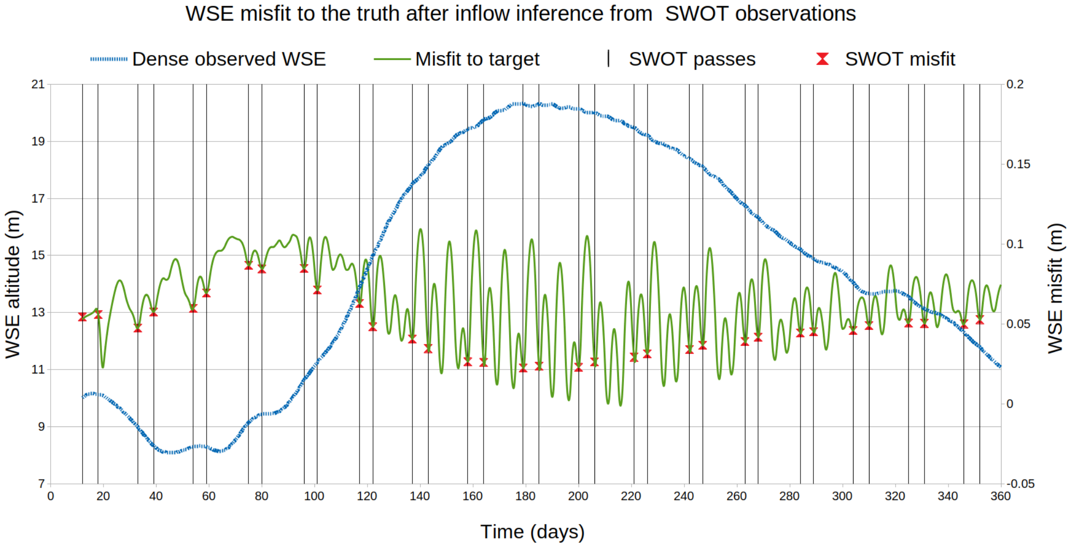

Figure 2.14: Difference between target and inferred WS elevation at 870 km, as observed by DenseSet and SWOTSet. The dotted line represents the inferred waterline inferred from SWOTSet (with Q_{FG}^{-30} as inflow prior), but observed by DenseSet. The difference between this waterline and the target waterline is the misfit to target. At SWOT pass times, the misfit is low as expected from an inference from SWOTSet. It only displays WS elevation oscillations at unobserved times.

derestimated Strickler coefficients. The high friction partially hides the hydraulic signature of the bathymetry and enables inference error inconsequential to the cost function. Downstream ($x = 600 - 870$ km), in the strong backwater control of the downstream BC, inferences tend to stay close to their prior values. Furthermore, inferences from the unrefined prior $b_{env}^{+2.6m}$ are smoother than those from the refined prior b_{FG}^{-30}. This testifies to the role of the a priori bathymetry shape knowledge contained in the prior when the WS elevation sensitivity to bathymetry is low. Strong backwater effects make the inference of channel parameters more difficult and parameter compensation appears due to the lessened sensitivity of the simulated WS (e.g. in green, at the last friction patch). The refined bathymetry prior b_{FG}^{-30} leads to inferred bathymetry and friction that are closer to the truth. It will be used in the extended control vector inferences below.

2.6.3 Inference of channel parameters and inflows

This section investigates the simultaneous inference of both unknown inflows and channel parameters on the large scale Negro river case; it combines all previously mentioned difficulties and corresponds to an ungauged configuration. In the following, the aim is to determine: 1) if SWOT data are sufficient to infer the extended control vector given unbiased prior parameters; 2) how the added spatial complexity from lateral inflows impacts spatial parameter inference. In addition, further investigations on the impact of lateral inflow prior shape, representing for example hydrological modeling uncertainty in a simple manner, are presented. The considered extended control vector is the following:

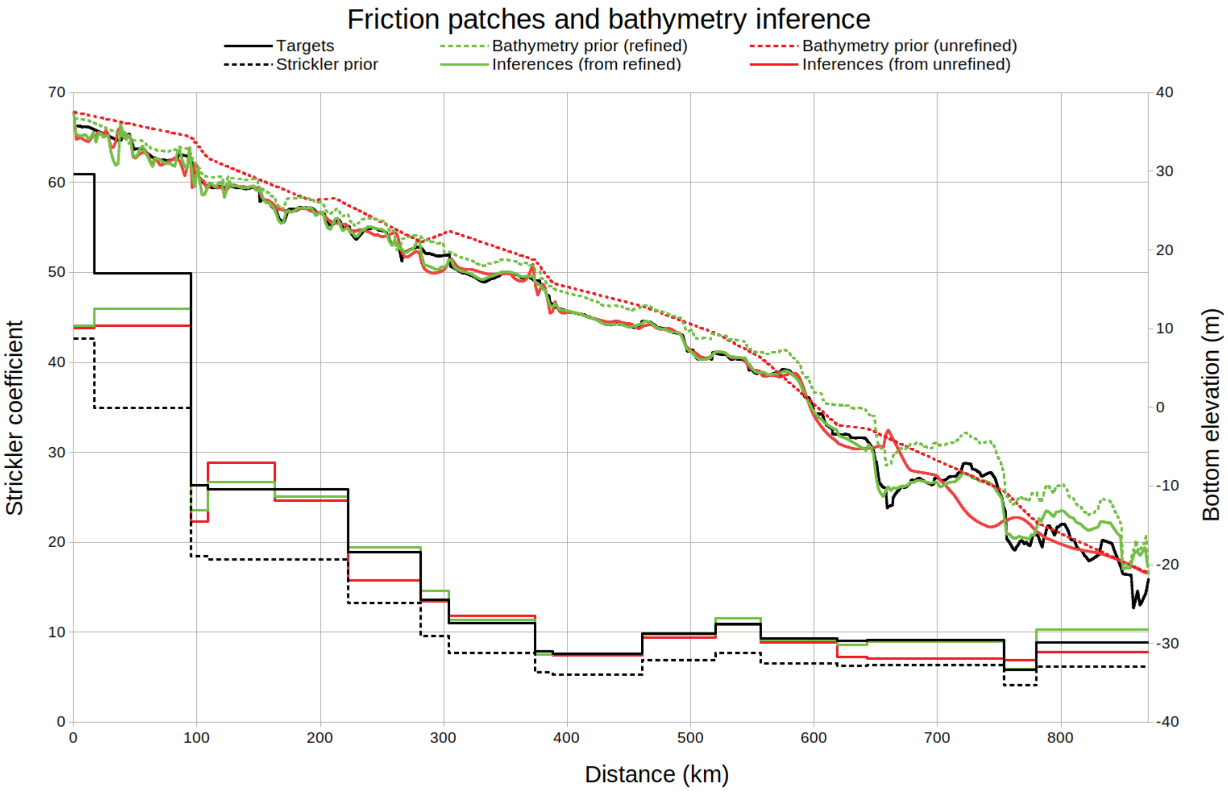

Figure 2.15: Bathymetry and friction pattern inferences using SWOTSet observability

$$c_{ext} = \left(Q_{l,x=65}\left(t\right), Q_{l,x=502}\left(t\right), Q_{l,x=657}\left(t\right), Q_{l,x=754}\left(t\right); b_1, ..., b_H; \alpha_1, ..., \alpha_N \right) \tag{2.7}$$

The inferences are performed from DenseSet and SWOTNoiseSet. The bathymetry and friction priors are b_{FG}^{-30} and K_{FG}^{-30} respectively. Four major lateral inflows located at $x = 65, 502, 657$ and 754 km (Fig. 2.12, bold dashed bars) are considered. Their reduced number facilitates the analysis of their spatial impacts. The other inflows are set to their target values. Two inflows prior types are used: Q_{FG}^{flat}, that gives no a priori on hydrograph shapes and Q_{FG}^{filter}, hydrographs obtained by applying a 80 days moving average filter to the true hydrographs. Prior flow values in Q_{FG}^{flat} are set to the target flow values from the first time step up to 120 days for the sake of initial hydraulic consistency. Inferences of all parameters for these inflow priors are presented in Fig. 2.16 and Fig. 2.17. The inferred control vectors are referred to as c^*_{flat} and c^*_{filter}. Inferred parameter scores can be found in Tab. 2.6.

Inferred spatial parameters patterns are similar to those obtained previously without unknown inflows in Subsection 2.6.2. c^*_{flat} features a fair bathymetry fit downstream ($x = 600 -$ 870 km) while c^*_{filter} stays close to the prior value. This may be due to the different range of the simulated hydraulic responses in the first iterations: using Q_{FG}^{flat} leads to an increase in WS elevation sensibility to bathymetry. Upstream ($x = 0 - 110$ km), increased bathymetry irregularities in c^*_{flat} are linked to the erroneous prior Q_{FG}^{flat} leading to bathymetry errors in the first iterations, coupled with lower inferred Strickler coefficients, hence a lessened impact of bathymetry on the water surface and the inability to correct the “initial” errors.

In terms of temporal behaviors, both priors give fair estimates of HCs for DenseSet. Inferences from SWOTNoiseSet are close to those from DenseSet with the presence of oscillations and the rising part of hydrographs are better fitted than decreasing ones, as observed in Subsection 2.6.1. In both c^*_{filter} and c^*_{flat} and for both observation sets, a correlation between sought inflows at $x = 502$; 657 and 754 km appears. The Branco river flow, at $x = 657$ km, is better inferred and its well fitted peaks are also found in the two smaller rivers (e.g. at 520 days), which are in its upstream and downstream influences zones (see Fig. 2.12, left). In all inferences, the total flow at the downstream BC closely matches that of the truth, which means that only hydraulic signature is misattributed across the 4 inferred temporal parameters, not on the total flow. In c^*_{filter}, more accurate inferences are obtained, with a smaller influence of the Branco river on other inflows in its influence zone and more accurate inference of small scale behaviors. The filtered prior Q_{FG}^{filter} introduces information on low frequency behaviors of the sought inflows, helping the assimilation process to converge to correct the target inflows. This configuration allows for a better fit of small scale variation in the controls.

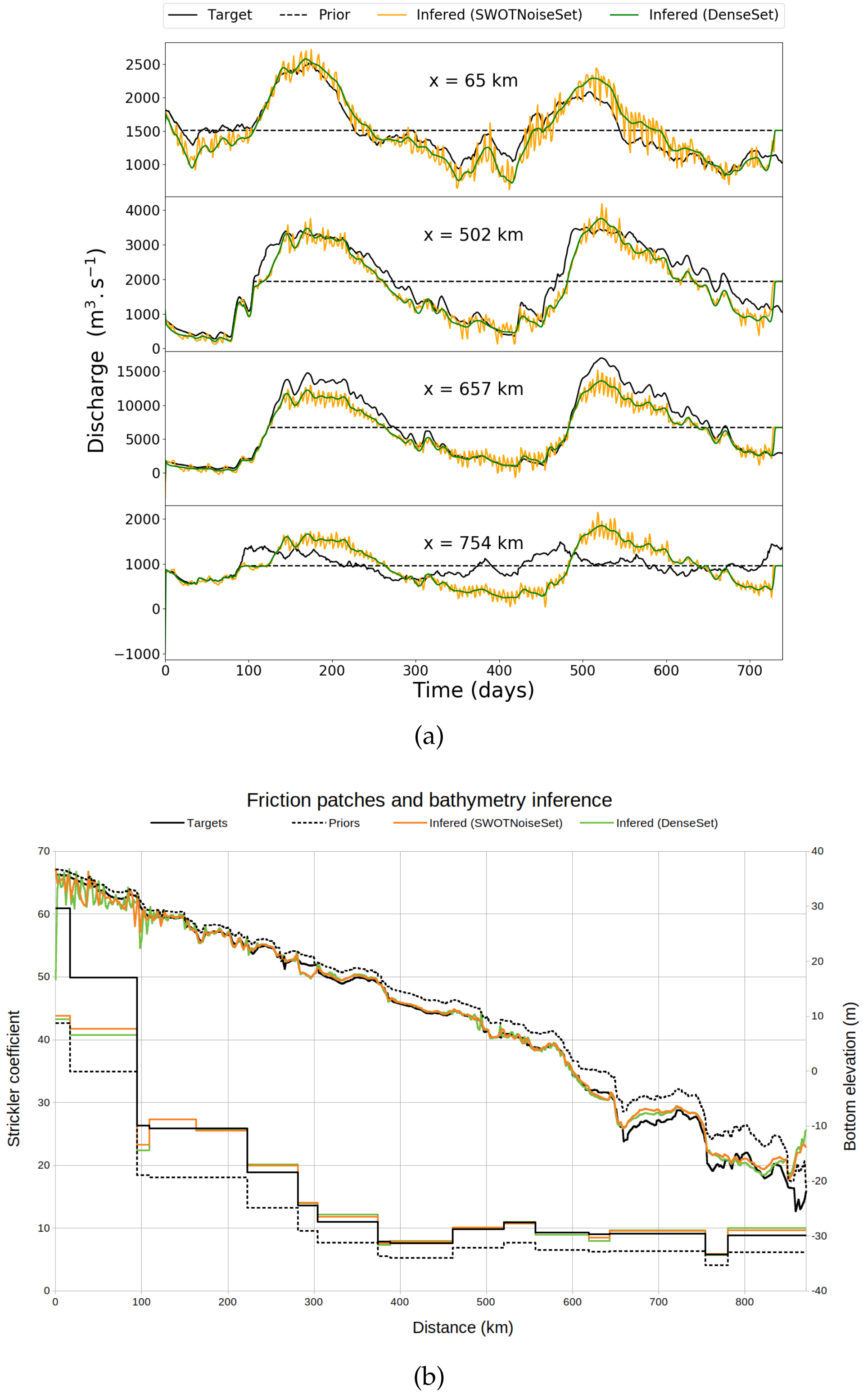

(a)

(b)

Figure 2.16: Inflow, bathymetry and friction patch inferences from SWOT synthetic data: c^*_{flat}, inferred control vector without a priori hydraulic behavior

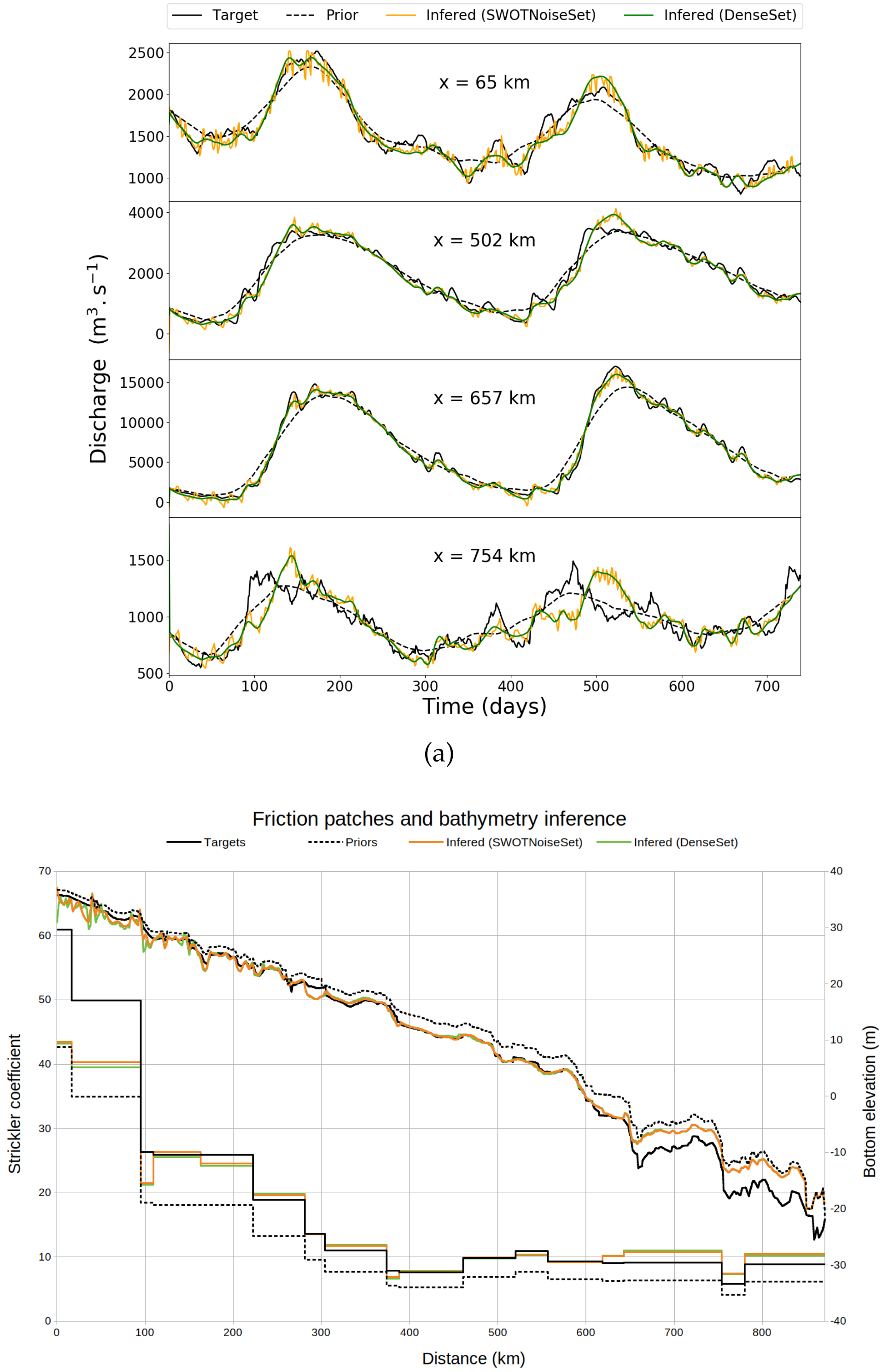

(a)

(b)

Figure 2.17: Inflow, bathymetry and friction patch inferences from SWOT synthetic data : c^*_{filter}, inferred control vector with a priori hydraulic behavior

Obs set	Prior	$RMSE\ [m^3/s]$ $(rRMSE\ [-])$				Nash-Sutcliffe			
		65 km	502 km	657 km	754 km	65 km	502 km	657 km	754 km
DenseSet	Q_{FG}^{flat}	189 (0.12)	329 (0.17)	1472 (0.22)	430 (0.45)	0.84	0.90	0.87	0.10
NoiseSWOTSet		209 (0.14)	360 (0.18)	1719 (0.26)	421 (0.44)	0.81	0.88	0.82	0.10
DenseSet	Q_{FG}^{filter}	101 (0.07)	195 (0.10)	412 (0.06)	158 (0.17)	0.94	0.97	0.99	0.49
NoiseSWOTSet		102 (0.07)	208 (0.11)	503 (0.07)	154 (0.16)	0.94	0.96	0.99	0.51

(a) Hydrograph scores

Obs set	Prior	$RMSE_\alpha$ $[\mathrm{m}^{1/3}/\mathrm{s}]$	$RMSE_b$ $[\mathrm{m}]$
DenseSet	Q_{FG}^{flat}	5.35	1.89
NoiseSWOTSet		5.12	1.64
DenseSet	Q_{FG}^{filter}	5.30	2.06
NoiseSWOTSet		5.13	1.99

(b) Channel parameters scores

Table 2.6: Inferred parameter scores for extended control inferences

2.7 Conclusion

This paper investigated the inference of river channel parameters and multiple inflows from water surface signatures in the context of satellite altimetry with the forthcoming SWOT mission and using water extents from optical data as well. The HiVDI inverse method presented in Larnier et al. [2021], based on the 1D Saint-Venant equations and a variational assimilation scheme adapted to account for lateral inflows (mass and momentum injections). Given hydraulically consistent prior guesses and regularization weights, it is successfully applied to synthetic test cases and a long reach of the anabranching Negro river in the Amazon basin using multi-satellite data.

Through low Froude synthetic cases, it is shown that the signature of a lateral inflow is visible downstream from the inflow point through the total flow signature and can be visible upstream in case of downstream control at the injection. Following this analysis and using the HiVDI variational assimilation method (global in time and space), a study of the minimum spatial density of water surface observations necessary to infer lateral inflows from their hydraulic signatures is carried out. Synthetic twin experiments yield the following results: (i) given high observation temporal frequency relative to model hydraulic response, perfect inflows inferences can be obtained; (ii) to correctly attribute signatures between multiple lateral inflows, a minimum of 1 observation point between each injection cell is necessary; (iii) when simultaneously inferring inflows and/or channel parameters, a sensitivity to parameter weights (see Section 2.A) appears; (iv) given a priori parameter weights, accurate inferences of inflows and channel parameters is achievable even with the minimum spatial observability.

A method for building effective river models in coherence with multi-satellite data and including realistic spatial variations is introduced based on multi-source data of water surface elevation, width and slopes. This method makes use of (i) multi-mission altimetric rating curves (see Paris et al. [2016]) or equivalently a distributed hydrological model and altimetry data and (ii) water surface width like those from current databases (see Allen and Pavelsky [2018]); it should be applicable to rivers from the future SWOT database. It is applied here to build a simple effective 1D model of the Negro river upstream from its confluence with the Solimões river. It fits currently available satellite water surfaces signatures and contains real-like spatial variabilities and flood wave propagation features.

The inference capabilities of spatially distributed channel parameters and inflows from synthetic SWOT observations are highlighted on the Negro river case given hydraulically coherent priors. The inference of temporal parameters in the form of 21 spatially distributed lateral inflow hydrographs leads to accurate estimates and low water surface misfit at observation times. High frequency observations give good inferences, with an expected sensitivity to both prior bias (see Garambois et al. [2020]; Larnier et al. [2021]) and prior shape.

SWOT-like observations lead to comparable inferences, with slight oscillations due to the frequential disparity between observations temporal controls combined to their spatial distribution and the resulting nonlinear flow propagation on the domain, as analyzed with identifiability maps. Those oscillations related to model-observations time scales could be overcome by introducing additional regularizations - not done here for the sake of hydraulic analysis. Inference of purely spatial parameters (bathymetry/friction) were carried out as well, leading to some complementary remarks: (i) channel parameters equifinality is most present in the downstream part of the model, where the waterline is influenced by the strong backwater effect of the boundary condition (Solimões river) which diminishes water surface sensitivity to other parameters; (ii) bathymetry prior shape influences the inferred bathymetry. Finally, simultaneous inference of channel parameters and spatially distributed inflows was achieved with satisfying accuracy. We show that, with the present method, large scale temporal parameter variations can be found from synthetic SWOT observations even without a priori knowledge of the shape of the hydrological response, but that small scale variations can be better inferred with a priori hydrograph shape knowledge.

Recall that the estimation of discharges and channel parameters from (SWOT) WS observations is a difficult inverse problem because of the correlated influence of flow controls on the observable water surface signatures - non uniqueness/equifinality issues. It is therefore necessary to use hydraulically consistent priors as investigated in Tuozzolo et al. [2019]; Garambois et al. [2020]; Larnier et al. [2021] with HiVDI method that contains low complexity flow relations for deriving robust prior guesses from databases and hydrological models, or even in situ depth/discharge data when available (see Larnier et al. [2021]) - not the scope of this paper. As already discussed in Larnier et al. [2021], the VDA solution depends on the priors which are the first guess value and the covariances matrices. Ongoing research efforts in the SWOT community, in view of global discharge estimates, focus on the determination of priors through the construction of a SWOT a priori database based on Andreadis et al. [2013]; Allen and Pavelsky [2018] and global/regional model outputs (see Durand et al. [2016]; Larnier et al. [2021]), constrained with available in situ gauge measurements. Note that a priori estimations/databases could be enriched or reprocessed during or after the SWOT mission lifetime and HiVDI would enable to refining discharge estimates (see Larnier et al. [2021]). Moreover, as shown in Larnier and Monnier [2020], priors obtained by deep learning can greatly improve global estimation.

More generally, reaching unbiased estimates of discharge, from downstream to upstream of river networks with varying densities of in situ discharge data hence ungauged river portions/basins, is a crucial challenge in hydrology that could benefit from the fusion of complementary in situ and remotely sensed data in integrated models. The present study brings insight in lateral inflows inference from hydraulic signatures and paves the way for further research on integrated hydraulic-hydrological assimilation chains for river networks and in coherence with multi-satellites observables (of local hydrodynamic signatures) to benefit from them in a regionalization perspective.

Searching for distributed channel parameters and inflows given temporally sparse SWOT data and a global assimilation method brings the issue of signal attribution to the forefront, especially at the scale of a river network. Further research should focus on tributaries that could be amenable to the use of SWOT and multi-satellite observations to better constrain estimates of lateral inflows and next distributed fluxes on network models considering hydraulic-hydrological couplings. The introduction of pertinent signatures, scales and constrains in the forward-inverse models (e.g. forward operators, covariance matrices, cost function terms) should help maximizing the use of various information sources and enable smooth discharge estimates and better signal attribution, given uneven and heterogeneous satellite data in combination with other complementary databases/knowledge. This could help leveraging better inferences of hydrological responses and flow structure within a river basin and eventually enable information feedback to rainfall-runoff modules and ultimately regionalization issues.

2.A The computational inverse method

The computational inverse method is based on Variational Data Assimilation (VDA) applied to the 1D Saint-Venant model (Eq. (2.1)). The computational inverse method is the one presented in Brisset et al. [2018]; Larnier et al. [2021] with an augmented composite control vector c (Eq. (2.4)): c contains a spatially distributed friction coefficient enabling to model complex flow zones (while it is an uniform friction law $K(h)$ in Larnier et al. [2021]). This definition of $K(x,h)$ enables to consider more heterogeneous bathymetry controls. c also contains lateral flow hydrographs $Q_{l,d}(t)\,,\, d \in [1..N_d]$ to deal with in/off-takes due to tributaries or underground flows. It is important to point out that the imposed downstream BC is an unknown of the inverse problem. It is constrained with the observed water elevations and inferred river bottom slope using a locally uniform flow hypothesis (i.e. Manning equation, see Subsection 2.3.1) - except in the last real case above. The cost function $j(c)$ is defined as:

$$j(c) = j_{obs}(c) + \gamma\, j_{reg}(c) \tag{2.8}$$

where $\gamma > 0$ is a weighting coefficient of the so-called "regularization term" $j_{reg}(c)$. The term $j_{obs}(c)$ measures the misfit between observed and modeled WS elevations such that:

$$j_{obs}(c) = \frac{1}{2}\,\|(Z(c) - Z_{obs})\|^2_{\mathcal{O}} \tag{2.9}$$

The norm $\|\cdot\|_{\mathcal{O}} = \|\mathcal{O}^{1/2}\cdot\|_2$ is defined from an a priori positive definite covariance matrix $\mathcal{O}$. Assuming uncorrelated observations $\mathcal{O} = diag(\sigma_Z)$. The modeled WS elevations Z depend on c

through the hydrodynamic model (Eq. (2.3.1)) and the inverse problem reads as

$$c^* = \mathrm{argmin}_c \, \mathrm{j}\left(c\right) \tag{2.10}$$

This optimal control problem is solved using a Quasi-Newton descent algorithm: the L-BFGS algorithm version presented in Gilbert and Lemaréchal [1989]. The cost gradient $\nabla j\left(c\right)$ is computed by solving the adjoint model; the latter is obtained by automatic differentiation using Tapenade software Hascoet and Pascual [2013]. Detailed know-hows on VDA may be found e.g. in the online courses Bouttier and Courtier [2002]; Monnier [2021].

To be solved efficiently this optimization problem needs to be "regularized". Indeed the friction and the bathymetry may trigger indiscernible surface signatures therefore leading to an ill-posed inverse problem; we refer e.g. to Kaltenbacher et al. [2008] for the theory of regularization of such inverse problems and to Larnier et al. [2021] for a discussion focused on the present inverse flow problem.

Following Larnier et al. [2021], the optimization problem (Eq. (2.10)) is regularized as follows. First the regularization term j_{reg} is added to the cost function (Eq. (2.8)). We simply set: $j_{reg}\left(c\right) = \frac{1}{2}\left\|b''\left(x\right)\right\|_2^2$. Therefore this term imposes (as weak constraints) the inferred bathymetry profile $b\left(x\right)$ to be an elastic interpolating the values of b at the control points (i.e. a cubic spline).

A specificity of the present context is the large inconsistency between the large observation grid (altimetry points) and the finer model grid. Between the sparse observations points (equivalently the control points), the bathymetry profile $b\left(x\right)$ is reconstructed as a piece-wise linear function. It is worth to point out that the resulting reconstruction is consistent with the physical analysis presented in Montazem et al. [2017]; Montazem [2018]. This study analyses the adequacy between the SW model (Eq. (2.3.1)) behavior and the WS signature.

Next and following Lorenc et al. [2000]; Weaver and Courtier [2001]; Larnier et al. [2021], the following change of control variable is made:

$$k = B^{-1/2}\left(\mathrm{c} - \mathrm{c}_{prior}\right) \tag{2.11}$$

where c is the original control vector, c_{prior} is a prior value of c and B is a covariance matrix. The choice of B is crucial in the VDA formulation; its expression is detailed below. After this change of variable the new optimization problem reads:

$$\min_k \mathrm{J}\left(k\right) \text{ with } \mathrm{J}\left(k\right) = j\left(c\right) \tag{2.12}$$

It is easy to show that this leads to the following new optimality condition: $B^{1/2}\nabla j\left(c\right) = 0$; somehow a preconditioned optimality condition. For more details and explanations we refer to Haben et al. [2011a,b] and Larnier et al. [2021] in the present inversion context.

Assuming uncorrelated controls the matrix B is defined as block diagonal such that $B = \mathrm{diag}\left(\mathrm{B_Q}, \mathrm{B_{Ql,1}}, \ldots, \mathrm{B_{Ql,D}}, \mathrm{B_b}, \mathrm{B_{ff}}, \mathrm{B_{fi}}\right)$. Still following Larnier et al. [2021], the covariance matrices B_Q, B_{Q_l} and B_b are set as the classical second order auto-regressive correlation matrices:

$$\left(B_Q\right)_{i,j} = \left(\sigma_Q\right)^2 \exp\left(-\frac{\left|t_j - t_i\right|}{\Delta t_Q}\right), \left(B_{Q_{l,d}}\right)_{i,j} = \left(\sigma_{Q_l}\right)^2 \exp\left(-\frac{\left|t_j - t_i\right|}{\Delta t_Q}\right) \text{ and } \left(B_b\right)_{i,j} = \left(\sigma_b\right)^2 \exp\left(-\frac{\left|x_j - x_i\right|}{L_b}\right) \tag{2.13}$$

The VDA parameters Δt_Q and L_b represent prior hydraulic scales and act as correlation lengths. We refer to Brisset et al. [2018] for a thorough analysis of the discharge inference in terms of frequencies and wave lengths and Larnier et al. [2021] in the present river-observation context. In the present study, the friction parameters applied to deca-kilometric patches are assumed to be uncorrelated thus the matrices B_α and B_β are diagonal:

$$\left(B_\alpha\right)_{i,i} = \left(\sigma_\alpha\right)^2, \left(B_\beta\right)_{i,i} = \left(\sigma_\beta\right)^2 \tag{2.14}$$

The scalar values $\sigma_\square$ may be viewed as variances ; their values are given in the numerical results section.

Finally, in a noised observation context and to avoid over-fitting noisy data, we denote by δ the noise level such that $\|Z_{obs} - Z_{true}\|^2 \leq \delta$ with Z_{obs} the observed and Z_{true} the true WS elevation profiles. A common technique to avoid over-fitting noisy data, in the context of Tykhonov's regularization of ill-posed problems, is Morozov's discrepancy principle, (see e.g. Kaltenbacher et al. [2008] and references therein): the regularization parameter γ (see Eq. (2.8)) is chosen a posteriori such that j does not decrease below the noise level.

2.B Extended friction calibration results for the Negro river

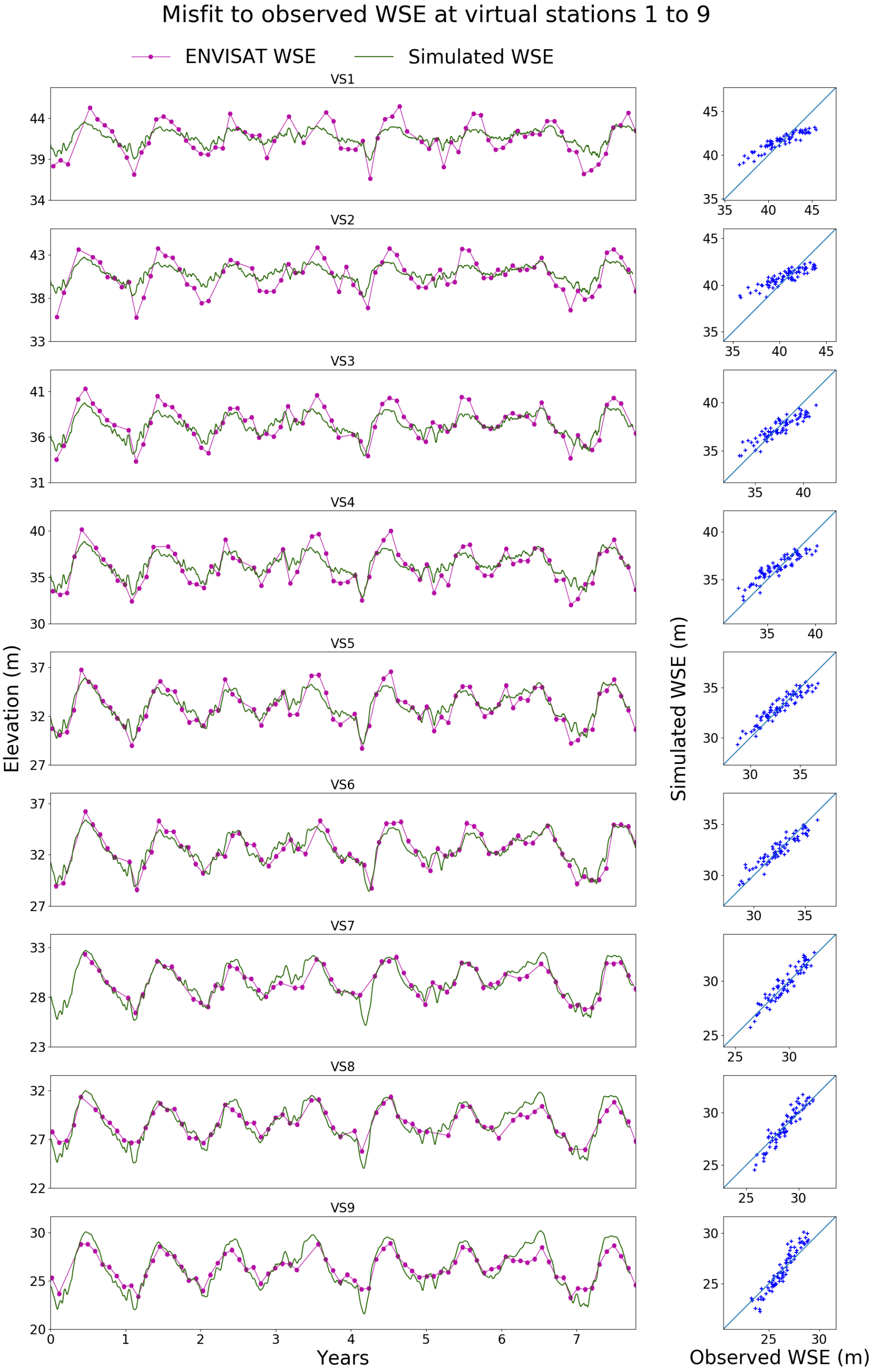

(a)

Figure 2.18: Envisat WS elevation misfit after friction calibration at all stations for *M2a* (1)

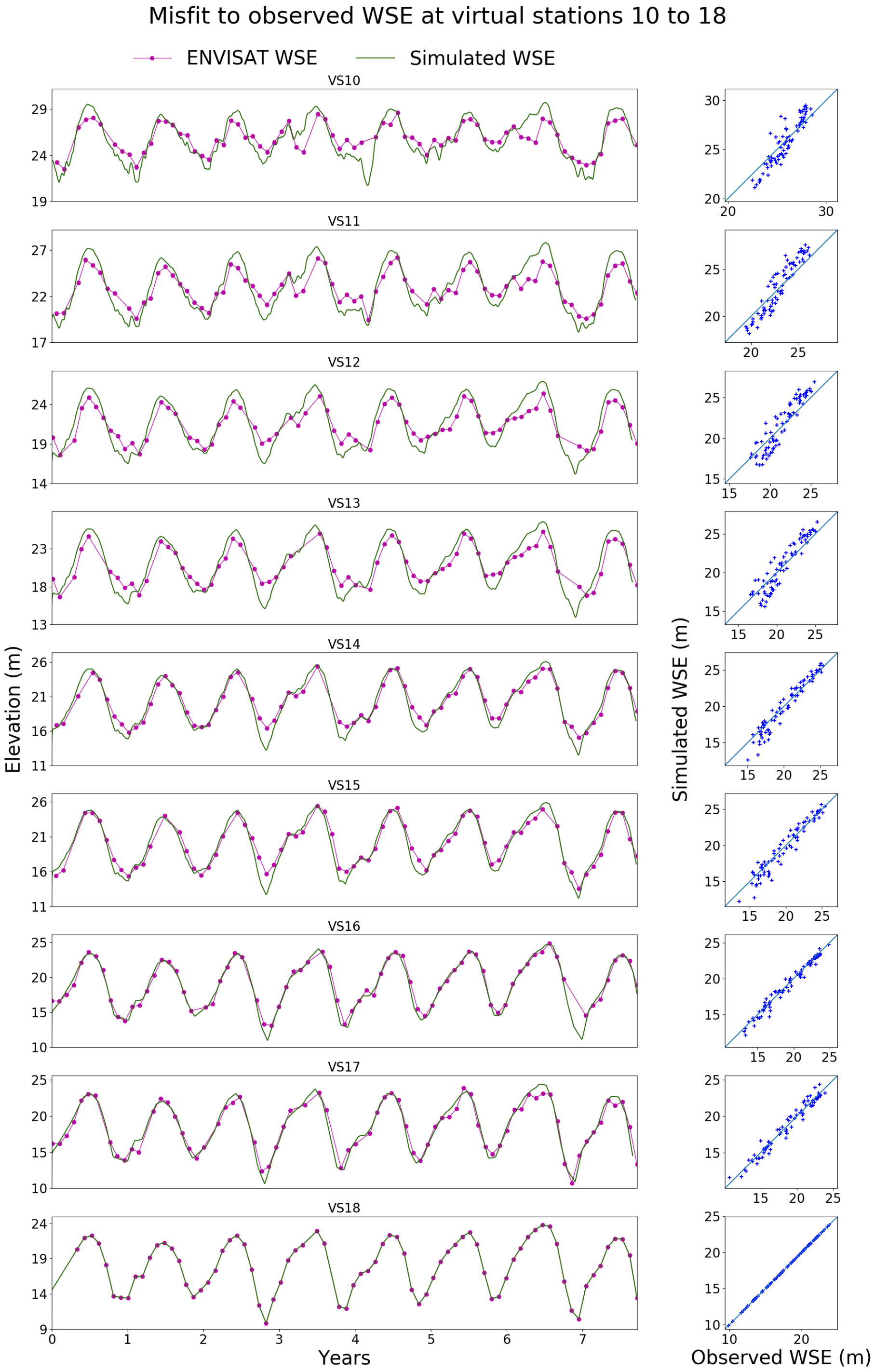

(b)

Figure 2.18: Envisat WS elevation misfit after friction calibration at all stations for *M2a* (2)

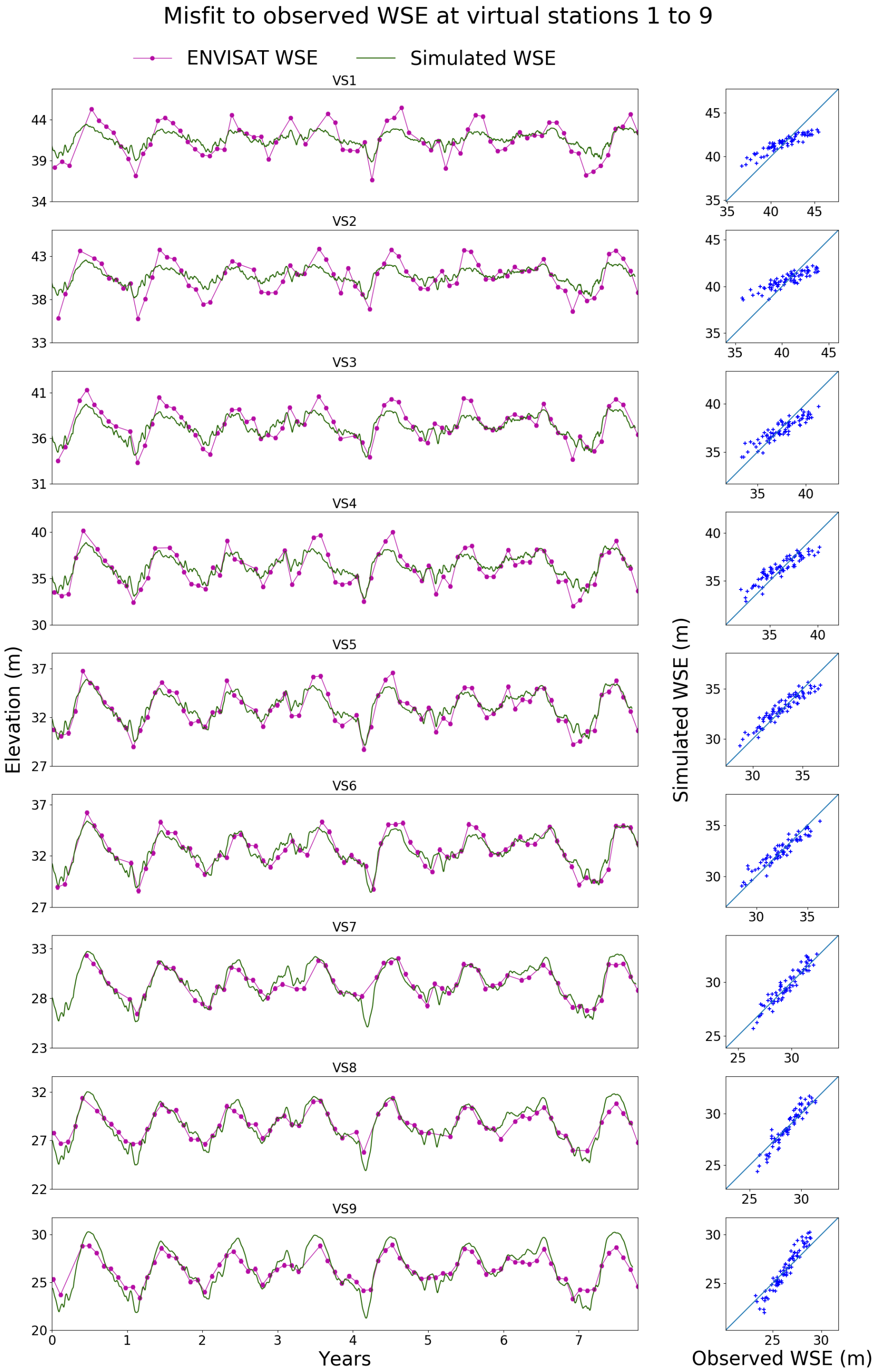

(c)

Figure 2.19: Envisat WS elevation misfit after friction calibration at all stations for *M2b* (1)

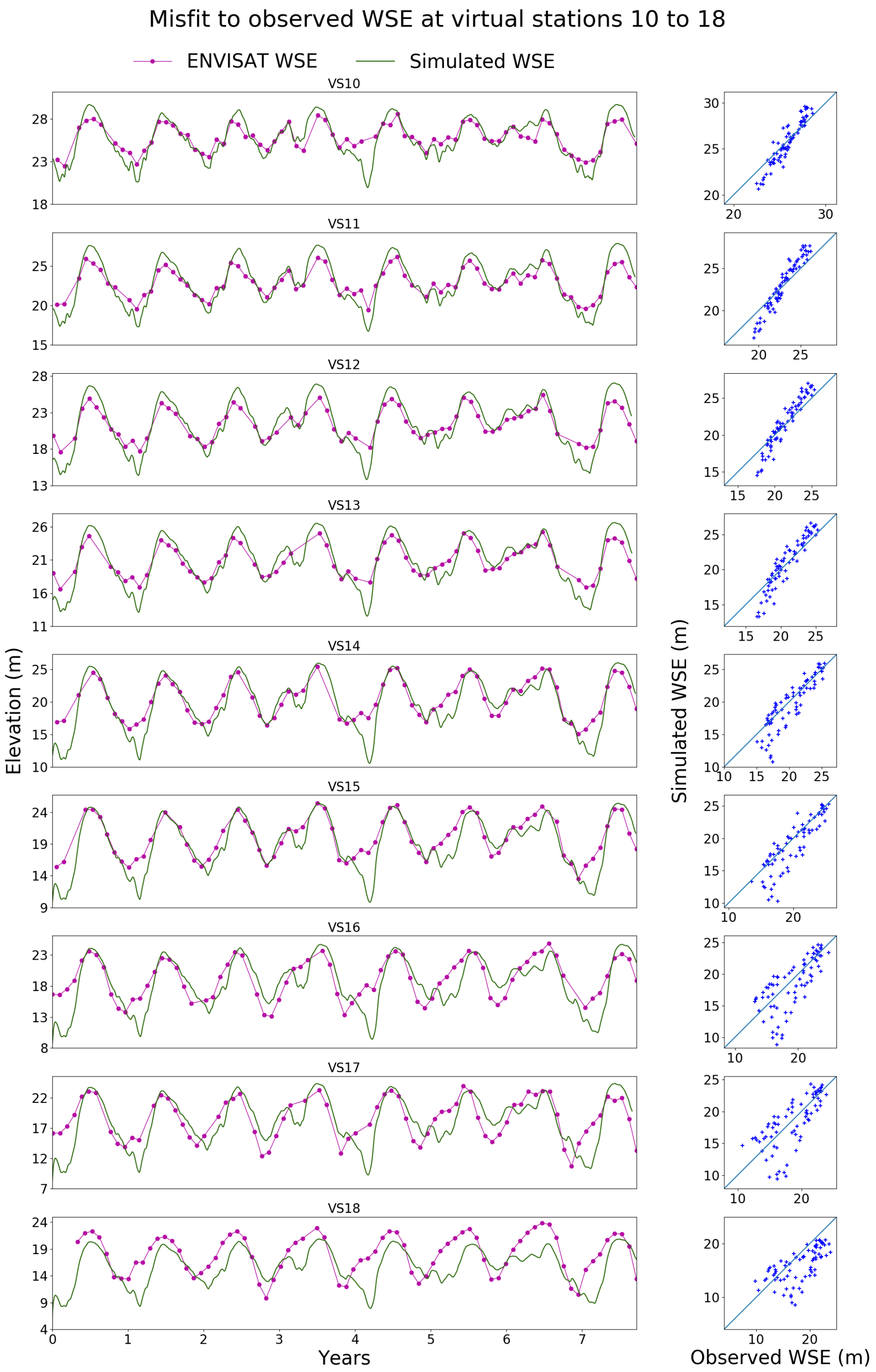

(d)

Figure 2.19: Envisat WS elevation misfit after friction calibration at all stations for *M2b* (2)

2.C Additional graphs and RMSE for lateral hydrograph inferences on the Negro river

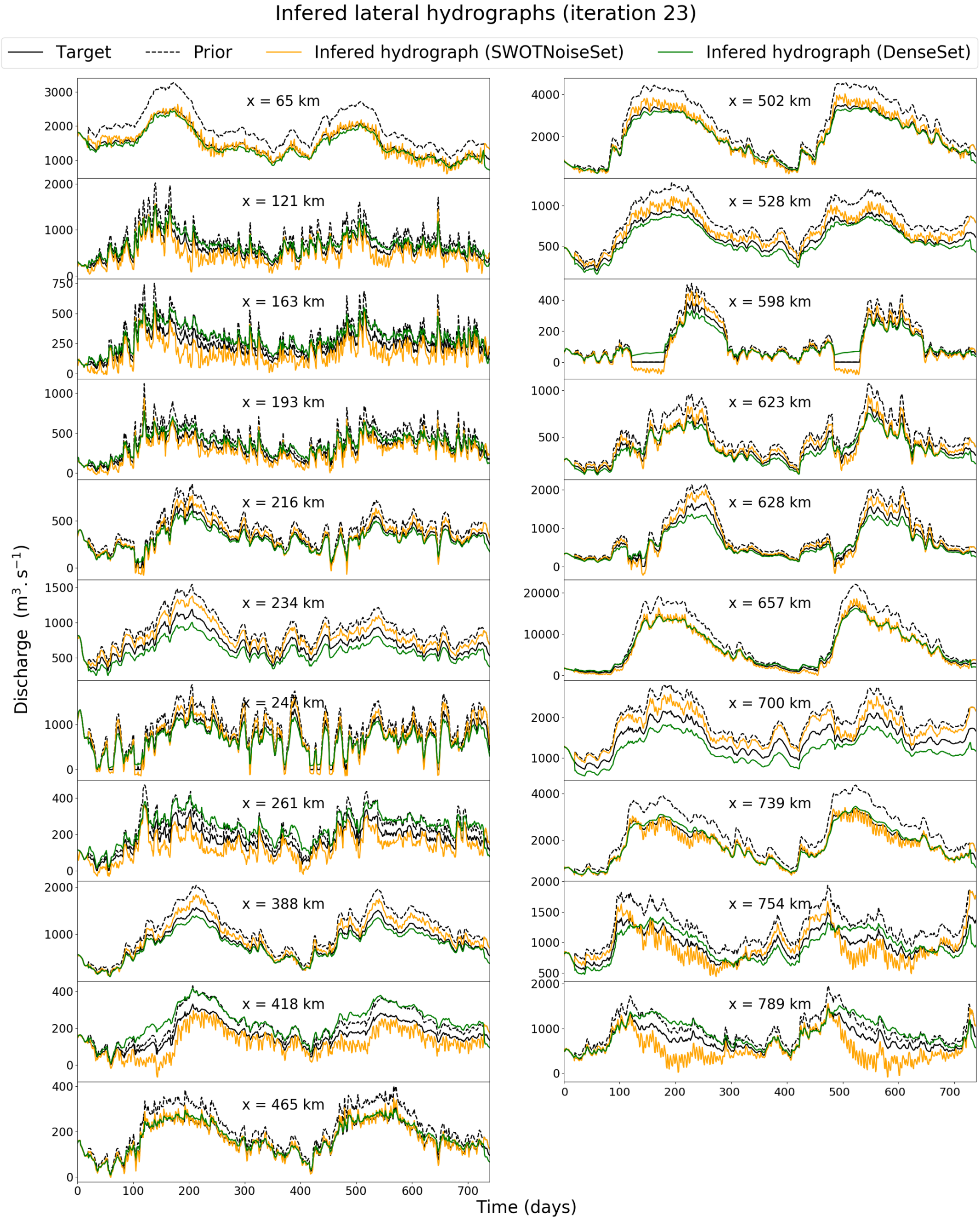

Figure 2.20: Lateral hydrograph inferences from SWOTNoiseSet and DenseSet, using the Q_{FG}^{+30} inflow prior

x [km]	μ [d]	σ $[\mathrm{m}^3/\mathrm{s}]$	DenseSet RMSE $[\mathrm{m}^3/\mathrm{s}]$	SWOTNoiseSet RMSE $[\mathrm{m}^3/\mathrm{s}]$
65	1	2500	79.62	122.34
121		1500	97.74	134.59
163		1000	64.17	70.44
193		1000	49.06	50.75
216		700	37.04	41.48
234		800	112.76	120.43
247		1000	89.82	105.24
261		800	56.57	45.62
388		1000	98.30	125.94
418		800	60.64	49.12
465		600	8.86	12.64
502		2000	116.21	194.86
528		1000	66.85	83.55
598		600	28.69	29.08
623		1000	40.75	44.83
628		1200	119.85	126.13
657		5000	421.26	578.31
700		1500	263.07	264.27
739		2800	127.97	173.35
754		2000	140.89	158.19
789		2400	249.73	283.92

(a) With prior Q_{FG}^{-30}

x [km]	μ [d]	σ $[\mathrm{m}^3/\mathrm{s}]$	DenseSet RMSE $[\mathrm{m}^3/\mathrm{s}]$	SWOTNoiseSet RMSE $[\mathrm{m}^3/\mathrm{s}]$
65	1	2500	134.66	156.34
121		1500	142.70	138.31
163		1000	69.46	66.83
193		1000	45.66	43.47
216		700	45.31	47.28
234		800	128.18	130.98
247		1000	122.21	125.72
261		800	35.82	33.85
388		1000	146.13	149.39
418		800	33.81	32.22
465		600	13.53	15.37
502		2000	212.87	235.58
528		1000	87.67	91.96
598		600	28.62	28.85
623		1000	39.51	43.31
628		1200	123.45	126.71
657		5000	581.03	775.15
700		1500	250.54	256.81
739		2800	157.54	194.14
754		2000	147.88	154.01
789		2400	293.07	297.37

(b) With prior Q_{FG}^{+30}

Table 2.7: Inferred lateral inflows parameter weights and RMSE

2.D Technical specifications

Host bridge: Intel Corporation 8th Gen Core Processor Host Bridge/DRAM Registers
PCI bridge: Intel Corporation Xeon E3-1200 v5/E3-1500 v5/6th Gen Core Processor PCIe Controller
Memory: 2x16Gb SODIMM DDR4 Synchronous 2667 MHz (0.4 ns)
Resolution mode: sequential
Resolution method: implicit-explicit Preissmann scheme
Sample run: inference of the full triplet on the Negro model (inferred control vector c^*_{filter} in Subsection 2.6.3)

- Control vector components: 4×740 flow points, 436 bathymetry points, 17 friction patches (3413 total sought values)
- Total run time (direct): under 15 min
- Total run time (inverse): 20.8 h
- Number of iterations: 35
- Average iteration time length: 35.8 min

Chapter 3

Multi-dimensional modeling of basin-networks

Contents

This chapter is based on Pujol et al. [2022]. The article's content is featured with minor layout adjustments.

3.1 Extended abstract

This chapter presents a novel multi-dimensional (multi-D) hydraulic-hydrological model intended to allow modeling of large and complex river network at the appropriate scales and at a low computational cost, see Fig. 3.1. In turn, this would allow exploring synergies between spatially distributed flow models and datasets over large domains, combining in situ observations with high-resolution hydro-meteorology and satellite data.

The multi-D hydraulic model consists in the 2D shallow water equations (Eq. 1.6) solved with a single finite volume solver (see Subsection 1.2.2). 1Dlike reaches are built through meshing methods that cause the 2D solver to generate into 1D (see Fig. 3.2). They are connected to 2D portions that act as local zooms, for modeling complex flow zones such as floodplains and confluences, via 1Dlike-2D interfaces (see Fig. 3.3). An existing parsimonious hydrological model, GR4H, is implemented and coupled to the hydraulic model. These developments are carried out within the DassFlow variational data assimilation framework. The adjoint of the whole tool chain is obtained by automatic code differentiation. The forward-inverse multi-D computational model is successfully validated on academic and real cases of increasing complexity. Assimilating multiple observations of flow signatures leads to accurate inferences of multi-variate and spatially distributed parameters among bathymetry-friction, upstream/lateral hydrographs, and hydrological model parameters. This notably demonstrates the possibility for information feedback towards upstream hydrological catchments, that is backward hydrology. A 1Dlike model of part of the Garonne river is built and accurately reproduces flow lines and propagations of a 2D reference model. A multi-D model of the complex Adour basin network, inflowed by the semi-distributed hydrological model, is built. High resolution flow simulations are obtained on a large domain, including fine zooms on floodplains, with a relatively low computational cost since the network contains mostly 1Dlike reaches. The current work constitutes an upgrade of the Dassflow computational platform. The source code and synthetic cases are open source and available upon request[1].

Section 3.3 presents the multi-D modeling approach, the flow model and integrated hydrological module and the inverse computational method. Section 3.4 presents the validation of the 1Dlike modeling strategy using academic and real case and investigation of the VDA capabilities of the integrated hydraulic-hydrological tool chain. Inferences of hydrological parameters are carried out on an academic confluence case. Inferences of channel parameters are carried out on the 1Dlike model of the Garonne river. Inferences of upstream hydrographs are carried out on the 1Dlike model of the Adour river network. The initial article conclusion is featured in Section 3.5.

---

[1] http://www.math.univ-toulouse.fr/DassFlow

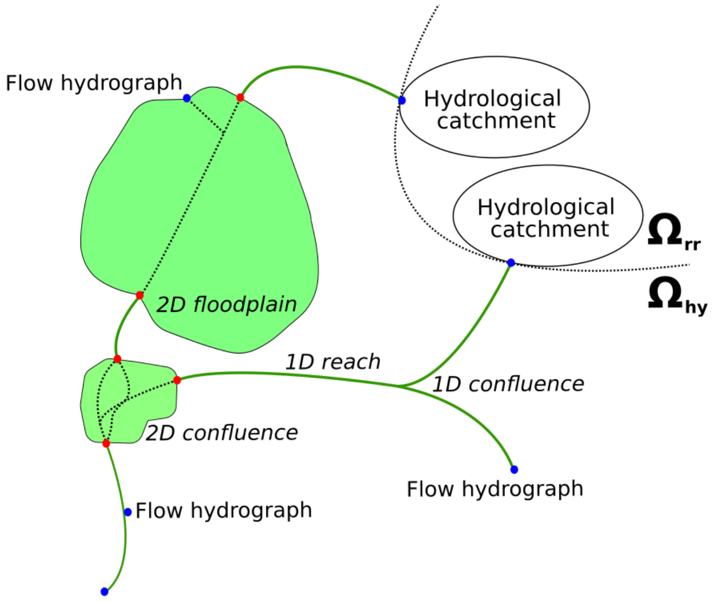

Figure 3.1: Conceptual meshing approach for integrated hydraulic-hydrological and multi-dimensional modeling of a river network. The computational domain Ω is composed of the hydrological domain Ω_{rr} connected to the hydraulic domain Ω_{hy}. Ω_{hy} contains 1Dlike meshes and classical 2D meshes, interfaced frontally at the red points. Inflows injected in Ω_{hy} (blue points) can come from classic inflowing methods or from the coupling to hydrological catchments from Ω_{rr}.

Figure 3.2: 1Dlike mesh (quadrangular cells linked in a chain, black) overlaid on top of a simulated water extent (water depth heatmap) from a 2D reference model of the Garonne river (see Subsection 3.4.3.1). The bankfull water extent is used to set lateral 1Dlike cell edges at the banks (DEM data was also used to determine bank placements, see Subsection 3.4.3.2). Out-of-bank flows are not modeled in the 1Dlike model.

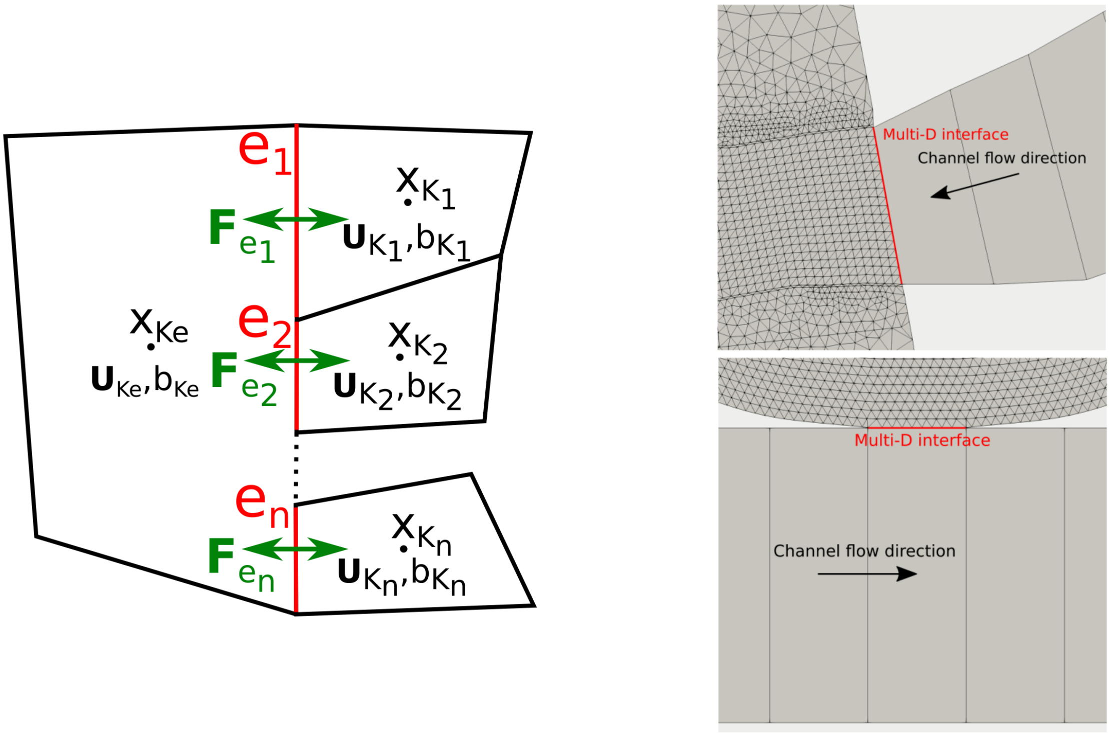

Figure 3.3: 1D2D interface implementation.
Left: Interfacing of the cell x_{Ke}, part of a 1Dlike mesh, to cells $x_{K,i}$, $i \in [1,n]$. Flows are calculated using an adapted 2D solver at each e_i, $i \in [1,n]$ interface. The flux over the 1Dlike edge e is given by $\mathbf{F}_e = \sum\limits_{i=1..n} m_{e_i} \mathbf{F}_{e_i} \left(\mathbf{U}^n_{K,i}, \mathbf{U}^n_{K_e}, \mathbf{n}_{e_i,K} \right)$.
Right: Example of multi-D interfaces. At the top, a "frontal" interfacing of a 1Dlike network to the channel part of a 2D mesh, featured in the Adour network model (see Subsection 3.4.3.2). At the bottom, an academic "lateral" interfacing of a 1Dlike river channel to a 2D floodplain. Both interface are numerically identical, but may be used for different purposes.

3.2 Introduction

The accurate estimation of storage and fluxes in surface hydrology is an essential scientific question linked to major socio-economic issues in floods and droughts forecasting, particularly with regards to the ongoing climate change and potential intensification of the water cycle and hydrological hazard (Masson-Delmotte et al. [2018]; Iturbide et al. [2020]). In this context, advanced numerical modeling tools are crucially needed to both perform meaningful and detailed representations of basin-scale hydrological processes and provide sensible local forecasts. The quantities of interest range from discharge hydrographs on upstream ungauged parts of the drainage network to their translation into flow depth, velocities and submersion times on downstream floodplains. This information is difficult to access, especially for floods over large territories. Indeed, given the complexity of physical processes involved, their limited observability and the resulting hydrological responses, hydrological modeling remains a hard task and internal state-fluxes are generally tinged with uncertainties (Beven [1993]; Schuite et al. [2019]; Milly [1994]). Moreover, the accuracy of high resolution hydraulic computations may still be affected by complex dynamics with wet-dry fronts, multi-scale and uncertain topography-structures and flow model parameters (e.g. friction), uncertain quantities at open boundaries (upstream inflows but also lateral ones due to sudden local runoff, downstream controls and backwater effects), internal in/outflows in urban areas, and large computational domains (Monnier et al. [2016]). Thus, integrated hydrological-hydraulic approaches are required (e.g. Nguyen et al. [2016]; Hocini et al. [2020]). Such approaches are now enabled by the increasing informative richness of multi-source datasets provided by high resolution hydrometeorology and satellite remote sensing in complement to in situ measurements. Nevertheless, reaching high resolution accuracy and computational efficiency for large scale applications remains a difficult challenge because of multi-scale non-linear hydrodynamic processes over large computational domains and multiple uncertainty sources.

These uncertainties could be reduced by the optimal combination of models and multi-source datasets, including high resolution maps, spatially sparse in situ flow measurements but also the growing amount of earth observation data provided by new generations of satellites, drones and sensors (e.g. Biancamaria et al. [2016, 2017]; Schumann and Domeneghetti [2016] among others). Indeed, remote sensing provides very interesting cartographic observations of the variabilities of worldwide catchments characteristics (topography, soil occupation, surface moisture, snow cover, ...), as well as an unprecedented and increasing hydraulic visibility over river networks (Garambois et al. [2017]; Montazem et al. [2019]; Rodríguez et al. [2020]). This growing wealth of multi-sensed information is key to the design and improvement of basin-scale models, as shown for accurate river network 1D hydraulic modeling enabled by recent multi-source altimetric and optical satellite data in Pujol et al. [2020] and in Malou et al. [2021] (see also references therein) or accurate 2D local floodplain models with radar sensed flooding extent (Hostache et al. [2010]). In order to exploit this wealth of hydrological and hydraulic information, the complexity of integrated models and assimilation methods has to be adapted to these data that are both heterogeneous in nature and of varied spatio-temporal resolutions. Moreover, an integrated flood modeling approach should also be computationally efficient in order to be applicable over entire catchments that is large computational domains. This study proposes a new integrated hydrological and multi-dimensional hydraulic modeling approach, based on the accurate and robust 2D hydraulic solver presented in Monnier et al. [2016]. It is capable of multi-variate optimization problems of high dimension using multi-source data.

Cascades of 2D hydrological-hydraulic models have been proposed in recent literature, for inundation mapping at large scales using worldwide DEM (e.g. Grimaldi et al. [2018]; Fleischmann et al. [2020]; Uhe et al. [2020]) with simplified hydraulic modeling) or at finer scale, e.g. at catchment scale for flash floods in Nguyen et al. [2016]; Hocini et al. [2020]. In those studies, conceptual hydrological models of upstream-lateral sub-catchments are used to inflow hydraulic models of river network and floodplains in a weak coupling approach, mostly performed via external coupling of numerical models. In Grimaldi et al. [2018]; Fleischmann et al. [2020]; Uhe et al. [2020], a simple 2D storage cell inundation model obtained from 1D non inertial model (Bates et al. [2010] following Hunter et al. [2008], implemented in LISFLOOD-FP model), enables raster based inundation modeling over very large domains at relatively low computational cost (see also Fleischmann et al. [2020] for coupling of this non inertial model with the large scale hydrological model MGB Collischonn et al. [2007]; Pontes et al. [2017]). In Hocini et al. [2020], an original 2D hydraulic modeling approach, using "precipiton" for the resolution of the full shallow water model, proposed by Davy et al. [2017], is used to compute steady inundation maps of various return periods at high resolution (5 m) for river networks and floodplains at catchment scale of several thousands of square kilometers (up to 5050 km^2). In Nguyen et al. [2016], an unsteady full 2D shallow water model (see Sanders et al. [2010]) is applied at relatively high resolution (10 or 30 m) in the river network and floodplains on a 808 km^2 catchment. Note that sequential data assimilation methods based on the Kalmann filter have been carried out extensively for mono-variate data assimilation with such models (see e.g. Brêda et al. [2019] with simplified hydraulics in a satellite observability context references therein and Table 3.1) at varying spatio-temporal resolutions. Current model development strives to propose combinations of high resolution accuracy and fast computation times over large domains and to incorporate multi-source data assimilation methods for large spatially and temporally distributed controls. This paper aims at providing an innovative and effective way to achieve these goals.

In order to combine local accuracy and computational efficiency, the association of full 1D and 2D hydraulic models is an appropriate approach for simulating a basin-scale network in a way that is both practical and adequately accurate. Methods for coupling models of different dimensions have been developed Miglio et al. [2005a,b]; Amara et al. [2004], classically using domain decomposition Gervasio et al. [2001], or more recently using local 2D 'zooms' overlapping with the 1D domain, in a variational data assimilation framework Gejadze and Monnier [2007]; Marin and Monnier [2009]. An iterative coupling strategy is applied in Barthélémy et al. [2018] between a 1D Mascaret and a 2D Telemac operational model and a sequential data assimilation technique is performed for correcting water levels forecasting. A summary of some established 1D and 2D numerical hydraulic models, external coupling methods and optimization-assimilation methods is presented in Table 3.1. One can spot DassFlow 2D Monnier et al. [2016] as the only 2D hydraulic model with a second order solver with accurate wet-dry front treatment, parallel computation and adjoint based variational data assimilation capabilities.

The present study details upgrades to the DassFlow variational data assimilation framework (Monnier et al. [2016]) in the form of a new multi-D hydraulic computational code and an integrated hydrological module. The proposed multi-D hydraulic code consists in a single finite volume solver applied to a 2D river network. The network is discretized into "1Dlike" reaches connected to high resolution 2D meshes in a single formulation of the SWE. The resulting product allows building large 1Dlike river networks, connected to fine local zooms. The method can lead to low computational costs over large networks and local fine scale accuracy at zooms where pertinent. The hydraulic model is coupled with a well-established conceptual hydrological model (GR4H state-space Santos et al. [2018]) in a semi-distributed setup. The variational platform can solve high-dimensional optimization problems with descent algorithms and using gradients computed with the adjoint model obtained via the automatic differentiation tool Tapenade (Hascoet and Pascual [2013]). It enables tackling multi-variate, i.e. with composite control vectors (bathymetry, friction, boundary conditions, hydrological parameters), data assimilation problems given multi-source dataset, heterogeneous in nature and spatio-temporal resolutions (see e.g. Brisset et al. [2018]; Pujol et al. [2020]). This integrated tool chain enables information feedback within the whole computational domain (basin) and especially from downstream to upstream. The source code and synthetic cases are available upon simple request [2].

The remainder of this article is organized as follows. In Section 2, the modeling hypothesis, the computational resolution and inverse methods are detailed. In Section 3, the multi-D coupling scheme is validated on a series of academic cases and several academic and real-like inference setups are investigated. The study is concluded in Section 4, which also outlines potential applications and improvement perspectives that the proposed method and findings bring.

Platform	Model	Mathematical model	Max order	Coupling 1D2D SWE	Parallel computation	DA	Sources available
HEC-RAS [40]	1D2D	(A, Q) and (h, u, v), both locally non-inertial SWE	1	Internal (2 solvers)	No	-	No
BreZo [232]	2D	(h, u, v), porosity	2	No	Yes	-	No
FullSWOF [71]	1D and 2D	(h, u, v) for both, full SWE	1	No	Yes	-	Yes
SW2D-LEMON [242; 121]	2D	(h, u, v), porosity	1	No	No	-	Yes
Floodos [68]	2D	(h, u, v), non-inertial SWE	1	No	No	-	Yes
b-flood [144]	2D	(h, u, v), full SWE	1	No	Yes	-	Yes
Telemac-Mascaret [96; 111]	1D and 2D	(A, Q) and (h, u, v), full SWE	1	External (2 solvers)	Yes	EnKF	Yes
LISFLOOD-FP [23]	1D2Dlike	(A, Q) non-inertial SWE	1	No	Yes	EnKF	Yes
DassFlow2D [179]	2D-1Dlike	(h, u, v), full SWE	2	Internal (same solver)	Yes	Var	Yes
DassFlow1D [38]	1D	(A, Q), full SWE	1	-	No	Var	Yes

Table 3.1: Some established freeware hydraulic models. "SWE" stands for Shallow Water Equations. The equations resolved are either formulated in (A, Q) (flow section $[\mathrm{m}^2]$ and at-a-section discharge $[\mathrm{m}^3/s]$) or in (h, u, v) (water depth $[\mathrm{m}]$ and 2D depth-integrated flow velocities $[\mathrm{m}/s]$). "Max order" refers to the maximum demonstrated scheme order.

---

[2] http://www.math.univ-toulouse.fr/DassFlow

3.3 The computational hydrological-hydraulic chain

This section presents the integrated and multi-dimensional hydrological-hydraulic model and the data assimilation approach. The model is designed for simulating spatio-temporal flow variabilities over an entire river network, from upstream hydrological responses to complex flow zones (confluences, multi-channel portions, floodplains, ...).

The modeling approach which is detailed below, is based on the following ingredients:

- An integrated multi-D hydraulic model: the 2D shallow water equations (SWE) with finite volume solvers from Monnier et al. [2016] are applied to "1Dlike"-2D composite meshes of river networks using a numerical flux splitting method and an effective friction power-law depending on flow depth.

- A numerically coupled hydrological model, the widely used GR4 model from Perrin et al. [2003] in its state-space version Santos et al. [2018], for the sake of model differentiability.

- A computational inverse method based on VDA algorithms from Monnier et al. [2016]; Brisset et al. [2018]; Larnier et al. [2021] enabling spatially distributed calibration and variational data assimilation with the whole chain.

3.3.1 Multi-D hydraulic-hydrological modeling principle

The flow model consists in a spatially-distributed modeling of hydrological responses coupled to a seamless multi-scale "1Dlike"-2D hydraulic model. The core idea of this work is to apply the 2D SW hydraulic model (Eq. 3.1) on a multi-D discretization $\mathcal{D}_{hy}$ of the computational domain Ω. The discretization (mesh) $\mathcal{D}_{hy}$ is composed of N mixed unstructured triangular/quadrangular cells with interfaces between 1Dlike and 2D zones (Fig. 3.6). Ω is composed of a hydrological domain Ω_{rr} connected to a hydraulic domain Ω_{hy} (Fig. 3.4). Γ_{hy-rr} is the border of Ω_{hy} containing interfaces with Ω_{rr}. The unstructured lattice covering Ω consists in hydrological units for describing upstream/lateral sub-catchments in Ω_{rr} and mixed unstructured triangular/quadrangular elements in Ω_{hy}.

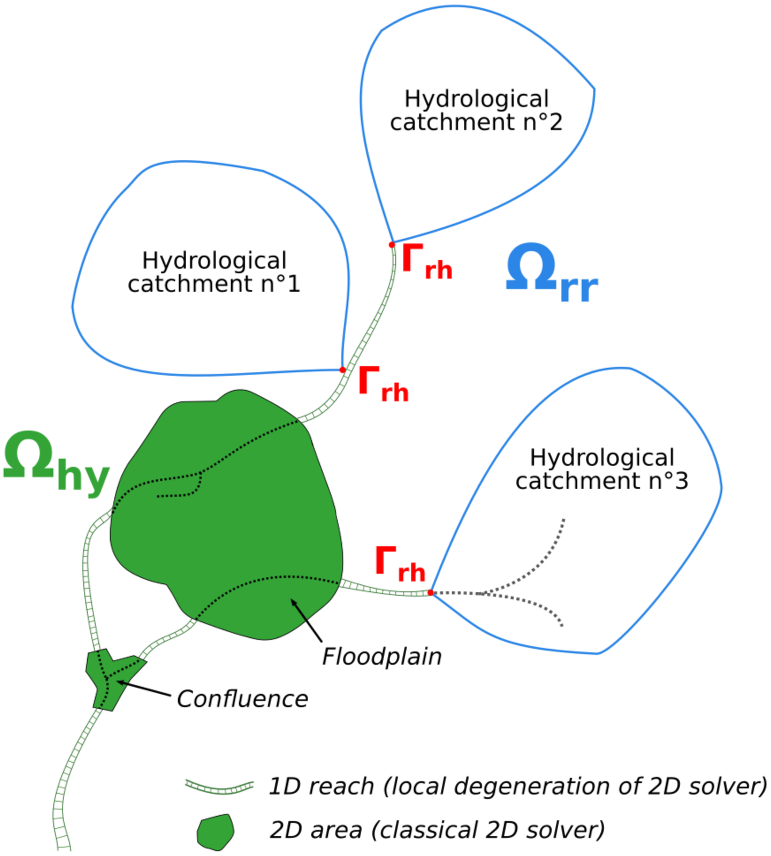

Figure 3.4: Conceptual meshing approach for integrated hydraulic-hydrological and multi-dimensional modeling of a river network. The computational domain Ω is composed of the hydrological domain Ω_{rr} connected to the hydraulic domain Ω_{hy} . Ω_{hy} contains 1Dlike meshes and classical 2D meshes, interfaced frontally at Γ_{rh}. Inflows injected in Ω_{hy} (blue points) can come from classic inflowing methods or from the coupling to hydrological catchments from Ω_{rr}.

3.3.2 Hydraulic module

Numerical hydraulic models describing open channel flows generally rely on the resolution of cross-sectionally or depth integrated flow equations, respectively the 1D Saint-Venant or 2D SWE (see e.g. Guinot [2010]). While 1D hydraulic models enable a physically sound representation of river flows variabilities in terms of wetted section A and discharge Q for instance, 2D hydraulic models in flow depth h and depth integrated velocity $\boldsymbol{u} = (u, v)^T$ enable to tackle more complex flow zones such as confluences/diffluences and floodplain flows. The 2D shallow water model used in the proposed approach is presented here with the adaptation of the finite volume solver from Monnier et al. [2016] for multi-D modeling. Note that 1D Saint-Venant equations are presented in appendix (3.B) along with their resolution method in DassFlow 1D (Brisset et al. [2018]; Larnier et al. [2021]) that is used for comparison in this study. Next, this section presents the hydrological module and the inverse algorithm.

3.3.2.1 Mathematical flow model

On the hydraulic computational domain $\Omega_{hy} \subset \mathbb{R}^2$ and for a time interval $]0,T]$, the 2D SWE with the Manning-Strickler friction term, in their conservative form, write as follows:

$$\partial_t \mathbf{U} + \partial_x \mathbf{F}(\mathbf{U}) + \partial_y \mathbf{G}(\mathbf{U}) \; = \; \mathbf{S}_g(\mathbf{U}) + \mathbf{S}_f(\mathbf{U})$$

$$\mathbf{U} = \begin{bmatrix} h \\ hu \\ hv \end{bmatrix}, \; \mathbf{F}(\mathbf{U}) = \begin{bmatrix} hu \\ hu^2 + \dfrac{gh^2}{2} \\ huv \end{bmatrix}, \; \mathbf{G}(\mathbf{U}) = \begin{bmatrix} hv \\ huv \\ hv^2 + \dfrac{gh^2}{2} \end{bmatrix}, \tag{3.1}$$

$$\mathbf{S}_g(\mathbf{U}) = \begin{bmatrix} 0 \\ -gh\nabla b \end{bmatrix}, \; \mathbf{S}_f(\mathbf{U}) = \begin{bmatrix} 0 \\ -g\dfrac{n^2 \left\|\mathbf{u}\right\|}{h^{1/3}}\mathbf{u} \end{bmatrix}$$

with h the water depth $[\mathrm{m}]$ and $\mathbf{u} = (u,v)^T$ the depth-averaged velocity $[\mathrm{m/s}]$ being the flow state variables. g is the gravity magnitude $[\mathrm{m/s^2}]$, b the bed elevation $[\mathrm{m}]$ and n the Manning-Strickler friction coefficient $[\mathrm{s/m^{1/3}}]$ being the flow model parameters. Classical initial and boundary conditions adapted to real cases are considered (see Monnier et al. [2016]; Couderc et al. [2013] for details).

An effective friction law consisting in a simple power-law $n = \alpha h^\beta$ is introduced, as previously done for 1D SWE for effective modeling with simplified multi-channel river geometry in Garambois et al. [2017]; Brisset et al. [2018].

3.3.2.2 Building-up equivalencies between 2D and 1D flow states

1Dlike reaches refer to river reaches where the following meshing strategy has been applied: quadrangular cells are built such that their interfaces are perpendicular to the main flow direction and span the whole river (bankfull) width as a traditional 1D XS would. Examples can be found in Fig. 3.9 and Fig. 3.16. This leads to a series of quadrangular cells, each linked to a single upstream and downstream cell. The 1Dlike approach implicitly assumes a rectangular XS shape which potentially impacts the representation of: (i) at-a-section hydraulic geometry (Leopold and Maddock [1953]), (ii) longitudinal hydraulic controls and flow variabilities.

In view to put the multi-D model in coherence with real flow physics, a continuity condition between 1D and 1Dlike models states and parameters is required. This continuity condition is enforced at-a-section, in a prismatic channel such that the uniform permanent flows, that is equilibrium, are preserved.

Let us consider a reference 1D model in (A,Q) variables with the bankfull width value W_{1D}. The friction term reads: $S_{f,1D} = \frac{n^2 Q|Q|}{A^2 R_h^{4/3}}$ (Appendix 3.B). In the corresponding 1Dlike model in (h,u,v) variables, see Section 3.3.2.1, the friction term reads: $S_{f,1Dlike} = \frac{n^2 ||\boldsymbol{u}||}{h^{1/3}} \boldsymbol{u}$

Considering 1D flow states over an idealized river section (Fig. 3.5, left) the hypothesis of local flow equilibrium (uniform, steady-state) with identical wetted areas A and WS widths W, the continuity condition implies that:

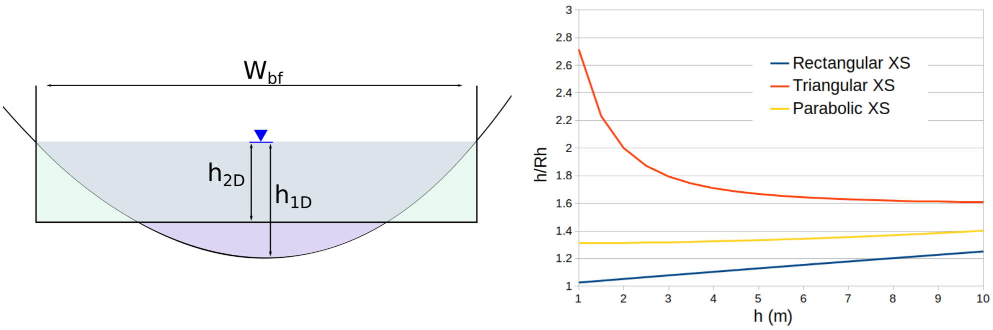

Figure 3.5: Equivalency of 1D and 2D flow states at equilibrium (permanent uniform flows): effective friction and bathymetry. Left: Equivalency between a 1D idealized XS (purple) and a 2D single-cell rectangular XS (green), with the same flow section A and WS elevation. Right: Variation of the hydraulic radius $R_h(h)$ for 3 XS shapes (of similar dimensions). This showcases the potential over- and under-estimation of state variables using "1Dlike equivalent friction" from Eq. (3.2).

$$n_{1Dlike} = n_{1D} \sqrt{\frac{A}{W} \frac{h_{1Dlike}^{1/3}}{R_{h,1D}^{4/3}}} \tag{3.2}$$

where n_{1Dlike} (resp. h_{1Dlike}) is the Manning-Strickler friction coefficient (resp. flow depth) in the 1Dlike model i.e. the coefficient in the 2D SWE (3.1).

With the additional assumption of a rectangular XS (as it will be assumed in some test cases), we have $h_{1Dlike} = {}^{A}/_{W_{1D}}$, which leads to $n_{1Dlike} = n_{1D} \left(\frac{h_{1D}}{R_{h,1D}}\right)^{2/3}$.

This "1Dlike equivalent friction" leads to a perfect fit in WS elevation of 1Dlike model and 1D model in a straight prismatic channel at the given uniform regime (results not shown here for brevity). Fig. 3.5, right, shows the evolution of the ratio $({}^{h}/_{R_h})$ vs h. For rectangular and parabolic XS, the ratio ${}^{n_{1Dlike}}/_{n_{1D}}$ is expected to increase with h. Thus, one can naturally expect an overestimation (resp. underestimation) of the actual friction coefficient by n_{1Dlike} at lower flows (resp. greater flows). This would lead to an overestimation (resp. underestimation) of the 1D WS elevation by the "equivalent" 1Dlike model. However, later it will be considered a power-law in h to model the friction coefficient (Subsection 3.3.2.1), which provides a better fit to the 1D WS elevations outside of the considered permanent flow.

Note that longitudinal controls and flow variabilities in 1Dlike models are assessed using synthetic cases in Subsection 3.4.2.2.

3.3.2.3 Multi-dimensional hydraulic model

Over a given cell $K \in \Omega_{hy}$ of area m_K, the piece-wise constant values $\mathbf{U}_K = \dfrac{1}{m_K} \int_K \mathbf{U} dK$ are approximated. Recall that the finite volume approach applied to the homogeneous part of the hyperbolic system of Eq. 3.1 (that is without the friction source term $\mathbf{S}_f$ but including a consistent discretization of the gravitational source term $\mathbf{S}_g$) writes as follows:

$$\bar{\mathbf{U}}_K^{n+1} = \mathbf{U}_K^n - \frac{\Delta t^n}{m_K} \sum_{e \in \partial K} m_e \mathbf{F}_e \left(\mathbf{U}_{K,i}^n, \mathbf{U}_{K_e}^n, \mathbf{n}_{e_i,K} \right) \tag{3.3}$$

1.7

where $\mathbf{U}_K^n$ and $\mathbf{U}_K^{n+1}$ are the piece-wise constant approximations of $\mathbf{U} = (h, hu, hv)^T$ at time t^n and t^{n+1} (with $t^{n+1} = t^n + \Delta t^n$), $\mathbf{F}_e$ stands for Riemann fluxes through each edge e of the border ∂K of the cell K, with each adjacent cell Ke. The length of edge e is m_e and $\mathbf{n}_{e,K}$ is the unit normal to e oriented from K to Ke.

The finite volume schemes are those developed in Couderc et al. [2013]; Monnier et al. [2016].The discretization of the friction source term is described in Appendix 3.A.

Based on the first and second order finite volume solvers of Couderc et al. [2013]; Monnier et al. [2016], a 1D2D coupling technique is introduced following a similar concept to Finaud-Guyot et al. [2018] (urban geometries and porosity context) to compute numerical fluxes on each interface between a 1Dlike quadrangular mesh cell connected to several 2D cells as schematized in Fig. 3.6.

At the multi-D interfaces, that is in the case of $n > 1$ cells $x_{K,i}$ $i \in [1..n]$ adjacent to the same interface of another cell Ke (see Fig. 3.6 for notations and e.g. Fig. 3.19 for a real-like example), a special treatment is applied. It consists in the Riemann fluxes being calculated for each cell K_i using the state from the same corresponding Ke cell over an interface of length m_{e_i}. In the end, the flux crossing the interface $e = \cup e_i$ is equal to the sum of the fluxes crossing the e_i interfaces: $\mathbf{F}_e = \sum_{i=1..n} m_{e_i} \mathbf{F}_{e_i} \left(\mathbf{U}_{K_i}^n, \mathbf{U}_{Ke}^n, \mathbf{n}_{e_i,K} \right)$.

This type of internal interface has been implemented in the numerical solvers from Monnier et al. [2016] in the DassFlow platform which includes a solver with second order accuracy in space. This solver, developed in Couderc et al. [2013]; Monnier et al. [2016], is accurate and robust for wet-dry front propagations and fully applies in the present context. Note that the lateral distribution of variables across the 1D2D interface is not constrained. The source code and synthetic cases are available upon simple request.

3.3.3 Hydrological module

In order to simulate the hydrological response of sub-catchments within a river basin, a hydrological module is coupled to the 2D SW flow model. The widely used, parsimonious and robust conceptual hydrological model GR4 (Perrin et al. [2003]), in its “state-space” version from Santos et al. [2018], was chosen. The original lumped hydrological model has been deployed in a semi-distributed manner in the DassFlow framework.

The model is composed of two non-linear stores for production (soil moisture accounting) and routing, and a Nash cascade composed of a series of linear stores replacing the unit hydrograph from Perrin et al. [2003]. Being a set of ODE with explicit dependency to parameters, this hydrological model is differentiable. Moreover, the Fortran code is differentiable with the automatic differentiation tool Tapenade Hascoet and Pascual [2013].

Let us consider a sub-catchment bv_i among sub-catchments $\{bv_1, ..., bv_C\}$ in the discretized river basin hydrological domain Ω_{rr}. The hydrological model can be seen as a dynamic operator

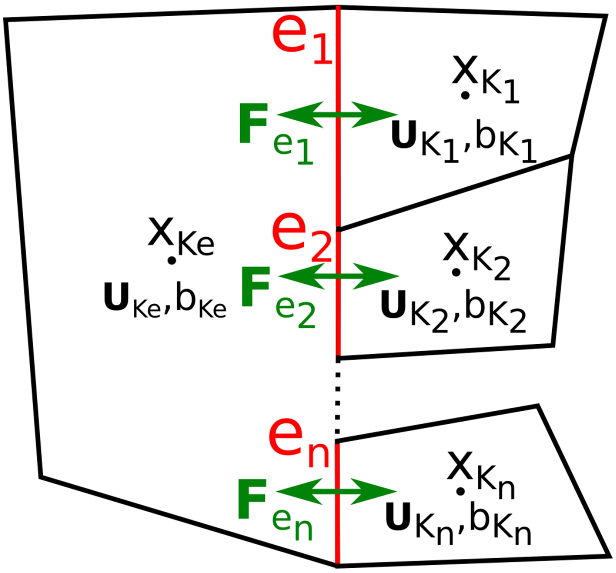

Figure 3.6: Internal multi-D domains interface, general case. At each cell center $\boldsymbol{x}$, the state variables $\mathbf{U} = (h, hu, hv)^T$ and the bathymetry b are defined. The total numerical flux is conserved: $\mathbf{F}_e = \sum_{i=1..n} m_{e_i} \mathbf{F}_{e_i} \left(\mathbf{U}^n_{K,i}, \mathbf{U}^n_{Ke}, \mathbf{n}_{e_i,K} \right)$.

$\mathcal{M}$ relating sub-catchment state variables vector $h\,(x_i, t)$ with observable input of spatially averaged (on sub-catchment x_i) rainfall $P\,(x_i, t)$ and potential evapotranspiration $E\,(x_i, t)$, observable outputs $Y\,(x, t)$ and "unobservable" parameters $\theta\,(x)$.

Omitting the sub-catchment index i for readability, the hydrological model consists in the following set of ordinary differential equations:

$$\frac{\mathrm{d}\boldsymbol{h}}{\mathrm{dt}} = \begin{cases} \dot{h_p} & = P_s - E_s - P_{erc} \\ \dot{h}_1 & = P_r - Q_{Sh,1} \\ \dot{h}_2 & = Q_{Sh,1} - Q_{Sh,2} \\ \dots & \dots \\ \dot{h}_{nres} & = Q_{Sh,nres-1} - Q_{Sh,nres} \\ \dot{h_r} & = Q_9 + F - Q_r \end{cases} \tag{3.4}$$

where P_s, E_s, P_r, $Q_{Sh,i}$, $i \in [1..nres]$, Q_9, F, Q_r are model internal fluxes given in appendix 3.C along with their internal parameters. The evolution of reservoir states and model outputs and inputs is presented for a sample rain event in Fig. 3.7.

The input of the hydrological model are the evapotranspiration and precipitation E_n and P_n, the output is discharge $q\,(t) = Q_r + Q_d$ [mm/h]. E_n and P_n are classically imposed from data time series as piece-wise constant on fixed temporal resolution (e.g. hourly). The numerical resolution is achieved with an implicit Euler algorithm with an adaptative sub-step algorithm enabling to reduce numerical errors especially for high flows (Santos et al. [2018]). The initial states of the stores is given by a 1 year warm-up run. The discharge q is injected into Ω_{hy} at a

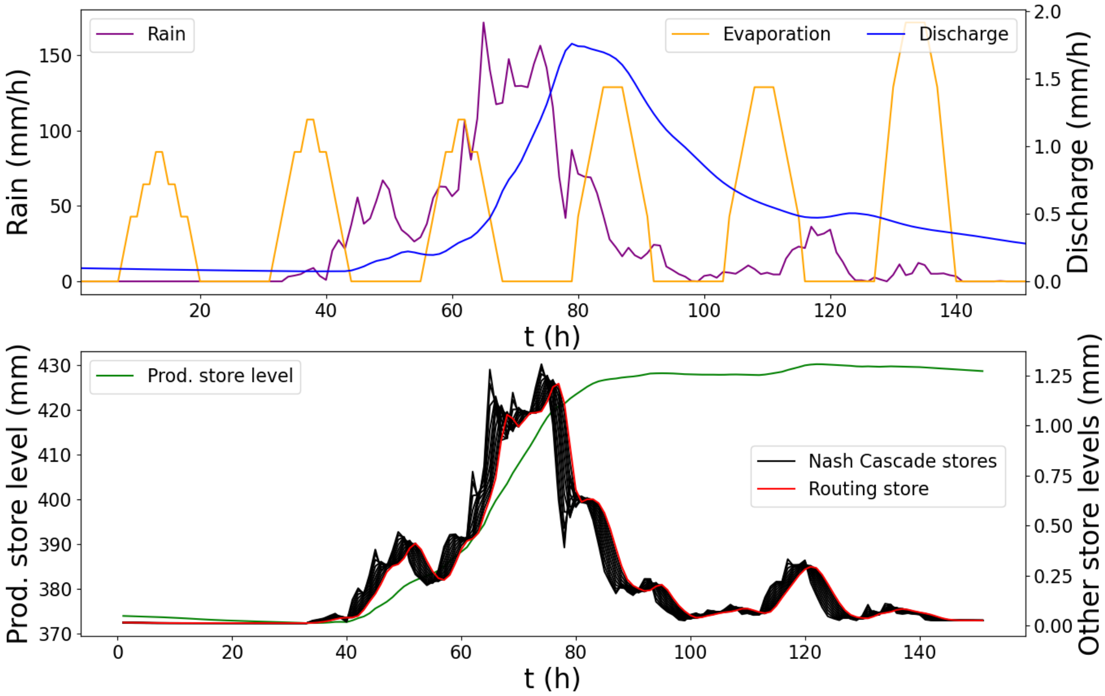

Figure 3.7: Evolution of GR4 inputs, output and reservoirs states during a sample rain event.
Top: temporal forcings (rain and evaporation) and modeled output (discharge).
Bottom: hydrological model states (reservoir levels).

sub-interface of Γ_{hy-rr}, either as an upstream or lateral flow.

The calibrated parameters will be the classical 4 parameters $(c_i)_{i\in 1..4}$ of GR4 (they will constitute the control vector considered in the forthcoming VDA experiments). Other parameters, such as several drainage law exponents or the number of Nash cascade stores are not optimized in this study. They are set at values from Santos et al. [2018].

3.3.4 Inverse algorithm: Variational Data Assimilation

Given spatio-temporal flow observables, provided by in situ and airborne sensors for instance, the inverse algorithm consisting in Variational Data Assimilation (VDA) aims at estimating the unknown or uncertain "input parameters" of the hydrological-hydraulic chain composed of a hydraulic model, presented in Section 3.3.2, and a hydrological model, presented in Section 3.3.3.

We consider the following set of spatio-temporal observations of water surface and discharge over the river domain $\Omega \subset \mathbb{R}^2$:

$$Z_{o,k}(t), \forall k \in [1..N_{o,Z}], Q_{o,k}(t), \forall k \in [1..N_{o,Q}] \tag{3.5}$$

with Z_o the observed WS elevation $[\mathrm{m}]$ above reference elevation, Q_o the observed discharge $[\mathrm{m}^3/\mathrm{s}]$, $N_{o,Z}$ the number of altimetric observations points and $N_{o,Q}$ the number of observed discharges over Ω.

Note that observed discharge Q_o may be a value of a hydraulic discharge at a flow XS in Ω_{hy}, or within the hydrological domain Ω_{rr} and especially at the outlet of a sub-catchment here. Also note that other water surface observables could be considered, such as water surface velocity observations or dynamic water masks - not the scope of this study.

Given river stage and/or discharge observations, the aim is here to estimate unknown or uncertain quantities of the hydrological-hydraulic model among: discharge hydrographs $Q_i\left(t\right), i \in [1, N]$ on the border of the hydraulic domain, spatially distributed hydraulic parameters (bathymetry elevation b or friction n) and hydrological models parameter sets $\left(c_i\right)_{i\in 1..4}$.
The control vector containing the sought quantities is denoted θ in what follows:

$$\theta = \left(\theta_{hy}, \theta_{rr}\right) = \left(\left(Q_1^0, ..., Q_1^T, ..., Q_N^1, ..., Q_N^T, n_1, ..., n_M, b_1, ..., b_M\right), \left(c_1, ..., c_P\right)\right) \tag{3.6}$$

with θ_{hy} and θ_{rr} the control vectors of respectively the hydraulic and the hydrological modules, N the number of inflows points and T the number of inflow values in time, M the number of modeled cells and P the number of hydrological units.

We consider a cost function j_{obs} aiming at measuring the discrepancy between simulated and observed flow quantities on the computational domain Ω. This cost function is defined as:

$$j_{obs}\left(\theta\right) = j_Q\left(\theta\right) \; or \; j_{obs}\left(\theta\right) = j_Z\left(\theta\right) \tag{3.7}$$

This cost function contains either misfit to WS elevation, $j_Z\left(\theta\right) = \frac{1}{2}\left\|Z_o\left(t\right) - Z\left(\theta, t\right)\right\|^2_{\mathcal{O}_{\mathcal{Z}}}$, or misfit to discharge, $j_Q\left(\theta\right) = \frac{1}{2}\left\|Q_o\left(t\right) - Q\left(\theta, t\right)\right\|^2_{\mathcal{O}_Q}$.

The metrics (symmetric positive definite matrices) $\mathcal{O}_{\mathcal{Z}}$ and $\mathcal{O}_Q$ are based on the inverse of the observation error covariances. This enables to regularize the inverse problem, see e.g. Bouttier and Courtier [2002]; Asch et al. [2016]; Monnier [2021] and references therein for related discussions.

Moreover, we classically enrich the cost function with a regularization term: $j\left(\theta\right) = j_{obs}\left(\theta\right) + \gamma j_{reg}\left(\theta\right)$ with j_{reg} a Tikhonov type regularization term. Here we consider a regularization on the bathymetry only: $j_{reg}\left(\theta\right) = \frac{1}{2}\sum_{i=1}^{M}\left(\left(\partial_x b_i\right)^2 + \left(\partial_y b_i\right)^2\right)$ with θ defined by (3.6).

The regularization term adds convexity to the cost function. Moreover, it here dampens the bathymetry highest frequencies. Recall that low Froude flows i.e. subcritical flows naturally act as a low pass filtering of the bathymetry shape, see Martin and Monnier [2015]; Gudmundsson [2003].

The total cost function j is minimized starting from a background value $\theta^{(0)}$. Following Lorenc et al. [2000], see also Larnier et al. [2021], the following change of variables is applied:

$$k = B^{-1/2}\left(\theta - \theta^{(0)}\right) \tag{3.8}$$

with B the covariance matrix of the background error.

Then by setting $J\left(k\right) = j\left(\theta\right)$, the optimization problem which is solved is actually the following:

$$\min_k J(k) \tag{3.9}$$

The first order optimality condition of this optimization problem (3.9) reads: $B^{1/2}\nabla j(\theta) = 0$. The change of variables based on the covariance matrix B acts as a preconditioning of the optimization problem. This optimization problem is solved using a first order gradient-based algorithm, more precisely the classical L-BFGS quasi-Newton algorithm (limited-memory Broyden-Fletcher-Goldfarb-Shanno bound-constrained, Zhu et al. [1997]) or, in some cases in this study, its bounded version L-BFGS-B (Zhu et al. [1997]) but without variable change 3.8. Detailed know-hows on VDA may be found e.g. in online courses (see e.g. Bouttier and Courtier [2002]; Monnier [2021]). The gradient is computed with the help of the adjoint model. The latter is obtained by automatic differentiation, using Tapenade Hascoet and Pascual [2013].

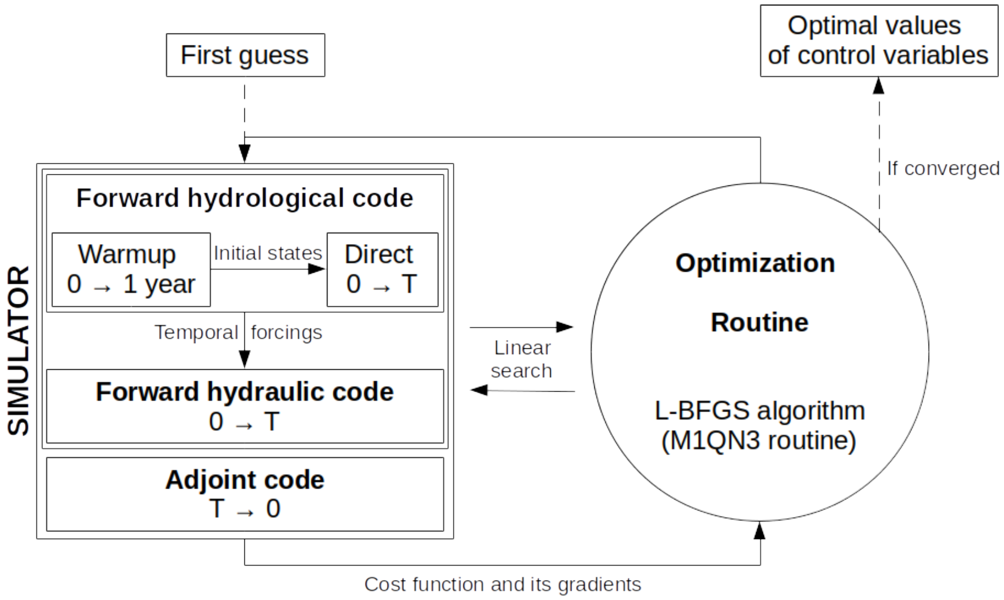

Figure 3.8: Complete VDA hydraulic-hydrological tool chain

The choice of the covariance matrix B, represents an important a priori and greatly influences the computed solution of the inverse problem. Assuming the unknown parameters are independent variables, the matrix B is defined as a block diagonal matrix:

$$B = blockdiag\left(B_{\Omega_{hy}}, B_{\Omega_{rr}}\right), \, with \; B_{\Omega_{hy}} = blockdiag\left(B_Q, B_n, B_{z_b}\right) \tag{3.10}$$

Each block matrix of $B_{\Omega_{hy}}$ is defined as a covariance matrix (positive definite matrix) using 2D kernels for spatial controls. Here following Larnier et al. [2021], we consider:

$$(B_Q)_{i,j} = (\sigma_Q)^2 \, exp\left(-\frac{|t_j - t_i|}{L_Q}\right) \tag{3.11}$$

$$(B_b)_{i,j} = (\sigma_b)^2 \, exp\left(-\frac{|x_j - x_i| + |y_j - y_i|}{L_b}\right), \; (B_n)_{i,j} = (\sigma_n)^2 \, exp\left(-\frac{|x_j - x_i| + |y_j - y_i|}{L_n}\right) \quad (3.12)$$

The parameters L_Q and (L_b, L_n) act as correlation lengths. These parameters are usually empirically defined. However the expression of B_b and the correlation lengths can be derived from physically-based estimations following Malou and Monnier [2021].

The following stopping criterion are used to stop the iterative optimization process if: i) the cost function does not decrease over a set number of iterations or ii) the current cost gradient, normalized by the initial cost gradient, goes under a set objective value. The multi-D hydrological-hydraulic tool chain presented above has been implemented in the latest version of Couderc et al. [2013].

3.4 Results and discussion

3.4.1 Numerical experiments design

Both synthetic and real cases are considered to test the forward and inverse modeling capabilities of the proposed computational chain for river networks and floodplains simulation. First, the multi-D hydraulic model (Section 3.3.2.3) is validated against reference hydraulic models on synthetic cases corresponding to typical hydraulic complexities: (i) simple straight channel, (ii) confluence and (iii) straight, rectangular and parabolic, channels with effective parameterization of friction and bathymetry. For fluvial regimes in the context of altimetry, these hydraulic complexities generate hydraulic controls. Following Montazem et al. [2019], we define hydraulic controls as characterized by a maximal deviation of the water depth from the normal depth (see e.g. Chow [1959]; Dingman [2009] for definition) at the reach scale. Next, a series of inference cases are considered in twin experiment setups. In a twin experiment, a reference model acts as a synthetic truth and is used to generate observations of model variables (e.g. $b + h$ in Ω_{hy} or Q in Ω_{rr}). No observation noise is considered in this study. The VDA method is then applied with these observations on an altered version of the reference model. Inferences of temporal forcings (inflow hydrographs $Q_i(t), i \in [1..N]$) are presented on a 1D2D confluence case. Inferences of channels parameters are presented on a straight 1Dlike case. Next, inferences of hydrological parameters $(c_i)_{i\in 1..4}$ are presented using hydraulic observables. Finally, the model is tested on two real cases: (i) the capability of the 1Dlike model to reproduce real flow lines and propagations, through effective bathymetry-friction $(b(x), n(x))$ inference, is assessed against a reference 2D model built on fine bathymetry of 75 km of the Garonne river and (ii) the whole multi-D hydraulic hydrological tool chain is tested at basin scale on the real complex case of the Adour River network.

3.4.2 Synthetic cases

First, the proposed multi-D hydraulic solver (Subsection 3.3.2.3) is evaluated and compared to a fine 2D reference model on two simple configurations, a straight channel and a confluence, that feature contain frontal interfaces between 1Dlike and 2D meshes. Next, to investigate the reproductibility of hydraulic controls using a 1Dlike meshing approach and effective modeling, this approach is compared to a 1D reference model in three typical channel configurations: (i) a rectangular prismatic channel, (ii) a rectangular channel with a slope break and (iii) a parabolic prismatic channel. Finally, inferences of inflow hydrographs $Q_i\left(t\right), i \in [1..N]$ and of a friction power-law $n = \alpha h^{\beta}$ are carried out using WS observables.

3.4.2.1 Forward multi-D hydraulic cases

Straight channel case

A prismatic rectangular channel and a multi-D mesh are considered (1Dlike to 2D to 1Dlike, see Fig. 3.9). The channel width is 300 m and its length is 2300 m. A rating curve is imposed downstream. This multi-D model is compared to a reference 2D model with refined mesh (mesh not shown, 2400 cells, average edge length $\backsim$ 25 m). The multi-D waterline is validated against the 2D model at permanent flow $\left(Q = 100\,\mathrm{m}^3/\mathrm{s}\right)$ and the modeled downstream discharges are compared for a flood hydrograph (Fig. 3.9(b)). Both first (not shown) and second order (Fig. 3.9) numerical solver allow a close fit to the target water line (Fig. 3.9, bottom).

At permanent flow, a slight misfit is observed between the 2D and multi-D WS elevations with the second order scheme (Fig. 3.9, top, relative misfit $< 0.15\%$ at 1000 m). This is due to approximation error in the multi-D model caused by large spatial steps in 1Dlike reaches ($dx = 200\,\mathrm{m}$). Indeed, this misfit is reduced by reducing the 1Dlike cells length (not shown). This is confirmed and showcased in the next subsection.

At the interface between 1Dlike and 2D meshes, a slight jump in WS elevations can be observed at all 2D cells (Fig. 3.9, top). This is due to the second order scheme, which is currently not designed for multi-D interfaces. Recall that no constraint is imposed on the lateral distribution of computed variables. The technical implementation of this reconstruction for 1D2D interfaces will be done in next version of DassFlow.

During a varied flow event, the outflow of both models is close to identical (Fig. 3.9, middle). The flow is correctly transmitted at multi-D interfaces and, at this scale, the 1Dlike meshes are adequate to model a flood wave propagation.

Simple confluence case

A simple symmetrical confluence is modeled using a multi-D mesh. The channel width is 300 m in the downstream reach and 150 m in the upstream reaches. Two inflow hydrographs are imposed at the two upstream interfaces. The maximum abscissa of the mesh points are 0 and 2075 m. The 2D part (average edge length $\backsim$ 5 m) contains a confluence flow zone (Fig. 3.10) while the 1Dlike mesh ($dx = 100\,\mathrm{m}$) covers the upstream and downstream reaches. At permanent flow, the multi-D model compares well with the reference 2D fine model (mesh not shown, 15 000 cells, average edge length $\backsim$ 5 m) and leads to similar conclusions to that of the above paragraphs. Using a shorter spatial step in the 1Dlike reaches (10 m) reduces the difference between reference and multi-D model and allows for a nearly perfect fit to the reference WS elevation at permanent flow (Fig. 3.10, in green). During a varied flow event, the outflows modeled with the multi-D model are very close to reference ones - slight differences during rising and falling limbs, same peak time, $NSE = 0.996$.

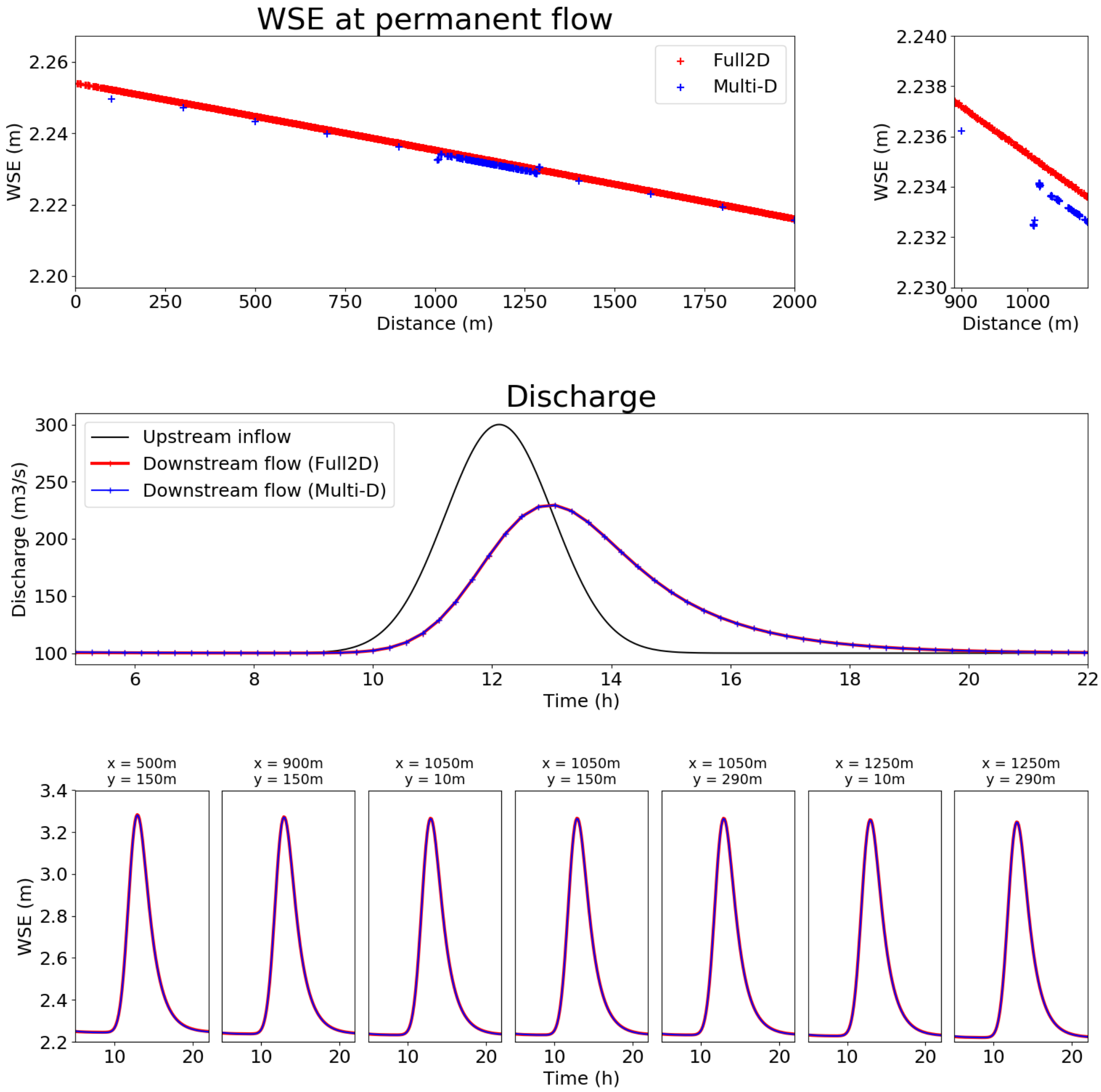

(a) Top: Waterlines for a permanent flow of 100 m^3/s. In red: reference 2D waterline. In blue: waterline for the mesh (left). The total misfit at the 1D2D upstream interface (at 1000 m) is around 10^{-3} m, for a relative misfit $< 0.15\%$ of the local depth. Middle: In black: upstream discharge during sample varied flow event. In red/blue (total overlap): downstream simulated flow for the considered meshes. Bottom: WS elevation observations for the varied flow event (total overlap).

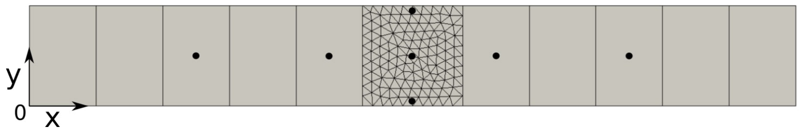

(b) Station locations are noted as black dots on the mesh (left).

Figure 3.9: Multi-D straight channel case results with second order scheme. The flow is subcritical with a maximum Froude value of 0.06.

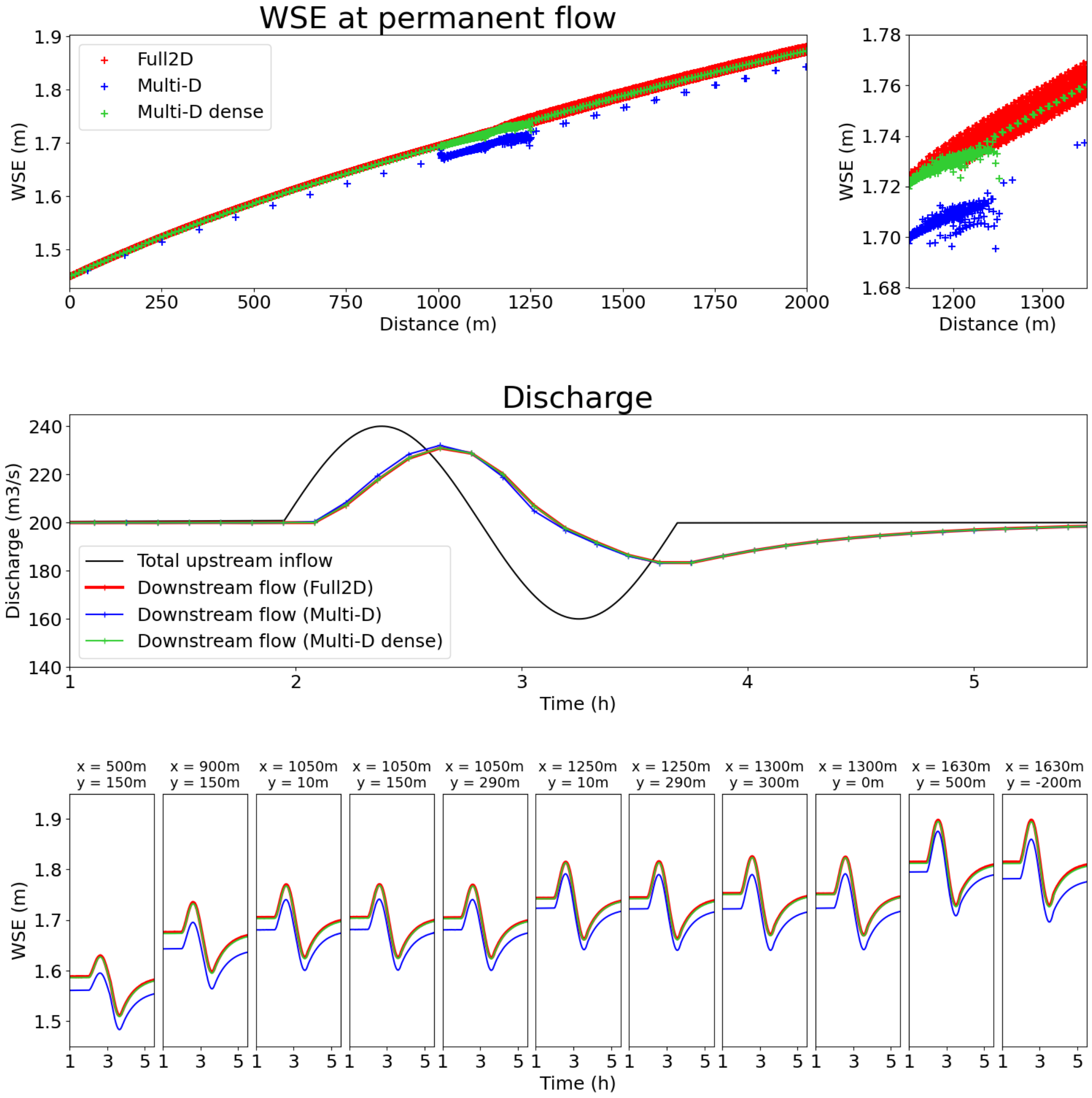

(a) Top: Waterlines for a permanent flow of 100 m^3/s at both upstream boundaries. In red: reference 2D waterline. In blue: waterline for the mesh (left). In green: waterline for a denser 1D2D mesh (not shown). Middle: In black: total upstream discharge during sample varied flow event (evenly distributed between upstream boundaries). In red/green/blue: downstream simulated flow for the considered meshes. Bottom: WS elevation observations for the varied flow event.

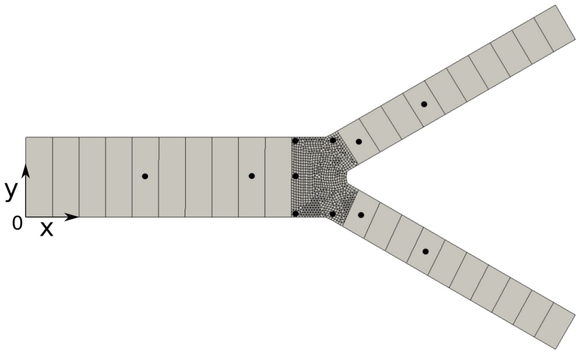

(b) Station locations, noted as black dots on the mesh.

Figure 3.10: Multi-D confluence case results with second order scheme

3.4.2.2 Hydraulic controls and effective friction

To investigate the reproductibility of hydraulic controls for fluvial flows, which are characterized by a maximal deviation of the water depth from the normal depth at the reach scale (see definition in Montazem et al. [2019]), using a 1Dlike approach, a set of typical channel variabilities and hydraulic controls are considered. Let us compare 1D and 1Dlike waterlines in a series of synthetic cases: (i) a straight rectangular channel, (ii) a straight rectangular channel with a mid-channel slope break and (iii) a straight parabolic channel.

Direct calibration Recall the equivalent friction formulation (Eq. 3.2) designed to make match the water line at-a-section and at equilibrium. For each 1Dlike case, waterlines with 1D friction ($n = 0.05\,\mathrm{s/m^{1/3}}$) and effective equivalent friction are generated. Effective friction values are calculated using (Eq. 3.2) and results from the corresponding 1D case. Reference 1D flow lines are computed with DassFlow solving 1D Saint-Venant equations in (A, Q) state variables with a Preissmann scheme (see 3.B and also Larnier et al. [2021]).

In a straight rectangular prismatic channel, with the 1D normal water depth imposed downstream (Fig. 3.11(a)), a backwater curve is computed by the DassFlow1D model (in red). With a 1D homogeneous friction ($n = 0.05\,\mathrm{s/m^{1/3}}$), the 1Dlike approach yields an underestimated waterline (in blue). An homogeneous effective friction allows to correct the underestimation and to better match the 1D normal water depth over the whole domain (in green). The remaining misfit can be attributed to numerical errors, especially numerical diffusion from the Preissmann scheme (1D model spatial step is $dx_{1D} = 100\,\mathrm{m}$).

A first complexification of this case consists in the introduction of a local hydraulic control point in the form of a slope break at $x = 10\,\mathrm{km}$ (Fig. 3.11(b)). In this setup, both 1D and 1Dlike models generate M2 backwater curves, see e.g. Dingman [2009]. The hydraulic control generated at the slope break is well represented with a 1Dlike approach, given the aforementioned numerical errors due to the coarse grid.

Another complexification of the first case consists in changing from a rectangular XS to a parabolic one (Fig. 3.5). In this case, both equivalent friction - a single homogeneous patch - and effective bathymetry, in the form of an homogeneous shift δ_b of the reference bathymetry, are needed to match the 1D WS elevation. Equivalent friction only allows to model identical wetted sections at permanent bankfull flow for a given channel width (Section 3.3.2.2). In this case, matching the 1D wetted section does not equate to matching its WS elevation, thus an effective bathymetry is used (Fig. 3.5(c)).

According to the above model comparisons, effective parameterization of channel parameters is sufficient to reproduce 1D behaviors with a 1Dlike approach for permanent bankfull flows in simple geometries. Outside of the permanent bankfull flow, a friction power-law $n = \alpha h^{\beta}$ can be used (Subsection 3.3.2.1). This friction aims at better 1Dlike representativity when modeled wetted surfaces (and other XS variables) are different in 1D and 1Dlike models for the same WS elevation.

Inverse calibration In the following comparison, power-law parameters α and β are obtained using VDA in a twin experiment setup. Observations are taken at two stations (Fig. 3.12). Prior values are $\alpha = 0.05\,\mathrm{s/m^{1/3}}$ and $\beta = 0$.

The classic friction law and a power-law with calibrated parameters are compared in Fig. 3.12 during a varied flow event. A range of water depth higher than the “bankfull” depth used

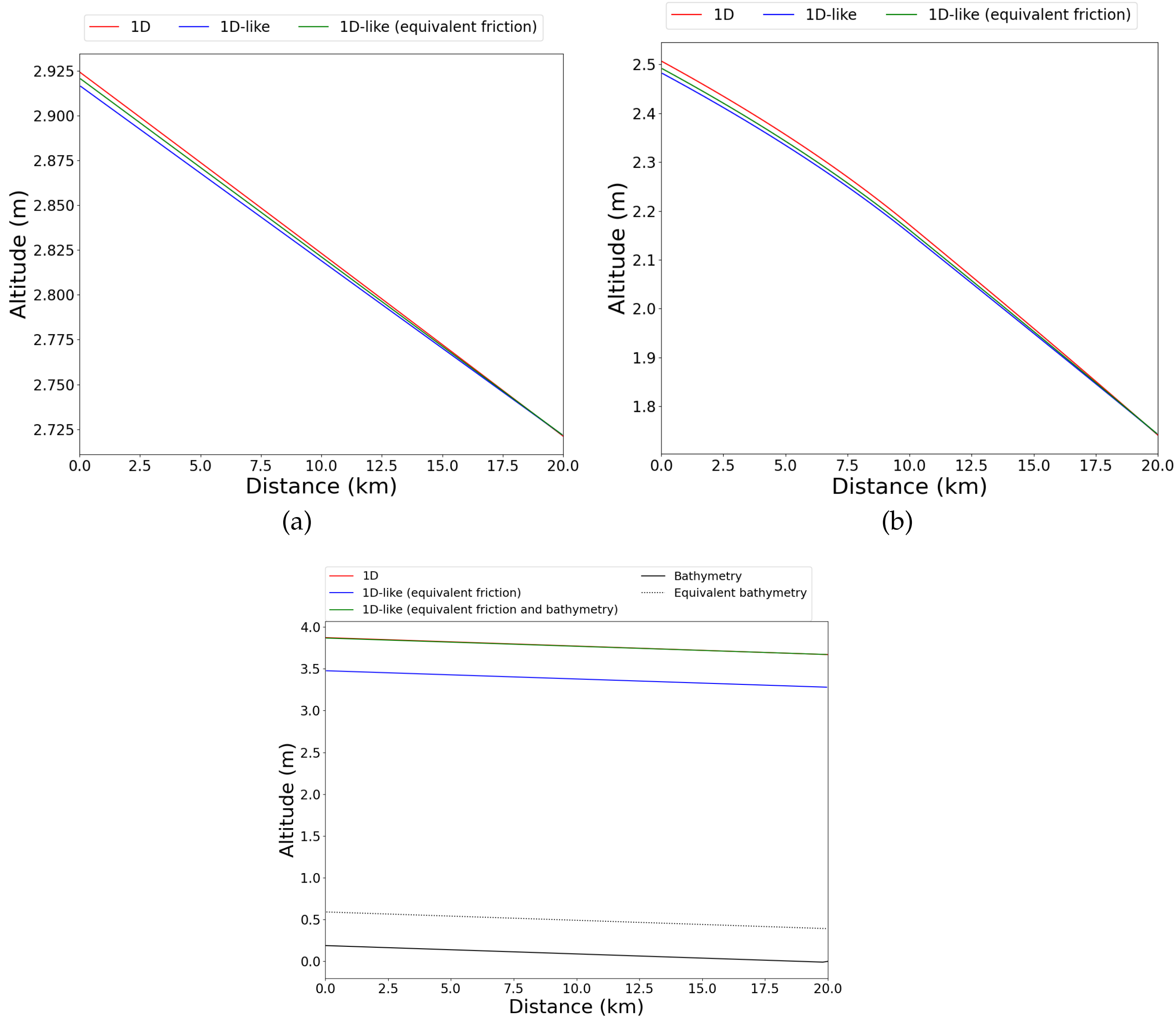

(a) (b)

(c)

Figure 3.11: Effective friction analysis for steady waterline in academic cases: (a) rectangular channel with constant slope, (b) rectangular channel with slope break, (c) parabolic channel with constant slope. Values of effective friction parameter α $\left[\mathrm{s}/\mathrm{m}^{1/3}\right]$: (a): 5.06×10^{-2}, (b): $(5.06 \times 10^{-2}, 5.04 \times 10^{-2})$, (c): 5.46×10^{-2}. Bathymetric shift δ_b [m]: (a): 0 , (b): 0 , (c): 0.591.
1D reference model: fixed time step 5 s spatial step 100 m; average Courant number equals 0.26
1Dlike models: adaptative time step with mean value of 9 s; 1Dlike cell length 100 m; average Courant number equals 0.48.

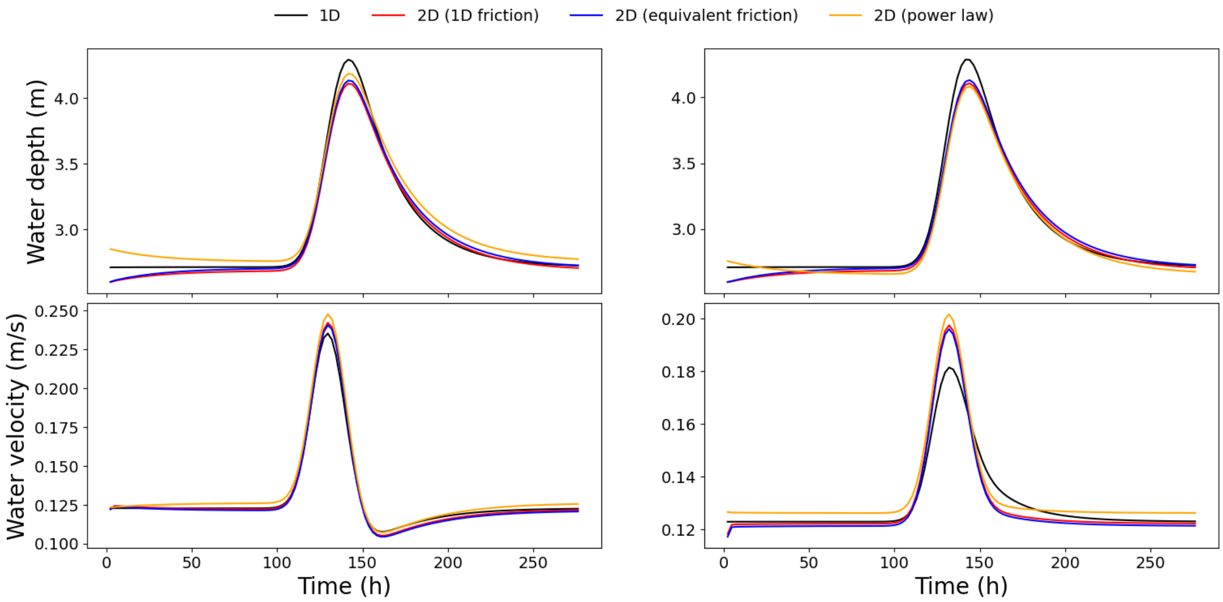

Figure 3.12: Effective friction analysis for an unsteady waterline in case (a). The power-law is given by $n = \alpha h^{\beta}$, with $\alpha = 0.0446$ and $\beta = 0.0634$. The injected hydrograph is symmetrical. Observations stations are at $x = 2.5\,\text{km}$ and $x = 7.5\,\text{km}$. Adaptative time step with average value of 13 s. 1Dlike cell length: 200 m. Average Courant number: 0.33.

to calculate equivalent friction parameters is simulated. This results in an increase in misfit to the 1D WS elevation at high flow (Fig. 3.12, in blue and red). The calibrated friction power-law (in orange) somewhat reduces the misfit during high flows in this simple synthetic channel and within the simulated water depth range.

3.4.2.3 Multi-D hydraulic-hydrological data assimilation

Temporal forcings inference

Simple inference tests are carried on the confluence case from Subsection 3.4.2.1, following Pujol et al. [2020], in a twin experiment setup. A control vector $c = (Q_1(t), Q_2(t))$ is considered, where Q_1 and Q_2 are sinusoidal inflow hydrographs injected at the upstream cell of the two upstream reaches. Pujol et al. [2020] shows that the minimal requirement to infer multiple spatially distributed temporal forcings simultaneously is to observe either (a) both of their unmixed signatures, at 1 point each, or (b) one of their unmixed signatures at 1 point and their mixed signatures at a second point. We verify this for configuration (b). Unmixed signatures observations are generated at a 1Dlike cell of the upstream reaches, mixed signatures observations are generated at a cell in the 2D part (Fig. 3.13, left, red crosses). Prior values for the inflow hydrographs are constant and set to their average value $\left(Q_1(t) = Q_2(t) = 100\,\text{m}^3/\text{s}\right)$. Using sets of two observations points, we are able to reproduce the results of Pujol et al. [2020] but with the proposed multi-D hydraulic model: the VDA algorithm enables to infer Q_1 and Q_2 close to perfectly from configurations (a) and (b) (Fig. 3.13, right).

Hydrological parameters inference

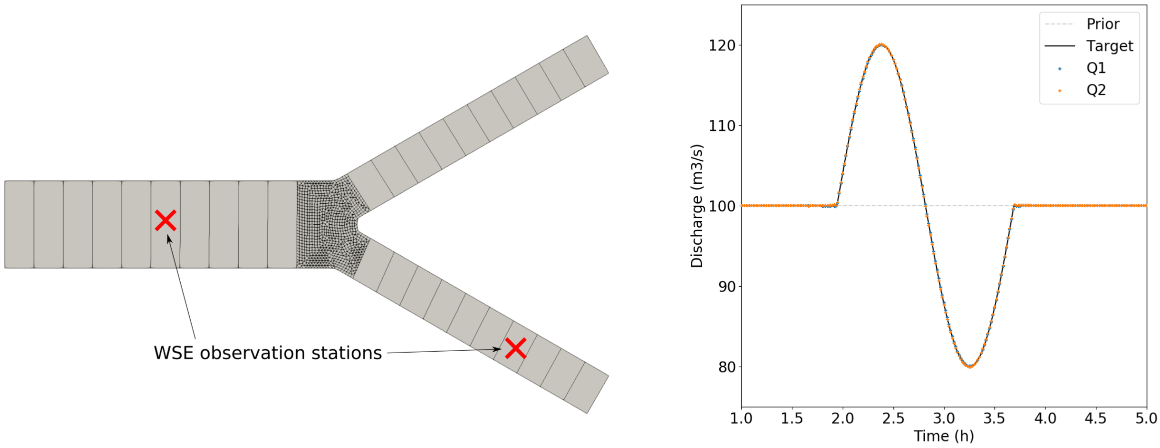

Figure 3.13: Inflow hydrographs inference on confluence synthetic case in observation setup (b) with one station on a reach upstream of the confluence and one observing mixed flows downstream in the 2D part (see mesh on the left). Given sufficient observability and an unbiased prior, inferred hydrographs (in blue and orange) are both at target (black, total overlap). The flow is subcritical with a maximum Froude value of 0.05.

In this second twin experiment, the issue of spatially distributed calibration of a hydrological model is studied, from multi-source observations of the river network. The confluence case above is used and this time, the upstream inflows are generated by GR4H module applied on two upstream catchments inflowing the hydraulic module. For each catchment, synthetic rain and evaporation time series and a hydrological parameter set $\theta_{rr} = (c_1, ..., c_4)$ are used to generate a discharge time series over a 1-year period (not shown). Mixed observables are used: WS elevation is observed at a single downstream point and hydrological model discharge is observed at the outlet of one of the catchments. They provide the same signal observability - mixed and unmixed signals - as in the above paragraph but with observations of different nature. Since the observed variables are of different nature and amplitude, we introduce a normalization. The cost function is here $j_{obs} = j_Z + j_Q$, with each term being normalized by the number of observations and by their range of variation such that: $j_Z = \frac{N_{o,Z}T_Z}{N_{o,Z}T_Z+N_{o,Q}T_Q} \frac{1}{(Z_{o,max}-Z_{o,min})^2} \sum_{1}^{N_{o,Z}} \sum_{1}^{T_Z} (Z_o(t) - Z(\theta,t))^2$ and $j_Q = \frac{N_{o,Q}T_Q}{N_{o,Z}T_Z+N_{o,Q}T_Q} \frac{1}{(Q_{o,max}-Q_{o,min})^2} \sum_{1}^{N_{o,Q}} \sum_{1}^{T_Q} (Q_o(t) - Q(\theta,t))^2$.

Those correspond to two separate normalized squared RMSE with $N_{o,Q}$ and $N_{o,Z}$ denoting the number of observations station and T_Q and T_Z the number of observation time steps.

The control vector $c = (\theta_{rr1}, \theta_{rr2})$ contains the two sets of 4 hydrological parameters each. For this synthetic case, an inequality constraint of the control parameters is imposed with the bounded L-BFGS-B algorithm (Zhu et al. [1997]). Indeed, restricted research intervals are considered for the three first parameters of each catchment, namely a 5% bracket around their target values used as prior, while c_4 is sought in its expected variation range from an erroneous prior (Table 3.2). Expected ranges for GR4H parameters are provided in Le Lay [2006], for the classical GR4 formulation.

In this setup, both j_Q and j_Z are reduced during the iterative steps and the inferred value for

Parameters	c_1	c_2	c_3	c_4
Target	520.01	-3.523	78.75	0.137
Prior				0.167 / 0.107
Inferred	520.00 / 519.46	-3.654 / -3.820	80 / 80	0.136 / 0.137

Table 3.2: Hydrological parameter inference results. Prior values are taken identical to target values, except for parameter c_4, where under- and over-estimated prior value are considered. Inferred value for all parameters including c_4 are very close to the target. The "/" separates values for the 2 distinct hydrological units.

both c_4 parameters are very close to the target value starting from an erroneous prior (Fig. 3.14, right). Bounded parameters c_1 and c_2 vary slightly between their bounds, while c_3 is locked at its lower bound from the first iteration.

3.4.3 Real cases

3.4.3.1 Garonne river: 1Dlike effective model of a 2D reference case

A 1Dlike model of a reach of the Garonne river, in southern France, is built from real data and calibrated here via assimilation of spatially distributed WS observations in a twin experiment setup. A full 2D model of 75 km of the Garonne river (not shown, 867 500 cells including floodplains, average edge length ∽ 25 m) is used to generate real-like observables on this well known case (Garambois and Monnier [2015]; Brisset et al. [2018]; Larnier et al. [2021]; Monnier et al. [2016]). First, river extent is derived from the 2D model output at bankfull flow $Q = 400\,\mathrm{m^3/s}$ with an homogeneous friction $n = 0.05\,\mathrm{s/m^{1/3}}$. This extent is in turn used to build a 1Dlike mesh, over the whole reach: single quadrangular cells cover the whole river width and are linked sequentially along the river reach (Fig. 3.15). 1Dlike cell interfaces are perpendicular to the flow direction, as would be XS in a 1D model. Each cell is about 100 m in longitudinal length. This mesh was generated using the SMS meshing tools. Cell bathymetry is first set using the lowest bathymetry point at each corresponding 2D XS.

Permanent bankfull flow calibration

A first expectedly imperfect 1Dlike model (Model A1) is built using the 1Dlike coarse mesh and expectedly underestimated bathymetry elevation, and an homogeneous friction parameter of $0.05\,\mathrm{s/m^{1/3}}$. The simulated steady WS elevation at bankfull flow is lower than that of the 2D model (average misfit of 0.858 m), which is expected since the 1D bathymetry is that of the lowest point of the 2D XS (Fig. 3.5). Furthermore, the 1Dlike friction is underestimated and leads to an underestimated simulated water depth (and flow surface). The WS elevation misfit does not seem to follow a significant trend from upstream to downstream, although it varies sharply at points of width variation (Fig. 3.16, e.g. around cell 410). Recall that the goal of this effective modeling approach is to accurately reproduce water surface signatures, including WS elevation and, tangentially, flow section (Subsection 3.3.2.2).

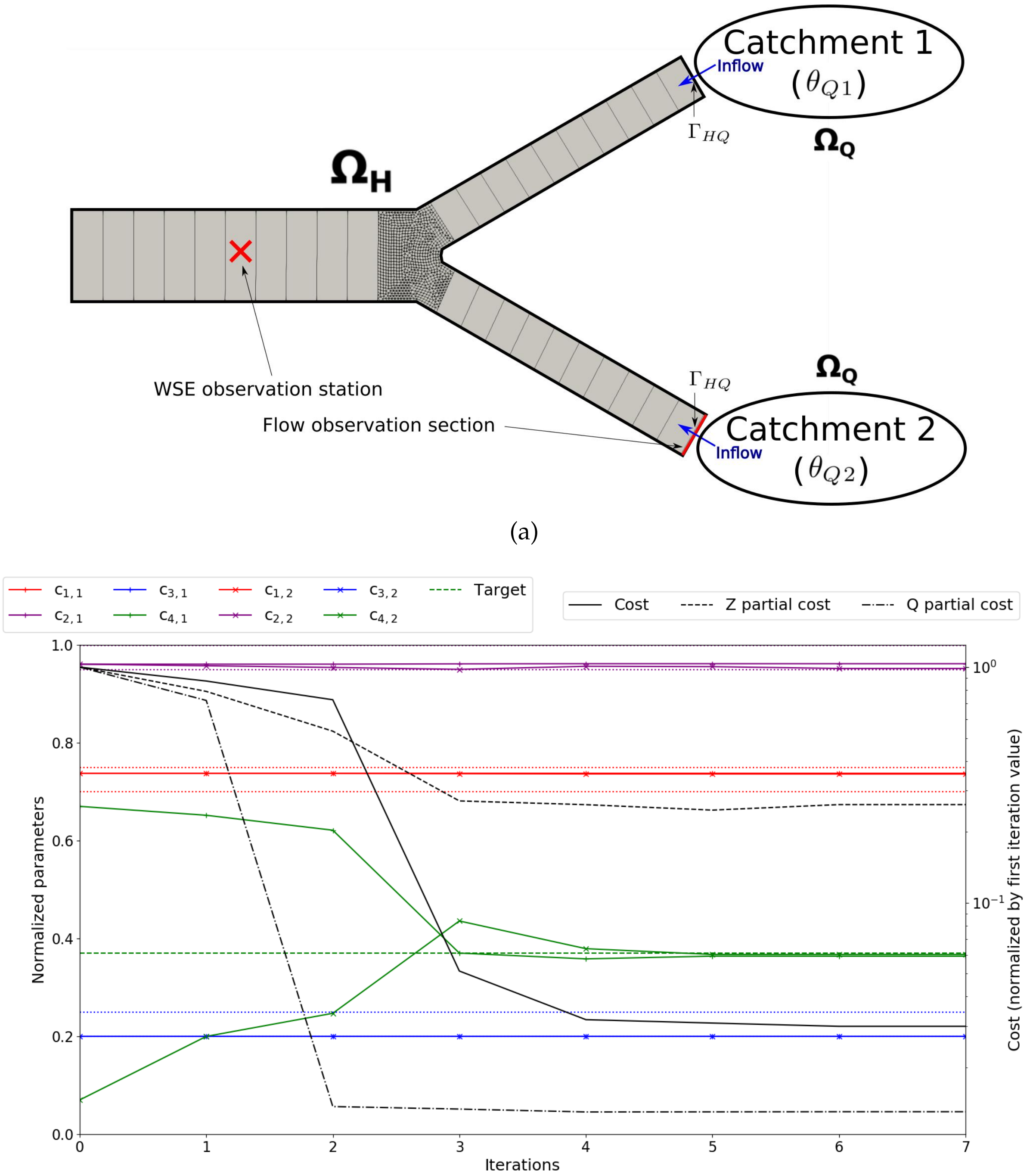

(a)

(b)

Figure 3.14: Simultaneous inference of GR4H hydrological parameters in two catchments from multi-source observations: WS elevation and flow observations.
(a) Multi-D hydraulic mesh and modeled hydrological catchments. Hydrological discharge at the outlet of Ω_{rr} is inflowed upstream in Ω_{hy}. Observation stations (red cross and red line) are used for inferring hydrological parameters.
(b) Inference of 2 sets of 4 hydrological parameters: normalized costs and parameter values over the course of the iterative optimum search. The x_4 background values are erroneous. x_1, x_2 and x_4 background values are set to target values.

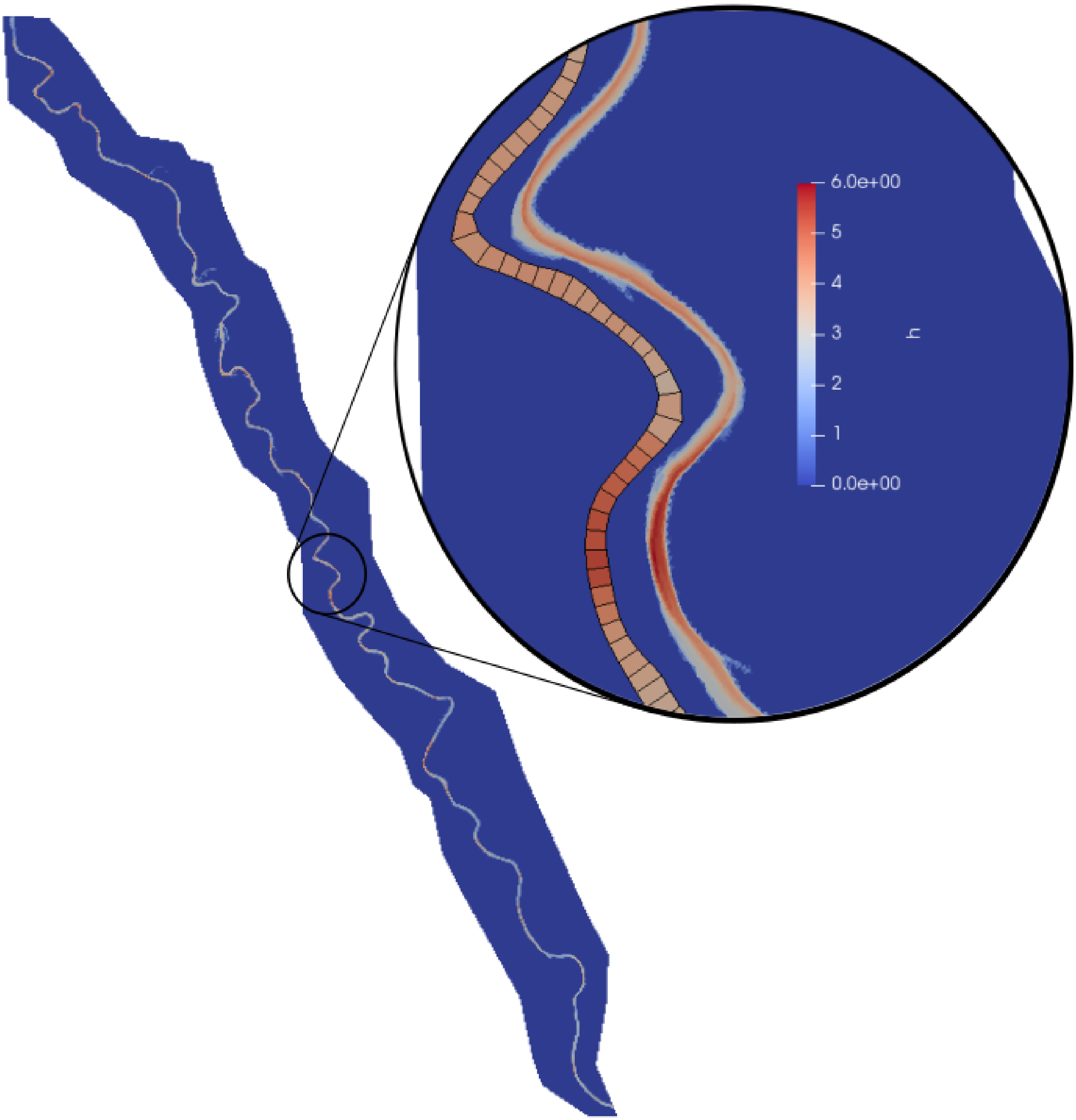

Figure 3.15: Garonne 2D model extent and simulated water depths using the 2D model and the 1Dlike model for a non-flooding event

Calibration by hand

We here propose to reduce the misfit using, on one hand, effective friction and, on another hand, bathymetry as follows. In Model A2, the introduction of an equivalent friction parameter (Eq. 3.2), calculated at each 1D cell using observations from 2D XSs, improves the WS elevation misfit (mean friction of $n = 0.062\,\mathrm{s/m^{1/3}}$, average WS elevation misfit of 0.562 m). It reduces misfit overall, but has no significant local influence (Fig. 3.16). In Model A3, we use the average WS elevation misfit from Model A2 to create a simple bathymetry shift δ_b that helps fit the observations. Equivalent friction parameters from Model A2 are kept and all bathymetry points are shifted by $\delta_b = 0.562\,\mathrm{m}$ (the bottom slope is conserved). The average WS elevation misfit at bankfull flow reaches 0.003 m for Model A3, which is a very satisfying result.

Calibration by VDA

Now, the same calibration problem is addressed with an inference based on the VDA method. It is applied to the same reference model permanent flow waterline, observed at each cell. The control vector contains a single homogeneous friction parameter, as before, and spatialized bathymetry $b\left(x\right)$ for each cell. To constrain the parameter search, two VDA processes are performed separately: a bathymetry regularization and a change of variable. Inference with bathymetry regularization leads to Model B1, with $\gamma = 1$ (Subsection 3.3.4). Inference with change of variable (Eq. 3.8) leads to Model B2, with $L_b = 500\,\mathrm{m}$ (Eq. 3.12). Both models lead to average misfits close to that of Model A3: 0.0839 m and 0.0844 m respectively.

Two other inference setups based on Model B1 are considered. The number of observations is divided by 10: 72 stations, homogeneously distributed at 1 per each 1 km, are considered. In Model B1a, no regularization term is considered ($\gamma = 0$). In Model B1b, a regularization is added ($\gamma = 1$, chosen by trial and error). This weight can be optimally determined using iterative regularization (Malou and Monnier [2022]). It is dependent on the spatial scales of observed signals and on the discretization of inferred parameters. As presented in Fig. 3.16 and in Table 3.3, both inferences lead to low misfits of the 2D permanent WS elevation. The regularization tends to reduce extreme bathymetric variations that tend to appear far from the observation points. The iterative minimization process can be followed through the cost function value and the parameter gradients (Fig. 3.17). Values are normalized over their initial (iteration 0) value. For Model B1a, the optimal control is reached after 40 iteration (for a normalized cost of 8.6×10^{-10}), while for Model B1b it is reached in 85 iterations (for a normalized cost of 5.5×10^{-5}). Both models follow the same trajectory up to around iteration 12, where the regularization term j_{reg} reaches the same order of scale as the WS elevation misfit term j_{obs}.

Variational calibration of channel parameter has allowed to fit a permanent regime water line. The following paragraphs study the reproduction of propagation in a calibrated models during a varied flow event.

Variational calibration for a flow event

Let us now consider a varied flow event, without flooding in the 2D model. This event last 10 days, with a peak discharge of $702\,\mathrm{m^3/s}$ at the start of day 2, a minimum discharge of $160\,\mathrm{m^3/s}$ and and average discharge of $382\,\mathrm{m^3/s}$. Given our previous inference attempts, we know that we can find a couple $\left(n, b\left(x\right)\right)$ or $\left(n, \delta_b\right)$ that minimizes the average misfit. For the

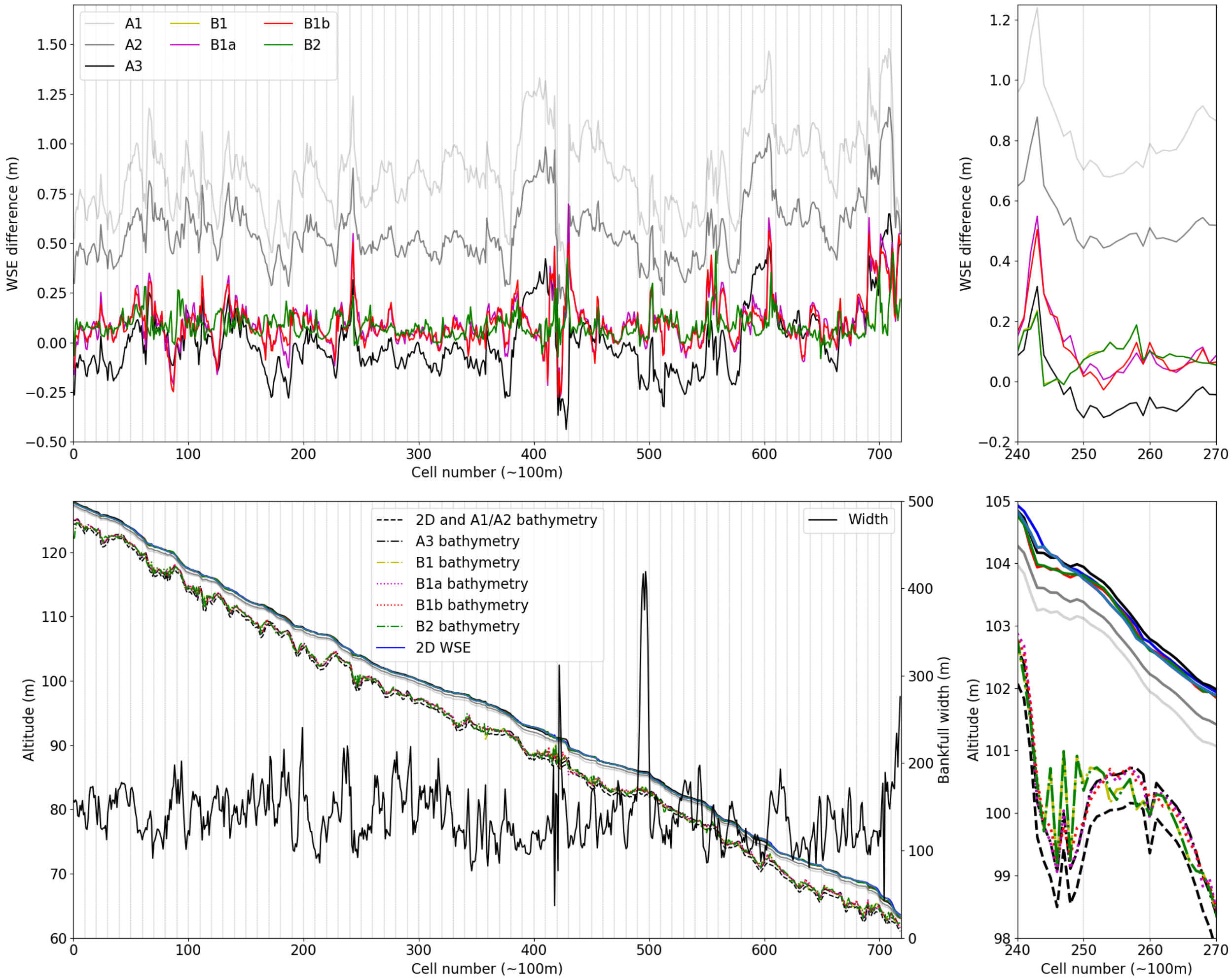

Figure 3.16: Comparison of 7 1Dlike models of 72 km of the Garonne river to a reference 2D SW fine model for a permanent flow (reference WS elevation in blue lines, bottom).
(Up) Left: WS comparison of 1Dlike models to 2D reference model at each spatial point. Right: Zoom on 3 km long reach of interest.
(Down) Left: WS elevation and bathymetry for the reference and 1D like models. Right: Zoom on 3 km long reach of interest.
For models A1, A2 and A3 (in grays), the bathymetry and homogeneous friction are manually calibrated. For model B1 (yellow), B1a (magenta), B1b (red) and B2 (green), the bathymetry and friction are calibrated by VDA. For models B1 and B2, inferences are carried out from observations at each cell (720 total). For models B1a and B1b, inferences are carried out from observations every 10 cells (i.e. around every 1 km, 72 stations total). Vertical bars indicate these 72 stations.

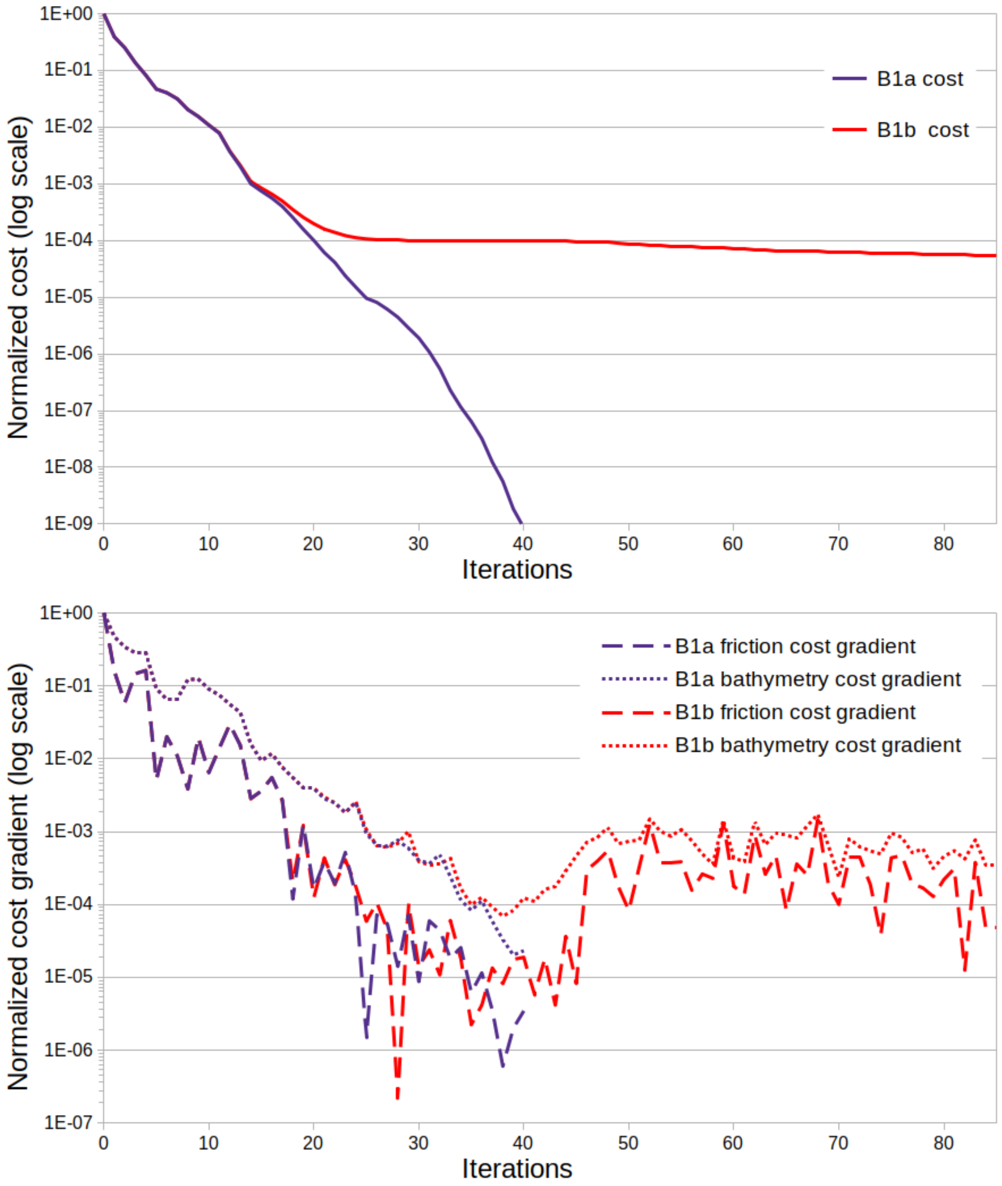

Figure 3.17: Normalized cost functions and gradients for inferences of distributed bathymetry and homogeneous friction, from 72 observation stations, in models B1a and B1b. Top: Total cost normalized by initial cost $j(\theta)/j\left(\theta^{(0)}\right)$ vs iterations. Bottom: Cost gradients normalized by initial gradient for the inferred parameters vs iterations.

Model name	Calibrated parameters	Calibration method	Flow regime	Obs. density	n or α	β	δ_b	Rel. misfit (PR)	RMSE (PR)	NSE (Varied)
2D	-	-	-	-	0.5	0	0			--
A1	-	Manual	PR	High	0.5		0	0.858	0.881	
A2	n				0.062		0	0.562	0.585	
A3	n, δ_b				0.062		0.562	0.003	0.167	
B1	$n, b\,(x,y)$	VDA			0.059		-	0.084	0.106	
B1a				Low	0.059			0.099	0.157	
B1b					0.057			0.099	0.152	
B2				High	0.059			0.084	0.157	
C	n, δ_b		Varied	High	0.054		0.669	-	-	0.99
D	β, δ_b				0.054	-0.017	0.099			0.98

Table 3.3: Garonne models parameters and metrics. "PR" stand for Permanent Regime. "High" observation density corresponds to 720 stations, or 1 station per 100 m. "Low" observation density corresponds to 72 stations, or 1 station per 1 km.

sake of simplicity, we consider the couple (n, δ_b). For a varied flow event, this couple would be an optimal parameterization for the average observed water line. A first inference trial is carried out for a densely observed (in space and time) varied flow. Using Model A1 as a prior for bathymetry and friction and observations from the 2D model, we find the following optimal parameters: $\left(n = 0.054\,\mathrm{s/m^{1/3}}, \delta_b = 0.669\,\mathrm{m}\right)$. The resulting optimal model is Model C.

To allow a better fit during high and low flows, we introduce the friction power-law $n = \alpha h^{\beta}$ (Subsection 3.3.2.1). Using observations from the 2D model during the varied flow event, we infer the couple (β, δ_b). The value of α is set to $0.054\,\mathrm{s/m^{1/3}}$, the inferred value from Model D. Three different β priors are tested: -0.5, 0, 0.5. δ_b is included in the control vector to allow modeling of more varied water depths, which may be needed to reach the optimum. All three inferences lead to the very close optimal control. Their averaging, a slight bathymetric shift $\delta_b = 0.099$ m and $\beta = -0.017$, leads to Model D. The direct simulation results of Model D is compared to the reference model. They correspond to an average WS elevation misfit of 0.026 m at high flow and of 0.11 m at low flow. Compared to Model C (average misfit of 0.086 m and 0.20 m at resp. high and low flow), this is an improvement. Note that NSE values for both model (Table 3.3) are both extremely close to 1.

The variational calibration of the global bathymetric shift δ_b and of an homogeneous friction value n in a 1D-like model has allowed to closely fit WS elevation observations of a 10 days flood wave over the reference Garonne model. The calibration of depth-dependent friction, in the form of the β parameter in $n = \alpha h^{\beta}$, has allowed an even closer fit to this reference WS elevation over the high and low flows, i.e. a better representation of the observed flood wave propagation.

3.4.3.2 Adour basin: multi-D hydrological-hydraulic model

The whole hydrological-multi-D-hydraulic tool chain is now tested in a real context both for forward and inverse problems resolution. A real and complex basin case is now considered: the Adour river basin in the South West of France, with a total drained area of 16 890 km^2 at the estuary. It is probably one of the most difficult basins to model in the country, because of contrasted hydrological regimes including nival effects in the south, flash floods on small ungauged catchments, complex river network morphology, anthropized floodplains and tidal effects from downstream.

In this section, a multi-D model, composed of 1Dlike meshes and 2D zooms over floodplain area is built from available data (Fig. 3.18, 2D area in green). Then, forward and inverse flow simulations on the river network are presented.

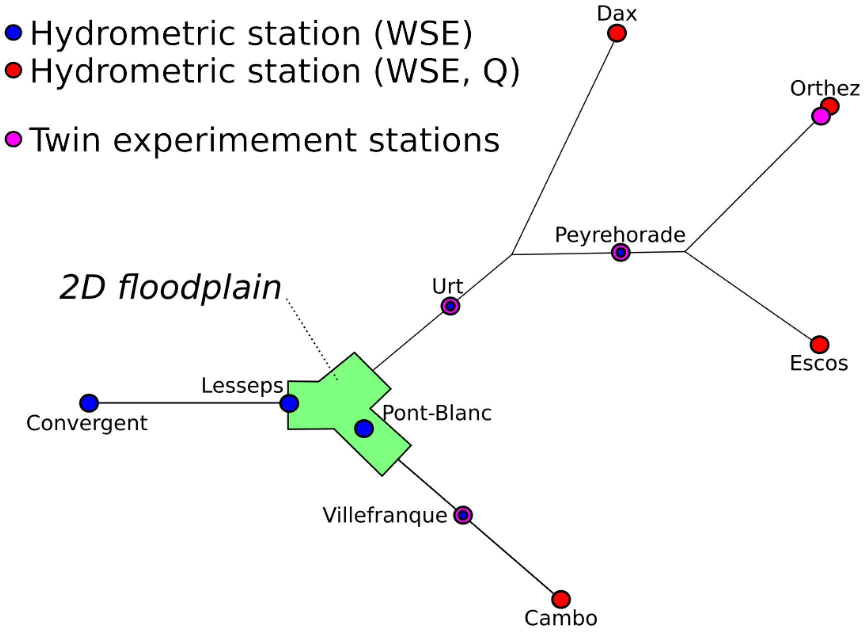

Figure 3.18: Schematic view of the complete Adour river network and observability. Dimensions are not respected: total river lengths equal ≈ 180 km, 2D floodplain area equals $\approx 5 \times 3\,\mathrm{km}^2$. Tidal BC influence (from the downstream BC at Convergent) is observed up to Dax (and further upstream), Peyrehorade and Villefranque.

Model construction and rainfall to inundation simulation

The following model of the Adour river combines a multi-D hydraulic network model and several hydrological models of sub-catchments (Fig. 3.18). It encompasses around 180 km of river reaches and includes the Adour river from its tidal boundary downstream of Bayonne up to a gauging station around 70 km upstream, and part of its main tributaries: the Nive river (around 45 km), the Oloron and Pau rivers (around 65 km in total). The river networks contains mostly single-branch reaches, with some notable flood areas around the city of Bayonne. The WS is observed in situ at 10 points, 5 of which are used as boundary conditions (Dax, Orthez, Escos, Cambo and Convergent, red points in Fig. 3.18). Out of the 5 remaining stations kept for data assimilation, 3 are located on river reaches (Peyrehorade, Urt and Villefranque, blue points in Fig. 3.18) and 2 are located in the Bayonne area (Pont-Blanc and Lesseps, blue points in Fig. 3.18).

At the 4 upstream points of the modeled river network, 4 sub-catchments are modeled with 4 lumped hydrological models (Subsection 3.3.3). Their drainage areas are respectively about 7811, 842, 2480 and 2464 km^2. The hourly discharge have been extracted from the HYDRO[3] database while the rainfall data from the radar observation reanalysis ANTILOPE J+1, which merges radar and in situ gauge observations, is provided by Météo France. The interannual temperature data is provided by the SAFRAN reanalysis, Météo France, and then used to calculate the potential evapotranspiration using the Oudin formula Oudin et al. [2005]. The rainfall and PET are at a spatial resolution of 1 km^2 square grid, and processed into hourly time step. Spatial averages of the rainfall and PET computed with SMASH distributed platform (Jay-Allemand et al. [2020]; Colleoni et al. [2021]) over the 4 catchments are used as inputs for the lumped GR4H model. Lumped parameter sets for the 4 GR4H models are simply obtained here using for each the airGR global calibration algorithm (Coron et al. [2017]). In this section, inferences are carried out only for upstream inflow hydrographs, not hydrological parameters. Indeed, the study of global calibration and regionalization issues of spatially distributed hydrological models is left for further research.

Our multi-D hydraulic modeling approach (Section 3.3) is applied to this complex case as follows. First, a "1Dlike-only" model of the whole network is built. Then, a multi-D model is built based on the "1Dlike-only" model, with the addition of a 2D mesh of a floodplain (Fig. 3.19, left).

On the "1Dlike-only" model, the goal is to analyze 1Dlike signal propagation representation at a low computational cost. The Adour 1Dlike model is built similarly to the Garonne 1Dlike model, using DEM data to determine minor bed bank line placement and build the quadrangular cells. Bathymetry comes from 25 × 25 m DEM data, aggregated from fine LiDAR data from public databases, extracted at each cell. This rough approximation is sufficient to show the potential of the DassFlow assimilation tool chain on a large scale river network. This "1Dlike-only" model contains 1409 cells.

Then, a multi-D model is obtained: the existing 2D mesh from a Telemac model is coupled to a 1Dlike mesh, similarly to the reference Telemac-Mascaret model from the regional flood forecast center SPC-GAD. The 1Dlike parts of the mesh are kept identical to the "1Dlike-only" model, while the 2D part is the mesh extracted from the Telemac-Mascaret model (Fig. 3.19, left) provided by SPC-GAD. For hydraulic coherence, bathymetry at coupled 1Dlike cells are taken as the average bathymetry of the linked 2D cells. This "1D2D" model contains 66 982 cells in the 2D area and 1342 cells in 1Dlike reaches. Results for a flooding event in the Bayonne 2D area are presented in Fig. 3.19, on the right. Modeled variables appear coherent over the 1D2D area and a high resolution flood map in coherence with flow conditions in the whole river network is obtained.

A 1 day (physical time) flooding event is computed in around 20 min (computation time) in the "1D2D" model (with 68 324 total cells, 6 threads in parallel). The same event leads to a 7 s computation time for the "1Dlike-only" model (with 1409 cells, same computational setup). Remember that computation time may vary depending on the number of wetted cells and on the adaptative time step calculation. This relatively low computation time, and the potential to decrease it further by using more threads in parallel, indicate that this multi-D method is suited to operational use. The code version this work is based on was proven scalable (Couderc et al. [2013]). Additions made to the current version should not change this, but no numerical testing

---

[3] http://www.hydro.eaufrance.fr ; french ministry in charge of environment

has been done.

Assimilation of WS observables to infer 4 upstream hydrographs

To investigate the 1Dlike effective modeling on a river network, a twin experiment setup is designed to infer large control vector from a realistic observability on the "1Dlike-only" model.

The considered control vector composed of the 4 upstream hydrographs is:

$$c = \left(Q_{Dax}\left(t\right), Q_{Esc}\left(t\right), Q_{Ort}\left(t\right), Q_{Cam}\left(t\right)\right) \tag{3.13}$$

Observations of WS elevation are generated at Peyrehorade, Urt and Villefranque stations, and additionally at a virtual station directly downstream from Orthez. These 4 points give theoretically sufficient observability to identify the 4 upstream hydrographs. Indeed, they sample mixed and unmixed signal similarly to the academic setup in Subsection 3.4.2.1). The observation pattern also corresponds to a reasonable expectation of spatial observability in French river networks. Prior hydrograph values are classically set to a constant average discharge value.

Simultaneous inference of the 4 hydrographs is satisfying. As shown in Fig. 3.20, left, upstream hydrographs injected at Cambo and Orthez are inferred very accurately ($NSE > 0.95$). This is due to their WS elevation signature being observed "unmixed" in the respective downstream reaches. The Escos hydrograph WS signature is observed at Peyrehorade, mixed with the Orthez hydrograph WS elevation signature. This leads to partial error of signature attribution and a less accurate inference ($NSE = 0.57$). The Dax hydrograph WS elevation signature is observed only at the Urt station, where its signal is mixed with that of Escos and Orthez. The resulting inference is the less accurate with a NSE of 0.50 and closer in shape to the inferred Escos and Orthez hydrographs. This hints at correlated influences of these hydrographs at observation stations and insufficient observability of the Dax hydrograph signal given the model hydrodynamics. Observed signals at the 4 stations are however all very accurate (Fig. 3.20, right). For upstream stations (Orthez and Villefranque), this is due to the accurate inference of upstream hydrographs. For stations under the influence of the tidal BC (Peyrehorade and Urt), this is due to the backwater influence of the BC, which compensates for the error in inferred hydrographs (namely at Dax, and less so at Escos).

In conclusion, this experiment shows the capability of the VDA tool chain to infer various upstream hydrographs on 1Dlike network models. Note that multi-D models are identical to the investigated 1Dlike model in terms of VDA capabilities. It paves the way towards investigations on multi-variate inferability of spatially distributed hydraulic-hydrological parameters.

In the future, investigation on the influence of data sparsity, observation weights and ill-posed problem constraints should be carried out.

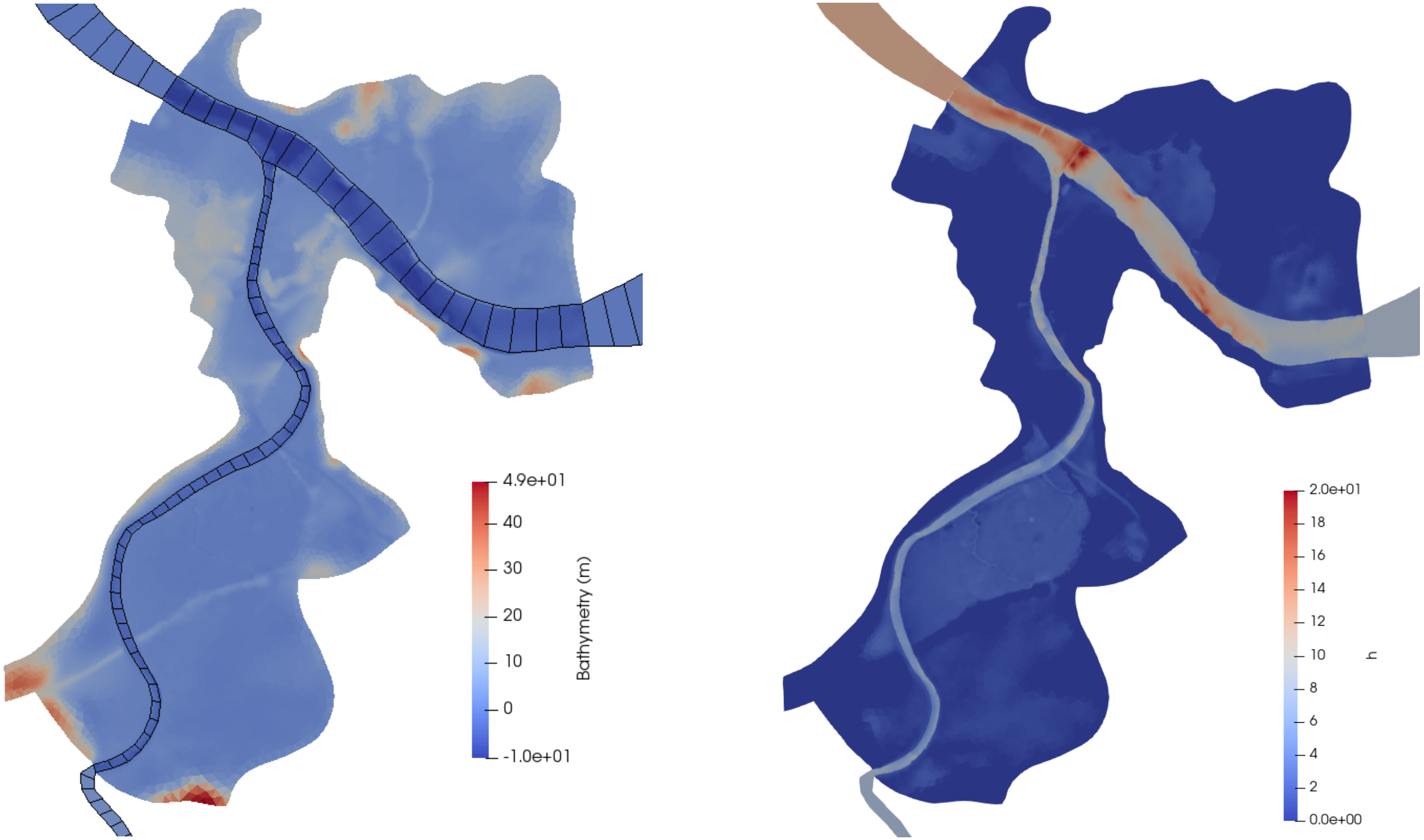

Figure 3.19: Zoom on the Bayonne area (green area in Fig. 3.18) using the 1Dlike and 1D2D approaches. Manning values are homogeneous throughout the network and floodplains at 0.05 s/m$^{1/3}$.
Left: Bathymetry in 1Dlike and 2D meshes. The 2D area has 66 982 cells and the coupled 1Dlike reaches account for 1342 cells. The south, east and west interfaces respectively feature 6, 18 and 14 2D cells. The exclusively 1Dlike mesh contains 1409 cells.
Right: Simulated water height for the 1D2D model for a sample flooding event (low tide, $Q_{Adour} = 650\,\mathrm{m}^3/\mathrm{s}$ and $Q_{Nive} = 58\,\mathrm{m}^3/\mathrm{s}$ at 1D2D interfaces).

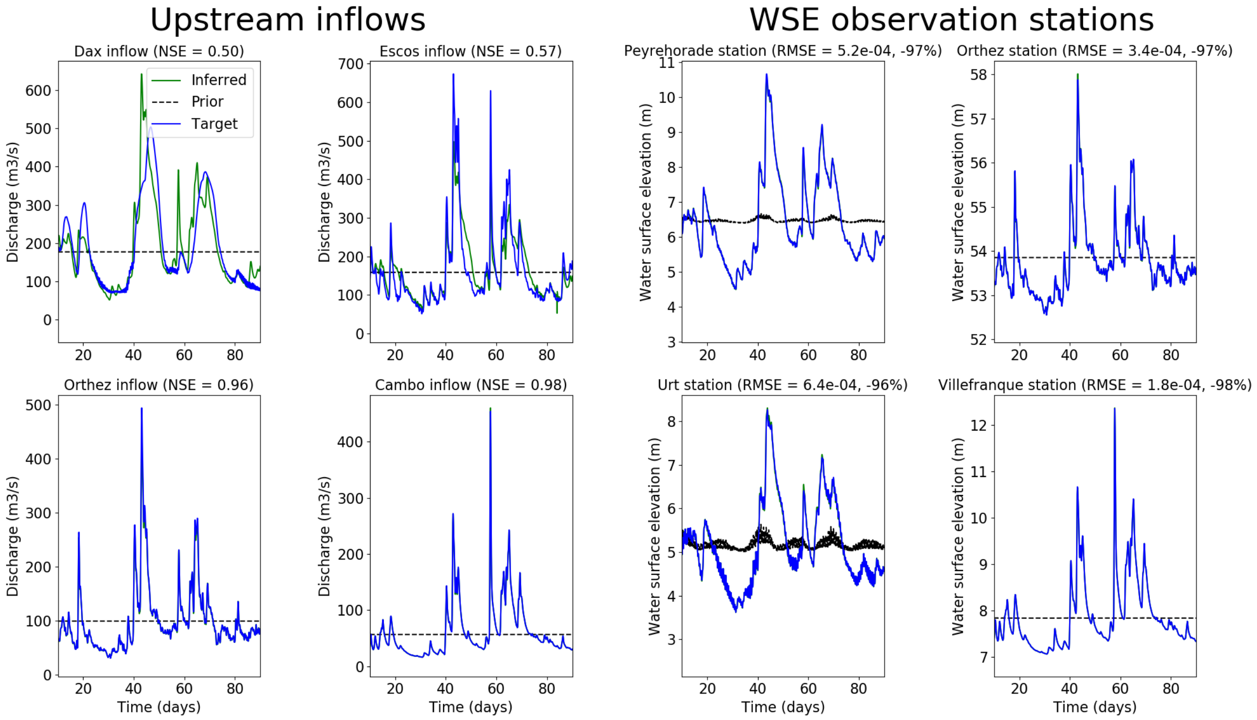

Figure 3.20: Upstream hydrograph inferences from 4 observation stations in twin experiment setup.
Left: In blue: upstream inflow hydrographs used to generate observations. In green: inferred hydrographs at 20 iterations. Dotted lines: background hydrograph value given for iteration 0 (mean target inflow over assimilation window). NSE values are given for their informative value but are not used in the assimilation process.
Right: In blue: target WS elevation. In green: WS elevation generated by the inferred hydrographs. Dotted lines: WS elevation generated by the background hydrographs. Downstream tidal boundary influence is felt at the two most downstream stations (Urt and Peyrehorade). RMSE value given are used to calculate cost in the assimilation process (Section 3.3.4).

3.5 Conclusions and perspectives

This article presents a new approach and numerical chain for the multi-D hydrological-hydraulic modeling of complex river networks with variational data assimilation capabilities. It is based on the VDA algorithm and the finite volume solvers (including second order one and accurate treatment of wet/dry front propagation) from Monnier et al. [2016]. The resolution of the full 2D shallow water equations (3.1) is performed with a single finite volume solver applied on a multi-D discretization of a river network domain. This lattice consists in “1Dlike” reaches meshed with irregular quadrangular cells connected, via 1Dlike-2D interfaces, to 2D zooms consisting in higher resolution unstructured meshes - either triangular or quadrangular. This hydraulic model is inflowed with a hydrological model enabling to describe upstream/lateral catchments inflow hydrographs. In this work, the parsimonious GR4 model is integrated (Perrin et al. [2003]), in its state space version (Santos et al. [2018]) for the sake of differentiability (for the VDA computations). This approach is implemented in the platform DassFlow (Couderc et al. [2013]). The adjoint of the whole tool chain is generated with Tapenade (Hascoet and Pascual [2013]) and validated. Forward-inverse capabilities with the new components is assessed on several cases of increasing complexity.

The 1Dlike effective hydraulic modeling approach as well as its coupling with higher resolution 2D zooms was validated, against: 1) reference 1D and 2D hydraulic models, on an array of academic; 2) complex real cases featuring 1D and 2D flow variabilities in river networks with confluences and floodplains. Those cases are also employed to test the coupling with the hydrological model implemented in a semi-distributed setup.

Considering single (resp. multiple) type(s) of flow signatures observations in those river networks through a single-(resp. multi)-objective observation cost function, the capabilities of the VDA method for inferring mono/multi-variate control vectors of large dimensions was successfully tested.

From the obtained results, the following conclusions can be raised:

1. A complete integrated multi-D model coupled with an hydrological model has been implemented and validated in a parallel environment. Moreover, this complete tool chain includes VDA capabilities based on the adjoint code.

2. The 1Dlike modeling approach enables to simulate fine physical flow states compared to reference 1D or 2D SW models; hydrograph propagation remains very close also.

3. The inference, from heterogeneous observations in the river network, of multi-variate controls among multiple inflow discharge hydrographs, bathymetry, friction of the multi-D hydraulic model but also hydrological model parameters is demonstrated. Very accurate inferences are obtained when the available information contained in system observability and priors is sufficient regarding the nature and quantity of unknown parameters (see discussion in Brisset et al. [2018]; Larnier et al. [2021]; Garambois et al. [2020] and references therein).

4. Information feedback from the river network to upstream hydrological models of subcatchments is shown.

5. Real flows on complex channel geometries can be accurately simulated with the 1Dlike model, despite its intrinsic rectangular XS, thanks to the calibration of effective geometry-friction patterns. The depth-dependent friction law helps to reduce misfits across flow regimes.

6. High resolution simulations of real flows can be obtained on complex river networks including floodplains and confluences with reduced simulation costs.

To our knowledge, the present numerical tool is the first one proposing, large scale multi-D river network modeling with VDA capabilities.

Short term perspectives will aim to taylor the data assimilation algorithm to perform complex data assimilation experiments at basin scale using various multi-source datasets. To be actually operational, improvements pertaining to the construction of 1Dlike models from global public databases are needed to deploy the multi-D approach to a large number of river networks. Coupling is ongoing with the SMASH spatially distributed hydrological platform (Jay-Allemand et al. [2020]; Colleoni et al. [2021]) on which is based the French flash flood warning system Vigi-Crues Flash (Garandeau et al. [2018]). Further work will also test the integrated chain on flash flood Mediterranean basins as well as on larger basins in a satellite observability context. The implementation of porosity models (Guinot et al. [2018] and references therein) represents a very interesting research direction regarding effective floodplains and 1Dlike reaches parameterizations. This is especially true with depth-dependent porosity (Özgen et al. [2017] and references therein) applied to complex channel geometries and with spatially distributed calibration.

3.A 2D (h, u, v) Shallow Water scheme

3.A.1 2D solver

Recall the rotational invariance property of the SWE (Eq. 3.1) which simplifies the sum of 2D problems in Eq. (1.7) to 1D Riemann problems. The fluxes $\mathbf{F}_e$ are computed using a Riemann solver. Each local Riemann problem depends on left and right states at the interface e.

The HLLC approximate Riemann solver is used. This gives the expressions:

$$\left\{\begin{array}{l} \left[\hat{\mathbf{F}}_e^{HLLC}\right]_{1,2} = \dfrac{s_{K_e}\left[\mathbf{F}\left(\hat{\mathbf{U}}_K\right)\right]_{1,2} - s_K\left[\mathbf{F}\left(\hat{\mathbf{U}}_{K_e}\right)\right]_{1,2} + s_K s_{K_e}\left(\left[\hat{\mathbf{U}}_{K_e}\right]_{1,2} - \left[\hat{\mathbf{U}}_K\right]_{1,2}\right)}{s_{K_e} - s_K} \\ \left[\hat{\mathbf{F}}_e^{HLLC}\right]_3 = \left[\hat{\mathbf{F}}_e^{HLLC}\right]_1 \hat{v}* \quad \text{with} \quad \hat{v}* = \left\{\begin{array}{ll} \hat{v}_K & \text{if} \quad s^* \geq 0 \\ \hat{v}_{K_e} & \text{if} \quad s^* < 0 \end{array}\right. \end{array}\right. \tag{3.14}$$

where the wave speed expression is those proposed in Vila [1986a]:

$$\begin{array}{l} s_K = \min\left(0, \hat{u}_K - \sqrt{gh_K}, \hat{u}_{K_e} - 2\sqrt{gh_{K_e}} + \sqrt{gh_K}\right) \\ s_{K_e} = \max\left(0, \hat{u}_{K_e} + \sqrt{gh_{K_e}}, \hat{u}_K + 2\sqrt{gh_K} - \sqrt{gh_{K_e}}\right) \end{array} \tag{3.15}$$

It has been demonstrated that this insures L^∞ stability, positivity and consistency with entropy condition under a CFL condition.

For the intermediate wave speed estimate, following Toro [2001] we set:

$$s^* = \frac{s_K h_{K_e} \hat{u}_{K_e} - s_{K_e} h_K \hat{u}_K - s_K s_{K_e}\left(h_{K_e} - h_K\right)}{h_{K_e}\left(\hat{u}_{K_e} - s_{K_e}\right) - h_K\left(\hat{u}_K - s_K\right)} \tag{3.16}$$

A Courant–Friedrichs–Levy (CFL) condition for the time step Δt^n applies, see e.g. Vila and Villedieu [2003].

3.A.2 Well-balancing

The numerical scheme must preserve the fluid at rest property, that is the gradient of bathymetry ∇z_b must not provide $\mathbf{u}^{n+1} \neq 0$ if $\mathbf{u}^n = 0$. In the presence of topography gradients (in particular those perpendicular to the streamlines) the basic topography gradient ∇z_b discretization in the

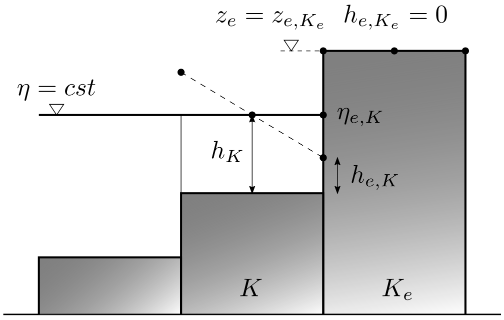

Figure 3.21: Typical situation of desired well-balanced property in presence of a wet/dry front. The WS elevation is here denoted by η (from Couderc et al. [2016]).

gravity source term $\mathbf{S}_g(\mathbf{U})$ generates spurious velocities. There is no discrete balance between the hydrostatic pressure and the gravity source term anymore: $\nabla\left(gh^2/2\right) \neq -gh\nabla z_b$.

Following Audusse et al. [2004], this issue is solved by considering the following change of variable.

From now, we consider the water depth $h^*_{e,K}$ defined from the "reconstructed" topography z_e (Fig. 3.21) at edge e as:

$$\begin{aligned} h^*_{e,K} &= \max\left(0, h_{e,K} + z_{e,K} - z_e\right) \\ \text{with} \quad & \begin{cases} z_{e,K} = \eta_{e,K} - h_{e,K} \\ z_e = \max\left(z_{e,K}, z_{e,K_e}\right) \end{cases} \end{aligned} \tag{3.17}$$

The conservative variable vector $\mathbf{U}^n_{e,K}$ in the semi-discrete scheme (Eq. 1.7) is now considered with the new variable:

$$\mathbf{U}^*_{e,K} = \begin{bmatrix} h^*_{e,K} \\ h^*_{e,K}\mathbf{u} \end{bmatrix} \tag{3.18}$$

Note that this new variable $h^*_{e,K}$ depends on the bathymetry values $(z_{e,K}, z_e)$.

The resulting well-balanced first order scheme reads:

$$\mathbf{U}^{n+1}_K = \mathbf{U}^n_K - \frac{\Delta t^n}{m_K} \sum_{e\in\partial K} m_e \left(\mathbf{F}_e(\mathbf{U}^{*n}_{e,K}, \mathbf{U}^{*n}_{e,K_e}, \mathbf{n}_{e,K}) + \mathbf{S}_p\left(\mathbf{U}^n_{e,K}, \mathbf{U}^{*n}_{e,K}, \mathbf{n}_{e,K}\right)\right) \tag{3.19}$$

with

$$\mathbf{S}_p\left(\mathbf{U}^n_{e,K}, \mathbf{U}^{*n}_{e,K}, z_K, z_{e,K}, \mathbf{n}_{e,K}\right) = \begin{bmatrix} 0 \\ \frac{g}{2}\left(\left(h^{n*}_{e,K}\right)^2 - \left(h^n_{e,K}\right)^2\right)\mathbf{n}_{e,K} \end{bmatrix} \tag{3.20}$$

3.A.3 Prediction-correction time scheme

The friction source term is taken into account in the complete SW system by deriving a prediction-correction time scheme, see e.g. Toro [2001].

We denote here by $\bar{\mathbf{U}}_K^{n+1}$ the FV solution at time t^{n+1} of the (well-balanced) scheme, either first or second order, of the SW system with the gravitational term $\mathbf{S}_g$ but without the friction term $\mathbf{S}_f$. Recall that we denote: $\mathbf{U} = (h, h\boldsymbol{u})^T$.

At each time step, from n to $n+1$,

- **Step 1:** computation of $\bar{\mathbf{U}}^{n+1}$, solution of the conservative SW system, i.e. the SW system *without* S_f, i.e. the FV solution of the following system:

$$\partial_t \boldsymbol{U} + \partial_x \boldsymbol{F}(\boldsymbol{U}) + \partial_y \boldsymbol{G}(\boldsymbol{U}) = \mathbf{S}_g(\boldsymbol{U}) \tag{3.21}$$

- **Step 2:** given the "predicted value" $\bar{\mathbf{U}}^{n+1}$, compute $\mathbf{U}^{n+1}$ solution of:

$$\partial_t \mathbf{U} = \mathbf{S}_f(\mathbf{U}) \tag{3.22}$$

General schemes (explicit, implicit or semi-implicit ones) including the friction source term $\mathbf{S}_f$ in the discretization of the model (Eq. 3.1) can be written as: for all K,

$$\mathbf{U}_K^{n+1} = \bar{\mathbf{U}}_K^{n+1} + \Delta_t^n \mathbf{S}_f\left(\bar{\mathbf{U}}_K^{n+1}, \bar{\mathbf{U}}_{K_e}^{n+1}\right) \tag{3.23}$$

Note that this splitting scheme is consistent at first order in Δt with the complete SWE. Splitting scheme second order in time is possible; it is not detailed later.

In the case of the Manning-Strickler law, the friction term reads: $\mathbf{S}_f = -gn^2 \begin{bmatrix} 0 \\ \frac{|\bar{u}|}{h^{\frac{1}{3}}}\bar{\boldsymbol{u}} \end{bmatrix}$.

Therefore the equation to be solved (Eq. 3.22) reads:

$$\partial_t \begin{pmatrix} h \\ h\bar{\boldsymbol{u}} \end{pmatrix} = -gn^2 \begin{pmatrix} 0 \\ \frac{|\bar{u}|}{h^{\frac{1}{3}}}\bar{\boldsymbol{u}} \end{pmatrix} \tag{3.24}$$

Since the friction source term $\mathbf{S}_f$ is zero in the mass conservation equation, we remark that $h^{n+1} = \bar{h}^{n+1}$. As a consequence, we consider the non-zero momentum component only: $\partial_t(h\bar{\boldsymbol{u}}) = -gn^2 \frac{|\bar{u}|}{h^{\frac{1}{3}}}\bar{\boldsymbol{u}}$

3.A.3.1 First order expression of $\mathbf{U}^{n+1}$

Let us consider the implicit scheme :

$$\frac{h^{n+1}\boldsymbol{u}^{n+1} - h^{n+1}\bar{\boldsymbol{u}}^{n+1}}{\Delta t^n} = -gn^2 \frac{\left|\boldsymbol{u}^{n+1}\right| \boldsymbol{u}^{n+1}}{\left(h^{n+1}\right)^{\frac{1}{3}}} \tag{3.25}$$

This implies that:

$$\left|\boldsymbol{u}^{n+1}\right| \boldsymbol{u}^{n+1} + \frac{\left(h^{n+1}\right)^{\frac{4}{3}}}{\Delta t^n g n^2}\left(\boldsymbol{u}^{n+1} - \bar{\boldsymbol{u}}^{n+1}\right) = 0 \tag{3.26}$$

Let us set $c = \frac{\left(h^{n+1}\right)^{\frac{4}{3}}}{\Delta t^n g n^2}$, $c \geq 0$. Note that $\left|\boldsymbol{u}^{n+1}\right| \boldsymbol{u}^{n+1} + c\boldsymbol{u}^{n+1} = c\bar{\boldsymbol{u}}^{n+1}$. Therefore for non vanishing velocities, it exists $\alpha \in]0,1]$ such that: $\boldsymbol{u}^{n+1} = \alpha \bar{\boldsymbol{u}}^{n+1}$. Adopting these notations, we obtain $\left|\bar{\boldsymbol{u}}^{n+1}\right| \bar{\boldsymbol{u}}^{n+1}\alpha^2 + c\bar{\boldsymbol{u}}^{n+1}\alpha - c\bar{\boldsymbol{u}}^{n+1} = 0$. This simplifies to:

$$\left|\bar{\boldsymbol{u}}^{n+1}\right| \alpha^2 + c\,\alpha - c = 0 \tag{3.27}$$

Since $\alpha \geq 0$, the root of this quadratic equation reads:

$$\alpha = \frac{-c + \sqrt{c^2 + 4c\left|\bar{\boldsymbol{u}}^{n+1}\right|}}{2\left|\bar{\boldsymbol{u}}^{n+1}\right|} \tag{3.28}$$

Let us define the function $\varepsilon = \frac{1}{c}\left|\bar{\mathbf{u}}^{n+1}\right| = \Delta t^n g n^2 \frac{\left|\bar{\mathbf{u}}^{n+1}\right|}{\left(h^{n+1}\right)^{4/3}}$. Observe that $\varepsilon = O\left(\Delta t^n\right)$, also $\varepsilon = O\left(\frac{\left|\bar{\mathbf{u}}^{n+1}\right|}{\left(h^{n+1}\right)^{4/3}}\right)$.By adopting this notation, Eq. (3.28) reads: $\alpha = \frac{\sqrt{1+4\epsilon}-1}{2\epsilon}$. After some rearrangements, we obtain $\alpha = \frac{2}{1+\sqrt{1+4\varepsilon}}$. At first order in ϵ, we get: $\alpha \sim \left(\frac{1}{1+\epsilon/4}\right) \sim 1 - \epsilon/4$.

Finally, we obtain:

$$\mathbf{U}_K^{n+1} = \begin{pmatrix} h^{n+1} \\ h^{n+1}\boldsymbol{u}^{n+1} \end{pmatrix} = \begin{bmatrix} \bar{h}^{n+1} \\ h^{n+1}\bar{\mathbf{u}}^{n+1}\left(\dfrac{2\left(\bar{h}^{n+1}\right)^{2/3}}{\left(\bar{h}^{n+1}\right)^{2/3} + \sqrt{\left(\bar{h}^{n+1}\right)^{\frac{4}{3}} + 4\Delta t^n g n^2\left|\bar{\mathbf{u}}^{n+1}\right|}}\right) \end{bmatrix} \tag{3.29}$$

with $\left|\bar{\mathbf{u}}^{n+1}\right|$ the solution of Eq. (3.21).

3.A.3.2 Second order scheme

In order to obtain a globally second order scheme, a higher-order time stepping scheme is needed. Let us briefly describe the ingredients of this second order well-balanced positive scheme that is strictly the same as the one proposed in Couderc et al. [2013]; Monnier et al. [2016]. Actual second order accuracy, considering source terms $\mathbf{S}_g$ and $\mathbf{S}_f$, is achieved through the combination of a Monotonic Upwind Scheme for Conservation Laws (MUSCL) spatial reconstruction and an IMEX RK time scheme (see Monnier et al. [2016] and references therein), as well as a spatial discretization of $\mathbf{S}_g$ and the semi-implicitation friction source term $\mathbf{S}_f$ given by in the subsection above.

A monoslope second order MUSCL scheme is adopted, see e.g. Chévrier and Galley [1993]; Buffard and Clain [2010]. It leads to new expressions of $\mathbf{U}_K^n$ and $\mathbf{U}_{K_e}^n$. With this linear reconstruction, one can expect a scheme with a second-order accuracy in space (for regular solutions only). In order to prevent large numerical dispersive instabilities, the computed vectorial slopes are limited by applying a maximum principle. Furthermore, to handle the presence of wet-dry fronts that can break the Finite Volume mass conservation property, a Barth limiter (Barth [2003]) is employed.

3.B 1D (A,Q) Saint-Venant equations

A river network Ω^{1D} is described by connected closed line segments. For a flow XS orthogonal to the main (longitudinal) flow direction of curvilinear abscissa $x \in \Omega^{1D}$ (distance from downstream), at time $t \in [0,T]$, let $A(x,t)$ be the flow cross-sectional area $\left[\mathrm{m}^2\right]$ and $Q(x,t)$ the discharge $\left[\mathrm{m}^3/\mathrm{s}\right]$ such that $Q = UA$ with $U(x,t)$ defined as the longitudinal XS averaged velocity $[\mathrm{m/s}]$. The 1D Saint-Venant equations in (A,Q) variables at a flow XS write as follows:

$$\begin{cases} \frac{\partial A}{\partial t} + \frac{\partial Q}{\partial x} & = 0 \\ \frac{\partial Q}{\partial t} + \frac{\partial}{\partial x}\left(\frac{Q^2}{A}\right) + gA\frac{\partial Z}{\partial x} & = -gA\frac{|Q|Q}{K^2A^2R_h^{4/3}} \end{cases} \tag{3.30}$$

where $Z(x,t)$ is the WS elevation $[m]$ and $Z = (b+h)$ with $b(x)$ $[m]$ the river bed level and $h(x,t)$ $[m]$ the water depth , $R_h(x,t) = {}^{A}/_{P_h}$ $[m]$ the hydraulic radius , $P_h(x,t)$ $[m]$ the wetted perimeter, g $\left[m/s^2\right]$ is the gravity magnitude. Let us recall the Froude number definition $\mathrm{Fr} = {}^{U}/_{c}$ comparing the average flow velocity U to pressure wave celerity $c = \sqrt{\frac{gA}{W}}$ where W $[m]$ is the flow top width.

The friction term S_f is classically parameterized with the empirical Manning-Strickler law established for uniform flows $\dfrac{|Q|\,Q}{K^2A^2R_h^{4/3}}$ where K $\left[\mathrm{m}^{1/3}/\mathrm{s}\right]$ is the Strickler coefficient.

The Saint-Venant equations are solved on each segment of the river network and the continuity of the flow between segments is ensured by applying an equality constrain on water levels at the confluence between two segments.

Boundary conditions are classically imposed (subcritical flows here) at boundary nodes with inflow discharges $Q(t)$ at upstream nodes and WS elevation $Z(t)$ at the downstream node; lateral hydrographs $q_l(t)$ at in/outflow nodes. The initial condition is set as the steady state backwater curve profile $Z_0(x) = Z(Q_{in}(t_0), q_{l,1..L}(t_0))$ for hot-start. This 1D Saint-Venant model is discretized using the classical implicit Preissmann scheme (see e.g. Cunge et al. [1980]) on a regular grid of spacing Δx using a double sweep method enabling to deal with flow regimes changes with a one-hour time step Δt. This is implemented into the computational software DassFlow (Brisset et al. [2018]; Larnier [2010]).

The numerical scheme is a semi-implicit finite difference scheme (generalized Preissmann scheme) with a double sweep Local Partial Inertial method to minimize the inertial terms (see documentation in Brisset et al. [2018]; Larnier [2010]).

3.C GR4 hydrological model operators

The state-space version of the lumped conceptual hydrological model GR4 presented in Santos et al. [2018] consists in the set of ordinary differential equations (ODE) given in Eq. (3.4) and recalled here for clarity:

$$\frac{\mathrm{d}\boldsymbol{h}}{\mathrm{dt}} = \begin{cases} \dot{h}_p & = P_s - E_s - P_{erc} \\ \dot{h}_1 & = P_r - Q_{Sh,1} \\ \dot{h}_2 & = Q_{Sh,1} - Q_{Sh,2} \\ ... & ... \\ \dot{h}_{nres} & = Q_{Sh,nres-1} - Q_{Sh,nres} \\ \dot{h}_r & = Q_9 + F - Q_r \end{cases} \tag{3.31}$$

They involve the following fluxes:

$$\begin{cases} E_s = & E\left(\frac{2h_S}{c_1} - \left(\frac{h_p}{c_1}\right)^{\alpha}\right) \\ P_S = & P\left(1 - \left(\frac{h_p}{c_1}\right)^{\alpha}\right) \\ P_{erc} = & \left(\frac{\nu}{c_1}\right)^{\beta-1} \frac{1}{\beta-1}\left(h_p^+\right)^{\beta} \\ P_R = & P\left(\frac{h_p}{c_1}\right)^{\alpha} + \left(\frac{\nu}{c_1}\right)^{\beta-1} \frac{1}{\beta-1}\left(h_p^+\right)^{\beta} \\ Q_{N1} = & \frac{n_{res}-1}{c_4} h_1^+ \\ ... & ... \\ Q_{N11} = & \frac{n_{res}-1}{c_4} h_{n_{res}}^+ \\ Q_9 = & \Phi \frac{n_{res}-1}{c_4} h_{n_{res}}^+ \\ Q_1 = & (1-\Phi)\frac{n_{res}-1}{c_4} h_{n_{res}}^+ \\ F = & \frac{c_2}{c_3^{\omega}}\left(h_r^+\right)^{\omega} \\ Q_D = & (1-\Phi)\frac{n_{res}-1}{c_4} h_{n_{res}+1} - \frac{c_2}{c_3^{\omega}}\left(h_r^+\right)^{\omega} \\ Q_R = & \frac{1}{\left(h_R^+\right)^{\gamma-1}(\gamma-1)}\left(h_r^+\right)^{\gamma} \end{cases} \tag{3.32}$$

The following parameter are set following Perrin et al. [2003] and Santos et al. [2018]: $\alpha = 2$, $\beta = 5$, $\gamma = 5$, $\omega = 3.5$, $\nu = 4/9$, $\Phi = 0.9$, $n_{res} = 11$.

Calibrated parameter for the Adour case were obtained using the airGR global calibration algorithm (Coron et al. [2017]) from the freely available package[4].

---

[4] https://webgr.inrae.fr/logiciels/airgr/

Parameter	Adour	Oloron	Pau	Nive
x_1	413.744	1844.567	1118.78	982.401
x_2	0.148	1.363	1.134	0.696
x_3	86.418	117.919	112.168	90.017
x_4*	55.466	12.739	11.059	6.980

Table 3.4: Calibrated hydrological parameters of the 4 upstream hydrological catchments from the Adour multi-D hydrographic network model. *Note that the x_4 calibrated parameters corresponds to the non-"state-space" GR4H version (not presented, see Perrin et al. [2003]), for which the calibration tool is provided. x_4 values in the present run with the "state-space" were set at 0.15.

Chapter 4

Perspectives and general conclusion

Contents

4.1 Work perspectives

The goal of this work was the hydrodynamic modeling of river basins in the context of their multi-source observability. In Chapter 2, hydraulic signatures were analyzed and used to infer parameters of a 1D model applied at large scale. In Chapter 3, a multi-D hydraulic-hydrological model was developed to allow for the representation of large scale hydrographic networks at adequate scales and at relatively low computational cost.

The developed code and methodology should be further confronted to operational-like scenarios, such as the inference of discharge hydrographs of ungauged tributaries using heterogeneous altimetric observations or the fine, space-time accurate, reproduction of flood-inundation events (e.g. using the unprecedented 2021 Adour floods recorded by the SHPC-GAD). Near future works will focus on the improvement of the current Adour network models through the refinement of the a priori bathymetry extracted from fine LiDAR DEM and the calibration of effective hydraulic and hydrological parameters. Initial investigations into the assimilation of 2D observation fields are presented in Subsection 4.1.2.

Further work should focus on the integration of more complex distributed or semi-distributed hydrological models into the DassFlow tool chain and on their optimal synergy with in situ and satellite data using VDA methods. Given the ill-posedness of the considered inverse problems, their resolution would benefit from the exploitation of all available data. Furthermore, the inference of channel parameters, temporal forcings and distributed hydrological parameters is dependent on the spatial and temporal scales of observations, but also on a priori information fed into the assimilation process through background values and regularizations. These issues would be studied further in multi-D catchment-scale hydrological-hydraulic models.

Another perspective would consist in investigating porosity based approaches in 2D SW solver (Guinot et al. [2017]) for subgrid parameterizations in 1Dlike channels to account for channel shape variability or in 2D zones with complex topography. Further works on lateral flood plain modeling (at an appropriate computational cost and scale), hydrological parameter estimation (see Subsection 3.4.2.3), and on depth-dependent effective porosities (Guinot [2012]), both in floodplains and 1Dlike reaches, would represent interesting directions.

Finally, future work should also focus on strategies for automatic generation of 1Dlike meshes on river networks from available data products. This would allow for an easier deployment of this new modeling approach proposed and facilitate the use of VDA methods in basin scale modeling with the DassFlow platform.

4.1.1 Inferences on a large scale hydrographic network

General perspectives and goals The current Adour models should be better fitted to available WS observations. Improved bathymetry extraction from data shared by the SHPC-GAD[1] and overall model calibration is an immediate perspective. The new a priori bathymetry (and friction) could be further calibrated using available WS observations (see e.g. observabilities in Table 4.1 and Fig. 4.1). Recent extreme events (e.g. the extreme 2021 floods in the Bayonne area) could be used for calibration of the 2D area of the multi-D model (see Subsection 4.1.2for early trials).

The 1D-like model of the Adour river and its tributaries should be further exploited to analyze parameter inferability on a regional-scale hydrographic network. This exploitation should be based on an analysis of signature propagations, linked to hydraulic parameters, to the upstream hydrographs and to the downstream tidal boundary, and an analysis of parameter sensitivity across the domain.

The newly developed wrapped version of the Fortran code (see Section 1.5) may ease the use of Python libraries, including machine/deep learning, which opens plenty of perspectives in hydrological modeling. In hydrological modeling, Kratzert et al. [2019]; Hashemi et al. [2021] use LSTM to learn time series and others, e.g. Gao et al. [2020], uses in prediction and forecasting. In hydraulic modeling, Kabir et al. [2020] uses surrogate models (deep convolutional neural networks) for real time flood inundation forecasting and Raissi et al. [2019] uses physics informed deep learning aimed at the synergetic combination of mathematical models and data.

Adour assimilation case In the following paragraph, we propose work perspectives centered around multi-sourced data exploitation, that can come from in situ, airborne of satellite sensors. Recall the stated importance of the spatio-temporal coverage contained given by this multi-sourced cocktail to infer spatio-temporally distributed parameters.

In the area of interest of the Adour basin (see Subsection 3.4.3.2), the majority of river reaches have a width of 50 m or above, with 100 m reached on most of the Adour river and downstream from the Pau-Oloron confluence. This means that SWOT wide-swath observations should cover almost all of the network and that nadir altimetry virtual stations should still cover a significant portion (see Table 4.1 and Fig. 4.1 for a sample of satellite observability). Given the capabilities of the variational method for inferring large control vectors, initial calibration of reach-scale parameters could be carried out from this synthetic remote-sensed data.

---

[1] Service d'Hydrométrie et de Prévision des Crues Gironde Adour Dordogne

Mission	Observability	Revisit time
Envisat	3 points on 2 tracks	27 days
Jason	2 points on same track	10 days
SWOT	3 swaths, each around 80% of whole network, all network seen	21 days

Table 4.1: Observability of Adour network WS from satellite sources

The dense temporal sampling of in situ station data (Fig. 4.1) also opens the way toward inferences of temporally dense hydraulic model forcings, possibly for operational use. The inference of ungauged/unknown/uncertain inflows was achieved in Chapter 3 in a 1D model and constitutes an achievable and interesting perspective in multi-D large scale models. The study of lateral fluxes represents an interesting research direction. These fluxes include gains and losses along river networks (Cholet et al. [2017]; Le Mesnil et al. [2021]), for example via two-ways couplings with hydrogeological models. At the regional scale, Baratelli et al. [2016] (and references therein) links 1D river channels and saturated and unsaturated zones through conceptual relations. At a finer scale, Jeannot et al. [2018] links overland flows (using 1D and 2D diffusive wave models) to subsurface flows (using depth-integrated Richards equations) with superposed meshes and a coupling source term.

A first step towards assimilating this in situ and remotely-sensed data would be the creation of a twin experiment setup and the generation a synthetic target model. Proposed experimental setups could include: (i) the inference of temporal forcings from in situ WS elevation data, (ii) the inference of friction patches from satellite observabilities and (iii) the inference of the bathymetry-friction couple from satellite observabilities including spatially dense patterns. The use of a priori information and regularizations is an important component of inverse problem resolution and should be studied in the multi-D Adour model.

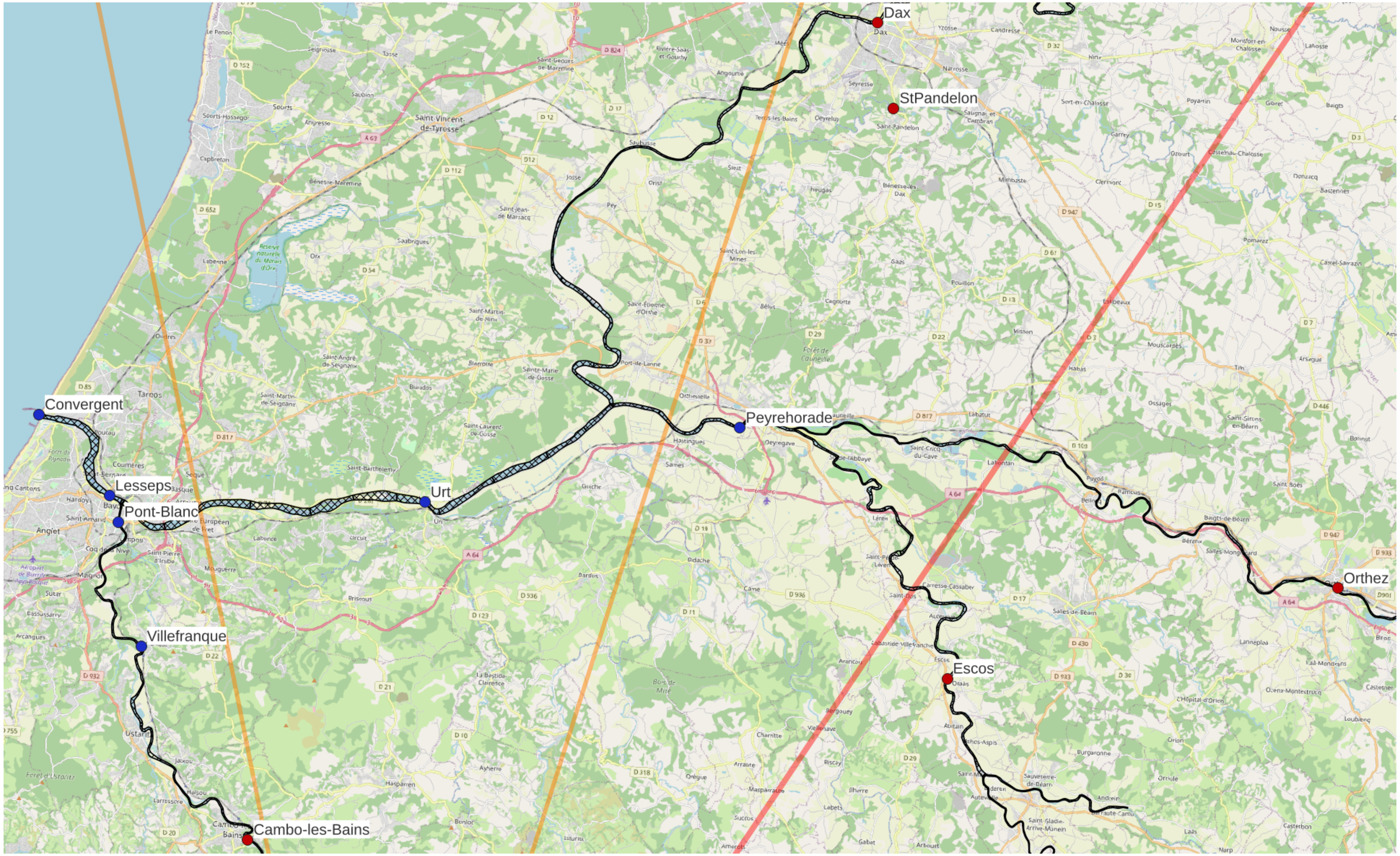

Figure 4.1: Satellite nadir tracks (Jason in red, Envisat in orange) and local permanent stations (Banque HYDRO network) over the Adour river network

4.1.2 Inferences from 2D surface observation fields

The integration of new observations, for example from surface velocity fields provided by LSPIV techniques (see e.g. Dramais et al. [2011]; Fujita and Kunita [2011]; Le Coz et al. [2010]) to constrain river network models, should be further explored. Indeed, surface velocity fields may represent constraining information as shown on simple test cases briefly presented here. Inferences from velocity observations are carried out in tandem with similar setups using WS elevation observations as a mean to compare them to better studied inverse problems (see e.g. Lai and Monnier [2009]).

A multi-D confluence test case has been used for preliminary tests (mesh first defined in Subsection 3.4.2.3) and is used here. The three 1Dlike reaches are given a flat bottom and the 2D confluence mesh is given two anti-symmetrical bathymetry irregularities (a bump (in red) and a pool (in blue), see Fig. 4.2, right), with the aim of generating complex WS deformations on par with real-like complexities. The model is inflowed by two known identical varied upstream hydrographs and a rating curve is imposed downstream.

Two spatial observability patterns are setup to correspond. They are i) a 2D spatial field in the form of $20 \times 20\,\mathrm{m}$ observation station grid (Fig. 4.2, left, in orange) and ii) local cross-sectional observation, in the two reaches, upstream from the confluence (Fig. 4.2, left, in green). They are meant to represent simplified in situ survey results, respectively LSPIV-like and ADCP-like data products. Both WS elevation and modeled velocities are observed, although they will be considered separately in the following inferences.

The model considered is the 2D (h, u, v) SW presented in Subsection 3.3.2 and 3.A). The control vector θ is composed exclusively of bathymetry points at the 2D confluence, i.e. 1Dlike cells are left out of the control vector. The prior bathymetry is flat over the whole case, which leads to bathymetry over-estimation (resp. under-estimation) at the north pool (resp. south bump) and corresponds to the target in the 1Dlike reaches. The following cost functions are considered, respectively for the assimilation of WS elevations and of flow velocities: $j_{h,obs}(\theta) = \frac{1}{2}\|Z_o(t) - Z(\theta,t)\|_{\mathcal{O}}^2$ and $j_{uv,obs}(\theta) = \frac{1}{2}\left(\|u_o(t) - u(\theta,t)\|_{\mathcal{O}}^2 + \|v_o(t) - v(\theta,t)\|_{\mathcal{O}}^2\right)$, with Z_o $[m]$ the observed WS elevation and $\boldsymbol{u}_o = (u_o, v_o)^T$ $[m/s]$ the observed flow velocity. Note that observation covariance matrices $\mathcal{O}$ might differ for altimetric and velocity observations, although this distinction is not explored in this work, where they are set equal to identity matrices. Also note that, in the considered twin experiments, no noise is considered and observation locations are cell centers, hence the observation space corresponds to the state space. The regularizations term writes $j_{reg} = \frac{1}{2}\sum_{i=1}^{M}\left(\left(\frac{\partial b_i}{\partial x}\right)^2 + \left(\frac{\partial b_i}{\partial y}\right)^2\right)$, with M the number of control cells, and is considered in the second set of inferences (Fig. 4.4).

Although the below inferences assume that the modeled flow velocity, i.e. depth-averaged velocity, is directly observable, through twin experiment setups, only the surface flow velocity is observable in practice. To account for this, observation operators accounting for known velocity profiles could be used, so as to translate observations into reasonable estimates of modeled depth-averaged velocity. The development of methods for this is outside the scope of this perspectives part and could be further studied.

Inferences from WS elevation observations with a grid pattern (pattern A, Fig. 4.3(a)) lead to accurate inferences at the observation points, with a global overestimation of the required correction. Outside of the immediate surroundings of the observation points, in the 2D zone, bathymetry remains mostly unchanged by the assimilation process (this is even more apparent in cases with lower sensitivity to bathymetry, not shown). Inferences from flow velocity observations with a grid pattern (pattern A, Fig. 4.3(c)) lead to global inferred bathymetry patterns in coherence with the target. Inferences are closer to the target at the bottom bathymetry bump, where flow velocity sensitivity to bathymetry is higher.

Inferences from cross-sectional upstream WS elevation observations (pattern B, Fig. 4.3(b)) lead to a fair inference of the downstream pattern and amplitude of the bathymetry irregularities. Local erroneous estimations appear, especially near 1Dlike-2D interfaces. This is explained by the correlated influences of local bathymetry backwater control over pattern B observability. Inferences from cross-sectional upstream flow velocity observations (pattern B, Fig. 4.3(d)) are even more subject to this behavior, with bathymetry overestimation at the southern upstream and the downstream 1D2D interfaces. Note that all inferences lead to low cost function values and modeled flow velocities close to reference ones.

The introduction of a bathymetry regularization term in the cost function leads to better inferences. For inferences using WS elevation observations, it leads to a smoother inferred bathymetry in coherence with patterns inferred without regularization, as expected from similar experiments of inferences in the 1Dlike model (see Subsection 3.4.3.1). Given grid WS elevation observation (Fig. 4.4(a) and (b)), inference results are unilaterally improved, as inferred bathymetry values are closer to the target in both cases. For inferences using flow velocity observations, results are also improved. Although, given pattern B observability, erroneous estimations at the downstream 1D2D interface are still present and a significant contribution of the observed bathymetry backwater control. This could be explained by the incomplete bathymetry reconstruction method at these interfaces (see Chapter 4).

Overall, these preliminary experimental setups highlight the interest of using 2D field for local bathymetry estimations. Surface velocity fields could also be used to constrain model flux, following the idea of local discharge estimation by LSPIV (Dramais et al. [2011]; Le Coz et al. [2010]). As a matter of facts, a misfit exists between depth averaged modeled flow velocities and observations of real surface velocities of a 3D turbulent flow. This requires to study adequate observation operators linking actual surface velocity and depth-averaged modeled velocity, through a priori knowledge of velocity profile shapes and taking into account measurement errors. Thus, given known bathymetry-friction over a XS (e.g. over an ADCP transect) and this observation operator at a a virtual station/XS, upstream discharge estimations could be carried out from surface velocity fields.

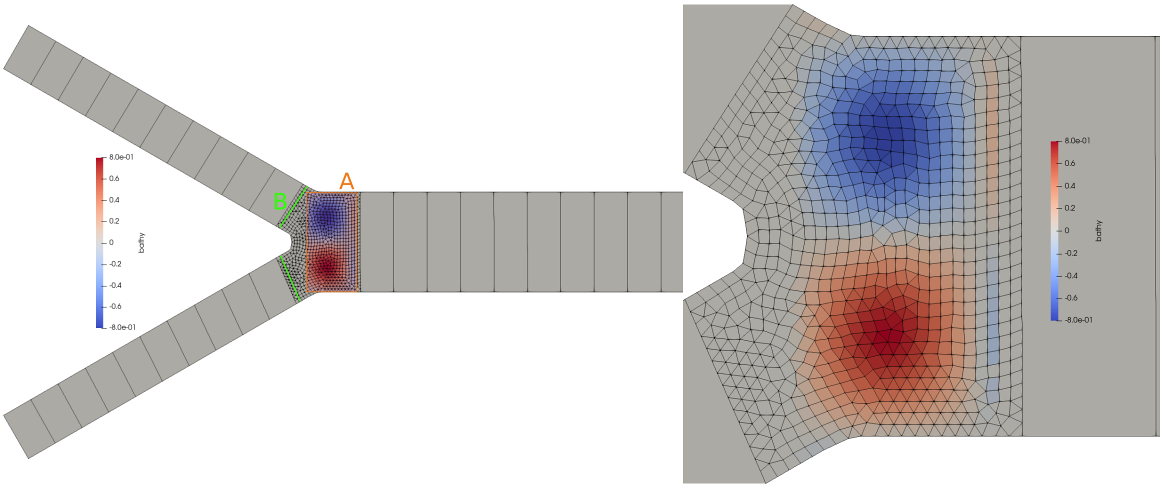

(a) Target bathymetry and considered observation fields. A: $20 \times 20\,\mathrm{m}$ grid, B: upstream cross-sectional measurements at the 2D confluence

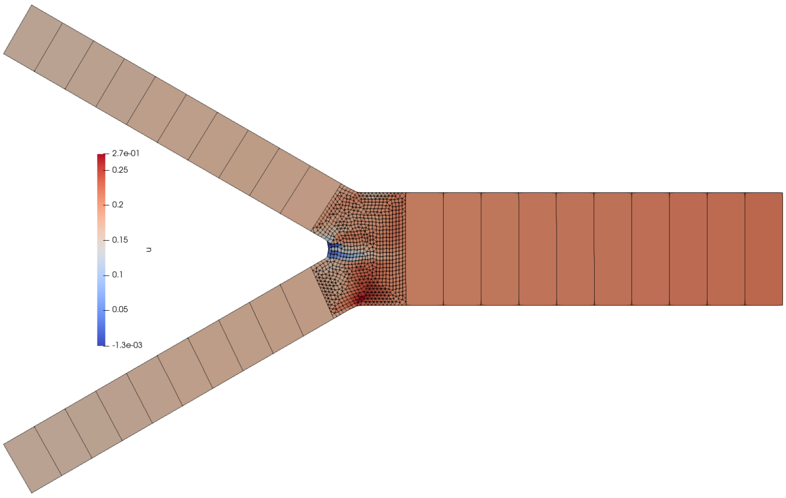

(b) Target x-velocity at $t = 7\,\mathrm{h}$

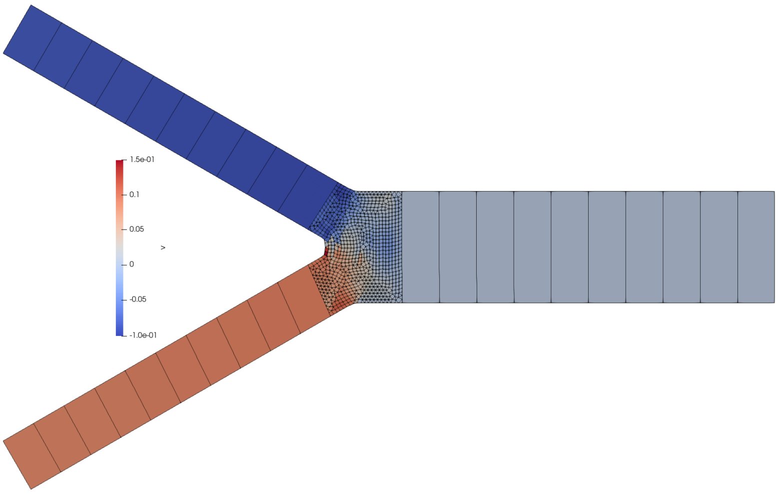

(c) Target y-velocity at $t = 7\,\mathrm{h}$

Figure 4.2: Confluence twin experiment setup

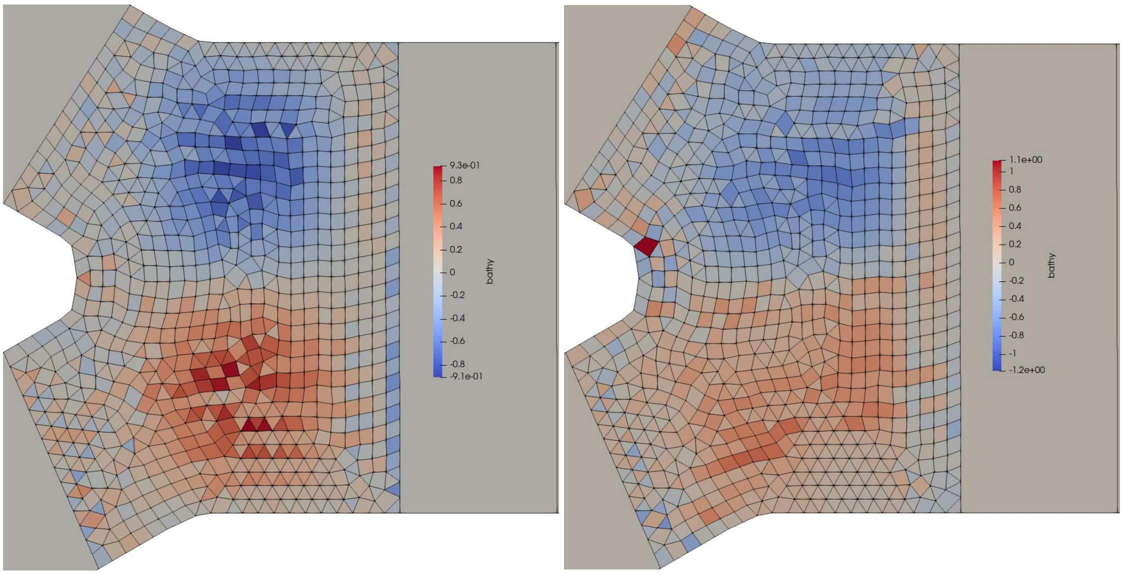

(a) Obs A + WSE (b) Obs B + WSE

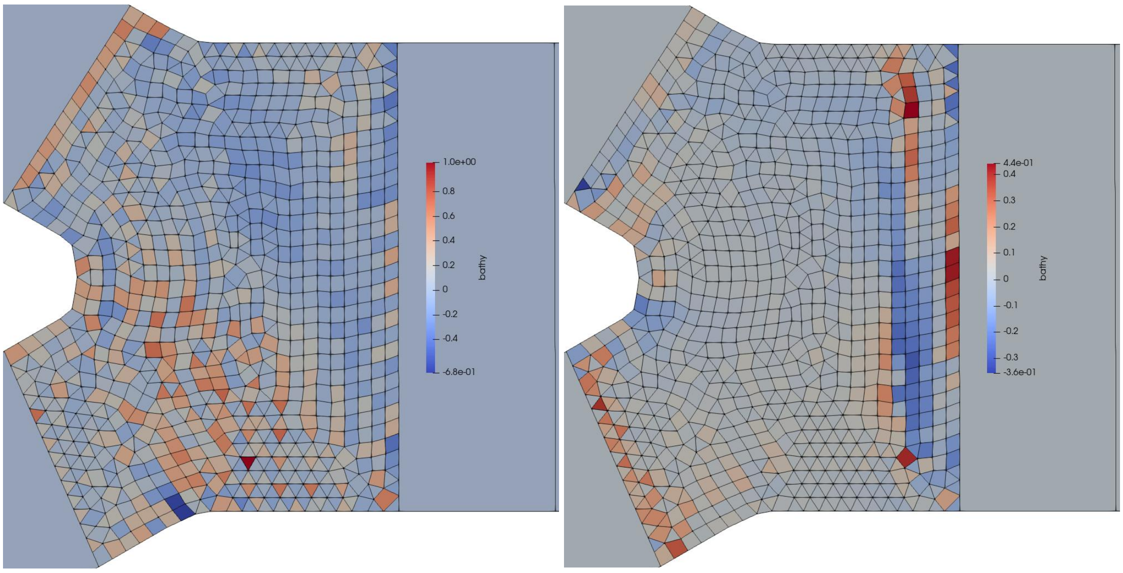

(c) Obs A + **u** (d) Obs B + **u**

Figure 4.3: Bathymetry inference results from 2D fields in the multi-D confluence case, from observation patterns A and B, from WS elevation and flow velocity observations. (a) From observability A of WS elevation. (b) From observability B of WS elevation. (c) From observability A of flow velocity. (d) From observability B of flow velocity.

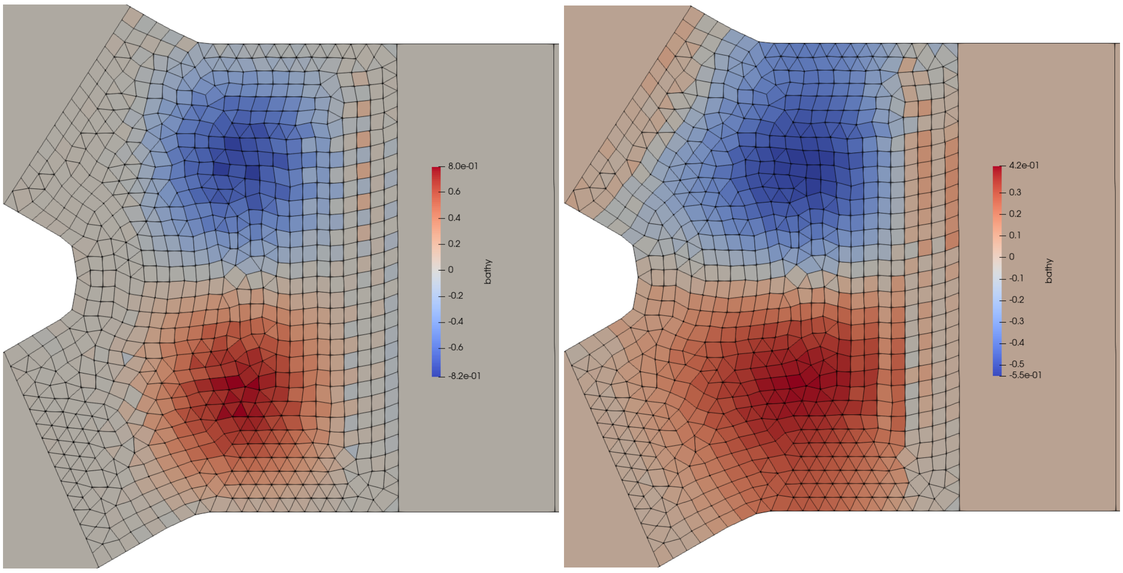

(a) Obs A + WSE (b) Obs B + WSE

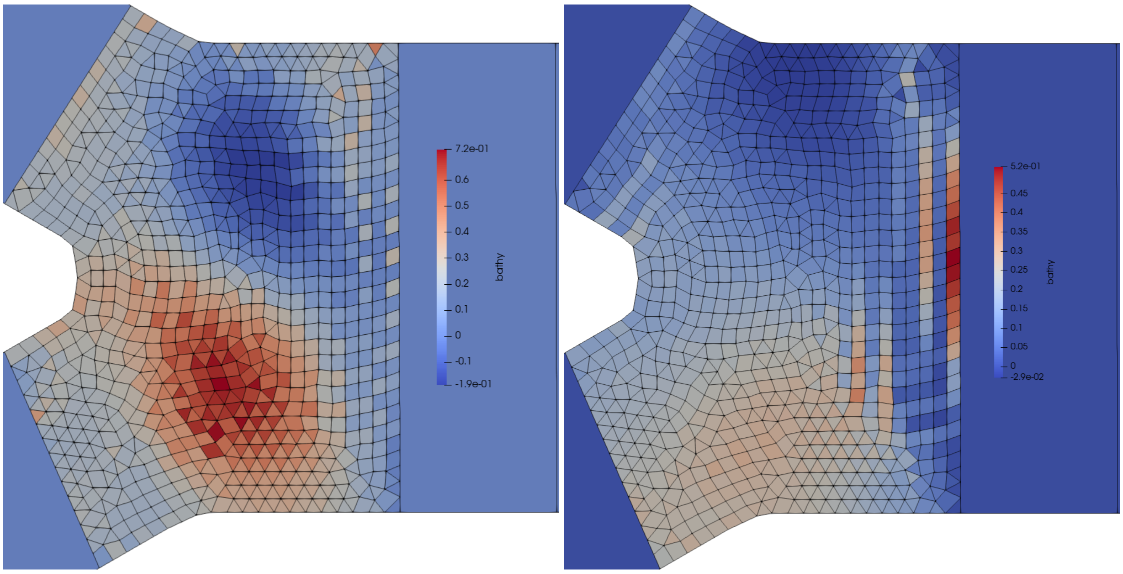

(c) Obs A + **u** (d) Obs B + **u**

Figure 4.4: Bathymetry inference results from 2D fields in the multi-D confluence case, from observation patterns A and B, from WS elevation and flow velocity observations, with bathymetry regularization. (a) From observability A of WS elevation. (b) From observability B of WS elevation. (c) From observability A of flow velocity. (d) From observability B of flow velocity.

4.2 General conclusion

In this thesis work, flow modeling in complex hydrographic networks is studied in context of their observability by satellites. Water surface elevations and extents, respectively provided by radar altimetry (classical nadir or wide-swath) and optical sensors, are considered in complement of in situ physiographic and flow data. In this context, the work deals with networks of relatively large rivers and with fluvial flows ($Fr < 1$). The main issues in fluvial networks modeling pertain to the challenging estimation of unobserved spatio-temporal river discharge and bathymetry-friction. This works aims to tackle this issue by making the most of observations of river surface deformations, including satellite and in situ observations.
These goals are related to several issues studied in this work with the aim to put in coherence model and data, which are (i) the effective hydraulic-hydrological modeling of river networks, including multi-scale hydraulic controls, (ii) the resolution of ill-posed inverse problems given heterogeneous and relatively sparse observability, compared to physical flow scales, of WS deformations and flows.

First, as synthesized in Chapter 1, this work builds upon previous knowledge and forward-inverse algorithms aimed at the inference of the bathymetry-friction couple and of a single upstream inflow. The difficulty of such inverse problems lies (i) in the correlated influences of the sought parameters on the observed water surface deformations, (ii) in the relatively sparse observation sampling when compared to the physical scale of signatures of hydraulic controls and (iii) in the heterogeneousness, in space, time and nature of observations. This work builds upon the DassFlow hydraulic modeling framework and its VDA algorithm enabling to tackle high dimensional inverse problems. The hydraulic inverse problems of interest, given WS observables, are even more challenging when considering distributed lateral inflows, which is yet necessary for modeling large river networks.

The article Pujol et al. [2020], presented in Chapter 2, studies the forward and inverse modeling capabilities of distributed channel parameters and multiple inflows in a 1D SW model, from multi satellite observations of the river surface. Lateral inflows are implemented into the 1D SW numerical model in the DassFlow framework. Inferences of geometric parameters and multiple inflow hydrographs of the hydraulic model are carried out on synthetic 1D cases. In particular, the inference of distributed lateral inflows are studied based on analyses of their hydraulic signature in WS which also contains the footprint of channel parameters. To better constrain the considered ill-posed problems, classical regularizations and a change of variables in the parameter space are used.
The hydraulic model, built from optical and historical altimetric data (Envisat), is coupled to the large scale hydrological model MGB and applied to a long portion of the Negro River in the Amazon basin. The effective hydraulic model, calibrated using multi-satellite observations, closely fits altimetry data and presents real-like spatial variabilities (backwater effects from control sections and downstream boundaries, lateral inflow influences). Note that this model building methodology was further applied in the Amazon basin in Malou et al. [2021] with multi-mission altimetry data (Sentinel, Jason) and used to derive altimetric stage-fall discharge laws based on simulated WS slopes. The global availability of such data enables the application of the approach on worldwide rivers.

Signal propagation and WS deformations are analyzed both on academic cases and on the Negro river with identifiability maps. In a twin experiment setup using noisy SWOT-like observability, simultaneous inferences of distributed bathymetry-friction and distributed inflow hydrographs lead to low misfit to WS observations. The study brings new insight into: (i) the large scale visibility of the signatures of distributed parameters and temporal forcings, using SWOT observability, (ii) the identifiability of large hydraulic control vectors using a variational method and satellite altimetry, (iii) the need to constrain these inferences with prior knowledge and (iv) the need to further taylor and scale hydrodynamic network models and assimilation methods to better synergize with rich multi-source observations.
The modeling of large river networks would benefit from (i) multi scale river network hydraulic modeling (ii) with integrated hydrology model. To model complex flow zones, such as floodplains and confluences, local fine scale representations are also needed. This can be achieved by integrating seamless 2D zooms into complete river network models. These considerations motivated the modeling methods developed in Chapter 3.

The article Pujol et al. [2022], featured in Chapter 3, presented a new method for the multi-D hydraulic-hydrological modeling of river networks. The new modeling approach implemented in DassFlow allows fine hydrodynamic modeling of flow propagation within large river networks with zooms over complex flow zones such as floodplains and confluences. It is based on an existing solver, in the parallel framework of the DassFlow platform. A so-called "1Dlike" mesh allows for an effective hydrodynamic representation of river reaches under 1D hydraulic assumptions, while still allowing for a low computational cost over large domains. Fine 2D meshes of complex flow areas, such as confluences and floodplains, are connected to the 1Dlike reaches through 1D-2D interfaces, for which the finite volume solver has been adapted. The river network model is inflowed by the parsimonious hydrological model GR4H, in its state-space version, which has been integrated to the assimilation tool chain.
The forward-inverse multi-D computational model is successfully validated on academic and real cases of increasing complexity, featuring typical 1D and 2D flow variabilities such as respectively channel hydraulic controls and confluences and floodplains. In particular, two hydraulic models based on real-like cases are built from reference models containing fine scale variabilities: (i) a 1Dlike model of a reach of the Garonne river, (ii) a large scale multi-D model of the Adour hydrographic network The 1Dlike modeling approach enables to simulate fine physical flow states compared to reference 1D or 2D shallow water models, hydrograph propagation remains very close also. The coupling with the hydrological model implemented in a semi-distributed setup is also successfully tested.
Inferences of multi-variate controls composed of hydraulic and hydrological parameters are carried out from multi-source observations. Effective bathymetry-friction fields of the multi-D hydraulic model are inferred from WS observations and lead to accurate flow simulations as shown on the Garonne River case with low misfit to observed WS elevations and accurate flood wave propagation. Inferences of spatially distributed hydrological parameters are successfully carried from WS and discharge observations in the river network, via multi-objective cost function. This shows the possibility of informational feedback from downstream hydraulic observations towards upstream hydrological modeling. Inferences of spatially distributed hydraulic temporal forcings are successfully carried out on the Adour river network model, based on observability

of WS elevation at in situ permanent stations. They lead to the successful estimation of poorly-known inflows.
This work presents a novel multi-dimensional hydraulic-hydrological numerical model with variational data assimilation in DassFlow framework. It allows multi-scale modeling over large domains and combining in situ observations with high-resolution hydro-meteorology and satellite data.

Over the course of this work, the synergy between hydraulic models of river networks and available WS observations is studied. It involves (i) the adaptation of a 1D SW hydraulic model for coupling with a spatially distributed hydrological model, (ii) the development of a multi-D hydraulic model , (iii) the integration of a hydrological module into the DassFlow framework and (iv) the resolution of a series of complex inverse problems using VDA.
The integration of multi-source observations into hydraulic-hydrological network models allows the inference of spatio-temporal parameters from heterogeneous sets of observed flow signatures.
Development carried out during this PhD lead to better modeling of river networks from altimetric and optical satellite data through numerical upgrades of the DassFlow platform. Model building methodologies are developed for flow simulations over complex river networks.
Further research should focus on coupling the multi-D model with a distributed hydrological model and on optimal model synergy with in situ, satellite and high resolution hydro-meteorological data in view of operational flood forecasting. Numerical model and method improvements will rely on pertinent effective modeling of hydrodynamic signatures in the multi-D model.

Appendix A

Shallow Water equations

This appendix details how the 1D and 2D SWE (Eq. A.4 and A.5 respectively) are obtained from the Navier-Stokes equations for an incompressible free surface flow of a Newtonian and viscous fluid - that is liquid water here. Let us consider an infinitesimally small volume of fluid far from the boundary layer. We assume that momentum loss can be modeled by a friction source term with the classical Manning formulation. Applying mass and momentum conservation principles to this volume (see mass fluxes representation on Fig. A.1) leads to the 3D Navier-Stokes equations that write (see e.g. Ancey [2018]):

$$\begin{cases} div\boldsymbol{u} & = 0 \\ \frac{\partial \boldsymbol{u}}{\partial t} + \boldsymbol{u}\nabla\boldsymbol{u} & = -\frac{1}{\rho}\nabla p + \boldsymbol{g} + gS\left(\boldsymbol{u}, n\right) \end{cases} \tag{A.1}$$

Or, projected on the (x, y, z) axes:

$$\begin{cases} \frac{\partial u_x}{\partial x} + \frac{\partial u_y}{\partial y} + \frac{\partial u_z}{\partial z} & = 0 \\ \frac{\partial u_x}{\partial t} + u_x\frac{\partial u_x}{\partial x} + u_y\frac{\partial u_x}{\partial y} + u_z\frac{\partial u_x}{\partial z} & = -gsin\left(\theta\right) - \frac{1}{\rho}\frac{\partial p}{\partial x} - gS_{f,x} \\ \frac{\partial u_y}{\partial t} + u_x\frac{\partial u_y}{\partial x} + u_y\frac{\partial u_y}{\partial y} + u_z\frac{\partial u_y}{\partial z} & = -gsin\left(\theta\right) - \frac{1}{\rho}\frac{\partial p}{\partial x} - gS_{f,y} \\ \frac{\partial u_z}{\partial t} + u_x\frac{\partial u_z}{\partial x} + u_y\frac{\partial u_z}{\partial y} + u_z\frac{\partial u_z}{\partial z} & = -gcos\left(\theta\right) - \frac{1}{\rho}\frac{\partial p}{\partial z} - gS_{f,z} \end{cases} \tag{A.2}$$

where g $\left[\mathrm{m/s^2}\right]$ is the gravitational constant, θ $[\mathrm{m/m}]$ the bottom slope (see Fig. A.2), ρ $\left[\mathrm{kg/m^3}\right]$ is the water volumetric mass, n $\left[\mathrm{s/m^{1/3}}\right]$ is the Manning friction coefficient, h $[\mathrm{m}]$ is the water depth , $\boldsymbol{u} = \left(u_x, u_y, u_z\right)^T$ $[\mathrm{m/s}]$ is the flow velocity and $p\left(x, y, t\right) = P_{atm} + \rho ghcos\left(\theta\right)$ is a pressure with P_{atm} $\left[\mathrm{kg/m/s^2}\right]$ the atmospheric pressure at the free surface.

Assuming the SWE hypotheses (recalled in the below box from Section 1.2.1) the mass and momentum equations of the incompressible Navier-Stokes equations are integrated over depth in what follows. For the sake of brevity, we will note $u_i\left(z = a\right), i \in [w, y, z]$ as $u_{i,a}$.

The BC for a free surface flow are:

BC1: At the river banks, assumed parallel to axis y, the boundary adherence condition gives $u_y = 0$.

BC2: At the river bottom, the boundary adherence condition gives $u_z = 0$.

BC3: The kinematic boundary condition dictates that fluid velocity directed perpendicular to a solid boundary must be 0. Thus, at the free surface we have $\frac{\partial h}{\partial t} + u_{x,H}\frac{\partial h}{\partial x} + u_{y,H}\frac{\partial h}{\partial y} = u_{z,H}$.

Shallow Water flow hypotheses, recalled here from Section 1.2:

- The fluid is of constant volumetric mass ρ, which implies it is incompressible and that no sediment transport is considered.
- The flow is gradually varied, which implies that the flow surface is close to a plane and varies slowly in space, and that there is no sharp change in the flow section. Thus, flow lines are parallel to each other and close to parallel to the river bottom, and vertical velocities are negligible. This is also called the long wave assumption, as it means that with regards to the water depth, signal wavelength is high (Boussinesq [1871]).
- The bottom slope (and thus the water surface slope) is low, such that the water depth can be measured as perpendicular to the river bottom.

The following demonstrations makes use of the Leibniz formula which writes:

$$\frac{d}{dx}\int_{a(x)}^{b(x)} f\left(x,t\right)dz = \int_{a(x)}^{b(x)} \frac{\partial f}{\partial x}\left(x,t\right)dz + \frac{db}{dx}\left(x\right) f\left(x,b\left(x\right)\right) - \frac{da}{ds}\left(x\right) f\left(x,a\left(x\right)\right) \tag{A.3}$$

where $f\left(x,t\right)$ and $\frac{\partial f}{\partial x}\left(x,t\right)$ are continuous in t and x in a region of the x,t plane, including where $a\left(x\right) \leq t \leq b\left(x\right)$ and $x_0 \leq x \leq x_1$, and where $a\left(x\right)$ and $b\left(x\right)$ are both continuous and have continuous derivatives for $x_0 \leq x \leq x_1$.

The complete SWE formulations demonstrated in the following sections of this appendix write:

1D full SWE

$$\begin{cases} \frac{\partial A}{\partial t} + \frac{\partial Q}{\partial x} & = 0 \\ \dfrac{\partial Q}{\partial t} + \dfrac{\partial}{\partial x}\left(\dfrac{Q^2}{A}\right) + gA\dfrac{\partial H}{\partial x} & = gA\left[-\frac{\partial b}{\partial x} - S_f\right] \end{cases} \tag{A.4}$$

where $u = \frac{1}{h(x,t)}\int_0^{h(x,t)} u_x\left(x,y,z,t\right)dz$ is the depth-averaged velocity, $A = \int_{w_1}^{w_2}\int_{\tilde{b}}^{H} h\left(x,y,t\right)dzdy$ is the flow section and $Q = \int_{w_1}^{w_2}\int_{\tilde{b}}^{H} u_x\left(x,y,t\right)dy$ the mass flux through A and $H\left(x,y,t\right)$ is the water surface elevation. S_f is generally given as a nonlinear friction term modeled using the classical Manning-Strickler's law $S_f = \dfrac{\left|Q\right|Q}{K^2A^2R_h^{4/3}}$, where K is an effective friction parameter (see Eq. 1.3). $R_h = {}^{A}/_{P}$ is the hydraulic radius, with P the wetted perimeter.

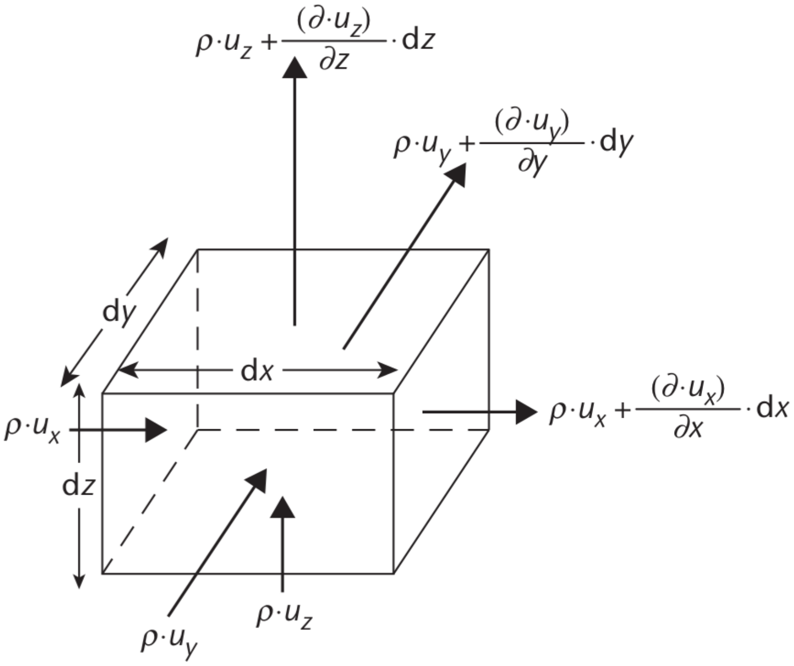

Figure A.1: Microscopic fluid control volume within an open surface flow with mass fluxes (from Dingman [2009]) .

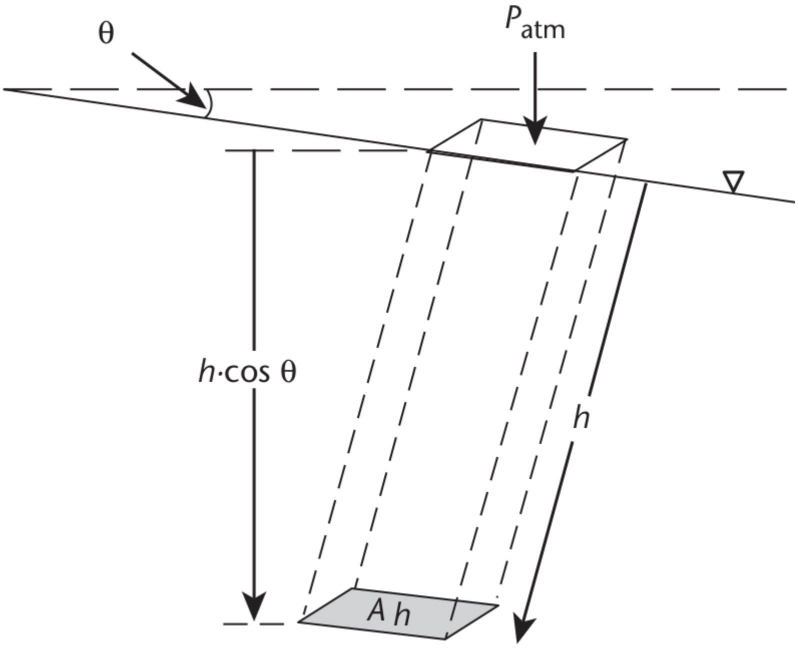

Figure A.2: Element of fluid in a free surface flow, projected on the flow direction axis. (from Dingman [2009]). h is the water depth measured perpendicularly to the water surface, P_{atm} is the atmospheric pressure, θ is the bottom slope in the direction the flow.

2D full SWE

$$\begin{cases} \frac{\partial h}{\partial t} + \frac{\partial hu}{\partial x} + \frac{\partial hv}{\partial y} & = 0 \\ \dfrac{\partial hu}{\partial t} + \dfrac{\partial hu^2}{\partial x} + gh\dfrac{\partial H}{\partial x} & = -gh\left[-\frac{\partial b}{\partial x} - S_{f,x}\right] \\ \dfrac{\partial hv}{\partial t} + \dfrac{\partial hv^2}{\partial y} + gh\dfrac{\partial H}{\partial y} & = -gh\left[-\frac{\partial b}{\partial x} - S_{f,y}\right] \end{cases} \tag{A.5}$$

where $u = \frac{1}{h(x,t)} \int_0^{h(x,t)} u_x\,(x,y,z,t)\,dz$ and $v = \frac{1}{h(x,t)} \int_0^{h(x,t)} u_y\,(x,y,z,t)\,dz$ are the depth-averaged velocity over axes x and y respectively and $H\,(x,y,t)$ is the water surface elevation. S_f is generally given as a nonlinear friction term modeled using the classical Manning-Strickler's law $\mathbf{S}_f = \begin{pmatrix} S_{f,x} \\ S_{f,y} \end{pmatrix} = \dfrac{n^2\,\|\mathbf{u}\|}{h^{1/3}}\mathbf{u}$, where n is an effective friction parameter (see Eq. 1.6).

A.1 Continuity equation integration over depth

In this subsection, the 2D formulation of the continuity equation for SW flows is demonstrated. Let us integrate Eq. A.2.1 over the water depth h:

$$\int_0^{h(x,t)} \frac{\partial u_x}{\partial x} dz + \int_0^{h(x,t)} \frac{\partial u_y}{\partial y} dy + \int_0^{h(x,t)} \frac{\partial u_z}{\partial z} dz = 0 \tag{A.6}$$

By using the Leibniz formula (Eq. A.3), we get:

$$\frac{\partial}{\partial x} \int_0^h u_x dz - \frac{dh}{dx} u_{x,h} + \frac{\partial}{\partial y} \int_0^h u_y dz - \frac{dh}{dy} u_{y,h} + [u_z]_0^h = 0 \tag{A.7}$$

Evaluating Eq. A.7 at the free surface gives the BC3 relation:

$$\frac{\partial h}{\partial t} + u_{x,H} \frac{\partial h}{\partial x} + u_{y,H} \frac{\partial h}{\partial y} = u_{z,H} \tag{A.8}$$

Using the boundary condition at the river bottom (BC2, $u_{z,0} = 0$) and Eq. A.8, Eq. A.7 writes:

$$\begin{aligned} \frac{\partial}{\partial x} \int_0^h u_x dz - \frac{dh}{dx} u_{x,h} + \frac{\partial}{\partial y} \int_0^h u_y dz - \frac{dh}{dy} u_{y,h} + \frac{\partial h}{\partial x} u_{x,h} + u_y \frac{\partial h}{\partial y} (h) + \frac{\partial h}{\partial t} &= 0 \\ \frac{\partial h}{\partial t} + \frac{\partial}{\partial x} \int_0^h u_x dz + \frac{\partial}{\partial y} \int_0^h u_z dz &= 0 \end{aligned} \tag{A.9}$$

Let us define the depth-averaged flow velocity $u\,(x,t) = \frac{1}{h(x,t)} \int_0^{h(x,t)} u_x\,(x,y,z,t)\,dz$ and $v\,(x,t) = \frac{1}{h(x,t)} \int_0^{h(x,t)} u_y\,(x,y,z,t)\,dz$. Eq. A.9 becomes the 2D formulation of the SWE:

$$\frac{\partial h}{\partial t} + \frac{\partial hu}{\partial x} + \frac{\partial hv}{\partial y} = 0 \tag{A.10}$$

By assuming a 1D flow and further integrating by channel width, over a cross-section perpendicular to the 1D flow, the 1D SWE are obtained in (A, Q) variables:

$$\frac{\partial A}{\partial t} + \frac{\partial Q}{\partial x} = 0 \tag{A.11}$$

To model a change in mass (e.g. due to rainfall, seepage or lateral flows), one can introduce $q_l = \frac{\partial Q}{\partial x}$, see e.g. Dingman [2009].

A.2 Momentum equation integration over depth

Let us consider the momentum conservation component of the x axis:

$$\frac{\partial u_x}{\partial t} + u_x\frac{\partial u_x}{\partial x} + u_y\frac{\partial u_x}{\partial y} + u_z\frac{\partial u_x}{\partial z} = -gsin\left(\theta\right) - \frac{1}{\rho}\frac{\partial p}{\partial x} - gS_{f,x} \tag{A.12}$$

Since $div\left(u_x\right) = u_x\left(\frac{\partial u_x}{\partial x} + \frac{\partial u_y}{\partial y} + \frac{\partial u_z}{\partial z}\right) = 0$, we can write:

$$\begin{aligned} u_x\frac{\partial u_x}{\partial x} + v\frac{\partial u_x}{\partial y} + w\frac{\partial u_x}{\partial z} &= u_x\frac{\partial u_x}{\partial x} + u_y\frac{\partial u_x}{\partial y} + u_z\frac{\partial u_x}{\partial z} + u_x\left(\frac{\partial u_x}{\partial x} + \frac{\partial u_y}{\partial y} + \frac{\partial u_z}{\partial z}\right) \\ &= 2u_x\frac{\partial u_x}{\partial x} + u_x\frac{\partial u_y}{\partial y} + u_y\frac{\partial u_x}{\partial y} + u_x\frac{\partial u_z}{\partial z} + u_z\frac{\partial u_x}{\partial z} \end{aligned} \tag{A.13}$$

$$u_x\frac{\partial u_x}{\partial x} + v\frac{\partial u_x}{\partial y} + w\frac{\partial u_x}{\partial z} = \frac{\partial u_x u_y}{\partial y} + \frac{\partial u_x u_z}{\partial z} + \frac{\partial u_x^2}{\partial x} \tag{A.14}$$

By injecting Eq. A.13 in Eq. A.12, we get:

$$\frac{\partial u_x}{\partial t} + \frac{\partial u_x u_y}{\partial y} + \frac{\partial u_x u_z}{\partial z} + \frac{\partial u_x^2}{\partial x} = -gsin\left(\theta\right) - \frac{1}{\rho}\frac{\partial p}{\partial x} - gS_{f,x} \tag{A.15}$$

Let us integrate between the river bottom $\tilde{b}\left(x,y\right)$ (see Fig. 1.12(a), we noted $b\left(x\right) = min_y\tilde{b}\left(x,y\right)$ the river bottom used in 1D modeling) and the free surface elevation $H\left(x,y,t\right)$ over the z-axis, and then between the channel banks at w_1 and w_2 over the y-axis.

$$\begin{aligned} \int_{w_1}^{w_2}\left[\int_{\tilde{b}(x,y)}^{H(x,y,t)}\left[\frac{\partial u_x}{\partial t} + \frac{\partial u_x u_y}{\partial y} + \frac{\partial u_x u_z}{\partial z} + \frac{\partial u_x^2}{\partial x}\right]dz\right]dy &= \int_{w_1}^{w_2}\int_{\tilde{b}(x,y)}^{H(x,y,t)}\left[-gsin\left(\theta\right) - \frac{1}{\rho}\frac{\partial p}{\partial x} - gS_{f,x}\right]dzdy \\ (A) + (B) + (C) + (D) &= (E) + (F) + (G) \end{aligned} \tag{A.16}$$

The Leibniz formula (Eq. A.3) is used to integrate each term separately:

Term (A)

$$\int_{\tilde{b}}^{H}\frac{\partial u_x}{\partial t}dz = \frac{\partial}{\partial t}\int_{\tilde{b}}^{H}u_x dz - \frac{\partial H}{\partial t}u_{x,H} + \frac{\partial H}{\partial t}u_{x,\tilde{b}} \tag{A.17}$$

By using BC2 ($u_{x,\tilde{b}} = 0$), we write:

$$\int_{\tilde{b}}^{H} \frac{\partial u_x}{\partial t} dz = \frac{\partial}{\partial t} \int_{\tilde{b}}^{H} u_x dz - \frac{\partial H}{\partial t} u_{x,H} \tag{A.18}$$

Let us integrate over width:

$$\int_{w_1}^{w_2} \int_{\tilde{b}}^{H} \frac{\partial u_x}{\partial t} dz dy = \int_{w_1}^{w_2} \left[\frac{\partial}{\partial t} \int_{\tilde{b}}^{H} u_x dz - \frac{\partial H}{\partial t} u_{x,H} \right] dy \tag{A.19}$$

$$\begin{aligned} \int_{w_1}^{w_2} \int_{\tilde{b}}^{H} \frac{\partial u}{\partial t} dz dy = & \left[\frac{\partial}{\partial t} \int_{w_1}^{w_2} \int_{\tilde{b}}^{H} u_x dz dy - \left[\frac{\partial w_2}{\partial t} \int_{\tilde{b}}^{H} u_x dz \right] (w_2) + \left[\frac{\partial w_1}{\partial t} \int_{\tilde{b}}^{H} u_x dz \right] (w_1) \right] \\ & - \int_{w_1}^{w_2} \frac{\partial H}{\partial t} u_{x,H} dy \end{aligned} \tag{A.20}$$

At the channel banks at w_1 and w_2 the integral over the water depth is 0, thus :

$$\int_{w_1}^{w_2} \int_{\tilde{b}}^{H} \frac{\partial u_x}{\partial t} dz dy = \frac{\partial}{\partial t} \int_{w_1}^{w_2} \int_{\tilde{b}}^{H} u_x dz dy - \int_{w_1}^{w_2} \frac{\partial H}{\partial t} u_{x,H} dy \tag{A.21}$$

And thus we obtain:

$$\boldsymbol{A} = \frac{\partial Q}{\partial t} - \int_{w_1}^{w_2} \frac{\partial H}{\partial t} u_{x,H} dy \tag{A.22}$$

Term (B)

$$\int_{\tilde{b}}^{H} \frac{\partial u_x u_y}{\partial y} dz = \frac{\partial}{\partial y} \int_{\tilde{b}}^{H} u_x u_y dz - \left[\frac{\partial H}{\partial y} u_x u_y \right] (H) + \left[\frac{\partial \tilde{b}}{\partial t} u_x u_y \right] (\tilde{b}) \tag{A.23}$$

By using BC2 ($u_{x,\tilde{b}} = 0$, $u_{y,\tilde{b}} = 0$), we write:

$$\begin{aligned} \int_{w_1}^{w_2} \int_{\tilde{b}}^{H} \frac{\partial u_x u_y}{\partial y} dz dy &= \int_{w_1}^{w_2} \left[\frac{\partial}{\partial y} \int_{\tilde{b}}^{H} u_x u_y dz - \left[\frac{\partial H}{\partial y} u_x u_y \right] (H) \right] dy && \text{(A.24)} \\ &= \int_{w_1}^{w_2} \frac{\partial}{\partial y} \int_{\tilde{b}}^{H} u_x u_y dz dy - \int_{w_1}^{w_2} \frac{\partial H}{\partial y} u_{x,H} u_{y,H} dy && \text{(A.25)} \\ &= \left[\int_{\tilde{b}}^{H} u_x u_y dz \right] (w_2) - \left[\int_{\tilde{b}}^{H} u_x u_y dz \right] (w_1) - \int_{w_1}^{w_2} \frac{\partial H}{\partial y} u_{x,H} u_{y,H} dy && \text{(A.26)} \end{aligned}$$

Using BC1 at the river banks, we obtain:

$$\boldsymbol{B} = - \int_{w_1}^{w_2} \frac{\partial H}{\partial y} u_{x,H} u_{y,H} dy \tag{A.27}$$

Term (C)

$$\int_{\tilde{b}}^{H} \frac{\partial u_x u_z}{\partial z} dz = [u_x u_z](H) - [u_x u_z](\tilde{b}) \tag{A.28}$$

By using BC2 ($u_{x,\tilde{b}} = 0$), we write:

$$\int_{\tilde{b}}^{H} \frac{\partial u_x u_z}{\partial z} dz = u_{x,H} u_{z,H} \tag{A.29}$$

And thus we obtain:

$$\boldsymbol{C} = \int_{w_1}^{w_2} u_{x,H} u_{z,H} dy \tag{A.30}$$

Term (D)

$$\begin{aligned} \int_{\tilde{b}}^{H} \frac{\partial u_x^2}{\partial x} dz &= \frac{\partial}{\partial x} \int_{\tilde{b}}^{H} u_x^2 dz - \frac{\partial H}{\partial x} u_{x,H}^2 + \frac{\partial H}{\partial t} u_z^2 \\ &= \frac{\partial}{\partial x} \int_{\tilde{b}}^{H} u_x^2 dz - \frac{\partial H}{\partial x} u_{x,H}^2 \end{aligned} \tag{A.31}$$

By using BC3 at the free surface, we know that $u(z) = 0$, we write:

$$\int_{w_1}^{w_2} \int_{\tilde{b}}^{H} \frac{\partial u^2}{\partial x} dz dy = \int_{w_1}^{w_2} \left[\left(\frac{\partial}{\partial x} \int_{\tilde{b}}^{H} u_x^2 dz - \frac{\partial H}{\partial x} u_{x,H}^2 \right) \right] dy \tag{A.32}$$

$$\begin{aligned} &= \frac{\partial}{\partial x} \int_{w_1}^{w_2} \int_{\tilde{b}}^{H} u_x^2 dz dy - \left(\frac{\partial w_2}{\partial x} \int_{\tilde{b}}^{H} u_x^2 dz \right) (w_2) + \left(\frac{\partial w_1}{\partial x} \int_{\tilde{b}}^{H} u_x^2 dz \right) (w_1) \\ &\quad - \int_{w_1}^{w_2} \frac{\partial H}{\partial x} u_{x,H}^2 dy \end{aligned} \tag{A.33}$$

At the channel banks at w_1 and w_2, the integral over the water depth is 0, thus :

$$\boldsymbol{D} = \frac{\partial}{\partial x} \int_{w_1}^{w_2} \int_{\tilde{b}}^{H} u_x^2 dz dy - \int_{w_1}^{w_2} \frac{\partial H}{\partial x} u_{x,H}^2 dy \tag{A.34}$$

The left side of Eq. A.16 becomes :

$$\begin{aligned}
\boldsymbol{(A)} + \boldsymbol{(B)} + \boldsymbol{(C)} + \boldsymbol{(D)} &= \frac{\partial Q}{\partial t} - \int_{w_1}^{w_2} \frac{\partial H}{\partial t} u_{x,H} dy - \int_{w_1}^{w_2} \frac{\partial H}{\partial y} u_{x,H} u_{y,H} dy + \int_{w_1}^{w_2} u_{x,H} u_{z,H} dy \qquad \text{(A.35)} \\
&+ \frac{\partial}{\partial x} \int_{w_1}^{w_2} \int_{\tilde{b}}^{H} u_x^2 dzdy - \int_{w_1}^{w_2} \frac{\partial H}{\partial x} u_{x,H}^2 dy \\
&= \frac{\partial Q}{\partial t} + \frac{\partial}{\partial x} \int_{w_1}^{w_2} \int_{\tilde{b}}^{H} u_x^2 dzdy + \int_{w_1}^{w_2} u_{x,H} \left(-\frac{\partial H}{\partial t} - \frac{\partial H}{\partial y} u_{y,H} + u_{z,H} - \frac{\partial H}{\partial x} u_{x,H} \right) dy \\
& \qquad \text{(A.36)}
\end{aligned}$$

At the free surface, we have $\frac{\partial H}{\partial t} + u_x \frac{\partial H}{\partial x} + u_y \frac{\partial H}{\partial y} = u_z$, thus $-\frac{\partial H}{\partial t} - \frac{\partial H}{\partial y} u_{y,H} + u_{z,H} - \frac{\partial H}{\partial x} u_{x,H} = 0$. The left term $(A) + (B) + (C) + (D)$ of Eq. A.16 write:

$$\frac{\partial Q}{\partial t} + \frac{\partial}{\partial x} \int_{w_1}^{w_2} \int_{\tilde{b}}^{H} u_x^2 dzdy = \frac{\partial Q}{\partial t} + \frac{\partial}{\partial x} \left(\frac{Q^2}{A} \right) \tag{A.37}$$

The right terms $(E) + (F) + (G)$ of Eq. A.16 write:

$$\begin{aligned}
\int_{w_1}^{w_2} \int_{\tilde{b}}^{H} \left(-gsin\left(\theta\right) - \frac{1}{\rho} \frac{\partial p}{\partial x} - gS_{f,x} \right) dzdy &= -\int_{w_1}^{w_2} \int_{\tilde{b}}^{H} \frac{1}{\rho} \frac{\partial \left(P_{atm} + \rho ghcos\left(\theta\right) \right)}{\partial x} dzdy \qquad \text{(A.38)} \\
&- Agsin\left(\theta\right) - AS_{f,x} \\
&= -gA \left(sin\left(\theta\right) + cos\left(\theta\right) \frac{\partial h}{\partial x} + S_{f,x} \right) \qquad \text{(A.39)}
\end{aligned}$$

With the assumption the the bottom slope θ is low, we reach this 1D formulation of the momentum equations:

$$\frac{\partial Q}{\partial t} + \frac{\partial}{\partial x} \left(\frac{Q^2}{A} \right) = -gA \left(\frac{\partial h}{\partial x} + S_f \right) \tag{A.40}$$

$$\frac{\partial Q}{\partial t} + \frac{\partial}{\partial x} \left(\frac{Q^2}{A} \right) + gA \frac{\partial H}{\partial x} = gA \left(S_g - S_f \right) \tag{A.41}$$

with $Q = \int_{w_1}^{w_2} \int_{\tilde{b}}^{H} u_x dzdy$, $S_g = -\frac{\partial b}{\partial x}$ and $S_f = \frac{\nu}{g} \frac{\partial^2 u_x}{\partial x^2}$.

Following Couderc et al. [2013], by projecting on the y-axis following the same method and omitting integration over the width, we get the 2D formulation:

$$\begin{cases}
\frac{\partial hu}{\partial t} + \frac{\partial hu^2}{\partial x} & = -gh \left(S_{g,x} - S_{f,x} \right) \\
\frac{\partial hv}{\partial t} + \frac{\partial hv^2}{\partial y} & = -gh \left(S_{g,y} - S_{f,y} \right)
\end{cases} \tag{A.42}$$

where $u = \frac{1}{h} \int_{\tilde{b}}^{H} u_x dz$ and $v = \frac{1}{h} \int_{\tilde{b}}^{H} u_y dz$.

Appendix B

Preissmann scheme with lateral flows

Let us consider the classical non-conservative form of the 1D Saint-Venant equations in (A, Q) variables, with added lateral inflow $q_l\,(x,t)$ source terms (see e.g. Roux [2004]; Dingman [2009]). :

$$\left\{\begin{array}{lcl} \dfrac{\partial A}{\partial t} + \dfrac{\partial Q}{\partial x} & = & q_l \\ \frac{\partial Q}{\partial t} + \frac{\partial}{\partial x}\left(\frac{Q^2}{A}\right) + gA\frac{\partial Z}{\partial x} & = & -gAS_f + q_l u_l \end{array}\right. \tag{B.1}$$

with $S_f = \dfrac{|Q|Q}{K^2 A^2 R_h^{4/3}}$ the Manning friction term, q_l the lateral unit discharge over a spatial step and u_l the inflow velocity.

This appendix details the discretization of the 1D SWE (Eq. B.1) including mass and momentum source terms due to lateral inflows with the Preissmann scheme. The formulation is implemented into the DassFlow platform and is adapted from Roux [2004], based on Cunge et al. [1980].

B.1 Preissmann discretization scheme

The semi-implicit Preissmann discretization scheme enables greater time steps than explicit schemes, which allows for shorter simulation times, and is useful for simulation of large spatio-temporal domains.

The generalized Preissmann scheme Cunge et al. [1980] is based on the following discretizations of a real valued function f at a spatial and temporal point $P\,(x,t)$, where $x \in \Omega$ denotes space in the considered discretization Ω and $t \in [0, T]$ denotes time within a time interval T. The scheme writes:

$$f|_P = \theta\left[\psi f_{i+1}^{n+1} + (1-\psi)\, f_i^{n+1}\right] + (1-\theta)\left[\psi f_{i+1}^{n} + (1-\psi)\, f_i^{n}\right] \tag{B.2}$$

$$\left.\frac{\partial f}{\partial t}\right|_P = \psi\frac{f_{i+1}^{n+1} - f_{i+1}^{n}}{\Delta t} + (1-\psi)\,\frac{f_i^{n+1} - f_i^{n}}{\Delta t} \tag{B.3}$$

$$\left.\frac{\partial f}{\partial x}\right|_P = \theta\frac{f_{i+1}^{n+1} - f_j^{n+1}}{\Delta x} + (1-\theta)\,\frac{f_{i+1}^{n} - f_j^{n}}{\Delta x} \tag{B.4}$$

where $j \in [1, N]$ is the space index, with N the number of grid points, that locates the cross-section taken in consideration and $n \in [1, T]$ the time index, with N the number of time steps. θ $(0 \leq \theta \leq 1)$ and ψ $(0 \leq \psi \leq 1)$ are respectively space and time weight. DassFlow1D uses values advised by Sart et al. [2010]: $\psi = 0.5$ and $\theta = 0.55$.

The following notations are adopted:

$$\Delta Q_{i+1} = Q_{i+1}^{n+1} - Q_{i+1}^{n}\, , \Delta Q_i = Q_i^{n+1} - Q_i^n \tag{B.5}$$

$$\Delta Z_{i+1} = Z_{i+1}^{n+1} - Z_{i+1}^{n}\, , \Delta Z_i = Z_i^{n+1} - Z_i^n \tag{B.6}$$

The following details the discretization with the Preissmann scheme, of mass conservation (Eq. B.8) in Subsection B.3.1 and next momentum (Eq. B.10) in section B.3.2.

B.2 Discretization summaries

Below is a short summary of the discretization obtained for the 1D Saint-Venant equations with the Preissmann scheme.

Continuity equation

For a given cross-section we have $\left.\dfrac{\partial A}{\partial Z}\right|_x = W$, so Eq. B.1.1 becomes:

$$W\frac{\partial Z}{\partial t} + \frac{\partial Q}{\partial x} = q_l \tag{B.7}$$

From Eq. B.7, the following discretization is obtained (see Subsection B.3.1):

$$CG.\Delta Q_{i+1} + CH.\Delta Z_{i+1} \quad = \quad CI.\Delta Q_i + CJ.\Delta Z_i + CK \tag{B.8}$$

where CG, CH, CI, CJ and CK are coefficients which depend on hydraulic and geometrical parameters, see details below in Subsection B.3.1. Note that only the CK coefficient is impacted by the lateral inflow term.

Momentum conservation equation

By writing $D = K_s A R_h^{2/3}$, Eq. B.1.2 can also be written as:

$$Q\,|Q| + D^2 \left[\frac{\partial Z}{\partial x} + \frac{1}{gA}\left(\frac{\partial Q}{\partial t} + \frac{\partial QU}{\partial x} - u_l q_l\right)\right] = 0 \tag{B.9}$$

From Eq. B.9, the following discretization is obtained (see Subsection B.3.2):

$$CL.\Delta Q_{i+1} + CM.\Delta Z_{i+1} \quad = \quad CN.\Delta Q_i + CO.\Delta Z_i + CP \tag{B.10}$$

where CL, CM, CN, CO and CP are coefficients that depend on hydraulic and geometric parameters, see details below in Subsection B.3.2.

B.3 Detailed SWE discretization

B.3.1 Mass conservation equation

The lateral discharge q_l term is considered between the cells j and $j+1$ and between the time steps n and $n+1$. It is denoted $q_l|_{j+1/2}^{n+1/2}$. For the sake of simplicity, its temporal discretization is chosen identical to that of other terms in the Preissmann scheme such that: $q_l|_{j+1/2}^{n+1/2} = \theta\ q_l|_{j+1/2}^{n+1} + (1-\theta)\ q_l|_{j+1/2}^{n}$. Temporal chronicles of $q_l|_{j+1/2}$ are given by the user.

In a cross-section located at x, $\left.\dfrac{\partial A}{\partial Z}\right|_x = W(h)$ where h is the water depth and W is the total width, so $\dfrac{\partial A}{\partial t} + \dfrac{\partial Q}{\partial x} = q_l$ gives:

$$W\frac{\partial Z}{\partial t} + \frac{\partial Q}{\partial x} = q_l \tag{B.11}$$

Discretization of Eq. B.11 according to the Preissmann scheme:

$$\begin{aligned}\left(\theta\frac{W_{j+1}^{n+1}-W_j^{n+1}}{2}+(1-\theta)\,\frac{W_{j+1}^{n}-W_j^{n}}{2}\right)\left(\frac{Z_{j+1}^{n+1}-Z_{j+1}^{n}}{2\Delta t}+\frac{Z_j^{n+1}-Z_j^{n}}{2\Delta t}\right)&\\ +\theta\left[\frac{Q_{j+1}^{n+1}-Q_j^{n+1}}{\Delta x}\right]+(1-\theta)\left[\frac{Q_{j+1}^{n}-Q_j^{n}}{\Delta x}\right] &= \theta {q_l}_{j+1/2}^{n+1}+(1-\theta)\,{q_l}_{j+1/2}^{n}\end{aligned} \tag{B.12}$$

$$\begin{aligned}\theta.\Delta Q_{j+1}+\frac{\Delta x}{4\Delta t}\left(W_{j+1}^{n+1}+W_j^{n}\right)\Delta H_{j+1} = {}& \theta\Delta Q_j-\frac{\Delta x}{4\Delta t}\left(W_{j+1}^{n}+W_j^{n}\right)\Delta Z_j-\left(Q_{j+1}^{n}-Q_j^{n}\right)\\ &+\Delta x.\left(\theta {q_l}_{j+1/2}^{n+1}+(1-\theta)\,{q_l}_{j+1/2}^{n}\right)\end{aligned} \tag{B.13}$$

The discretized mass equation obtained is written as:

$$CG.\Delta Q_{j+1}+CH.\Delta Z_{j+1} = CI.\Delta Q_j+CJ.\Delta Z_j+CK \tag{B.14}$$

With:

$$CG = \theta \tag{B.15}$$

$$CH = \frac{\Delta x}{4\Delta t}\left(W_{j+1}^{n}+W_j^{n}\right) \tag{B.16}$$

$$CI = \theta \tag{B.17}$$

$$CJ = -\frac{\Delta x}{4\Delta t}\left(W_{j+1}^{n}+W_j^{n}\right) \tag{B.18}$$

$$CK = -\left(Q_{j+1}^{n}-Q_j^{n}\right)+\Delta x\left(\theta {q_l}_{j+1/2}^{n+1}+(1-\theta)\,{q_l}_{j+1/2}^{n}\right) \tag{B.19}$$

B.3.2 Momentum conservation equation

Let us recall Eq. B.1.2:

$$\frac{\partial Q}{\partial t} + \frac{\partial}{\partial x}\left(\frac{Q^2}{A}\right) + gA\frac{\partial Z}{\partial x} = -gA\frac{|Q|Q}{K^2A^2R_h^{4/3}} + u_l q_l \tag{B.20}$$

Multiplying by D^2 ($D = K_s A R_h^{2/3}$) and dividing by gA leads to:

$$Q\,|Q| + D^2\left[\frac{\partial Z}{\partial x} + \frac{1}{gA}\left(\frac{\partial Q}{\partial t} + \frac{\partial QU}{\partial x} - u_l q_l\right)\right] = 0 \tag{B.21}$$

This appendix focuses on the discretization of the lateral inflow source term. The other terms are discretized by successive linearizations in Roux [2004].

Discretization of $u_l q_l$ The term $u_l q_l$ corresponds to the momentum injected between sections j and $j+1$. We write its discretization $u_l|_{j+1/2}^{n+1/2}\, q_l|_{j+1/2}^{n+1/2}$, which means it intervenes between sections j and $j+1$ and time steps n and $n+1$. For the sake of simplicity, the temporal discretization of $u_l|_{j+1/2}^{n+1/2}\, q_l|_{j+1/2}^{n+1/2}$ will be identical to that of other terms in the Preissmann scheme. We write:

$$u_l|_{j+1/2}^{n+1/2}\, q_l|_{j+1/2}^{n+1/2} = \theta\,(u_l q_l)|_{j+1/2}^{n+1} + (1-\theta)\,(u_l q_l)|_{j+1/2}^{n} \tag{B.22}$$

To avoid the need to provide values for $u_l|_{j+1/2}$, and seeing that the flow velocity on the tributary depends on the hydrodynamics of the main reach, especially in subcritical regime, the velocity terms is estimated from calculated velocities in the reach (U_j and U_{j+1}). This work is focused on fluvial flow modeling in a context of satellite observability and does not feature subcritical and critical regimes at lateral inflow injection points.

$$u_l|_{j+1/2}^{n+1/2} = \alpha\; U|_j^{n+1/2} + (1-\alpha)\; U|_{j+1}^{n+1/2} \tag{B.23}$$

where α is the spatial weight of u_l. It is set to 0.5, so that the lateral injection velocity is the average of computed channel velocities at the upstream and downstream cross-sections.

By introducing (B.23) in the discretization of $u_l q_l$, we can write:

$$u_l|_{j+1/2}^{n+1/2}\, q_l|_{j+1/2}^{n+1/2} = \theta\,(u_l q_l)|_{j+1/2}^{n+1} + (1-\theta)\,(u_l q_l)|_{j+1/2}^{n} \tag{B.24}$$

$$= \theta\left(\alpha U|_j^{n+1} + (1-\alpha)\, U|_{j+1}^{n+1}\right) q_l|_{j+1/2}^{n+1} \tag{B.25}$$

$$+ (1-\theta)\left(\alpha U|_j^{n} + (1-\alpha)\, U|_{j+1}^{n}\right) q_l|_{j+1/2}^{n}$$

Rearrangement of $\alpha U|_j^{n+1} + (1-\alpha)\, U|_{j+1}^{n+1}$ Let us rearrange the lateral inflow source term discretization such that it is expressed by its dependency on ΔZ and ΔQ.

Flow velocity U at time $n+1$ writes:

$$U^{n+1} = U^n + \left.\frac{\partial U}{\partial Z}\right|^n \Delta Z + \left.\frac{\partial U}{\partial Q}\right|^n \Delta Q \tag{B.26}$$

$$= U^n - \left.\frac{QW}{A^2}\right|^n \Delta Z + \left.\frac{1}{A}\right|^n \Delta Q \tag{B.27}$$

By replacing Eq. B.27 in $\alpha U|_j^{n+1} + (1-\alpha) U|_{j+1}^{n+1}$ we get:

$$\begin{aligned}\alpha U|_j^{n+1} + (1-\alpha)\, U|_{j+1}^{n+1} &= \alpha \left(U|_j^n - \left.\frac{QW}{A^2}\right|_j^n \Delta Z_j + \left.\frac{1}{A}\right|_j^n \Delta Q_j \right) \\ &+ (1-\alpha) \left(U|_{j+1}^n - \left.\frac{QW}{A^2}\right|_{j+1}^n \Delta Z_{j+1} + \left.\frac{1}{A}\right|_{j+1}^n \Delta Q_{j+1} \right)\end{aligned} \tag{B.28}$$

$$\begin{aligned}&= \alpha U|_j^n + (1-\alpha)\, U|_{j+1}^n + (1-\alpha) \left.\frac{1}{A}\right|_{j+1}^n \Delta Q_{j+1} \\ &+ \alpha \left.\frac{1}{A}\right|_j^n \Delta Q_j - (1-\alpha) \left.\frac{QW}{A^2}\right|_j^n \Delta Z_{j+1} - \alpha \left.\frac{QW}{A^2}\right|_j^n \Delta Z_j\end{aligned} \tag{B.29}$$

Thus, the discretization of $u_l|_{j+1/2}^{n+1/2}\, q_l|_{j+1/2}^{n+1/2}$ in Eq. B.25 becomes:

$$\begin{aligned}u_l|_{j+1/2}^{n+1/2}\, q_l|_{j+1/2}^{n+1/2} = \theta &\left[\alpha U|_j^n + (1-\alpha)\, U|_{j+1}^n + (1-\alpha) \left.\frac{1}{A}\right|_{j+1}^n \Delta Q_{j+1} \right. \\ &\left. +\alpha \left.\frac{1}{A}\right|_j^n \Delta Q_j - (1-\alpha) \left.\frac{QW}{A^2}\right|_j^n \Delta Z_{j+1} - \alpha \left.\frac{QW}{A^2}\right|_j^n \Delta Z_j \right] q_l|_{j+1/2}^{n+1} \\ &+ (1-\theta) \left(\alpha U|_j^n + (1-\alpha)\, U|_{j+1}^n \right) q_l|_{j+1/2}^n\end{aligned} \tag{B.30}$$

This can be written in compact form as:

$$u_l\big|_{j+1/2}^{n+1/2}\ q_l\big|_{j+1/2}^{n+1/2} = CLat_1 + CLat_2\Delta Q_{j+1} + CLat_3\Delta Q_j + CLat_4\Delta Z_{j+1} + CLat_5\Delta Z_j \tag{B.31}$$

With:

$$\begin{aligned}
CLat_1 = {} & \theta\ q_l\big|_{j+1/2}^{n+1}\left(\alpha\ U\big|_j^n + (1-\alpha)\ U\big|_{j+1}^n\right) \\
& + (1-\theta)\ q_l\big|_{j+1/2}^{n}\left(\alpha\ U\big|_j^n + (1-\alpha)\ U\big|_{j+1}^n\right) && \text{(B.32)} \\
CLat_2 = {} & \theta\,(1-\alpha)\ \frac{1}{A}\bigg|_{j+1}^{n}\ q_l\big|_{j+1/2}^{n+1} && \text{(B.33)} \\
CLat_3 = {} & \alpha\ \frac{1}{A}\bigg|_{j}^{n}\ q_l\big|_{j+1/2}^{n+1} && \text{(B.34)} \\
CLat_4 = {} & -\theta\,(1-\alpha)\ \frac{QW}{A^2}\bigg|_{j+1}^{n}\ q_l\big|_{j+1/2}^{n+1} && \text{(B.35)} \\
CLat_5 = {} & -\theta\alpha\ \frac{QW}{A^2}\bigg|_{j}^{n}\ q_l\big|_{j+1/2}^{n+1} && \text{(B.36)}
\end{aligned}$$

The discretization of the terms from eq:Conservation of Momentum to Discretize other than $u_l q_l$ is detailed in Roux [2004]. The current work adapted the method for the lateral source term, with the $CLat_i$, $i \in [1,5]$ terms. By regrouping the discretized terms of Eq. B.21 from Roux [2004] and the above, we obtain the following discretized momentum conservation equation:

$$\begin{aligned}
& CB_1 + CB_2\Delta Q_{j+1} + CB_3\Delta Q_j + \left(CC_1 + CC_4\Delta Z_{j+1} + CC_5\Delta Z_j\right) \\
& * \left[CD_1 + CD_4\Delta Z_{j+1} + CD_5\Delta Z_j + \left(CH_1 + CH_4\Delta Z_{j+1} + CH_5\Delta Z_j\right)\right. \\
& * \left(CE_2\Delta Q_{j+1} + CE_3\Delta Q_j + CF_1 + CF_2\Delta Q_{j+1} + CF_3\Delta Q_j + CF_4\Delta Z_{j+1} + CF_5\Delta Z_j\right. \\
& \left.\left. - CLat_1 - CLat_2\Delta Q_{j+1} - CLat_3\Delta Q_j - CLat_4\Delta Z_{j+1} - CLat_5\Delta Z_j\right)\right] = 0
\end{aligned} \tag{B.37}$$

Rearranging the above expression, we can rewrite the above formula as:

$$CL\Delta Q_{j+1} + CM\Delta Z_{j+1} = CN\Delta Q_j + CO\Delta Z_j + CP \tag{B.38}$$

With:

$$\begin{aligned}
CL = {} & CB_2 + CC_1CH_1\left(CE_2 + CF_2 - CLat_2\right) && \text{(B.39)} \\
CM = {} & CC_4\left(CD_1 + CH_1\left(CF_1 - CLat_1\right)\right) && \text{(B.40)} \\
& + CC_1\left(CD_5 + CH_1\left(CF_5 - CLat_5\right) + CH_5\left(CF_1 - CLat_1\right)\right) \\
CN = {} & -\left[CB_3 + CC_1CH_1\left(CE_3 + \left(CF_3 - CLat_3\right)\right)\right] && \text{(B.41)} \\
CO = {} & -\left(CC_5\left(CD_1 + CH_1\left(CF_1 - CLat_1\right)\right)\right. && \text{(B.42)} \\
& \left. + CC_1\left(CD_5 + CH_1\left(CF_5 - CLat_5\right) + CH_5\left(CF_1 - CLat_1\right)\right)\right) \\
CP = {} & -\left[CB_1 + CC_1\left(CD_1 + CH_1\left(CF_1 - CLat_1\right)\right)\right] && \text{(B.43)}
\end{aligned}$$

Bibliography

Assimilation of virtual wide swath altimetry to improve Arctic river modeling. *Remote Sensing of Environment*, 115(2):373 – 381, 2011. ISSN 0034-4257. URL https://doi.org/10.1016/j.rse.2010.09.008.

The Global Observing System for Climate: Implementation Needs. 2016.

T. Abrate, P. Hubert, and D. Sighomnou. A study on hydrological series of the niger river. *Hydrological sciences journal*, 58(2):271–279, 2013. URL https://doi.org/10.1080/02626667.2012.752575.

Agência Nacional de Águas e Saneamento Básico (ANA). Brasil hydrografia. http://www.portalbrasil.net/brasil_hidrografia.htm. Accessed: 2020-02-06.

G.H. Allen and T.M. Pavelsky. Patterns of river width and surface area revealed by the satellite-derived North American River Width data set. *Geophysical Research Letters*, 42(2):395–402, 2015. URL https://doi.org/10.1002/2014GL062764.

G.H. Allen and T.M. Pavelsky. Global extent of rivers and streams. *Science*, 2018. ISSN 0036-8075. URL https://doi.org/10.1126/science.aat0636.

G.H. Allen, C.H. David, K.M. Andreadis, F. Hossain, and J.S. Famiglietti. Global estimates of river flow wave travel times and implications for low-latency satellite data. *Geophysical Research Letters*, 45(15):7551–7560, 2018. URL https://doi.org/10.1029/2018GL077914.

D. Alsdorf, P. Bates, J. Melack, M. Wilson, and T. Dunne. Spatial and temporal complexity of the Amazon flood measured from space. *Geophysical Research Letters*, 34(8), 2007. URL https://doi.org/10.1029/2007GL029447.

E.H. Altenau, T.M. Pavelsky, D. Moller, C. Lion, L.H. Pitcher, G.H. Allen, P.D. Bates, S. Calmant, M. Durand, and L.C. Smith. AirSWOT measurements of river water surface elevation and slope: Tanana River, AK. *Geophysical Research Letters*, 44(1):181–189, 2017. URL https://doi.org/10.1002/2016GL071577.

M. Amara, D. Capatina-Papaghiuc, and D. Trujillo. Hydrodynamical modelling and multidimensional approximation of estuarian river flows. *Computing and Visualization in Science*, 6(2): 39–46, 2004. URL https://doi.org/10.1007/s00791-003-0106-z.

C. Ancey. *Hydraulique à surface libre*. Ecole Polytechnique Fédérale de Lausanne Ecublens, 2018.

F. Anctil. *Hydrologie, cheminements de l'eau*. 2005.

K.M. Andreadis, E.A. Clark, D.P. Lettenmaier, and D.E. Alsdorf. Prospects for river discharge and depth estimation through assimilation of swath-altimetry into a raster-based hydrodynamics model. *Geophysical Research Letters*, 34(10).

K.M. Andreadis, G. Schumann, and T. Pavelsky. A simple global river bankfull width and depth database. *Water Resources Research*, 49(10):7164–7168, 2013. ISSN 1944-7973. URL http://dx.doi.org/10.1002/wrcr.20440.

G.T. Aronica, F. Franza, P.D. Bates, and J.C. Neal. Probabilistic evaluation of flood hazard in urban areas using monte carlo simulation. *Hydrological Processes*, 26(26):3962–3972, 2012. URL https://doi.org/10.1002/hyp.8370.

M. Asch, M. Bocquet, and M. Nodet. *Data assimilation: methods, algorithms, and applications*. Fundamentals of Algorithms. SIAM, 2016. URL https://hal.inria.fr/hal-01402885.

E. Audusse, F. Bouchut, M.-O. Bristeau, R. Klein, and B. Perthame. A fast and stable well-balanced scheme with hydrostatic reconstruction for shallow water flows. *SIAM J. Sci. Comput.*, 25(6):2050–2065, June 2004. ISSN 1064-8275. URL http://dx.doi.org/10.1137/S1064827503431090.

G. Balsamo, A. Agusti-Panareda, C. Albergel, G. Arduini, A. Beljaars, J. Bidlot, E. Blyth, N. Bousserez, S. Boussetta, A. Brown, et al. Satellite and in situ observations for advancing global earth surface modelling: A review. *Remote Sensing*, 10(12):2038, 2018. URL https://doi.org/10.3390/rs10122038.

F. Baratelli, N. Flipo, and F. Moatar. Estimation of stream-aquifer exchanges at regional scale using a distributed model: Sensitivity to in-stream water level fluctuations, riverbed elevation and roughness. *Journal of Hydrology*, 542:686–703, 2016. URL https://doi.org/10.1016/j.jhydrol.2016.09.041.

A. Barré de Saint-Venant. Théorie du mouvement non-permanent des eaux, avec application aux crues des rivières et à l'introduction des marées dans leur lit. *CR Acad. Sci. Paris*, 73(147-154): 5, 1871.

T. Barth. Numerical methods for conservative laws on structured and unstructured meshes. Technical report, VKI Lecture Series, 2003.

S. Barthélémy, S. Ricci, T. Morel, N. Goutal, E. Le Pape, and F. Zaoui. On operational flood forecasting system involving 1D/2D coupled hydraulic model and data assimilation. *Journal of Hydrology*, 562:623–634, 2018. URL https://doi.org/10.1016/j.jhydrol.2018.05.007.

P. Bates, M. Trigg, J. Neal, and A. Dabrowa. LISFLOOD-FP. *User manual. School of Geographical Sciences, University of Bristol. Bristol, UK*, 2013.

P.D. Bates, M.S. Horritt, and T.J. Fewtrell. A simple inertial formulation of the shallow water equations for efficient two-dimensional flood inundation modelling. *Journal of Hydrology*, 387 (1-2):33–45, 2010. URL https://doi.org/10.1016/j.jhydrol.2010.03.027.

L. Begnudelli and B.F. Sanders. Unstructured grid finite-volume algorithm for shallow-water flow and scalar transport with wetting and drying. *Journal of hydraulic engineering*, 132(4): 371–384, 2006. URL https://doi.org/10.1061/(ASCE)0733-9429(2006)132:4(371).

A.R. Bertalanffy, K.E. Boulding, W.R. Ashby, M. Mead, and G. Bateson. *General System Theory*. New York: George Braziller, 1968.

K.J. Beven. Prophecy, reality and uncertainty in distributed hydrological modelling. *Advances in Water Resources*, 16:41–51, 1993. URL https://doi.org/10.1016/0309-1708(93)90028-E.

K.J. Beven. Uniqueness of place and process representations in hydrological modelling. *Hydrology and earth system sciences*, 4(2):203–213, 2000. URL https://doi.org/10.5194/hess-4-203-2000,2000.

K.J. Beven. A manifesto for the equifinality thesis. *Journal of Hydrology*, 320:18–36, 2006. URL https://doi.org/10.1016/j.jhydrol.2005.07.007.

S. Biancamaria, D.P. Lettenmaier, and T.M. Pavelsky. The SWOT Mission and Its Capabilities for Land Hydrology. *Surveys in Geophysics*, 37(2):307–337, Mar 2016. ISSN 1573-0956. URL http://dx.doi.org/10.1007/s10712-015-9346-y.

S. Biancamaria, F. Frappart, A.-S. Leleu, V. Marieu, D. Blumstein, Jean-Damien Desjonquï¿½res, F. Boy, A. Sottolichio, and A. Valle-Levinson. Satellite radar altimetry water elevations performance over a 200m wide river: Evaluation over the garonne river. *Advances in Space Research*, 59(1):128 – 146, 2017. ISSN 0273-1177. URL https://doi.org/10.1016/j.asr.2016.10.008.

C.M. Birkett. Contribution of the TOPEX NASA Radar Altimeter to the global monitoring of large rivers and wetlands. *Water Resources Research*, 34(5):1223–1239, 1998. URL https://doi.org/10.1029/98WR00124.

D.M. Bjerklie, C.M. Birkett, .W. Jones, C. Carabajal, J.A. Rover, J.W. Fulton, and P.-A. Garambois. Satellite remote sensing estimation of river discharge: Application to the Yukon river Alaska. *Journal of Hydrology*, 561:1000 – 1018, 2018. ISSN 0022-1694. doi: 10.1016/j.jhydrol.2018.04.005. URL http://www.sciencedirect.com/science/article/pii/S0022169418302464.

D. Bousmar and Y. Zech. Momentum transfer for practical flow computation in compound channels. *Journal of hydraulic engineering*, 125(7):696–706, 1999. URL https://doi.org/10.1061/(ASCE)0733-9429(1999)125:7(696).

J. Boussinesq. Théorie de l'intumescence liquide appelée onde solitaire ou de translation se propageant dans un canal rectangulaire. *CR Acad. Sci. Paris*, 72(755-759):1871, 1871.

F. Bouttier and P. Courtier. Data assimilation concepts and methods march 1999. *Meteorological training course lecture series. ECMWF*, page 59, 2002. URL http://msi.ttu.ee/~elken/Assim_concepts.pdf.

J.P.L.F. Brêda, R.C.D. Paiva, J.M. Bravo, O.A. Passaia, and D.M. Moreira. Assimilation of satellite altimetry data for effective river bathymetry. *Water Resources Research*, 55(9):7441–7463, 2019. URL https://doi.org/10.1029/2018WR024010.

P. Brisset, J. Monnier, P.-A. Garambois, and H. Roux. On the assimilation of altimetric data in 1D Saint-Venant river flow models. *Advances in water resources*, 119:41–59, 2018. URL https://doi.org/10.1016/j.advwatres.2018.06.004.

The Editors of Encyclopaedia Britannica. Water Cycle. Accessed 28 October 2021. URL https://www.britannica.com/science/water-cycle.

G.W. Brunner. HEC-RAS River Analysis System. Hydraulic Reference Manual. Version 1.0. Technical report, Hydrologic Engineering Center Davis CA, 1995. URL https://apps.dtic.mil/sti/citations/ADA311952.

T. Buffard and S. Clain. Monoslope and Multislope MUSCL Methods for unstructured meshes. *Journal of Comptutational Physics*, 229:3745–3776, 2010. URL https://doi.org/10.1016/j.jcp.2010.01.026.

D.G. Cacuci, I.M. Navon, and M. Ionescu-Bugor. *Computational Methods for Data Evaluation and Assimilation*. Taylor and Francis CRC Press: Boca Raton, 2013.

J. Callède, D.M. Moreira, and S. Calmant. Détermination de l'altitude du zéro des stations hydrométriques en Amazonie brésilienne. Application aux lignes d'eau des Rios Negro, Solimões et Amazone. *Journal of Water Science*, 26(2):153–171, 2013. URL https://doi.org/10.7202/1016065ar.

S. Calmant, F. Seyler, and J-F. Cretaux. Monitoring continental surface waters by satellite altimetry. *Surveys in Geophysics*, 29(4-5):247–269, 2008. ISSN 0169-3298. URL http://dx.doi.org/10.1007/s10712-008-9051-1.

S. Calmant, J-F. Cretaux, and F. Remy. Principles of Radar Satellite Altimetry for Application on Inland Waters. In Nicolas Baghdadi and Mehrez Zribi, editors, *Microwave Remote Sensing of Land Surface*, pages 175 – 218. Elsevier, 2016. ISBN 978-1-78548-159-8. URL https://doi.org/10.1016/B978-1-78548-159-8.50004-9.

M. Carlier. *Hydraulique générale et appliquée*. Eyrolles, Paris, France, 1982.

A. Carrassi, M. Bocquet, L. Bertino, and G. Evensen. Data assimilation in the geosciences: An overview of methods, issues, and perspectives. *Wiley Interdisciplinary Reviews: Climate Change*, 9(5):e535, 2018. URL https://doi.org/10.1002/wcc.535.

A. Carrassi, M. Bocquet, J. Demaeyer, C. Grudzien, P. Raanes, and S. Vannitsem. Data assimilation for chaotic dynamics. *Data Assimilation for Atmospheric, Oceanic and Hydrologic Applications (Vol. IV)*, pages 1–42, 2022. URL https://doi.org/10.1007/978-3-030-77722-7_1.

W. Castaings, D. Dartus, F.-X. Le Dimet, and G.-M. Saulnier. Sensitivity analysis and parameter estimation for distributed hydrological modeling: potential of variational methods. *Hydrology and Earth System Sciences*, 13(4):503–517, 2009. URL https://doi.org/10.5194/hess-13-503-2009.

P. Chassaing. Fluid mechanics. Elements of a first course; Mécanique des fluides. Éléments d'un premier parcours. 1997.

S. Chen, P.-A. Garambois, P. Finaud-Guyot, G. Dellinger, R. Mosé, A. Terfous, and A. Ghenaim. Variance based sensitivity analysis of 1D and 2D hydraulic models: An experimental urban flood case. *Environmental Modelling Software*, 109:167 – 181, 2018. ISSN 1364-8152. URL https://doi.org/10.1016/j.envsoft.2018.08.008.

P. Chévrier and H. Galley. A Van Leer finite volume scheme for the Euler equations on unstructured meshes. *ESAIM: Mathematical Modelling and Numerical Analysis*, 27(2):183–201, 1993. URL https://www.esaim-m2an.org/articles/m2an/pdf/1993/02/m2an1993270201831.pdf.

C. Cholet, J.-B. Charlier, R. Moussa, M. Steinmann, and S. Denimal. Assessing lateral flows and solute transport during floods in a conduit-flow-dominated karst system using the inverse problem for the advection-diffusion equation. *Hydrology and Earth System Sciences*, 21(7):3635–3653, 2017. URL https://doi.org/10.5194/hess-21-3635-2017.

V.T. Chow. *Open-channel Hydraulics*. Mc Graw-Hill, New-York, USA, 1959.

V.T. Chow. Handbook of applied hydrology. *McGraw-Hill Book Co., New-York, 1467 pages*, 1964.

CHR. *The Rhine under the influence of man â River engineering works, shipping, water management*. Journal of Hydrology, 1993. ISBN 90-70980-17-7. URL https://doi.org/10.1016/0022-1694(95)90011-X.

G.-M. Christopher and S.L. Arturo. Tutorial on the use of TELEMAC-2D Hydrodynamics model and Pre-/Post-processing with BlueKenue for flood-inundation mapping in Unsteady Flow Conditions. Technical report, Oregon State University-School of Civil and Construction Engineering, 2013. URL http://www.opentelemac.org/index.php/training-and-tutorials.

CNES. SWOT hydrology toolbox. URL https://github.com/CNES/swot-hydrology-toolbox.

G. Cochonneau, F. Sondag, J-L. Guyot, B. Geraldo, N. Filizola, P. Fraizy, A. Laraque, P. Magat, J-M. Martinez, L. Noriega, E. Oliveira, J. Ordonez, R. Pombosa, Seyler F., J. Sidgwick, and P. Vauchel. *L'Observatoire de Recherche en Environnement, ORE HYBAM sur les grands fleuves amazoniens*. 2006. ISBN 978-1-901502-78-7.

F. Colleoni, P.-A. Garambois, P. Javelle, M. Jay-Allemand, Gejadze I., D. Organde, and P. Arnaud. SMASH v1.0 platform for spatially distributed hydrological modeling and data assimilation: hypothesis testing and signatures analysis. *submitted*, 2021.

W. Collischonn, D. Allasia, B.C. Da Silva, and C.E.M. Tucci. The MGB-IPH model for large-scale rainfall-runoff modelling. *Hydrological Sciences Journal*, 52(5):878–895, 2007. URL https://doi.org/10.1623/hysj.52.5.878.

W. Collischonn, A.S. Fleischmann, R.C.D. Paiva, and A. Mejia. Hydraulic causes for basin hydrograph skewness. *Water Resources Research*, 53(12):10603–10618, 2017. URL https://doi.org/10.1002/2017WR021543.

L. Coron, G. Thirel, O. Delaigue, C. Perrin, and V. Andréassian. The suite of lumped GR hydrological models in an R package. *Environmental modelling & software*, 94:166–171, 2017. URL https://doi.org/10.1016/j.envsoft.2017.05.002.

F. Couderc, R. Madec, J. Monnier, and J.-P. Vila. DassFow-Shallow, Variational Data Assimilation for Shallow-Water Models: Numerical Schemes, User and Developer Guides. Research report, University of Toulouse, CNRS, IMT, INSA, ANR, 2013. URL https://hal.archives-ouvertes.fr/hal-01120285.

F. Couderc, R. Madec, J. Monnier, and J.-P. Vila. DassFlow v2.00.00 : User and Developer Guide. Technical report, 2016.

J. A. Cunge, M. Holly, F., and A. Verwey. *Practical Aspects of Computational River Hydraulics*. Pitam Publishing, 1980.

J.S. Da Silva, F. Seyler, S. Calmant, O.C. Rotunno Filho, E. Roux, A.A.M. Aranjo, and J-L. Guyot. Water level dynamics of Amazon wetlands at the watershed scale by satellite altimetry. *International Journal of Remote Sensing*, 33(11):3323–3353, 2012. URL http://dx.doi.org/10.1080/01431161.2010.531914.

P. Davy, T. Croissant, and D. Lague. A precipiton method to calculate river hydrodynamics, with applications to flood prediction, landscape evolution models, and braiding instabilities. *Journal of geophysical research: earth surface*, 122(8):1491–1512, 2017. URL https://doi.org/10.1002/2016JF004156.

A. De Lavenne, V. Andréassian, G. Thirel, M.-H. Ramos, and C. Perrin. A regularization approach to improve the sequential calibration of a semidistributed hydrological model. *Water Resources Research*, 55(11):8821–8839, 2019.

G. De Marsily. *Les eaux continentales*. EDP sciences, 2012.

O. Delestre, F. Darboux, F. James, C. Lucas, C. Laguerre, and S. Cordier. FullSWOF: Full shallow-water equations for overland flow. *The Journal of Open Source Software*, 2(20):448, 2017. doi: https://doi.org/10.21105/joss.00448.

S.L. Dingman. *Fluvial hydraulics*. Oxford University Press, 2009.

G. Dramais, J. Le Coz, B. Camenen, and A. Hauet. Advantages of a mobile lspiv method for measuring flood discharges and improving stage-discharge curves. *Journal of Hydro-Environment Research*, 5(4):301–312, 2011. URL https://doi.org/10.1016/j.jher.2010.12.005.

M. Durand, K.M. Andreadis, D.E. Alsdorf, D.P. Lettenmaier, D. Moller, and M. Wilson. Estimation of bathymetric depth and slope from data assimilation of swath altimetry into a hydrodynamic model. *Geophysical Research Letters*, 35(20), 2008. URL https://doi.org/10.1029/2008GL034150.

M. Durand, L. Fu, D.P. Lettenmaier, D.E. Alsdorf, E. Rodríguez, and D. Esteban-Fernandez. The Surface Water and Ocean Topography Mission: Observing Terrestrial Surface Water and Oceanic Submesoscale Eddies. *Proceedings of the IEEE*, 98(5):766–779, May 2010. URL https://doi.org/10.1109/JPROC.2010.2043031.

M. Durand, J. Neal, E. Rodríguez, K.M. Andreadis, L.C. Smith, and Y. Yoon. Estimating reach-averaged discharge for the river Severn from measurements of river water surface elevation and slope. *Journal of Hydrology*, 511:92–104, 2014. URL https://doi.org/10.1016/j.jhydrol.2013.12.050.

M. Durand, C.J. Gleason, P-A. Garambois, D. Bjerklie, L.C. Smith, H. Roux, E. Rodriguez, P.D. Bates, T.M. Pavelsky, J. Monnier, X. Chen, G. Di Baldassarre, J-M. Fiset, N. Flipo, R.P.d.M. Frasson, J. Fulton, N. Goutal, F. Hossain, E. Humphries, J.T. Minear, M.M. Mukolwe, J.C. Neal, S. Ricci, B.F. Sanders, G. Schumann, J.E. Schubert, and L. Vilmin. An intercomparison of remote sensing river discharge estimation algorithms from measurements of river height, width, and slope. *Water Resources Research*, 52(6):4527–4549, 2016. URL https://doi.org/10.1002/2015WR018434.

A. Efstratiadis and D. Koutsoyiannis. One decade of multi-objective calibration approaches in hydrological modelling: a review. *Hydrological Sciences Journal-Journal Des Sciences Hydrologiques*, 55(1):58–78, 2010. URL https://doi.org/10.1080/02626660903526292.

G. Fabre. "Éléments d'hydrologie" par A. Champoux et C. Toutant, 1989. *Karstologia*, 16(1):55–55, 1990.

A.C. Fassoni-Andrade, R.C.D. de Paiva, and A.S. Fleischmann. Lake topography and active storage from satellite observations of flood frequency. *Water Resources Research*, 56(7), 2020. URL https://doi.org/10.1029/2019WR026362.

A.C. Fassoni-Andrade, A.S. Fleischmann, F. Papa, R.C. Dias de Paiva, S. Wongchuig, J.M. Melack, A.A. Moreira, A. Paris, A. Ruhoff, C. Barbosa, et al. Amazon hydrology from space: scientific advances and future challenges. *Reviews of Geophysics*, 2021. URL https://doi.org/10.1029/2020RG000728.

B.M. Fekete and C.J. Vorosmarty. The current status of global river discharge monitoring and potential new technologies complementing traditional discharge measurements. *IAHS - PUB*, 2002.

N. Filizola. Transfert sédimentaire actuel par les fleuves amazoniens. 2003. URL https://horizon.documentation.ird.fr/exl-doc/pleins_textes/divers16-02/010037029.pdf.

N. Filizola, N. Spínola, W. Arruda, Fr. Seyler, S. Calmant, and J. Silva. The Rio Negro and Rio Solimões confluence point-hydrometric observations during the 2006/2007 cycle. *River, Coastal and Estuarine Morphodynamics-RCEM*, 2009:1003–1006, 2009.

P. Finaud-Guyot. *Macroscopic flood modelling: Taking into account directional flows and main channel-floodplain transfer*. PhD thesis, Université Montpellier 2, 2009. URL http://www.opengrey.eu/item/display/10068/836076.

P. Finaud-Guyot, P.-A. Garambois, S. Chen, G. Dellinger, A. Ghenaim, and A. Terfous. 1D/2D porosity model for urban flood modeling: case of a dense street networks. In *E3S Web of Conferences*, volume 40, page 06010, 2018. URL https://hal.archives-ouvertes.fr/hal-02381266.

A.S. Fleischmann, R.C.D. Paiva, W. Collischonn, M.V. Sorribas, and P.R.M. Pontes. On river-floodplain interaction and hydrograph skewness. *Water Resources Research*, 52(10):7615–7630, 2016. URL https://doi.org/10.1002/2016WR019233.

A.S. Fleischmann, W. Collischonn, R. Paiva, and C.E. Tucci. Modeling the role of reservoirs versus floodplains on large-scale river hydrodynamics. *Natural Hazards*, 99(2):1075–1104, Nov 2019. ISSN 1573-0840. URL https://doi.org/10.1007/s11069-019-03797-9.

A.S. Fleischmann, R.C.D. Paiva, W. Collischonn, V.A. Siqueira, A. Paris, D.M. Moreira, F. Papa, A.A. Bitar, M. Parrens, F. Aires, et al. Trade-offs between 1-D and 2-D regional river hydrodynamic models. *Water Resources Research*, 56(8), 2020. URL https://doi.org/10.1029/2019WR026812.

N. Flipo, C. Monteil, M. Poulin, C. de Fouquet, and M. Krimissa. Hybrid fitting of a hydrosystem model: Long-term insight into the Beauce aquifer functioning (France). *Water Resources Research*, 48(5), 2012. URL https://doi.org/10.1029/2011WR011092.

N. Flipo, A. Mouhri, B. Labarthe, S. Biancamaria, A. Rivière, and P. Weill. Continental hydrosystem modelling: the concept of nested streamndash;aquifer interfaces. *Hydrology and Earth System Sciences*, 18(8):3121–3149, 2014. URL https://doi.org/10.5194/hess-18-3121-2014.

F. Frappart, S. Calmant, M. Cauhope, F. Seyler, and A. Cazenave. Preliminary results of ENVISAT RA-2-derived water levels validation over the Amazon basin. *Remote Sensing of Environment*, 100(2):252 – 264, 2006. ISSN 0034-4257. doi: http://doi.org/10.1016/j.rse.2005.10.027.

D.L. Fread, M. Jin, and J.M. Lewis. An LPI numerical implicit solution for unsteady mixed-flow simulation. In *North American Water and Environment Congress & Destructive Water*, pages 322–327. ASCE, 1996.

L.-L. Fu, D. Alsdorf, R. Morrow, E. Rodriguez, and N. Mognard. SWOT: the surface water and ocean topography mission: wide-swath altimetric elevation on Earth. Technical report, Pasadena, CA: Jet Propulsion Laboratory, National Aeronautics and Space, 2012. URL http://hdl.handle.net/2014/41996.

I. Fujita and Y. Kunita. Application of aerial LSPIV to the 2002 flood of the Yodo River using a helicopter mounted high density video camera. *Journal of Hydro-environment Research*, 5(4): 323–331, 2011. URL https://doi.org/10.1016/j.jher.2011.05.003.

J.-C. Galland, N. Goutal, and J.-M. Hervouet. Telemac: A new numerical model for solving shallow water equations. *Advances in water resources*, 14(3):138–148, 1991.

S. Gao, Y. Huang, S. Zhang, J. Han, G. Wang, M. Zhang, and Q. Lin. Short-term runoff prediction with GRU and LSTM networks without requiring time step optimization during sample generation. *Journal of Hydrology*, 589:125188, 2020. URL https://doi.org/10.1016/j.jhydrol.2020.125188.

P.-A. Garambois and J. Monnier. Inference of effective river properties from remotely sensed observations of water surface. *Advances in Water Resources*, 79:103–120, 2015. URL https://doi.org/10.1016/j.advwatres.2015.02.007.

P.-A. Garambois, S. Calmant, H. Roux, A. Paris, J. Monnier, P. Finaud-Guyot, A.S. Montazem, and J.S. da Silva. Hydraulic visibility: Using satellite altimetry to parameterize a hydraulic model of an ungauged reach of a braided river. *Hydrological Processes*, 31(4):756–767, 2017. ISSN 1099-1085. URL http://dx.doi.org/10.1002/hyp.11033.

P.-A. Garambois, K. Larnier, J. Monnier, P. Finaud-Guyot, J. Verley, A.S. Montazem, and S. Calmant. Variational estimation of effective channel and ungauged anabranching river discharge from multi-satellite water heights of different spatial sparsity. *Journal of Hydrology*, 581:124409, 2020. ISSN 0022-1694. URL https://doi.org/10.1016/j.jhydrol.2019.124409.

L. Garandeau, A. Belleudy, P. Javelle, D. Organde, B. Janet, J. Demargne, C. De Saint-Aubin, and C. Fouchier. Vigicrues Flash, un service automatique d'avertissement pour les crues rapides. In *De la prévision des crues à la gestion de crise*, page 11, Avignon, France, November 2018. Société Hydrotechnique de France. URL https://hal.inrae.fr/hal-02608801.

I. Gejadze and P.-O. Malaterre. Discharge estimation under uncertainty using variational methods with application to the full Saint-Venant hydraulic network model. *International Journal for Numerical Methods in Fluids*, 83(5):405–430, 2017. ISSN 1097-0363. URL http://dx.doi.org/10.1002/fld.4273.

I. Gejadze and J. Monnier. On a 2D zoom for the 1D shallow water model: Coupling and data assimilation. *Computer methods in applied mechanics and engineering*, 196(45-48):4628–4643, 2007. URL https://doi.org/10.1016/j.cma.2007.05.026.

P. Gervasio, J.-L. Lions, and A. Quarteroni. Heterogeneous coupling by virtual control methods. *Numerische Mathematik*, 90(2):241–264, 2001. URL https://doi.org/10.1007/s002110100303.

A.C.V. Getirana, M.-P. Bonnet, O.C. Rotunno Filho, W. Collischonn, J.-L. Guyot, F. Seyler, and W.J. Mansur. Hydrological modelling and water balance of the Negro River basin: evaluation based on in situ and spatial altimetry data. *Hydrological processes*, 24(22):3219–3236, 2010. URL https://doi.org/10.1002/hyp.7747.

M. Ghil and P. Malanotte-Rizzoli. Data assimilation in meteorology and oceanography. In *Advances in geophysics*, volume 33, pages 141–266. Elsevier, 1991. URL https://doi.org/10.1016/S0065-2687(08)60442-2.

S. Gibson, A. Simon, E. Langendoen, N. Bankhead, and J. Shelley. A physically-based channel-modeling framework integrating HEC-RAS sediment transport capabilities and the USDA-ARS bank-stability and toe-erosion model (BSTEM). In *Federal Interagency Sediment Conference, SedHyd Proceedings*, 2015.

J. C. Gilbert and C. Lemaréchal. Some numerical experiments with variable-storage quasi-Newton algorithms. *Mathematical programming*, 45(1-3):407–435, 1989. URL https://link.springer.com/content/pdf/10.1007/BF01589113.pdf.

C.J. Gleason and L.C. Smith. Toward global mapping of river discharge using satellite images and at-many-stations hydraulic geometry. *Proceedings of the National Academy of Sciences*, 111 (13):4788–4791, 2014. ISSN 0027-8424. URL http://doi.org/10.1073/pnas.1317606111.

S. Godunov and I. Bohachevsky. Finite difference method for numerical computation of discontinuous solutions of the equations of fluid dynamics. *Matematičeskij sbornik*, 47(3):271–306, 1959. URL https://hal.archives-ouvertes.fr/hal-01620642.

N. Goutal and F. Maurel. A finite volume solver for 1D shallow-water equations applied to an actual river. *International Journal for Numerical Methods in Fluids*, 38(1):1–19, 2002. URL https://doi.org/10.1002/fld.201.

W.H. Graf and M.S. Altinakar. *Hydraulique fluviale: écoulement et phénomènes de transport dans les canaux à géométrie simple*, volume 16. PPUR presses polytechniques, 2000.

R. Grayson and G. Blöschl. *Spatial patterns in catchment hydrology: observations and modelling*. CUP Archive, 2001.

W.H. Green and G.A. Ampt. Studies on soil phyics. *The Journal of Agricultural Science*, 4(1):1–24, 1911. URL https://doi.org/10.1017/S0021859600001441.

S. Grimaldi, Y. Li, J.P. Walker, and V.R.N. Pauwels. Effective representation of river geometry in hydraulic flood forecast models. *Water Resources Research*, 54(2):1031–1057, 2018. URL https://doi.org/10.1002/2017WR021765.

G.H. Gudmundsson. Transmission of basal variability to a glacier surface. *Journal of Geophysical Research: Solid Earth*, 108(B5), 2003. URL https://doi.org/10.1029/2002JB002107.

L. Guertault, B. Camenen, C. Peteuil, A. Paquier, and J.-B. Faure. One-dimensional modeling of suspended sediment dynamics in dam reservoirs. *Journal of Hydraulic Engineering*, 142(10): 04016033, 2016. URL https://doi.org/10.1061/(ASCE)HY.1943-7900.0001157.

V. Guinot. *Wave propagation in fluids: models and numerical techniques, second edition.*, volume 49. 2010.

V. Guinot. Multiple porosity shallow water models for macroscopic modelling of urban floods. *Advances in Water Resources*, 37:40–72, 2012. URL https://doi.org/10.1016/j.advwatres.2011.11.002.

V. Guinot, B.F. Sanders, and J.E. Schubert. Dual integral porosity shallow water model for urban flood modelling. *Advances in water resources*, 103:16–31, 2017. URL https://doi.org/10.1016/j.advwatres.2017.02.009.

V. Guinot, C. Delenne, A. Rousseau, and O. Boutron. Flux closures and source term models for shallow water models with depth-dependent integral porosity. *Advances in Water Resources*, 122:1–26, 2018. URL https://doi.org/10.1016/j.advwatres.2018.09.014.

S.A. Haben, A.S. Lawless, and N.K. Nichols. Conditioning and preconditioning of the variational data assimilation problem. *Computers & Fluids*, 46(1):252–256, 2011a. URL https://doi.org/10.1016/j.compfluid.2010.11.025.

S.A. Haben, A.S. Lawless, and N.K. Nichols. Conditioning of incremental variational data assimilation, with application to the Met Office system. *Tellus A*, 63(4):782–792, 2011b. URL https://doi.org/10.1111/j.1600-0870.2011.00527.x.

A. Harten, P.D. Lax, and B. van Leer. On upstream differencing and godunov-type schemes for hyperbolic conservation laws. *SIAM review*, 25(1):35–61, 1983. URL https://doi.org/10.1137/1025002.

L. Hascoet and V. Pascual. The Tapenade automatic differentiation tool: principles, model, and specification. *ACM Transactions on Mathematical Software (TOMS)*, 39(3):1–43, 2013. URL http://dx.doi.org/10.1145/2450153.2450158.

R. Hashemi, P. Brigode, P.-A. Garambois, and P. Javelle. How can regime characteristics of catchments help in training of local and regional LSTM-based runoff models? *Hydrology and Earth System Sciences Discussions*, 2021:1–33, 2021. URL https://doi.org/10.5194/hess-2021-511.

A. Hauet, M. Jodeau, J. Le Coz, B. Marchand, A. die Moran, R. Le Boursicaud, and G. Dramais. Application de la méthode LSPIV pour la mesure de champs de vitesse et de débits de crue sur modèle réduit et en rivière. *La Houille Blanche*, (3):16–22, 2014. URL https://doi.org/10.1051/lhb/2014024.

K. Havnø, M.N. Madsen, J. Dørge, et al. Mike 11-a generalized river modelling package. *Computer models of watershed hydrology.*, pages 733–782, 1995.

K.K. Hirschboeck. Flood hydroclimatology. *Flood geomorphology*, 27:49, 1988.

N. Hocini, O. Payrastre, F. Bourgin, E. Gaume, P. Davy, D. Lague, L. Poinsignon, and F. Pons. Performance of automated flood inundation mapping methods in a context of flash floods: a comparison of three methods based either on the Height Above Nearest Drainage (HAND) concept, or on 1D/2D shallow water equations. *Hydrology and Earth System Sciences Discussions*, 2020:1–23, 2020. URL https://doi.org/10.5194/hess-2020-597.

M. Honnorat, X. Lai, F-X. le Dimet, and J. Monnier. Variational data assimilation for 2D fluvial hydraulics simulation. *CMWR XVI-Computational Methods for Water Ressources. Copenhagen, june 2006.* URL https://hal.archives-ouvertes.fr/hal-00908191.

C. Hopkinson. The influence of flying altitude, beam divergence, and pulse repetition frequency on laser pulse return intensity and canopy frequency distribution. *Canadian Journal of Remote Sensing*, 33(4):312–324, 2007. URL https://doi.org/10.5589/m07-029.

R. Hostache, X. Lai, J Monnier, and C. Puech. Assimilation of spatially distributed water levels into a shallow-water flood model. Part II: Use of a remote sensing image of Mosel River. *Journal of Hydrology*, 390:257–268, 2010. URL https://doi.org/10.1016/j.jhydrol.2010.07.0036.

N.M. Hunter, P.D. Bates, S. Neelz, G. Pender, I. Villanueva, N.G. Wright, D. Liang, R.A. Falconer, B. Lin, S. Waller, et al. Benchmarking 2D hydraulic models for urban flooding. In *Proceedings of the Institution of Civil Engineers-Water Management*, volume 161, pages 13–30. Thomas Telford Ltd, 2008. URL https://doi.org/10.1680/wama.2008.161.1.13.

N.N.T. Huynh. Wrapping Python-Fortran du code DassFlow2D. Master's thesis, 2020.

M. Iturbide, J.M. Gutiérrez, L.M. Alves, Jo. Bedia, R. Cerezo-Mota, E. Cimadevilla, A.S. Cofiño, A. Di Luca, S.H. Faria, I.V. Gorodetskaya, et al. An update of IPCC climate reference regions for subcontinental analysis of climate model data: definition and aggregated datasets. *Earth System Science Data*, 12(4):2959–2970, 2020. URL https://doi.org/10.5194/essd-12-2959-2020.

M. Jay-Allemand, P. Javelle, I. Gejadze, P. Arnaud, P.-O. Malaterre, J.-A. Fine, and D. Organde. On the potential of variational calibration for a fully distributed hydrological model: application on a mediterranean catchment. *Hydrology and Earth System Sciences*, 24(11):5519–5538, 2020. URL https://doi.org/10.5194/hess-24-5519-2020.

B. Jeannot, S. Weill, D. Eschbach, L. Schmitt, and F. Delay. A low-dimensional integrated subsurface hydrological model coupled with 2-D overland flow: Application to a restored fluvial hydrosystem (Upper Rhine River-France). *Journal of hydrology*, 563:495–509, 2018. URL https://doi.org/10.1016/j.jhydrol.2018.06.028.

S. Kabir, S. Patidar, X. Xia, Q. Liang, J. Neal, and G. Pender. A deep convolutional neural network model for rapid prediction of fluvial flood inundation. *Journal of Hydrology*, 590:125481, 2020. ISSN 0022-1694. URL https://doi.org/10.1016/j.jhydrol.2020.125481.

R.E. Kalman. A new approach to linear filtering and prediction problems. 1960.

B. Kaltenbacher, A. Neubauer, and O. Scherzer. *Iterative regularization methods for nonlinear ill-posed problems*, volume 6. Walter de Gruyter, 2008.

J.R. Kermode. f90wrap: an automated tool for constructing deep Python interfaces to modern Fortran codes. *Journal of Physics: Condensed Matter*, 32(30):305901, 2020. URL https://doi.org/10.1088/1361-648x/ab82d2.

J.W. Kirchner. Getting the right answers for the right reasons: Linking measurements, analyses, and models to advance the science of hydrology. *Water Resources Research*, 42(3), 2006. URL https://doi.org/10.1029/2005WR004362.

G. Kirstetter, O. Delestre, P.-Y. Lagrée, S. Popinet, and C. Josserand. B-flood 1.0: an open-source Saint-Venant model for flash flood simulation using adaptive refinement. *Geoscientific Model Development Discussions*, pages 1–24, 2021. URL https://doi.org/10.5194/gmd-14-7117-2021.

S.J. Kline, W.C. Reynolds, F.A. Schraub, and P.W. Runstadler. The structure of turbulent boundary layers. *Journal of Fluid Mechanics*, 30(4):741–773, 1967. URL https://doi.org/10.1017/S0022112067001740.

C.J. Koblinsky, R.T. Clarke, A.C. Brenner, and H. Frey. Measurement of river level variations with satellite altimetry. Technical report, Wiley Online Library, 1993. URL https://doi.org/10.1029/93WR00542.

F. Kratzert, D. Klotz, G. Shalev, G. Klambauer, S. Hochreiter, and G. Nearing. Towards learning universal, regional, and local hydrological behaviors via machine learning applied to large-sample datasets. *Hydrology and Earth System Sciences*, 23(12):5089–5110, 2019. URL https://doi.org/10.5194/hess-23-5089-2019.

X. Lai and J. Monnier. Assimilation of spatially distributed water levels into a shallow-water flood model. Part I: Mathematical method and test case. *Journal of Hydrology*, 377:1–11, 2009. URL https://doi.org/10.1016/j.jhydrol.2009.07.058. 1-2.

M. Lang, C. Perret, E. Renouf, E. Sauquet, and A. Paquier. Incertitudes sur les débits de crue. *La Houille Blanche*, 92(6):33–41, 2006. URL https://doi.org/10.1051/lhb:2006098.

E.J. Langendoen, A. Mendoza, J.D. Abad, P. Tassi, D. Wang, R. Ata, K. El kadi Abderrezzak, and J.-M. Hervouet. Improved numerical modeling of morphodynamics of rivers with steep banks. *Advances in water resources*, 93:4–14, 2016. URL https://doi.org/10.1016/j.advwatres.2015.04.002.

K. Larnier. *Modélisation thermohydraulique d'un tronçon de Garonne en lien avec l'habitat piscicole : Approches statistique et déterministe*. PhD thesis, Toulouse, 2010. URL http://ethesis.inp-toulouse.fr/archive/00001263/.

K. Larnier and J. Monnier. Hybrid neural network-variational data assimilation algorithm to infer river discharges from swot-like data. *Nonlinear Processes in Geophysics Discussions*, pages 1–30, 2020. URL https://doi.org/10.5194/npg-2020-32.

K. Larnier, J. Monnier, P.-A. Garambois, and J. Verley. River discharge and bathymetry estimation from swot altimetry measurements. *Inverse Problems in Science and Engineering*, 29(6):759–789, 2021. URL https://doi.org/10.1080/17415977.2020.1803858.

E.M. Latrubesse and E. Franzinelli. The late quaternary evolution of the negro river, amazon, brazil: Implications for island and floodplain formation in large anabranching tropical systems. *Geomorphology*, 70(3):372 – 397, 2005. ISSN 0169-555X. URL https://doi.org/10.1016/j.geomorph.2005.02.014. Tropical Rivers.

J. Le Coz, A. Hauet, G. Pierrefeu, G. Dramais, and B. Camenen. Performance of image-based velocimetry (LSPIV) applied to flash-flood discharge measurements in Mediterranean rivers. *Journal of Hydrology*, 394(1):42–52, 2010. ISSN 0022-1694. URL https://doi.org/10.1016/j.jhydrol.2010.05.049.

M. Le Lay. *Modélisation hydrologique dans un contexte de variabilité hydro-climatique. Une approche comparative pour l'étude du cycle hydrologique à méso-échelle au Bénin.* PhD thesis, Institut National Polytechnique de Grenoble - INPG, 2006. URL https://tel.archives-ouvertes.fr/tel-00116912.

M. Le Mesnil, R. Moussa, J.-B. Charlier, and Y. Caballero. Impact of karst areas on runoff generation, lateral flow and interbasin groundwater flow at the storm-event timescale. *Hydrology and Earth System Sciences*, 25(3):1259–1282, 2021. URL https://doi.org/10.5194/hess-25-1259-2021.

C.-C. Lee and C.-K. Wang. Effect of flying altitude and pulse repetition frequency on laser scanner penetration rate for digital elevation model generation in a tropical forest. *GIScience & Remote Sensing*, 55(6):817–838, 2018. URL https://doi.org/10.1080/15481603.2018.1457131.

L.B. Leopold and T.J. Maddock. The hydraulic geometry of stream channels and some physiographic implications. *USGS Numbered Series*, 252:57pp, 1953. URL https://pubs.er.usgs.gov/publication/pp252.

X. Liang, D.P. Lettenmaier, E.F. Wood, and S.J. Burges. A simple hydrologically based model of land surface water and energy fluxes for general circulation models. *Journal of Geophysical Research: Atmospheres*, 99(D7):14415–14428, 1994.

F. Lobligeois. *Mieux connaître la distribution spatiale des pluies améliore-t-il la modélisation des crues ? Diagnostic sur 181 bassins versants français*. Phd thesis, AgroParisTech, March 2014. URL https://hal.inrae.fr/tel-02600722.

A.C. Lorenc, S.P. Ballard, R.S. Bell, N.B. Ingleby, P.L.F. Andrews, D.M. Barker, J.R. Bray, A.M. Clayton, T. Dalby, D. Li, et al. The Met. Office global three-dimensional variational data assimilation scheme. *Quarterly Journal of the Royal Meteorological Society*, 126(570):2991–3012, 2000. URL https://doi.org/10.1002/qj.49712657002.

K. Ludwig and M. Bremicker. Freiburger schriften zur hydrologie.

S. Ma. Wrapping Python-Fortran du code DassFlow2D. Master's thesis, 2021.

T. Malou and J. Monnier. Double-scale diffusive wave model dedicated to spatial river observation and associated covariance kernel for variational data assimilation. In *EGU General Assembly Conference Abstracts*, pages EGU21–10355, 2021. URL https://doi.org/10.5194/egusphere-egu21-10355.

T. Malou and J. Monnier. Covariance kernels investigation from diffusive wave equations for data assimilation in hydrology. *Inverse Problems*, 2022. URL https://doi.org/10.1088/1361-6420/ac509d.

T. Malou, P.-A. Garambois, A. Paris, J. Monnier, and K. Larnier. Generation and analysis of stage-fall-discharge laws from coupled hydrological-hydraulic river network model integrating sparse multi-satellite data. *Journal of Hydrology*, 603:126993, 2021. URL https://ui.adsabs.harvard.edu/abs/2020AGUFMH082...09M.

J. Margat and V. Andréassian. *L'eau*, volume 155. Le Cavalier Bleu, 2008.

J. Marin and J. Monnier. Superposition of local zoom models and simultaneous calibration for 1D-2D shallow water flows. *Mathematics and Computers in Simulation*, 80(3):547–560, 2009. URL https://doi.org/10.1016/j.matcom.2009.09.001.

N. Martin and J. Monnier. Inverse rheometry and basal properties inference for pseudoplastic geophysical flows. *European Journal of Mechanics-B/Fluids*, 50:110–126, 2015. URL https://doi.org/10.1016/j.euromechflu.2014.11.011.

V. Masson-Delmotte, P. Zhai, H.-O. Pörtner, D. Roberts, J. Skea, P.R. Shukla, A. Pirani, W. Moufouma-Okia, C. Péan, R. Pidcock, et al. Global warming of 1.5Â°c. *An IPCC Special Report on the impacts of global warming*, 1(5), 2018. URL http://pure.iiasa.ac.at/15716.

T. Mathevet. *Quels modèles pluie-débit globaux au pas de temps horaire? Développements empiriques et comparaison de modèles sur un large échantillon de bassins versants*. PhD thesis, ENGREF Paris, 2005. URL https://hal.inrae.fr/tel-02587642.

C. Michel. Un modèle pluie-débit journalier à trois paramètres. *La Houille Blanche*, (2):113–122, 1989. URL https://doi.org/10.1051/lhb/1989007.

E. Miglio, S. Perotto, and F. Saleri. Model coupling techniques for free-surface flow problems: Part I. *Nonlinear Analysis: Theory, Methods & Applications*, 63(5-7):e1885–e1896, 2005a. URL https://doi.org/10.1016/j.na.2005.03.083.

E. Miglio, S. Perotto, and F. Saleri. Model coupling techniques for free-surface flow problems: Part II. *Nonlinear Analysis: Theory, Methods & Applications*, 63(5-7):e1897–e1908, 2005b. URL https://doi.org/10.1016/j.na.2005.03.085.

P.C.D. Milly. Climate, soil water storage, and the average annual water balance. *Water Resources Research*, 30(7):2143–2156, 1994. URL https://doi.org/10.1029/94WR00586.

M.S. Mizielinski, M.J. Roberts, P.L. Vidale, R. Schiemann, M.-E. Demory, J. Strachan, T. Edwards, A. Stephens, B.N. Lawrence, M. Pritchard, et al. High-resolution global climate modelling: the UPSCALE project, a large-simulation campaign. *Geoscientific Model Development*, 7(4):1629–1640, 2014. URL https://doi.org/10.5194/gmd-7-1629-2014.

J. Monnier. Variational Data Assimilation and Model Learning. Lecture, November 2021. URL https://hal.archives-ouvertes.fr/hal-03040047.

J. Monnier, F. Couderc, D. Dartus, K. Larnier, R. Madec, and J.-P. Vila. Inverse algorithms for 2D shallow water equations in presence of wet dry fronts: Application to flood plain dynamics. *Advances in Water Resources*, 97:11–24, 2016. URL https://doi.org/10.1016/j.advwatres.2016.07.005.

J. Monnier, L. Pujol, L. Villenave, and P.-A. Garambois. DassFlow v3.0 : User and Developer Guide. Technical report, 2022.

A. Montazem. *Représentation et segmentation hydraulique effective de rivières pour le calcul de débit par altimetrie SWOT à l'échelle globale*. Phd thesis, Universite de Toulouse III Paul Sabatier, Toulouse, France, 2018. URL https://tel.archives-ouvertes.fr/tel-03468685.

A. Montazem, P.-A. Garambois, P. Finaud-Guyot, S. Calmant, J. Monnier, and D. Moreira. Physical basis for river segmentation from water surface observables. In *AGU Fall Meeting Abstracts*, volume 2017, pages H44H–06, December 2017. URL https://ui.adsabs.harvard.edu/abs/2017AGUFM.H44H..06S.

A.S. Montazem, P.-A. Garambois, S. Calmant, P. Finaud-Guyot, J. Monnier, D.M. Moreira, J.T. Minear, and S. Biancamaria. Wavelet-based river segmentation using hydraulic control-preserving water surface elevation profile properties. *Geophysical Research Letters*, 46(12):6534–6543, JUN 28 2019. ISSN 0094-8276. URL https://doi.org/10.1029/2019GL082986.

D.M. Moreira. *Apport des données de géodésie spatial pour l'étude du bassin hydrologique amazonien*. PhD thesis, LEGOS - Laboratoire d'Etudes en Géophysique et Océanographie Spatiale, 2016. URL http://www.theses.fr/2016TOU30372.

M.L. Mul, R.K. Mutiibwa, J.W.A. Foppen, S. Uhlenbrook, and H.H.G. Savenije. Identification of groundwater flow systems using geological mapping and chemical spring analysis in South Pare Mountains, Tanzania. *Physics and Chemistry of the Earth, Parts A/B/C*, 32(15-18):1015–1022, 2007. URL https://doi.org/10.1016/j.pce.2007.07.004.

C.A. Mulatu, A. Crosato, E.J. Langendoen, M.M. Moges, and M.E. McClain. Alteration of the Fogera Plain flood regime due to Ribb Dam construction, Upper Blue Nile Basin, Ethiopia. *Journal of Applied Water Engineering and Research*, pages 1–22, 2021. URL https://doi.org/10.1080/23249676.2021.1961618.

A. Musy and C. Higy. *Hydrologie: Une science de la nature*, volume 21. PPUR presses polytechniques, 2004.

J. Neal, G. Schumann, and P.D. Bates. A subgrid channel model for simulating river hydraulics and floodplain inundation over large and data sparse areas. *Water Resources Research*, 48(11), 2012. URL https://doi.org/10.1029/2012WR012514.

J. Negrel. *Estimation du débit des fleuves à partir de mesures satellitaires des variables de surface sans mesures in situ*. PhD thesis, Montpellier 2, 2011. URL https://hal.archives-ouvertes.fr/tel-02596771/.

S. Nepal, J. Chen, D.J. Penton, L.E. Neumann, H. Zheng, and S. Wahid. Spatial GR4J conceptualization of the Tamor glaciated alpine catchment in Eastern Nepal: evaluation of GR4JSG against streamflow and MODIS snow extent. *Hydrological processes*, 31(1):51–68, 2017. URL https://doi.org/10.1002/hyp.10962.

P. Nguyen, A. Thorstensen, S. Sorooshian, K. Hsu, A. AghaKouchak, B.F. Sanders, V. Koren, Z. Cui, and M. Smith. A high resolution coupled hydrologic-hydraulic model (HiResFlood-UCI) for flash flood modeling. *Journal of Hydrology*, 541:401–420, 2016. URL https://doi.org/10.1016/j.jhydrol.2015.10.047.

N. Nikora, V. Nikora, and T. O'Donoghue. Velocity profiles in vegetated open-channel flows: combined effects of multiple mechanisms. *Journal of Hydraulic Engineering*, 139(10):1021–1032, 2013. URL https://doi.org/10.1061/(ASCE)HY.1943-7900.0000779.

V. Nikora, K. Koll, I. McEwan, S. McLean, and A. Dittrich. Velocity distribution in the roughness layer of rough-bed flows. *Journal of Hydraulic Engineering*, 130(10):1036–1042, 2004. URL https://doi.org/10.1061/(ASCE)0733-9429(2004)130:10(1036).

T. Oki, D. Entekhabi, and T.I. Harrold. The global water cycle. *Global energy and water cycles*, 10:27, 1999.

F.E. O'Loughlin, J. Neal, G.J.P. Schumann, E. Beighley, and P.D. Bates. A LISFLOOD-FP hydraulic model of the middle reach of the Congo. *Journal of Hydrology*, page 124203, 2019. ISSN 0022-1694. doi: http://doi.org/10.1016/j.jhydrol.2019.124203.

World Meteorological Organization. GCOS/GTOS plan for terrestrial climate-related observations, version 2.0. URL https://library.wmo.int/doc_num.php?explnum_id=3891.

World Meteorological Organization. GCOS systematic observation requirements for satellite-based products for climate 2011 update: Supplemental details to the satellite-based component of the implementation plan for the global observing system for climate in support of the UNFCCC (2010 update)., 2011. URL https://library.wmo.int/doc_num.php?explnum_id=3710.

H. Oubanas, I. Gejadze, P.-O. Malaterre, M. Durand, R. Wei, R.P.M. Frasson, and A. Domeneghetti. Discharge estimation in ungauged basins through variational data assimilation: The potential of the SWOT mission. *Water Resources Research*, 54(3):2405–2423, 2018a. URL https://doi.org/10.1002/2017WR021735.

H. Oubanas, I. Gejadze, P.-O. Malaterre, and F. Mercier. River discharge estimation from synthetic SWOT-type observations using variational data assimilation and the full Saint-Venant hydraulic model. *Journal of Hydrology*, 559:638 – 647, 2018b. ISSN 0022-1694. URL http://doi.org/10.1016/j.jhydrol.2018.02.004.

L. Oudin, F. Hervieu, C. Michel, C. Perrin, V. Andréassian, F. Anctil, and C. Loumagne. Which potential evapotranspiration input for a lumped rainfall-runoff model?: Part 2 Towards a simple and efficient potential evapotranspiration model for rainfall-runoff modelling. *Journal of hydrology*, 303(1-4):290–306, 2005. URL https://doi.org/10.1016/j.jhydrol.2004.08.026.

S. Ouillon. *Modélisation mathématique de l'hydrodynamique à surface libre et du transport en suspension de sédiments non cohésifs: aide à l'interprétation d'images spatiales*. PhD thesis, Toulouse, INPT, 1993. URL http://www.theses.fr/1993INPT039H.

I. Özgen, J.-H. Zhao, D.-F. Liang, and R. Hinkelmann. Wave propagation speeds and source term influences in single and integral porosity shallow water equations. *Water Science and Engineering*, 10(4):275–286, 2017. URL https://doi.org/10.1016/j.wse.2017.12.003.

R.C.D. Paiva, D.C. Buarque, W. Collischonn, M-P. Bonnet, F. Frappart, S. Calmant, and E.M. Carlos. Large-scale hydrologic and hydrodynamic modeling of the amazon river basin. *Water Resources Research*, 49(3):1226–1243, 2013a. URL https://doi.org/10.1002/wrcr.20067.

R.C.D. Paiva, W. Collischonn, and D.C. Buarque. Validation of a full hydrodynamic model for large-scale hydrologic modelling in the Amazon. *Hydrological Processes*, 27(3):333–346, 2013b. URL https://doi.org/10.1002/hyp.8425.

R.C.D. de Paiva, W. Collischonn, M.-P. Bonnet, L.G.G. De Goncalves, S. Calmant, A. Getirana, and J. Santos da Silva. Assimilating in situ and radar altimetry data into a large-scale hydrologic-hydrodynamic model for streamflow forecast in the amazon. *Hydrology and Earth System Sciences*, 17(7):2929–2946, 2013c. URL https://doi.org/10.5194/hess-17-2929-2013.

A.N. Papanicolaou, M. Elhakeem, and B. Wardman. Calibration and verification of a 2D hydrodynamic model for simulating flow around emergent bendway weir structures. *Journal of Hydraulic Engineering*, 137(1):75–89, 2011. URL https://doi.org/10.1061/(ASCE)HY.1943-7900.0000280.

A. Paris, R.C.D. de Paiva, J.S. da Silva, D.M. Moreira, S. Calmant, P.-A. Garambois, W. Collischonn, M-P. Bonnet, and F. Seyler. Stage-discharge rating curves based on satellite altimetry and modeled discharge in the Amazon basin. *Water Resources Research*, 52(5):3787–3814, 2016. URL https://doi.org/10.1002/2014WR016618.

E. Park and E.M. Latrubesse. The hydro-geomorphologic complexity of the lower amazon river floodplain and hydrological connectivity assessed by remote sensing and field control. *Remote Sensing of Environment*, 198:321 – 332, 2017. ISSN 0034-4257. URL http://doi.org/10.1016/j.rse.2017.06.021.

S.K. Park and L. Xu. *Data Assimilation for Atmospheric, Oceanic and Hydrologic Applications (Vol. II)*. Springer, 2013.

T.M. Pavelsky, M.T. Durand, K.M. Andreadis, R.E. Beighley, R.C.D. Paiva, G.H. Allen, and Z.F. Miller. Assessing the potential global extent of SWOT river discharge observations. *Journal of Hydrology*, 519:1516–1525, 2014. URL https://doi.org/10.1016/j.jhydrol.2014.08.044.

J-F. Pekel, A. Cottam, and N. Gorelick. High-resolution mapping of global surface water and its long-term changes. *Nature*, 540(418):19, 2016. URL https://doi.org/10.1038/nature20584.

D. Peredo, M.-H. Ramos, V. Andréassian, and L. Oudin. Investigating hydrological model versatility to simulate extreme flood events. *Hydrological Sciences Journal*, (just-accepted), 2022. URL https://doi.org/10.1080/02626667.2022.2030864.

C. Perrin, C. Michel, and V. Andréassian. Improvement of a parsimonious model for streamflow simulation. *Journal of hydrology*, 279(1-4):275–289, 2003. URL https://doi.org/10.1016/S0022-1694(03)00225-7.

C. Perrin, C. Michel, and V. Andréassian. Modèles hydrologiques du génie rural (GR). *Cemagref, UR Hydrosystèmes et Bioprocédés*, 2007.

G. Pichard. Les crues sur le bas Rhône de 1500 à nos jours. Pour une histoire hydro-climatique. *Méditerranée*, 82(3):105–116, 1995. URL https://www.persee.fr/doc/medit_0025-8296_1995_num_82_3_2908.

P.M. Pontes, F.M. Fan, A.S. Fleischmann, R.C.D. Paiva, D.C. Buarque, V.A. Siqueira, P.F. Jardim, M.V. Sorribas, and W. Collischonn. MGB-IPH model for hydrological and hydraulic simulation of large floodplain river systems coupled with open source GIS. *Environmental Modelling & Software*, 94:1–20, 2017. URL https://doi.org/10.1016/j.envsoft.2017.03.029.

S. Proust, D. Bousmar, N. Riviere, A. Paquier, and Y. Zech. Nonuniform flow in compound channel: A 1-D method for assessing water level and discharge distribution. *Water resources research*, 45(12), 2009. URL https://doi.org/10.1029/2009WR008202.

L. Pujol, P.-A. Garambois, P. Finaud-Guyot, J. Monnier, K. Larnier, R. Mosé, S. Biancamaria, H. Yesou, D. Moreira, A. Paris, and S. Calmant. Estimation of multiple inflows and effective channel by assimilation of multi-satellite hydraulic signatures: The ungauged anabranching negro river. *Journal of Hydrology*, 591:125331, 2020. ISSN 0022-1694. URL https://doi.org/10.1016/j.jhydrol.2020.125331.

L. Pujol, P.-A. Garambois, and J. Monnier. Multi-dimensional hydrological-hydraulic coupling with multi-variate variational data assimilation for river networks and floodplains: forward and inverse cases with DassFlow. *Geoscientific Model Development*, 2022. submitted.

M. Raissi, P. Perdikaris, and G.E. Karniadakis. Physics-informed neural networks: A deep learning framework for solving forward and inverse problems involving nonlinear partial differential equations. *Journal of Computational physics*, 378:686–707, 2019. URL https://doi.org/10.1016/j.jcp.2018.10.045.

W.J. Rawls, L.R. Ahuja, D.L. Brakensiek, A. Shirmohammadi, et al. *Infiltration and soil water movement.* McGraw-Hill Inc., 1992.

F. Remy, P. Mazzega, S. Houry, C. Brossier, and J.F. Minster. Mapping of the topography of continental ice by inversion of satellite-altimeter data. *Journal of Glaciology*, 35(119):98–107, 1989. URL https://doi.org/10.3189/002214389793701419.

J.K. Ridley and K.C. Partington. A model of satellite radar altimeter return from ice sheets. *Remote Sensing*, 9(4):601–624, 1988. URL https://doi.org/10.1080/01431168808954881.

E. Rodríguez. SWOT Surface Water and Ocean Topography Mission (SWOT). JPL document, 2012. URL https://swot.jpl.nasa.gov/system/documents/files/2176_2176_D-61923_SRD_Rev_B_20181113.pdf.

E. Rodríguez, Esteban-Fernandez D., E. Peral, C.W. Chen, J-W. Blesser, and B. Williams. *Wide-Swath Altimetry: A Review. In D. Stammer A. Cazenave (Eds.).* 2018. ISBN 9781315151779.

E. Rodríguez, M. Durand, and R.P.M. Frasson. Observing rivers with varying spatial scales. *Water resources research*, 56(9), 2020. URL https://doi.org/10.1029/2019WR026476.

H. Roux. *Estimation de paramètres en hydraulique fluviale, à partir de données caractéristiques de l'imagerie aérienne*. PhD thesis, 2004. URL http://ethesis.inp-toulouse.fr/archive/00000040/.

H. Roux and D. Dartus. Parameter identification using optimization techniques in open-channel inverse problems. *J. of Hyd. Res.*, 43:311–320, 2005. URL https://doi.org/10.1080/00221680509500125. 3.

H. Roux and D. Dartus. Use of parameter optimization to estimate a flood wave: Potential applications to remote sensing of rivers. *J. of Hydrology*, 328:258–266, 2006. URL https://doi.org/10.1016/j.jhydrol.2005.12.025.

H. Roux, D. Labat, P. A. Garambois, M.-M. Maubourguet, J. Chorda, and D. Dartus. A physically-based parsimonious hydrological model for flash floods in mediterranean catchment. *Nat. Hazards Earth Syst. Sci. J1 - NHESS*, 161:2567–2582, 2011. URL https://doi.org/10.5194/nhess-11-2567-2011. Special Issue.

P.G. Samuels. Backwater lengths in rivers. *Proceedings of the Institution of Civil Engineers*, 87(4): 571–582, 1989. URL https://doi.org/10.1680/iicep.1989.3779.

B.F. Sanders, J.E. Schubert, and R.L. Detwiler. ParBreZo: A parallel, unstructured grid, Godunov-type, shallow-water code for high-resolution flood inundation modeling at the regional scale. *Advances in Water Resources*, 33(12):1456–1467, 2010. URL https://doi.org/10.1016/j.advwatres.2010.07.007.

L. Santos, G. Thirel, and C. Perrin. Continuous state-space representation of a bucket-type rainfall-runoff model: a case study with the GR4 model using state-space GR4 (version 1.0). *Geoscientific Model Development*, 11(4):1591–1605, 2018. URL https://doi.org/10.5194/gmd-11-1591-2018.

C. Sart, J.-P. Baume, P.-O. Malaterre, and V. Guinot. Adaptation of Preissmann's scheme for transcritical open channel flows. *Journal of Hydraulic Research*, 48(4):428–440, 2010. URL https://doi.org/10.1080/00221686.2010.491648.

R. Schneider, P.N. Godiksen, H. Villadsen, H. Madsen, and P. Bauer-Gottwein. Application of CryoSat-2 altimetry data for river analysis and modelling. *Hydrology and Earth System Sciences*, 21(2):751–764, 2017. URL https://doi.org/10.5194/hess-21-751-2017.

J. Schuite, N. Flipo, N. Massei, A. Rivière, and F. Baratelli. Improving the spectral analysis of hydrological signals to efficiently constrain watershed properties. *Water Resources Research*, 55(5):4043–4065, 2019. doi: 10.1029/2018WR024579. URL https://agupubs.onlinelibrary.wiley.com/doi/abs/10.1029/2018WR024579.

G. Schumann and A. Domeneghetti. Exploiting the proliferation of current and future satellite observations of rivers. *Hydrological Processes*, 30(16):2891–2896, 2016. URL https://doi.org/10.1002/hyp.10825.

D.-J. Seo, L. Cajina, R. Corby, and T. Howieson. Automatic state updating for operational streamflow forecasting via variational data assimilation. *Journal of hydrology*, 367(3-4):255–275, 2009. URL https://doi.org/10.1016/j.jhydrol.2009.01.019.

V.P. Singh. *Kinematic wave modeling in water resources: Environmental hydrology*. John Wiley & Sons, 1997.

SMEAG. Le bassin versant de la garonne. https://www.smeag.fr/le-bassin-versant-de-la-garonne.html. Accessed: 2021-10-28.

B. Sridharan, P.D. Bates, D. Sen, and S.N. Kuiry. Local-inertial shallow water model on unstructured triangular grids. *Advances in Water Resources*, 152:103930, 2021. URL https://doi.org/10.1016/j.advwatres.2021.103930.

J.G.C. Steinstraesser, C. Delenne, P. Finaud-Guyot, V. Guinot, J.K. Casapia, and A. Rousseau. SW2D-LEMON: a new software for upscaled shallow water modeling. In *Simhydro 2021-6th International Conference Models for complex and global water issues-Practices and expectations*, 2021. URL https://hal.inria.fr/hal-03224050.

D. Strelnikova, G. Paulus, S. Käfer, K.-H. Anders, P. Mayr, H. Mader, U. Scherling, and R. Schneeberger. Drone-based optical measurements of heterogeneous surface velocity fields around fish passages at hydropower dams. *Remote Sensing*, 12(3):384, 2020. URL https://doi.org/10.3390/rs12030384.

P. Swerling. First order error propagation in a stagewise differential smoothing procedure for satellite observations. *J. Astronaut. Sci.*, 6:46–52, 1959.

A. Tarantola. *Inverse problem theory and methods for model parameter estimation*, volume 89. SIAM, 2005.

F. Tauro, A. Petroselli, and E. Arcangeletti. Assessment of drone-based surface flow observations. *Hydrological Processes*, 30(7):1114–1130, 2016. URL https://doi.org/10.1002/hyp.10698.

H. Tavakolifar, E. Shahghasemi, and S. Nazif. Evaluation of climate change impacts on extreme rainfall events characteristics using a synoptic weather typing-based daily precipitation downscaling model. *Journal of Water and Climate Change*, 8(3):388–411, 2017. URL https://doi.org/10.2166/wcc.2017.107.

V. Tayefi, S.N. Lane, R.J. Hardy, and D. Yu. A comparison of one-and two-dimensional approaches to modelling flood inundation over complex upland floodplains. *Hydrological Processes: An International Journal*, 21(23):3190–3202, 2007. URL https://doi.org/0.1002/hyp.6523.

O. Thual. *Hydrodynamique de l'environnement*. Ecole polytechnique, 2010.

Y. Tian, Y.-P. Xu, and X.-J. Zhang. Assessment of climate change impacts on river high flows through comparative use of GR4J, HBV and Xinanjiang models. *Water resources management*, 27(8):2871–2888, 2013. URL https://doi.org/10.1007/s11269-013-0321-4.

A. Tikhonov and V. Arsenine. Méthode de résolution de problémes mal posés. *Moscow: Mir*, 1977.

E. Todini. The ARNO rainfall-runoff model. *Journal of hydrology*, 175(1-4):339–382, 1996. URL https://doi.org/10.1016/S0022-1694(96)80016-3.

E.F. Toro. *Shock-capturing methods for free-surface shallow flows*. Wiley, 2001.

E.F Toro. The HLL and HLLC Riemann solvers. In *Riemann solvers and numerical methods for fluid dynamics*, pages 315–344. Springer, 2009. URL https://link.springer.com/chapter/10.1007/b79761_10.

O. Toussoun and Congrès international de géographie (11: 1925: Le Caire). *Mémoire sur l'histoire du Nil*. Imprimerie de l'Institut français d'archéologie orientale, 1992.

M. Trevethan, R. Ventura Santos, M. Ianniruberto, A. Santos, M. De Oliveira, and C. Gualtieri. Influence of tributary water chemistry on hydrodynamics and fish biogeography about the confluence of Negro and Solimões rivers, Brazil. In *Proceedings of the 11th International Symposium on EcoHydraulics (ISE 2016), Melbourne, Australia*, pages 2–7, 2016.

S. Tuozzolo, G. Lind, B. Overstreet, J. Mangano, M. Fonstad, M. Hagemann, R.P.M. Frasson, K. Larnier, P.-A. Garambois, J. Monnier, and M. Durand. Estimating river discharge with swath altimetry: A proof of concept using AirSWOT observations. *Geophysical Research Letters*, 46(3):1459–1466, 2019. URL https://doi.org/10.1029/2018GL080771.

P. Uhe, D. Mitchell, P. D. Bates, N. Addor, J. Neal, and H. E. Beck. Model cascade from meteorological drivers to river flood hazard: flood-cascade v1.0. *Geoscientific Model Development Discussions*, 2020:1–34, 2020. URL https://doi.org/10.5194/gmd-2020-280.

S. Uhlemann. *Understanding trans-basin floods in Germany: data, information and knowledge*. PhD thesis, Universität Potsdam, 2013. URL https://nbn-resolving.org/urn:nbn:de:kobv:517-opus-68868.

J.-P. Vila. Simplified Godunov schemes for 2x2 systems of conservation laws. *SIAM J. Numer. Anal.*, 23(6):1173–1192, December 1986a. ISSN 0036-1429. URL http://dx.doi.org/10.1137/0723079.

J-P. Vila. *Théorie et approximation numérique de problèmes hyperboliques non linéaires applications aux équations de Saint-Venant et à la modélisation des avalanches de neige dense*. PhD thesis, Université Paris VI, 1986b. URL http://www.theses.fr/1986PA066092.

J.-P. Vila and P. Villedieu. Convergence of an explicit finite volume scheme for first order symmetric systems. *Numerische Mathematik*, 94(3):573–602, 2003. URL https://doi.org/10.1007/s00211-002-0396-y.

A.-E. Vozinaki, G.G. Morianou, D.D. Alexakis, and I.K. Tsanis. Comparing 1D and combined 1D/2D hydraulic simulations using high-resolution topographic data: A case study of the Koiliaris basin, Greece. *Hydrological Sciences Journal*, 62(4):642–656, 2017. URL https://doi.org/10.1080/02626667.2016.1255746.

A. Weaver and P. Courtier. Correlation modelling on the sphere using a generalized diffusion equation. *Quarterly Journal of the Royal Meteorological Society*, 127(575):1815–1846, 2001. URL https://doi.org/10.1002/qj.49712757518.

M.S. Wigmosta, L.W. Vail, and D.P. Lettenmaier. A distributed hydrology-vegetation model for complex terrain. *Water resources research*, 30(6):1665–1679, 1994. URL https://doi.org/10.1029/94WR00436.

A.T. Wolf, J.A. Natharius, J.J. Danielson, B.S. Ward, and J.K. Pender. International river basins of the world. *International Journal of Water Resources Development*, 15(4):387–427, 1999. URL https://doi.org/10.1080/07900629948682.

C.-Y. Xu, L. Xiong, and V.P. Singh. *Black-Box Hydrological Models*, pages 1–48. Springer Berlin Heidelberg, Berlin, Heidelberg, 2017. ISBN 978-3-642-40457-3. URL https://doi.org/10.1007/978-3-642-40457-3_21-1.

Y. Yoon, M. Durand, C.J. Merry, E.A. Clark, K.M. Andreadis, and D.E. Alsdorf. Estimating river bathymetry from data assimilation of synthetic SWOT measurements. *Journal of Hydrology*, 464 - 465(0):363 – 375, 2012. ISSN 0022-1694. URL http://doi.org/10.1016/j.jhydrol.2012.07.028.

Y. Yoon, P.-A. Garambois, R. Paiva, M. Durand, H. Roux, and E. Beighley. Improved error estimates of a discharge algorithm for remotely sensed river measurements: Test cases on Sacramento and Garonne rivers. *Water Resources Research*, 52(1):278–294, 2016. URL https://doi.org/10.1002/2015WR017319.

R.J. Zhao, Y.-L. Zhang, L.R. Fang, X.R. Liu, and Q.S. Zhang. The Xinanjiang model. *Hydrological Forecasting Proceedings Oxford Symposium*, 129:351–356, 1980. URL https://ci.nii.ac.jp/naid/10015695212/en/.

C. Zhu, R.H. Byrd, P. Lu, and J. Nocedal. Algorithm 778: L-BFGS-B: Fortran subroutines for large-scale bound-constrained optimization. *ACM Transactions on Mathematical Software (TOMS)*, 23 (4):550–560, 1997. URL https://doi.org/10.1145/279232.279236.

List of Figures

List of Tables

List of Acronyms

1D	Mono-dimensional
2D	Bi-dimensional
ADCP	Acoustic Doppler Current Profiler
ANA	Agência Nacional de Águas e Saneamento Básico
BC	Boundary Condition
CFL	Courant-Friedrichs-Lewy
CPRM	Companhia de Pesquisas de Recursos Minerais
DEM	Digital Elevation Model
ENVISAT	ENVIronment SATellite
GAD	Gironde-Adour-Dordogne
GCOS	Global Climate Observation System
GIS	Geographic Information System
GPS	Global Positioning System
HC	hydraulic control
HiVDI	Hierarchical Variational Discharge Inversion
HLL	Harten-Lax-van Leer
HLLC	Harten-Lax-van Leer-Contact
HRU	Hydrological Response Unit
IMEX	IMplicit-EXplicit
L-BFGS-B	Limited memory Broyden-Fletcher-Goldfarb-Shanno Bound
LiDAR	Light Detection And Ranging
LPI	Local Partial Inertia
LSPIV	Large Scale Particle Image Velocimetry
LSTM	Long Short Term Memory
ML	Machine Learning
Multi-D	Multi-Dimensional
MUSCL	Monotonic Upwind Scheme for Conservation Laws
NSE	Nash-Sutcliffe Efficicency
ODE	Ordinary Differential Equation
PDE	Partial Differential Equation
RMSE	Root Mean Square Error
SAR	Synthetic Aperture Radar
SHPC	Service d’Hydrométrie et de Prévision des Crues
SW	Shallow Water
SWOT	Surface Water Ocean Topography
VDA	Variational Data Assimilation
VS	Virtual Station
WMO	World Meteorological Organization
WSE	Water Surface Elevation
XS	Cross-Section

Léo PUJOL

OPTIMAL SYNERGY OF MULTI-SOURCE DATA AND HYDRAULIC-HYDROLOGICAL MODELS FOR THE CARTOGRAPHIC MODELING OF COMPLEX HYDROSYSTEMS

Résumé

Cette thèse présente des approches de modélisation hydrauliques-hydrologiques des réseaux hydrographiques permettant d'exploiter des données multi-sources par assimilation variationnelle. Une mise en cohérence est recherchée entre la complexité des modélisations numériques des grandeurs physiques et leur observabilité hétérogène. Une des difficultés des problèmes inverses étudiés vient de l'effet corrélé des paramètres sur les signatures hydrodynamiques et de leur observabilité éparse et hétérogène en espace, temps et nature.
L'inférence de paramètres inconnus ou incertains (friction, bathymétrie, hydrogrammes latéraux) dans des modèles hydrauliques complets 1D et 2D appliqués à large échelle spatiale, à partir d'observations altimétriques et optiques est étudiée. Une nouvelle méthode multi-échelle pour la modélisation et assimilation hydraulique-hydrologique sur de réseaux hydrographiques est présentée. Des inférences précises sont obtenues quand la quantité d'information contenue dans les observables et les informations a priori est suffisante au regard des inconnues estimées.

Mots-clés:
Assimilation variationnelle, Modèles hydrauliques-hydrologiques, Equations de Saint-Venant, Altimétrie satellite, Observations multi-sourcées, Modèle multi-dimensionnel

Abstract

This manuscript presents hydraulic-hydrological modeling approaches for hydrographic networks that can exploit the multi-sourced data using variational assimilation. It aims at a synergy between the complex numerical modeling of physical quantities and the heterogeneous observability of hydrodynamic signatures. One of the difficulties of the assimilation comes from the correlated effect of parameters on quantities of interest and from their sparse observability, heterogeneous in space, time and nature.
The inference of unknown or uncertain parameters (friction, bathymetry, lateral inflows) in full shallow water 1D and 2D models applied at a large spatial scale, using altimetric and optical observations is studied. A new multi-scale method for the modeling and assimilation on hydraulic-hydrological models of hydrographic networks is presented. Accurate inferences are obtained when observables and a priori information provide sufficient knowledge of the inferred unknowns.

Keywords:
Variational Data assimilation, Hydraulic-hydrological models, Shallow Water equations, Satellite altimetry, Multi-sourced observations, Multi-dimensional model